

HAWAII

Planetary Geology Field Studies - PTYS 594A

May 17-30, 2014

UNIVERSITY OF ARIZONA - LUNAR AND PLANETARY LABORATORY

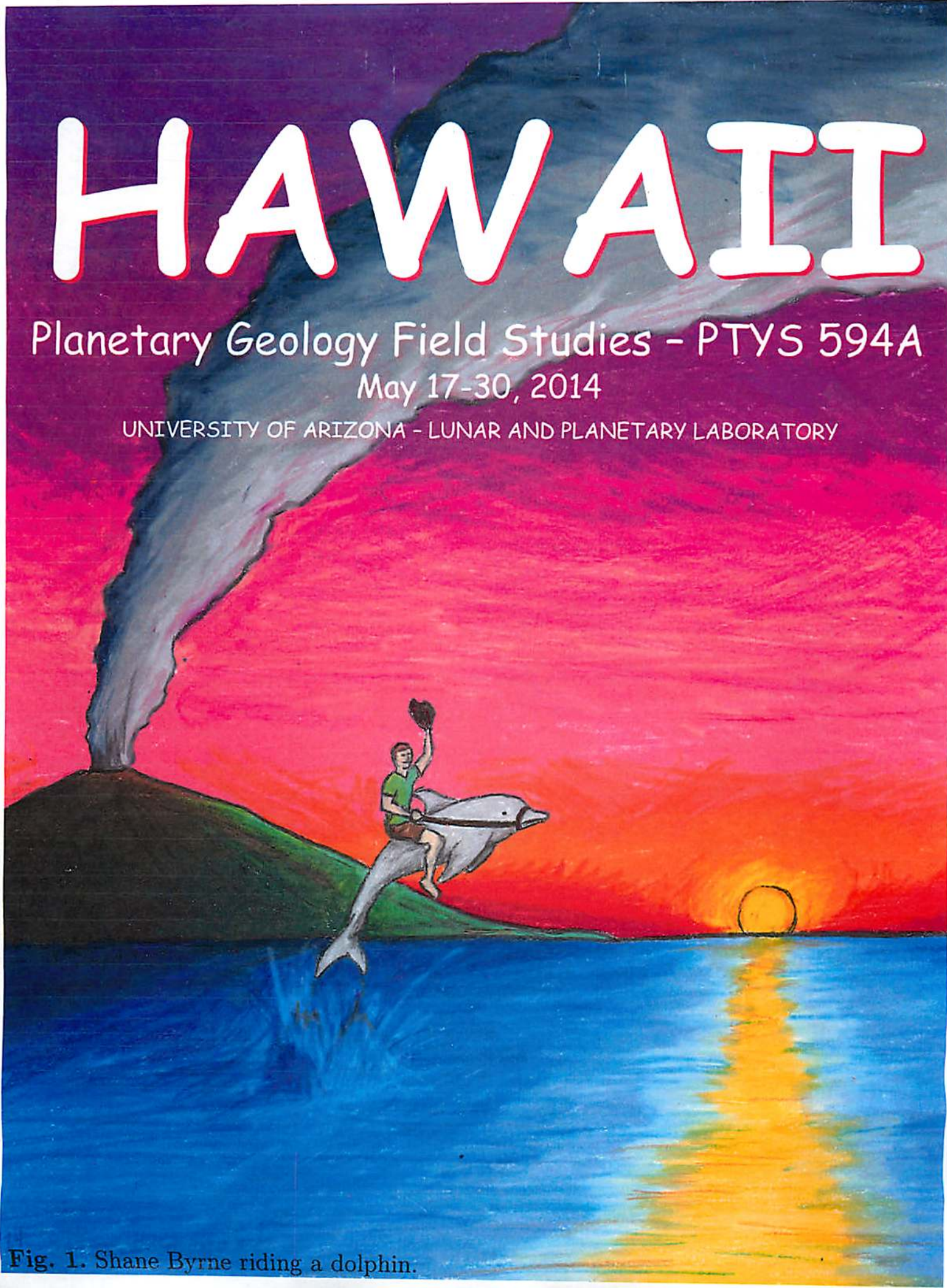


Fig. 1. Shane Byrne riding a dolphin.



Table of Contents

FIELD GEOLOGY REFERENCE GUIDE (1)

KILAUEA IKI

<u>Catherine Elder - Lava Lakes</u>	<u>28</u>
<u>Sky Beard - Basic Characteristics of Lava Fountains</u>	<u>40</u>
<u>Ali Bramson - Kilauea Iki: Drilling and Seismic Investigations</u>	<u>46</u>

ACTIVE FLOW SITE

<u>Chet Maleszewski - Cooling and Thermal Characteristics of Lava Flows</u>	<u>53</u>
<u>Ethan Schaefer - Lava Flow Rheology</u>	<u>56</u>

INTRODUCTION DAY

<u>Hannah Tanquary - Magma Plumes and the Hawaiian Islands</u>	<u>60</u>
<u>Kelly Miller - Chemical Zoning in Magma Plumes</u>	<u>63</u>
<u>Christa Van Laerhoven - Hawaiian-Emperor Seamount Chain and the Lithosphere</u>	<u>68</u>
<u>Youngmin JeongAhn - The Six Main Volcanoes on the Big Island</u>	<u>74</u>

MAUNA KEA

<u>Sarah Peacock - Mauna Loa Lava Flows</u>	<u>78</u>
<u>Tiffany Kataria - Astronomy, Telescopes, and Related Cultural Issues on Mauna Kea</u>	<u>82</u>
<u>Donna Viola - Astrobiology on Hawaii</u>	<u>88</u>
<u>Margaret Landis - Mauna Kea Glaciation</u>	<u>91</u>
<u>Jamie Molaro - Glacial History of Mauna Kea</u>	<u>95</u>
<u>Cecilia Leung - Atmospheric Studies: Trade Winds, CO₂, & Climate</u>	<u>101</u>

MISCELLANEOUS

<u>Michelle Thompson - Weathering Environments</u>	<u>107</u>
<u>Thaddeus Komacek - Phreatomagmatic Eruptions</u>	<u>114</u>
<u>Xianyu Tan - The Transport of Magma from Volcanoes</u>	<u>120</u>
<u>Molly Simon - Flora and Fauna of the Hawaiian Islands</u>	<u>128</u>
<u>James Keane - Mass Wasting</u>	<u>131</u>
<u>Sarah Morrison - Volcanic Monitoring</u>	<u>142</u>
<u>Patricio Becerra - Tephra Production and Stratigraphy</u>	<u>146</u>
<u>Alfred McEwen - Io Volcano Observer</u>	<u>150</u>
<u>Alfred McEwen - HiTREE</u>	<u>156</u>

IN-CAR ENTERTAINMENT (158)

Common Rock Forming Minerals

Dark-Colored minerals			
Hardness	Cleavage	Physical Properties	Name
Hardness >5	Excellent or good	Dark gray, blue-gray or black. May be iridescent. Cleavage in 2 planes at nearly right angles. Striations. Hardness-6	Plagioclase Feldspar
		Brown, gray, green or red. Cleavage in 2 planes at nearly right angles. Exsolution Lamellae. Hardness-6	Potassium Feldspar
		Opaque black. 2 cleavage planes at 60° and 120°. Hardness- 5.5	Hornblende (Amphibole)
	Poor or absent	Opaque red, gray, hexagonal prisms with striated flat ends. Hardness- 9	Corrundum
		Gray, brown or purple. Greasy luster. Massive or hexagonal prisms and pyramids. Transparent or translucent. Hardness- 7	Quartz Black or brown-Smoky, Purple-Amethyst
		Opaque red or brown. Waxy luster. Hardness- 7. Conchoidal Fracture	Jasper
Opaque black. Waxy luster. Hardness- 7		Flint	
Transparent- translucent dark red to black. Hardness- 7		Garnet	
Hardness < 5	Excellent or good	Colorless, purple, green, yellow, blue. Octahedral cleavage. Hardness- 4	Flourite
		Green. Splits along 1 excellent cleavage plane. Hardness- 2-3	Chlorite
		Black to dark brown. Splits along 1 excellent cleavage plane. Hardness- 2.5-3	Biotite mica
	Poor or absent	Opaque green, yellow or gray. Silky or greasy luster. Hardness- 2-5	Serpentine
		Opaque white, gray or green. Can be scratched with fingernail. Soapy feel. Hardness- 1	Talc
		Opaque earthy red to light brown. Hardness- 1.5-6	Hematite

Light-colored minerals				
Hardness	Cleavage	Physical Properties	Name	
Hardness >5	Excellent or good	White or gray. Cleavage in 2 planes at nearly right angles. Striations. Hardness-6	Plagioclase Feldspar	
		Orange, brown, white, gray, green or pink. Cleavage in 2 planes at nearly right angles. Exsolution Lamellae. Hardness-6	Potassium Feldspar	
		Pale brown, white or gray. Long slender prisms. Cleavage in 1 plane. Hardness- 6-7	Sillimanite	
	Poor or absent	Opaque red, gray, white hexagonal prisms with striated flat ends. Hardness- 9	Corrundum	
		Colorless, white, gray or other colors. Greasy luster. Massive or hexagonal prisms and pyramids. Transparent or translucent. Hardness- 7	Quartz White-Milky, Yellow-Citrine, Pink-Rose	
		Opaque gray or white. Waxy luster. Hardness- 7. Conchoidal Fracture	Chert	
Colorless, white, yellow, light brown. Translucent opaque. Laminated or massive. Cryptocrystalline. Hardness- 7		Chalcedony		
Hardness < 5	Excellent or good	Pale olive green. Conchoidal fracture. Transparent or translucent. Hardness- 7	Olivine	
		Colorless, white, yellow, blue, green. Excellent cleavage in 3 planes. Breaks into rhombohedrons. Effervesces in HCl. Hardness- 3	Calcite	
		Colorless, white, yellow, blue, green. Excellent cleavage in 3 planes. Breaks into rhombohedrons. Effervesces in HCl only if powdered. Hardness- 3.5-4	Dolomite	
		White with tints of brown. Short tabular crystals or roses. Very heavy. Hardness- 3-3.5	Barite	
		Colorless, white or gray. Massive or tabular crystals, blades or needles. Can be scratched by fingernail. Hardness- 2	Gypsum	
		Colorless, white. Cubic crystals. Salty taste. Hardness- 2.5	Halite	
		Colorless, purple, green, yellow, blue. Octahedral cleavage. Hardness- 4	Flourite	
		Colorless, yellow, brown. Splits along 1 excellent cleavage plane. Hardness- 2-2.5	Muscovite mica	
		Poor or absent	Yellow crystals or earthy masses. Hardness 1.5-2.5	Sulfur
			Opaque green, yellow or gray. Silky or greasy luster. Hardness- 2-5	Serpentine
			Opaque white, gray or green. Can be scratched with fingernail. Soapy feel. Hardness- 1	Talc
		Opaque earthy white to light brown. Hardness- 1-2	Kaolinite	

Metallic			
	Streak	Physical Properties	Name
Hardness > 5	Dark Gray	Brass yellow	Pyrite
		Dark gray-black, attracted to magnet	Magnetite
Hardness < 5	Brown	Silvery black to black tarnishes gray	Chromite
	Red Red-Brown	Silvery gray, black, or brick red	Hematite
	Dark Gray	Brass yellow, tarnishes dark brown or purple	Chalcopyrite
		Iridescent blue, purple or copper red, tarnishes dark purple	Bornite
		Silvery gray, tarnishes dull gray Cleavage good to excellent	Galena
		Dark gray to black, can be scratched with fingernail	Graphite

Sedimentary Rocks

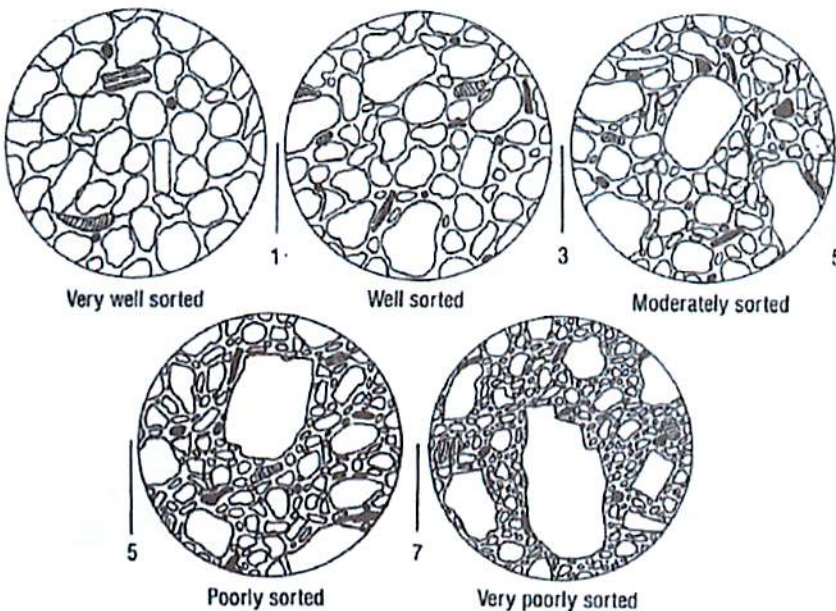
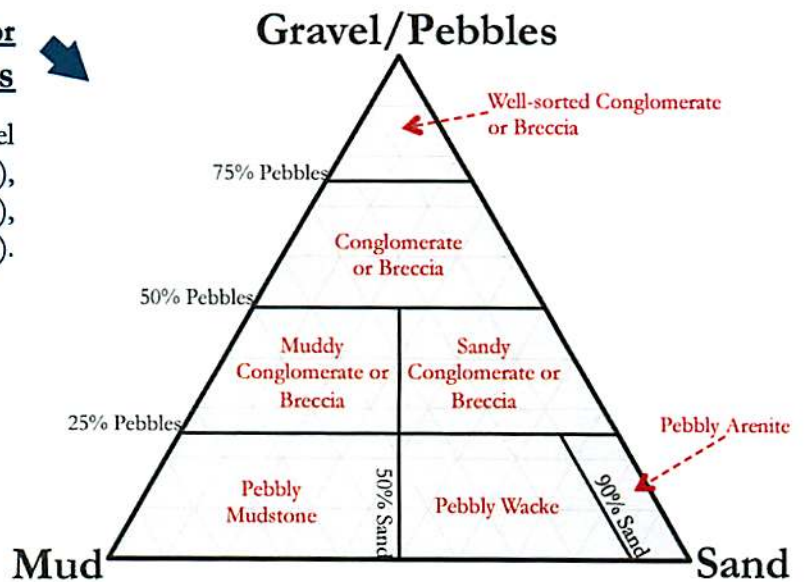
	Mudrocks (containing > 50% mud)			Rocks with <50% mud
	Silt dominant (> 2/3 of rock)	Clay and Silt	Clay dominant (> 2/3 of rock)	Sand-sized or larger grains dominant
Non-laminated	Siltstone	Mudstone	Claystone	Conglomerates, Breccias, Sandstones, etc.
Laminated	Laminated Siltstone	Mudshale	Clayshale	

← **Classification Scheme for Mudrocks**

Scheme based on clay/silt content, and whether the rock is laminated (layered) or not.

Classification Scheme for Sub-Conglomerates and Sub-Breccias

Scheme based on percent of a rock composed of: gravel or pebbles (size >2 mm), sand (2 mm > size > 1/16 mm), and mud (size < 1/16 mm).



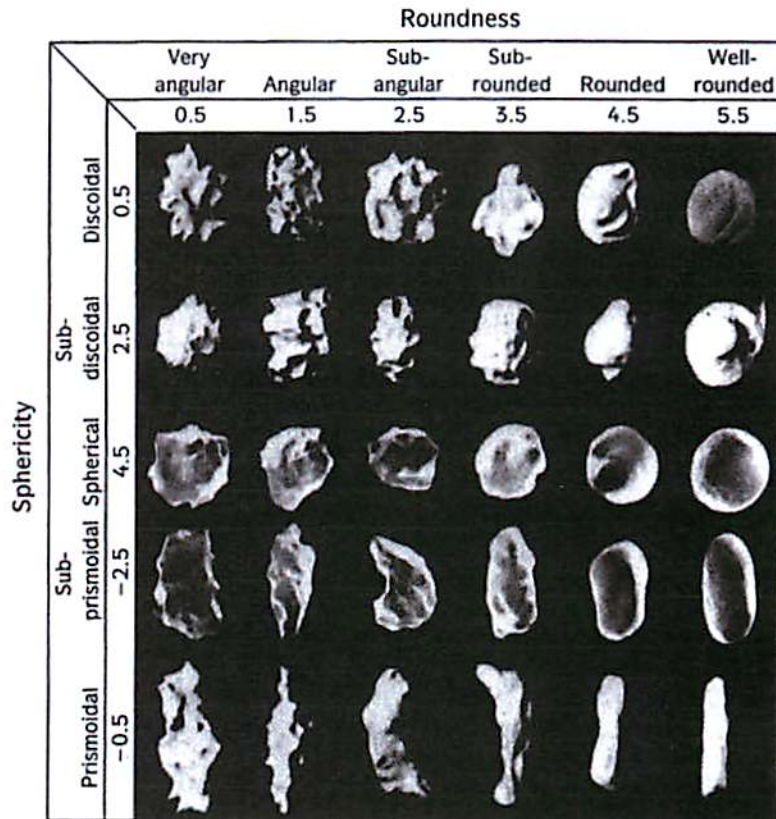
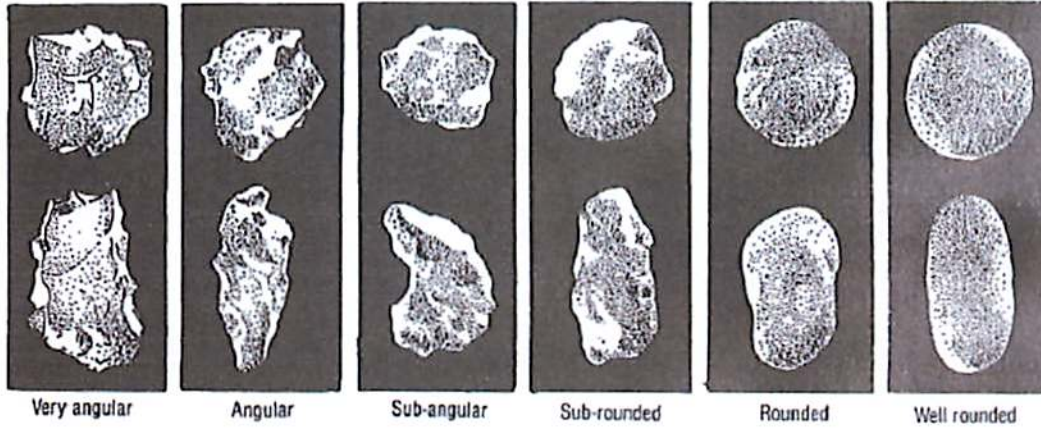
← **Estimating Sorting**

Example hand-lens view of detritus.
From Compton, 1985

Sedimentary Rocks

Degrees of Rounding

Example hand-lens view of detritus of varying degrees of roundedness. The top row are equidimensional (spherical) grains, while the lower row are elongated grains. From Compton, 1985 and Davis & Reynolds, 1996, respectively.

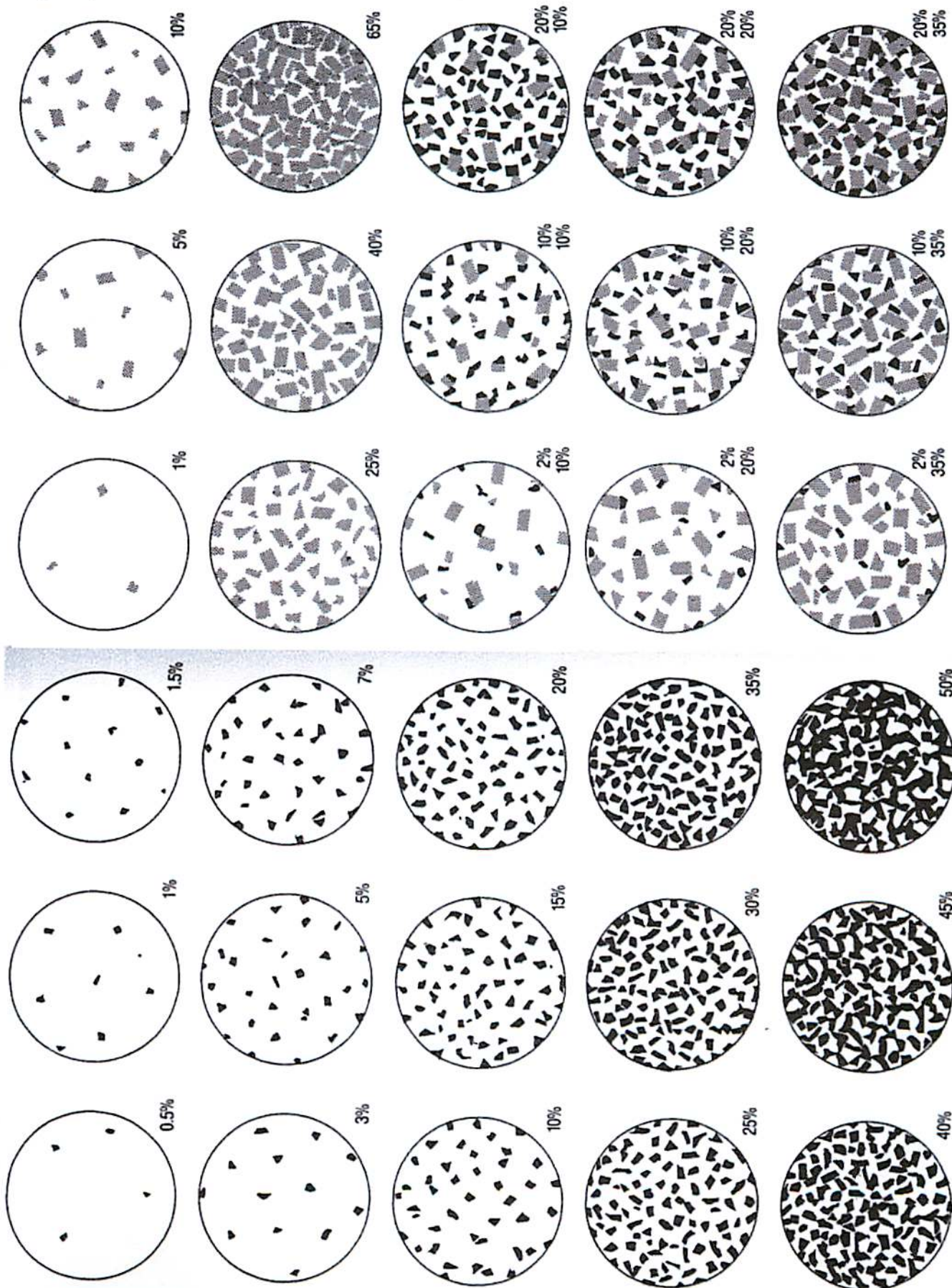


Sedimentary Rocks

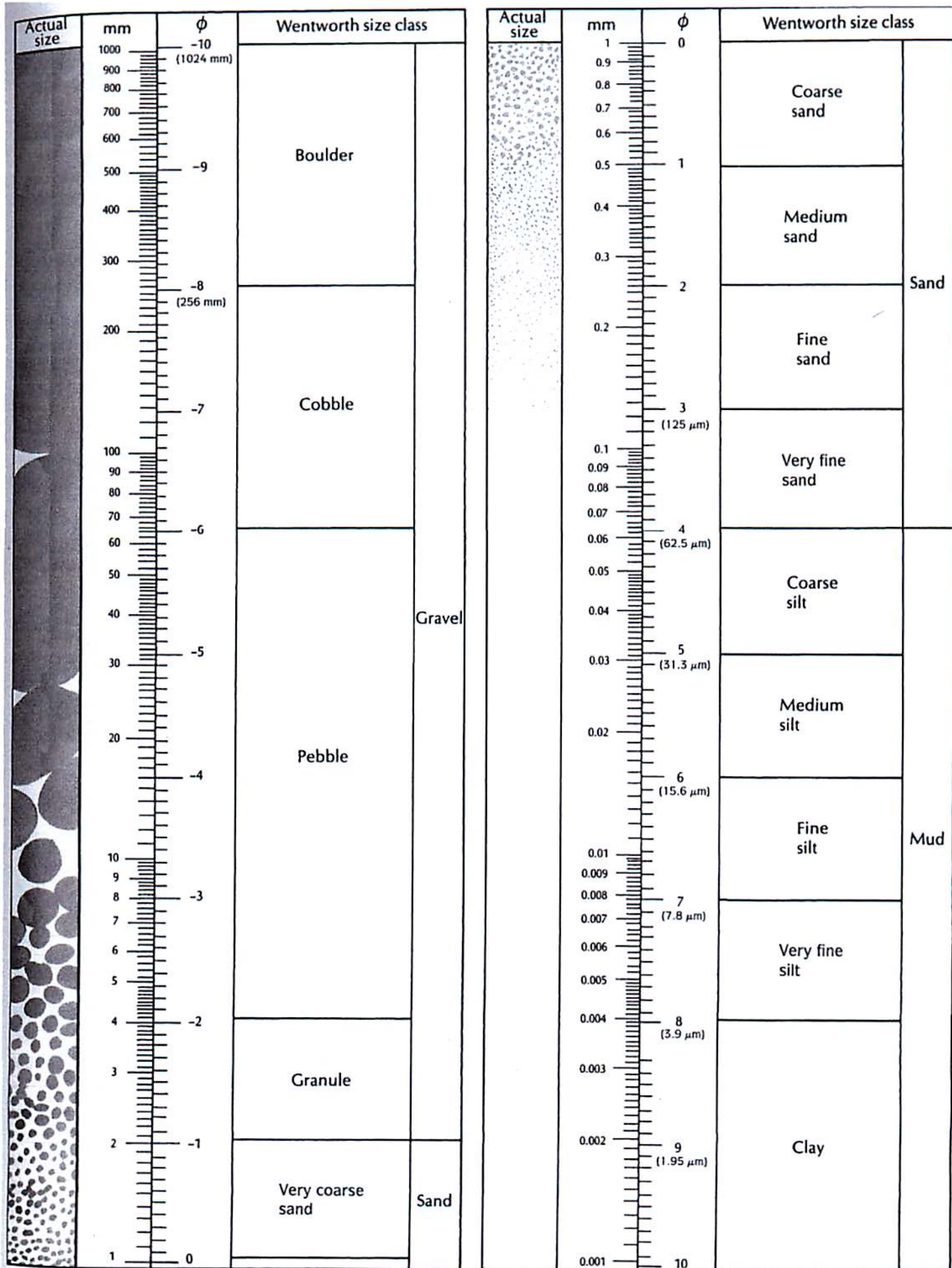
Percentage Diagrams for Estimating Composition by Volume



Example hand-lens view of rocks with varying composition. To find weight percents, simply multiply each volume percent by the specific gravity of that mineral, and re-normalize. Compton, 1985



Sedimentary Rocks








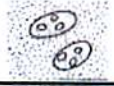




Sedimentary Rocks: Carbonates

Folk Classification Scheme for Carbonate Rocks



Folk's classification scheme is based upon the composition (and type of allochems) within a limestone. Figures from Prothero and Schwab, 2004

Principle Allochems in Limestone	Limestone Type			
	Cemented by Sparite		Cemented by Micritic Matrix	
Skeletal Grains (Bioclasts)	Biosparite		Biomicrite	
Ooids	Oosparite		Oomicrite	
Peloids	Pelsparite		Pelmicrite	
Intraclasts	Intrasparite		Intramicroite	
Limestone formed in place	Biolithite		Terrestrial Limestone	



Dunham Classification Scheme for Carbonate Rocks

Dunham's classification scheme is based upon depositional textures within a limestone.

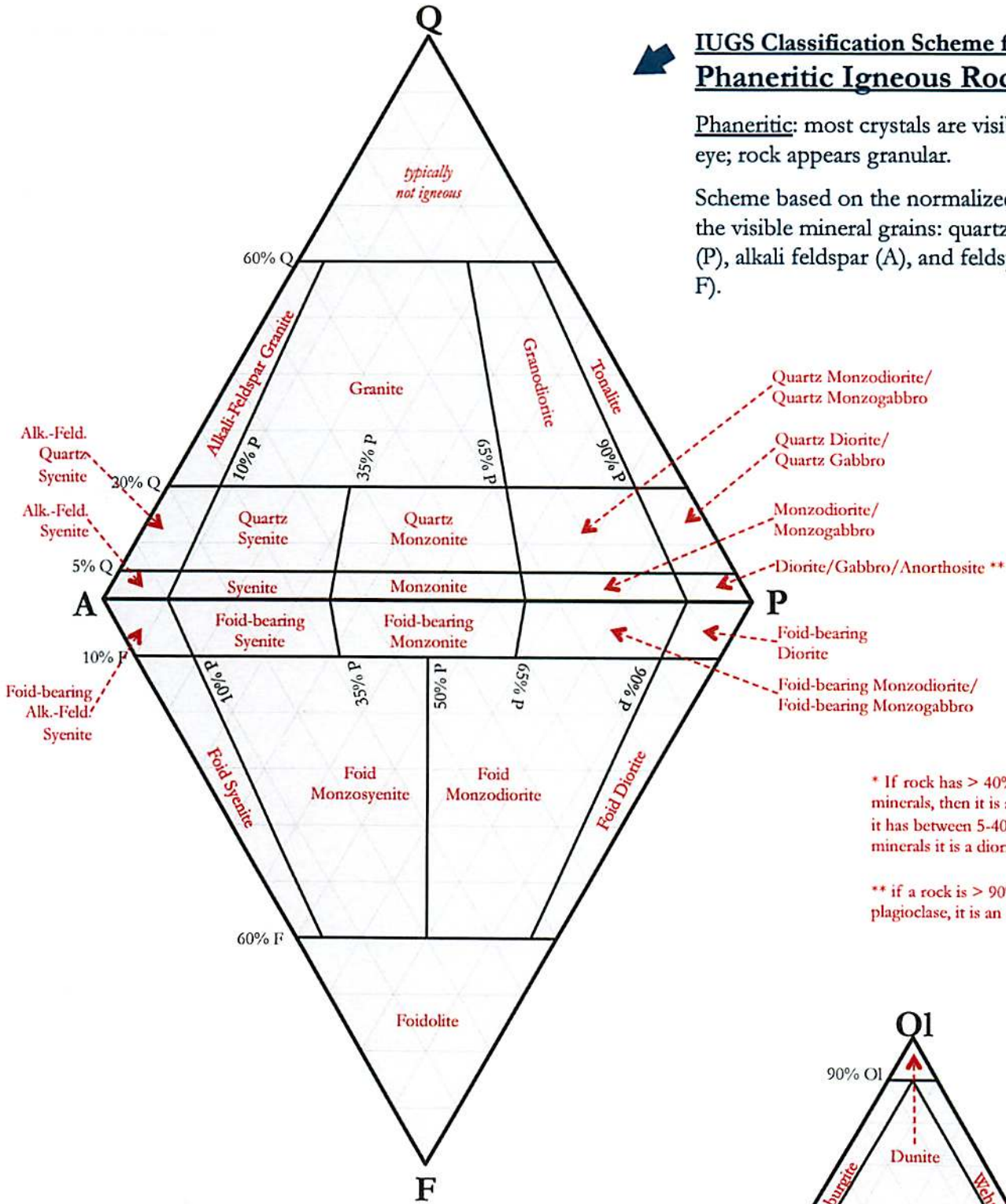
Allochthonous Limestone (original components not organically bound during deposition)				Autochthonous Limestone (original components organically bound during deposition; reef rocks)					
Of the allochems, less than 10% are larger than 2 mm			Of the allochems, greater than 10% are larger than 2 mm						
Contains carbonate mud		No mud		Matrix supported	Grain supported	Organisms acted as baffles	Organisms are encrusting and binding	Organisms building a rigid framework	
Grain supported		Grain supported							
Less than 10% grains	More than 10% grains								
Mudstone	Wackestone	Packstone	Grainstone	Floatstone	Rudstone	Bafflestone	Bindstone	Framestone	

Igneous Rocks

IUGS Classification Scheme for Phaneritic Igneous Rocks

Phaneritic: most crystals are visible to the naked eye; rock appears granular.

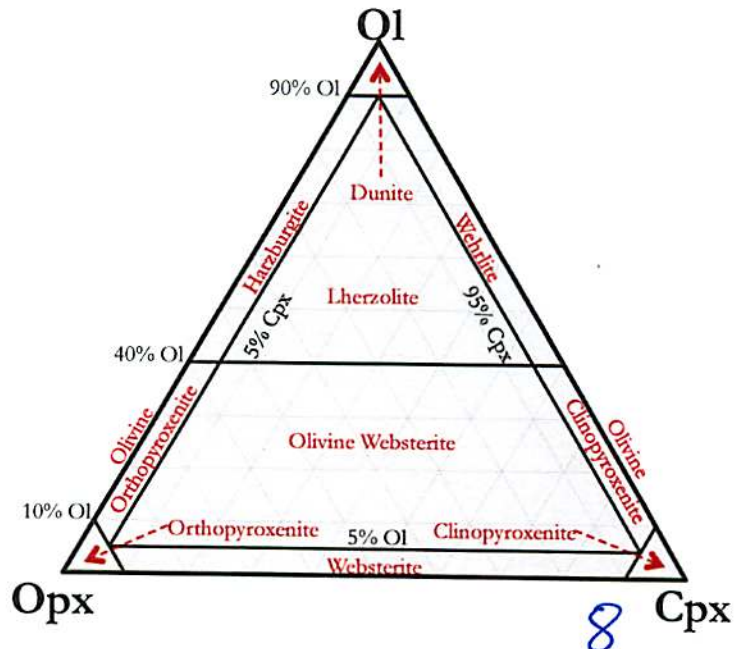
Scheme based on the normalized percentages of the visible mineral grains: quartz (Q), plagioclase (P), alkali feldspar (A), and feldspathoids (foids, F).



IUGS Classification Scheme for Phaneritic Ultramafic Igneous Rocks (1)

Ultramafic: more than 90% of the total minerals are mafic.

Scheme based on the normalized percentages of the visible minerals: olivine (Ol), orthopyroxene (Opx), and clinopyroxene (Cpx).

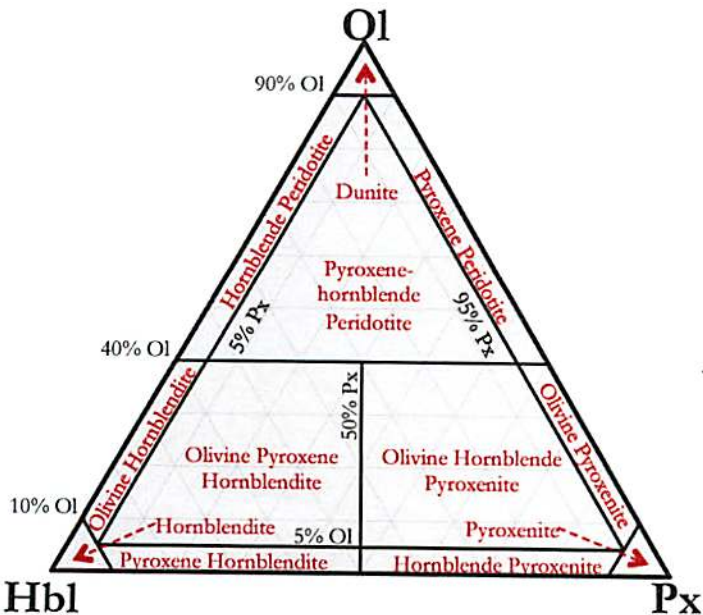
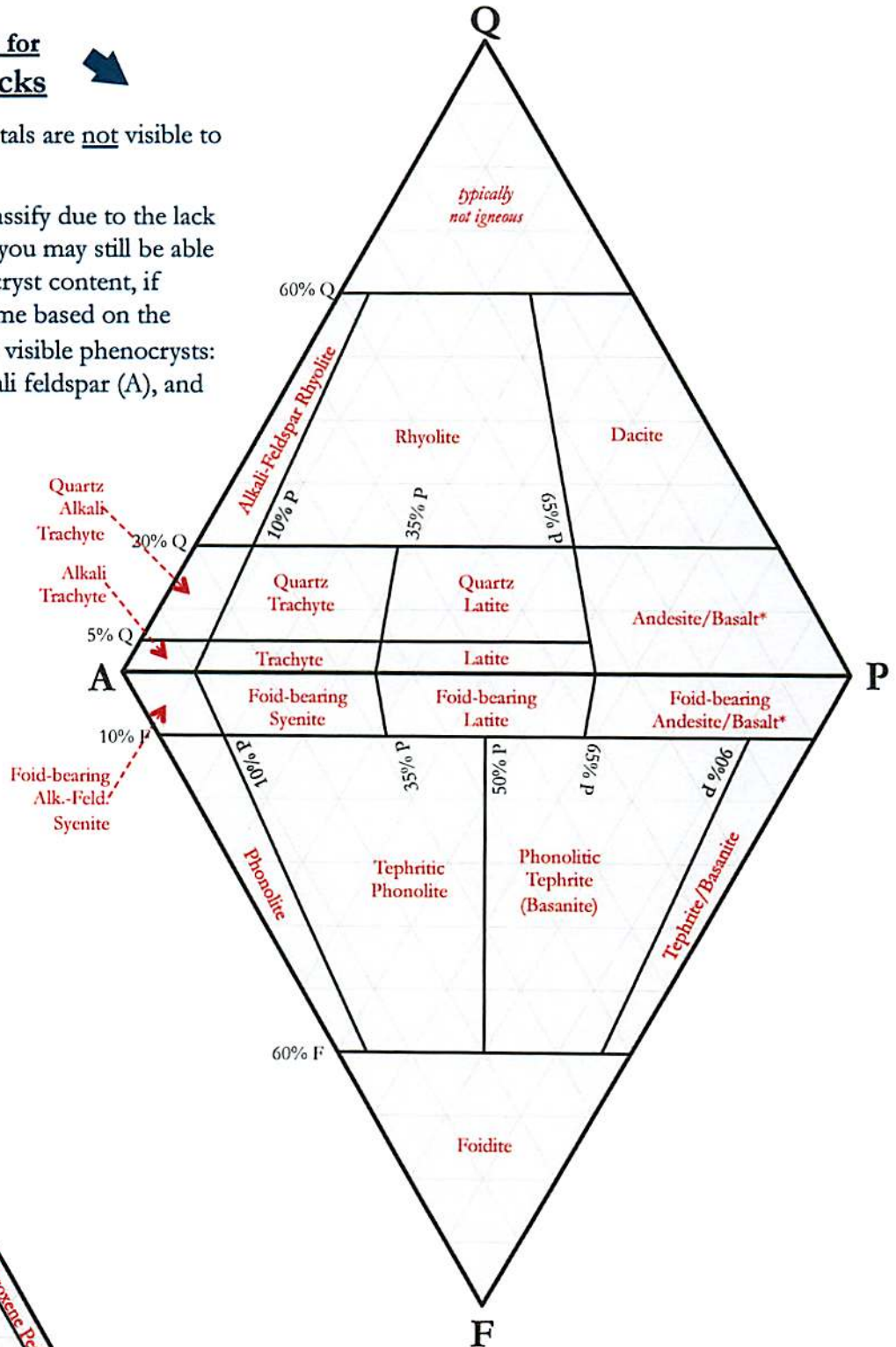


Igneous Rocks

IUGS Classification Scheme for Aphanitic Igneous Rocks

Aphanitic: the majority of crystals are not visible to the naked eye.

Aphanitic rocks are hard to classify due to the lack of visible minerals. However, you may still be able to identify them based on phenocryst content, if phenocrysts are present. Scheme based on the normalized percentages of the visible phenocrysts: quartz (Q), plagioclase (P), alkali feldspar (A), and feldspathoids (foids, F).



IUGS Classification Scheme for Phaneritic Ultramafic Igneous Rocks (2)

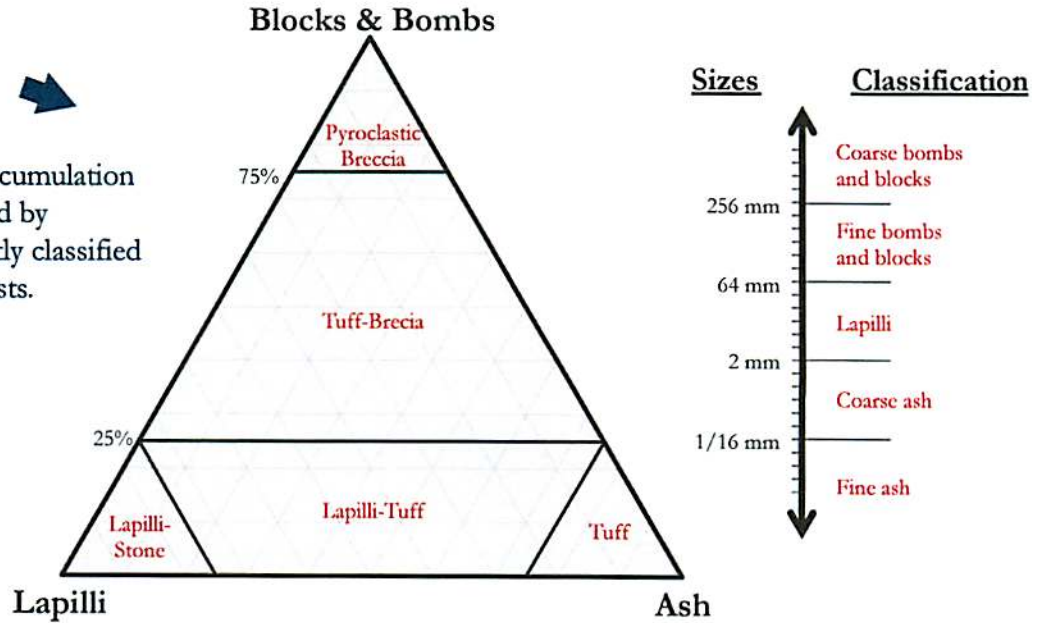
Ultramafic: more than 90% of the total minerals are mafic.

Scheme based on the normalized percentages of the visible minerals: olivine (Ol), hornblende (Hbl), and pyroxene (Px).

Igneous Rocks

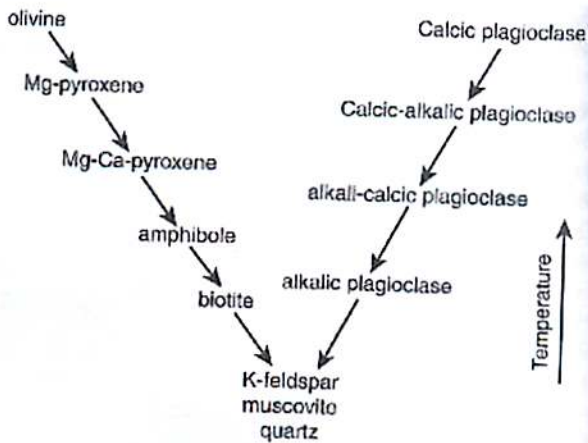
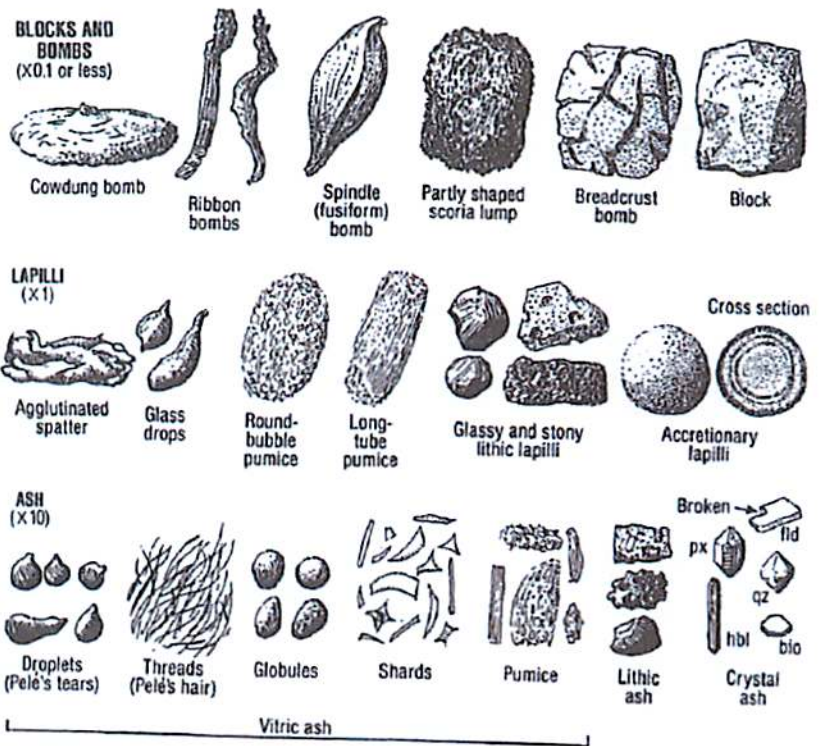
Classification Scheme for Pyroclastic Igneous Rocks

Pyroclastic rocks are formed via the accumulation of fragments of volcanic rock scattered by volcanic explosions. They are frequently classified based upon the size distribution of clasts.



Types of Tephra (Pyroclasts)

In each row, the viscosity of the lava increases to the right. From Compton, 1985.



Bowen's Reaction Series

From Winter, 2010.

Metamorphic Rocks



Classification Scheme for Metamorphic Rocks

Based upon texture and mineralogical composition.

Structure & Texture	Characteristic Properties	Characteristic Mineralogy	Rock Name	
Foliate (layered)	Increasing grain size, and degree of metamorphism ↓	Dull luster; very flat fracture surface; grains are too small to readily see; more dense than shale	No visible minerals	Slate
		Silky sheen; Crenulated (wavy) fracture structure; A few grains visible, but most are not	Development of mica and/or hornblende possible	Phyllite
		Sub-parallel orientations of individual mineral grains; wavy-sheet like fracture; often contains porphyroblasts; thinly foliated	Abundant feldspar; Quartz and mica are common; hornblende possible	Schist
		Sub-parallel, alternating bands or layers of light and dark material; coarsely foliated; blocky fracture	Abundant feldspars; Quartz, mica, and hornblende are common	Gneiss
Foliate (layered)	Interlocking crystals; effervesces in dilute HCl; softer than glass	Calcite	Marble	
	Nearly equigranular grains; fracture across grains (not around them); sub-vitreous appearance; smooth feel compared to sandstone	Quartz	Quartzite	



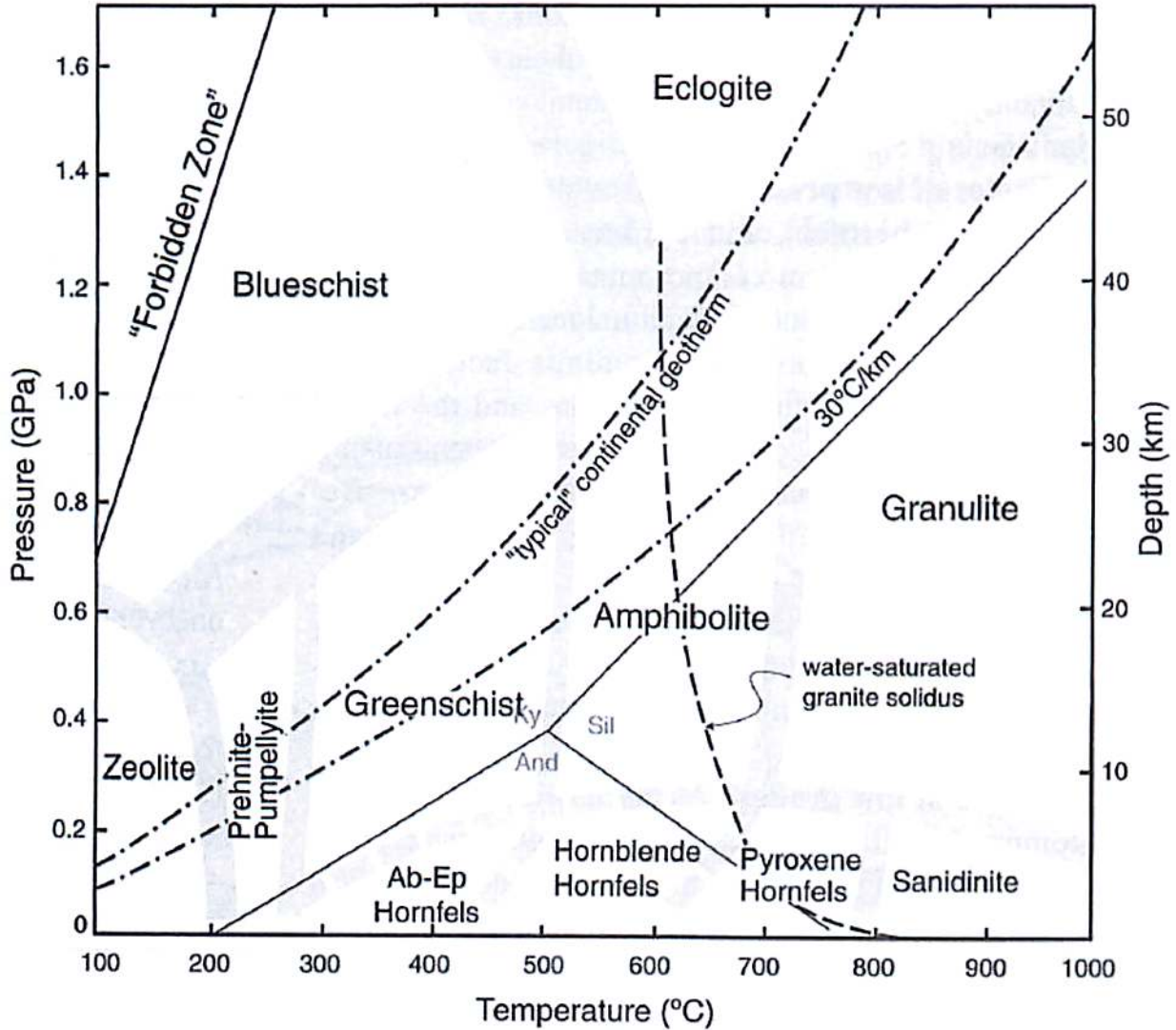
Mineralogy for Metamorphic Rock Facies

Facies	Definitive Mineral Assemblages in Mafic Rocks
Zeolite	zeolites: especially laumontite, wairakite, analcime (in place of other Ca-Al silicates such as prehnite, pumpellyite and epidote)
Prehnite-Pumpellyite	prehnite + pumpellyite (+ chlorite + albite)
Greenschist	chlorite + albite + epidote (or zoisite) + actinolite ± quartz
Amphibolite	hornblende + plagioclase (oligoclase, andesine) ± garnet
Granulite	orthopyroxene + clinopyroxene + plagioclase ± garnet
Blueschist	glaucophane + lawsonite or epidote/zoisite (± albite ± chlorite ± garnet)
Eclogite	pyralspite garnet + omphacitic pyroxene (± kyanite ± quartz), no plagioclase
Contact Facies	mineral assemblages in mafic rocks of the facies of contact metamorphism do not differ substantially from those of the corresponding regional facies at higher pressure

Metamorphic Rocks

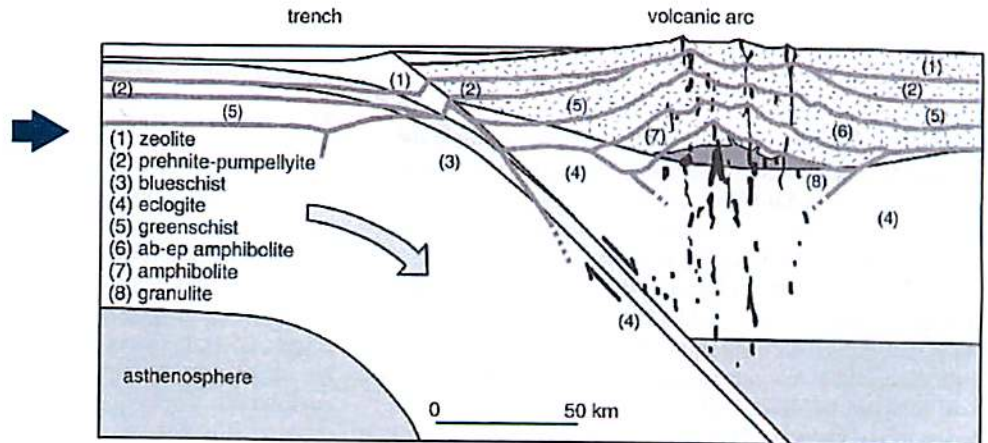
Metamorphic Rock Facies, P vs. T diagram

From Winter, 2010



Schematic of Island Arc, and the origins of Metamorphic Facies

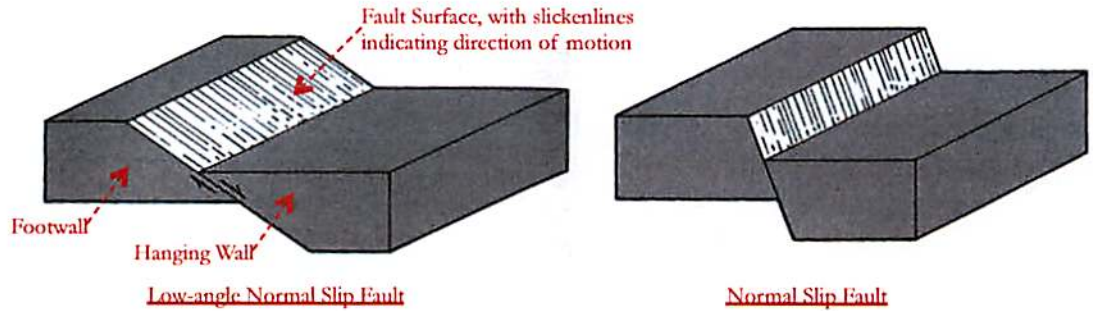
A schematic cross section of an island arc. Light gray lines are isotherms. From Winter, 2010



Structural Geology: Normal Faults

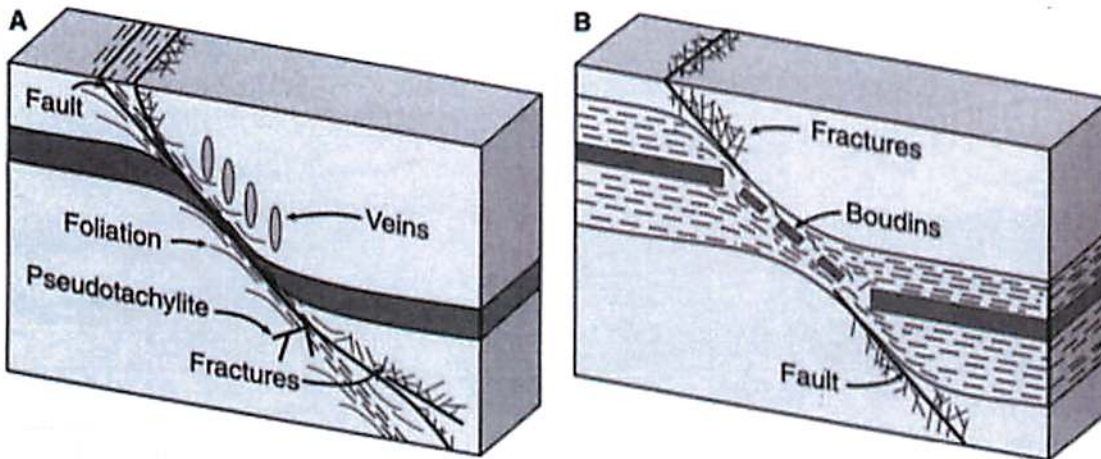
Normal Faults

In normal faults, the footwall goes up with respect to the hanging wall. Normal faults are indicative of extension. Figures from Davis & Reynolds, 1996.



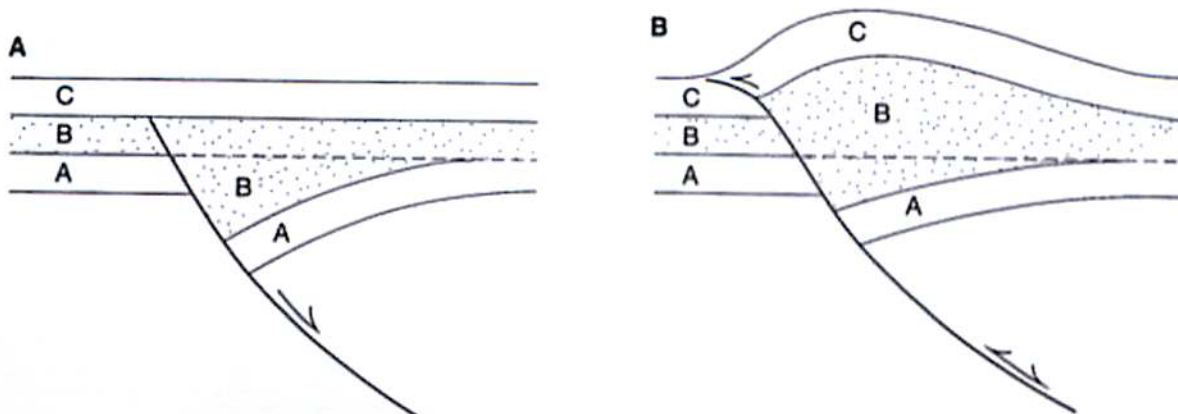
Effects of Brittle or Ductile Shear in Normal Faults

The block diagrams below illustrate the effects of changing the nature of deformation, between brittle deformation (which results in clear fault planes, fractures and fault rocks), ductile deformation (which causes deformation over a larger shear zone). Often, strata of different rheologies will behave differently, as is shown in the figure at right. The dashed layer was weak and deformed ductilely, while the middle grey layer was rigid and formed boudins. Figures from Davis & Reynolds, 1996.



Inversion Tectonics

If the regional stresses change, previously inactive faults can reactivate, and change their sense of motion. In the figure at left, layer-A was formed prior to the formation of a normal fault. Layer-B and layer-C were deposited after the formation, and shut down of the fault. In the figure at the right, the fault has reactivated, though as a reverse fault. The resulting stratigraphic sequence is a combination of effects one would expect from both normal and reverse faults. Figures from Davis & Reynolds, 1996.

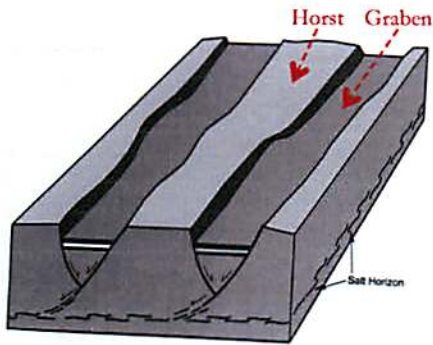
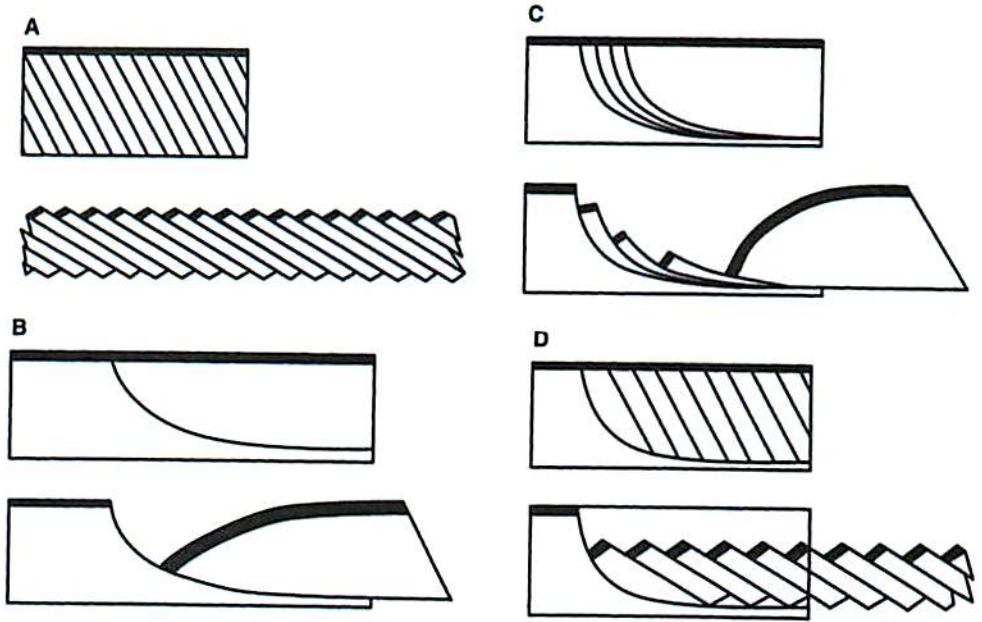


Structural Geology: Normal Faults

Normal Faults Geometries



Various normal fault geometries are possible. They all allow for lithospheric extension. (A) Domino style faulting. (B) Llistric normal faulting with reverse drag. (C) Imbricate listric normal faulting. Note that listric faulting can cause extreme rotation of faulted blocks. (D) Llistric normal faulting bounding a family of planar normal faults. Figures from Davis & Reynolds, 1996.



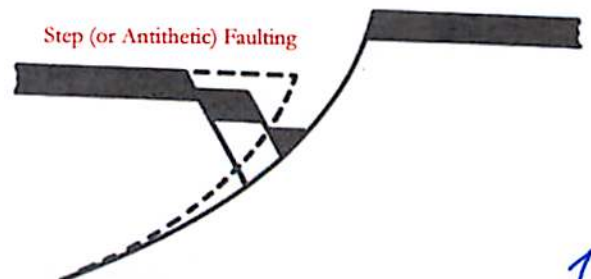
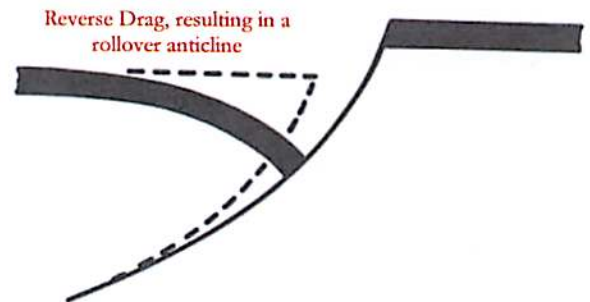
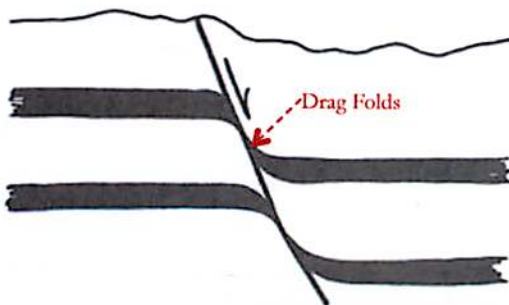
Horsts & Grabens

Classical formation describing fault-bounded uplifted (horsts) and down-dropped blocks (grabens). Figures from Davis & Reynolds, 1996.

Drag Folds, Reverse Drag, and Step Faulting



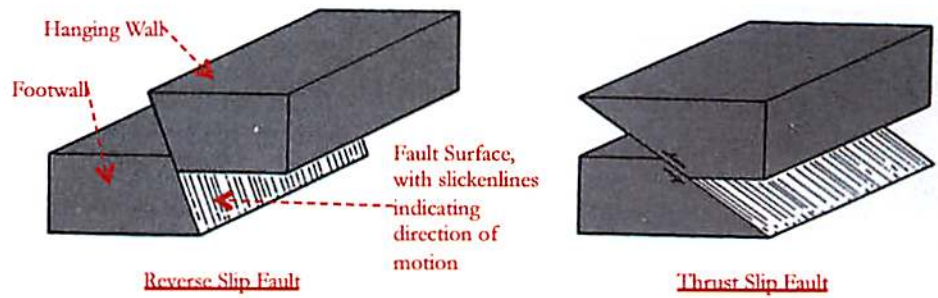
Faulting does not always produce clean displacement along the fault surface. Fault blocks are frequently folded or fractured, and the nature of these deformations are non-trivial. Figures from Davis & Reynolds, 1996.



Structural Geology: Reverse & Thrust Faults

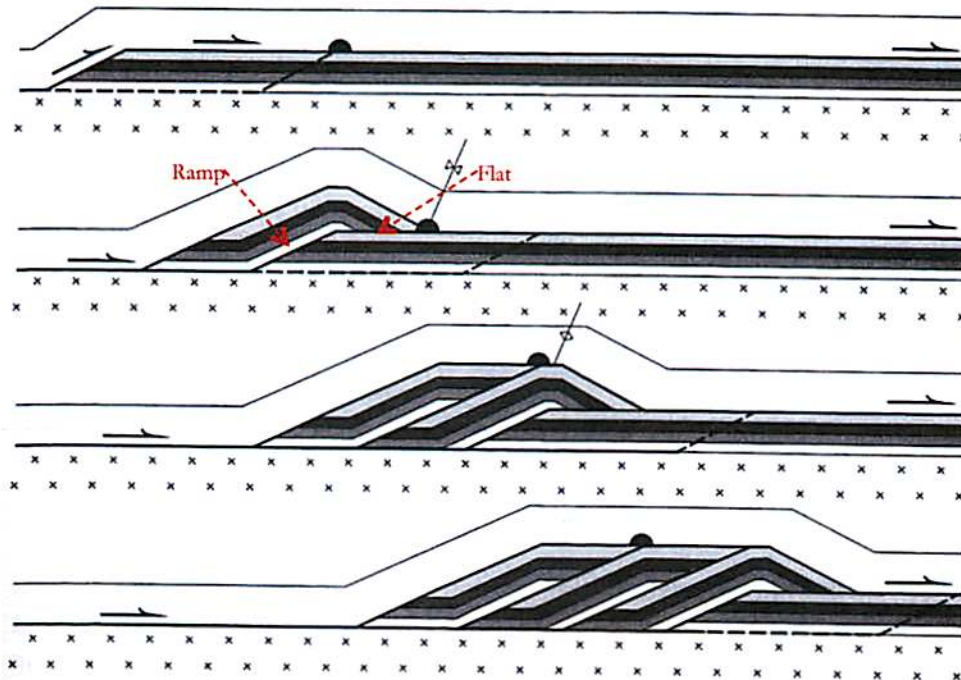
Reverse Faults ➔

In reverse faults, the footwall goes down with respect to the hanging wall. Normal faults are indicative of compression. Thrust faults are reverse faults with fault dips <45 degrees. Figures from Davis & Reynolds, 1996.



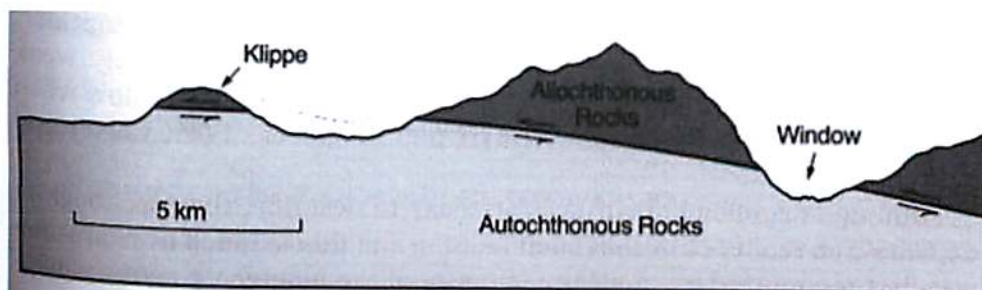
“Ramp-Flat” Geometry of Typical Thrust Fault Systems ↓

In a regional thrust, faulted blocks are “thrust” on top of younger strata. The exact geometry of these thrust systems can vary significantly. Figures from Davis & Reynolds, 1996.

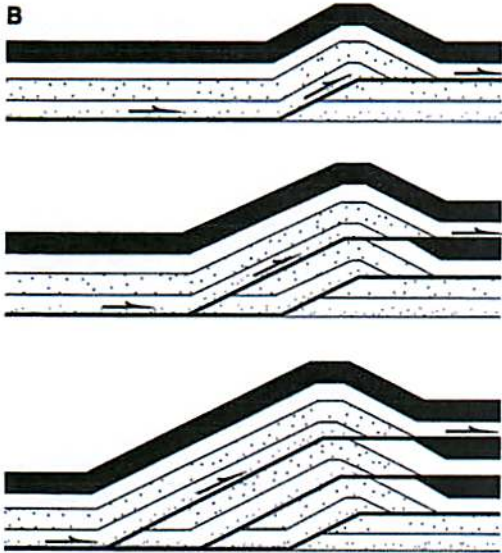


Klippe & Windows ↓

Thrust faults move large blocks of non-indigenous rock (referred to as “allochthonous” rock) over emplaced rock (referred to as “autochthonous” rock). If the overlying allochthonous rock is eroded, it can create windows into the lower underlying autochthonous rock. Erosion can also create islands of isolated allochthonous rock, called klippe. Figures from Davis & Reynolds, 1996.



Structural Geology: Reverse & Thrust Faults

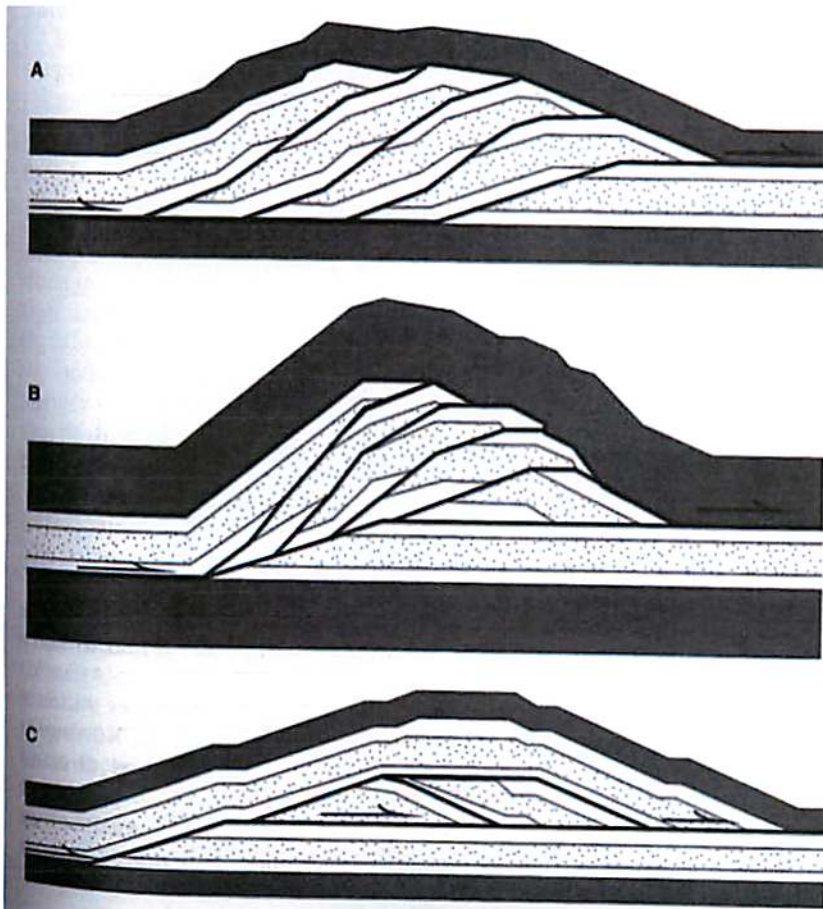
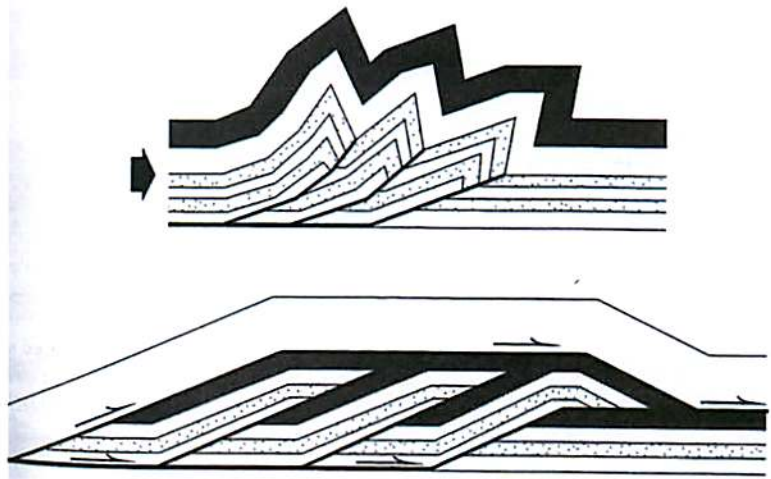


← Out-of-Sequence Thrust Fault System

Unlike “in-sequence” thrust fault systems (as shown on the previous page, the “roof” of the thrust block in an out-of-sequence system becomes the “flat” for subsequent fault blocks. Figures from Davis & Reynolds, 1996.

Imbricate Fans vs. Duplexes ↓

Two thrust fault geometries: imbricate fans (top) and duplexes (bottom). Figures from Davis & Reynolds, 1996.



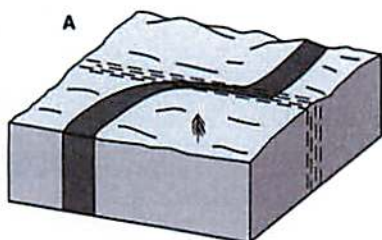
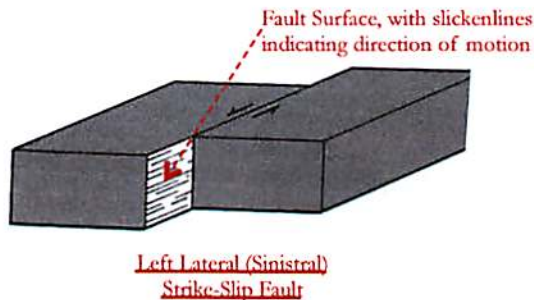
← Forms of Duplexes

The exact form of a duplex or imbricate fan depends on the spacing of ramps and the amount of slip. (A) A normal duplex develops when slice length exceeds the fault slip. (B) An antiformal duplex develops when slice length and fault slip are effectively equal. (C) A forward-dipping duplex develops when the fault slip is greater than the slice length. Figures from Davis & Reynolds, 1996.

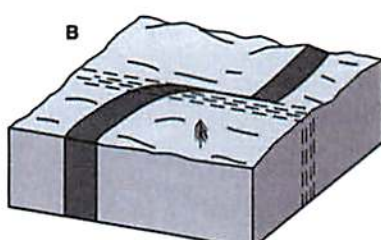
Structural Geology: Strike-Slip or Transform Faults

Strike-Slip Faults →

In reverse faults, the footwall goes down with respect to the hanging wall. Normal faults are indicative of compression. Thrust faults are reverse faults with fault dips <45 degrees. Figures from Davis & Reynolds, 1996.



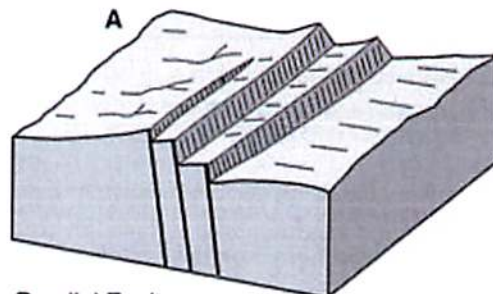
Continuous Shear Zone



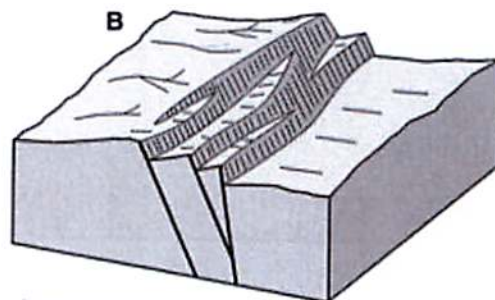
Discontinuous Shear Zone

← Ductile Shear Zones

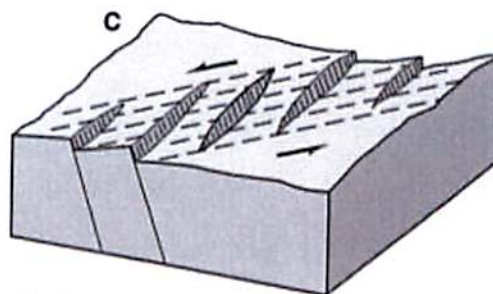
Shear in a strike-slip fault is not always located in a single plane. Sometimes, shear takes place over an extended region. Figures from Davis & Reynolds, 1996.



Parallel Faults



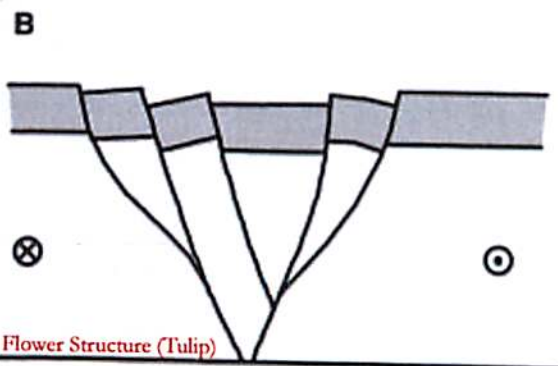
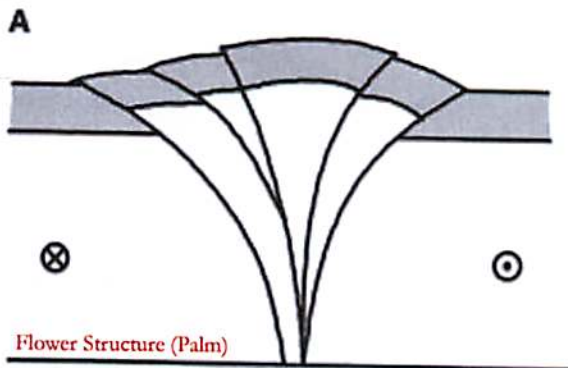
Anastomosing Faults



En Echelon Faults

Brittle Shear Zones ↘

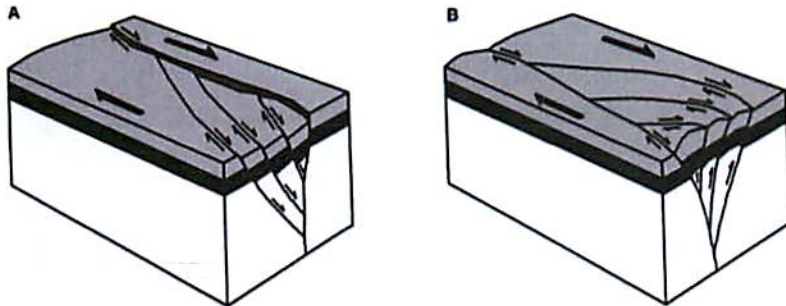
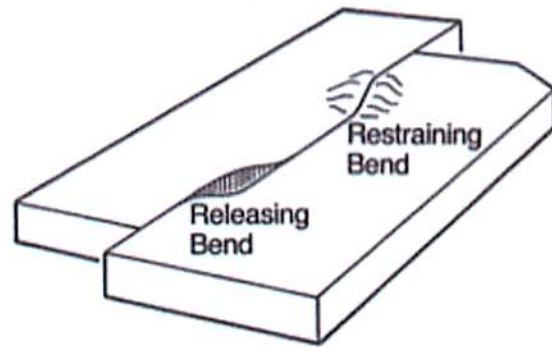
Figures from Davis & Reynolds, 1996.



Structural Geology: Strike-Slip or Transform Faults

Bends in Strike-Slip Faults →

Strike-slip faults along irregularly curved faults creates localized regions of extension and compression. Figures from Davis & Reynolds, 1996.

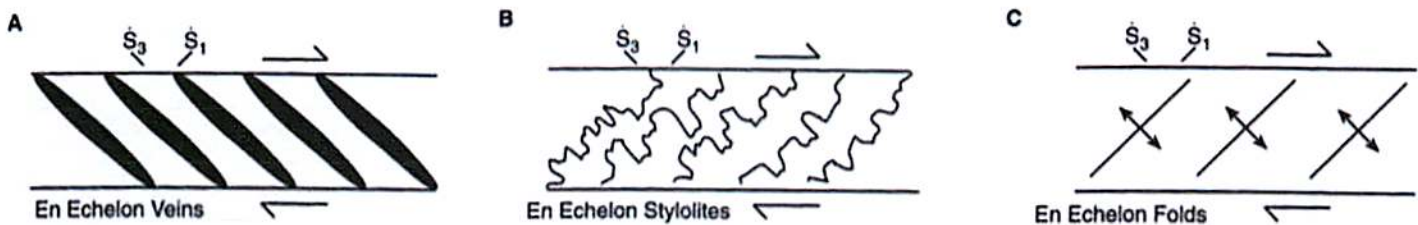


← Strike-Slip Duplexes

(A) Extensional duplexes can form at releasing bends. (B) Compressional duplexes can form at restraining bends. Figures from Davis & Reynolds, 1996.

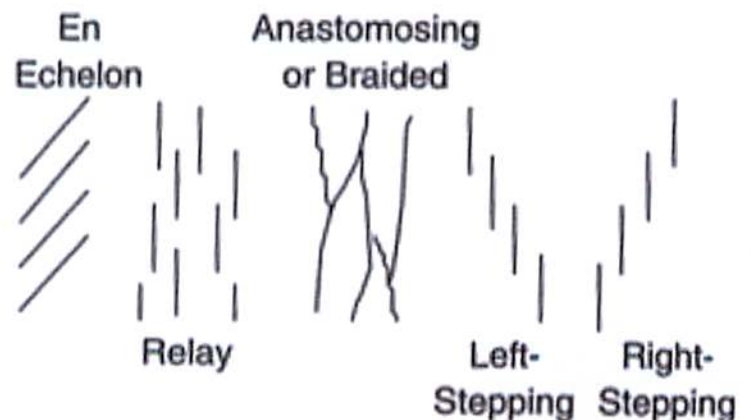
Slip Indicators in Strike-Slip Systems ↓

In strike-slip systems, the maximum (S_1) and minimum compressional stresses (S_3) are at an angle with respect to the sense of shear. This can lead to the formation of both large scale folds and faults, or small scale fractures or veins, which are indicative to the sense of motion. Figures from Davis & Reynolds, 1996.



Even more Geometric Arrangements of Strike-Slip Faults →

Figures from Davis & Reynolds, 1996.

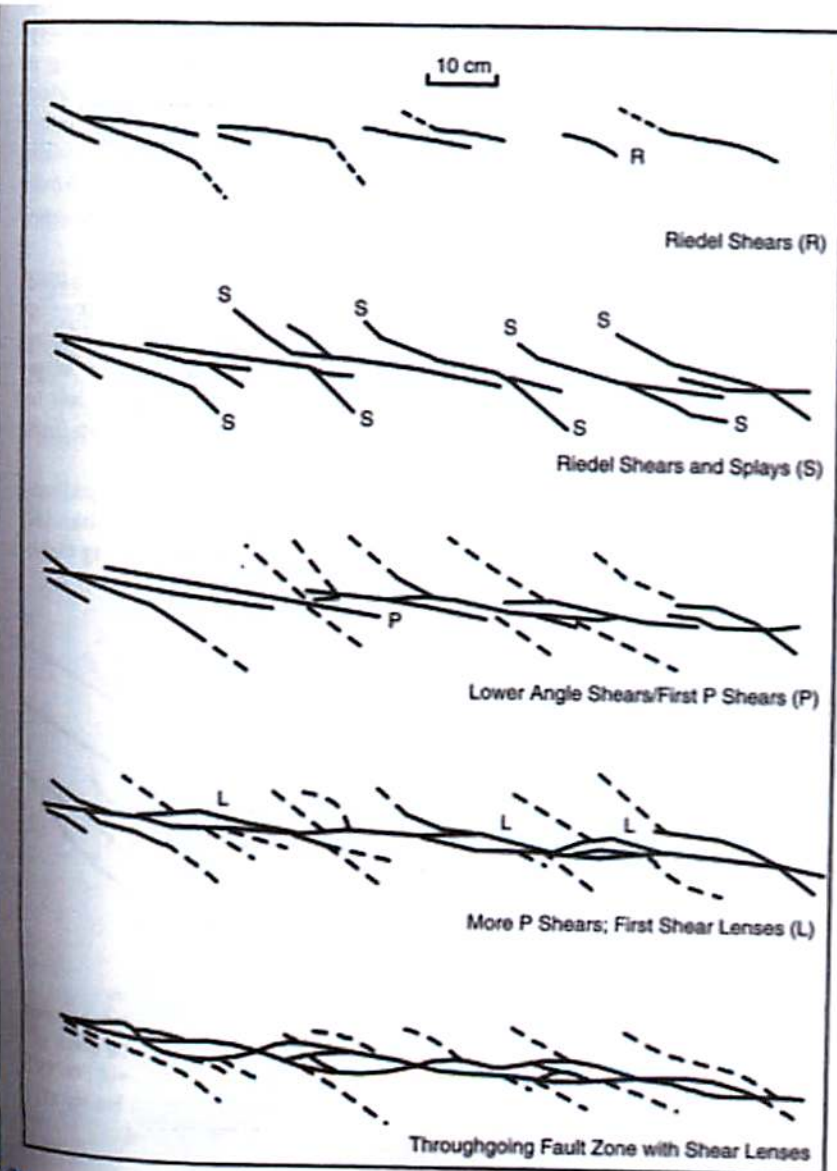
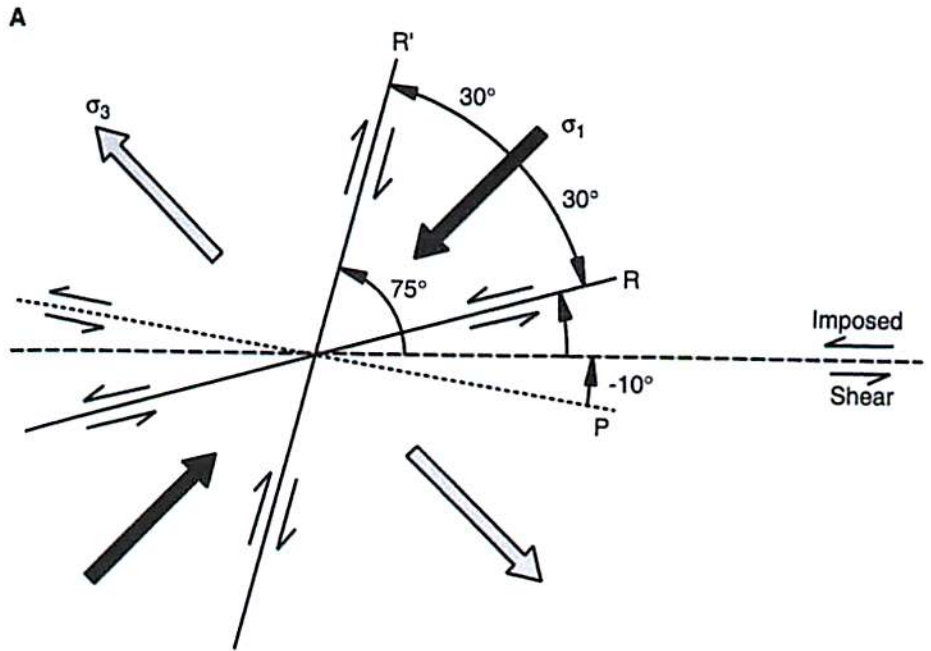


Structural Geology: Strike-Slip or Transform Faults

Riedel Shears



When under compression, rocks tend to form fail with faults forming 30° from the primary compressional stress. In a strike-slip fault, the primary compressional stress (σ_1) is 45° away from the plane of strike-slip shearing. The combination of these two facts results in fractures at interesting angles with respect to the motion of shear. These are called Riedel shears. The figure below shows a left-handed strike-slip zone. Figures from Davis & Reynolds, 1996.

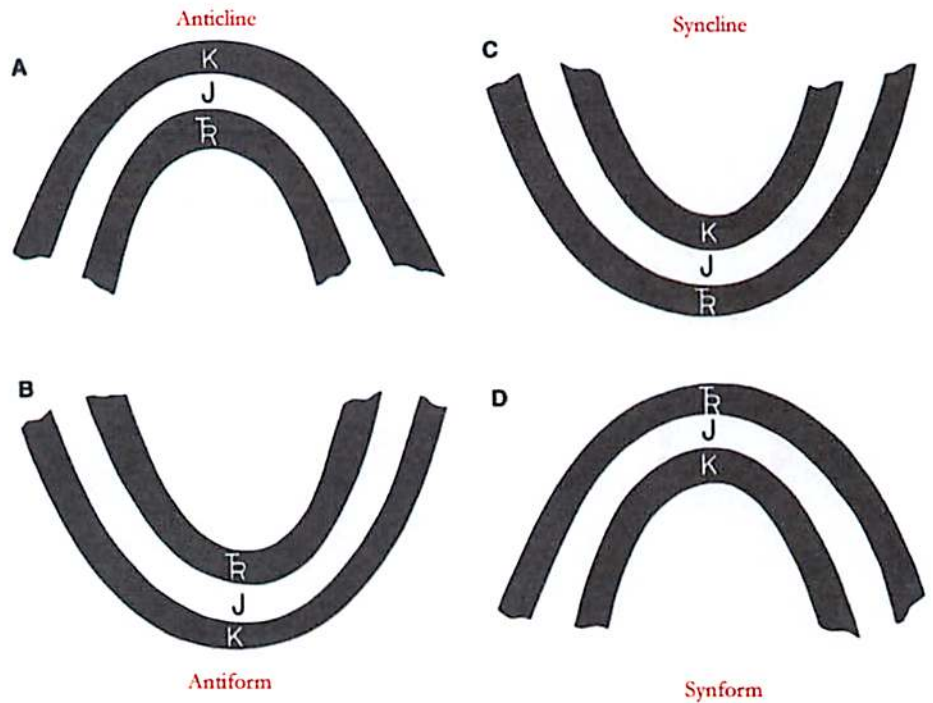


The figure at left illustrate the formation sequence of Riedel shears and other splays and shears in a right-handed strike-slip zone. Figures from Davis & Reynolds, 1996.

Structural Geology: Folds

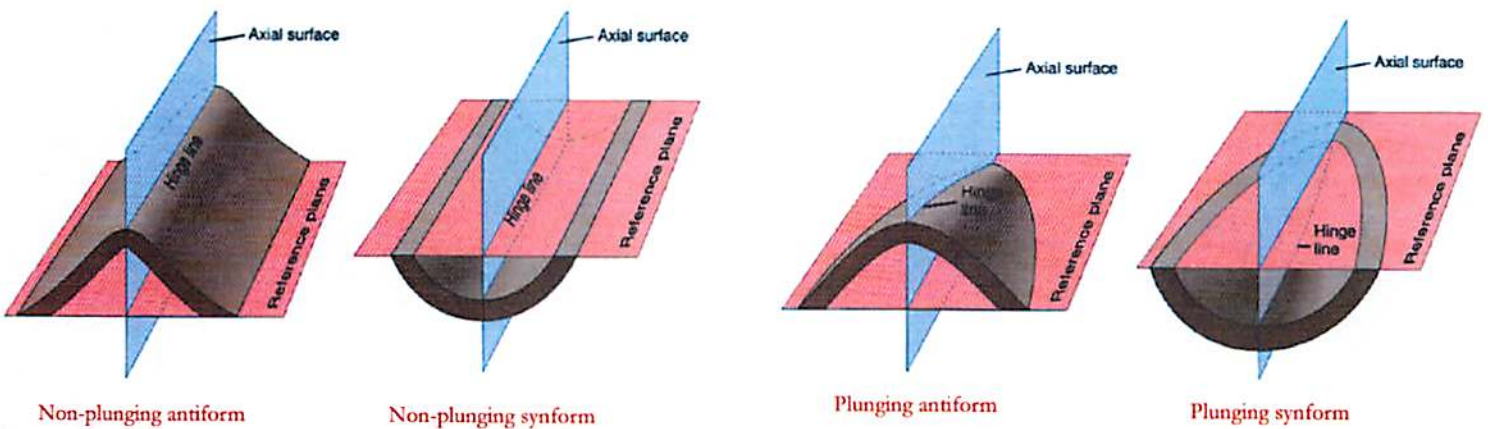
Anticlines & Antiforms, and Synclines & Synforms

Antiforms are concave-down folds, while Synforms are concave-up folds. Anticlines are antiforms where we know that the younger strata lie on top of older strata. Similarly, Synclines are antiforms where younger strata lie on top of older strata. Figures from Davis & Reynolds, 1996.



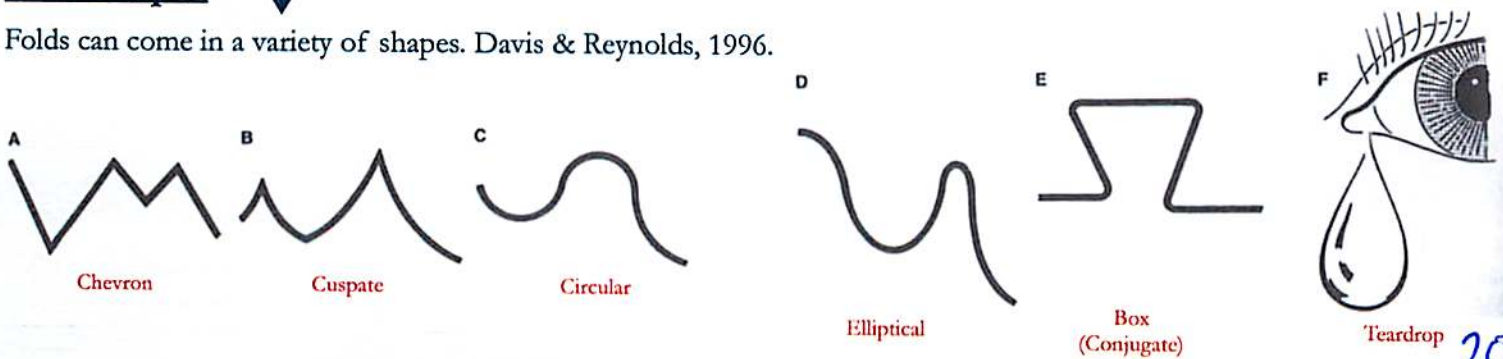
Plunging Folds

Folds (defined by hinge lines and axial surfaces) are not necessarily perpendicular to the Earth's surface. They can be dipping into or out of the surface. This can create interesting patterns of exposed surface rock, or even topography. Figures from Jones, 2001.



Fold Shapes

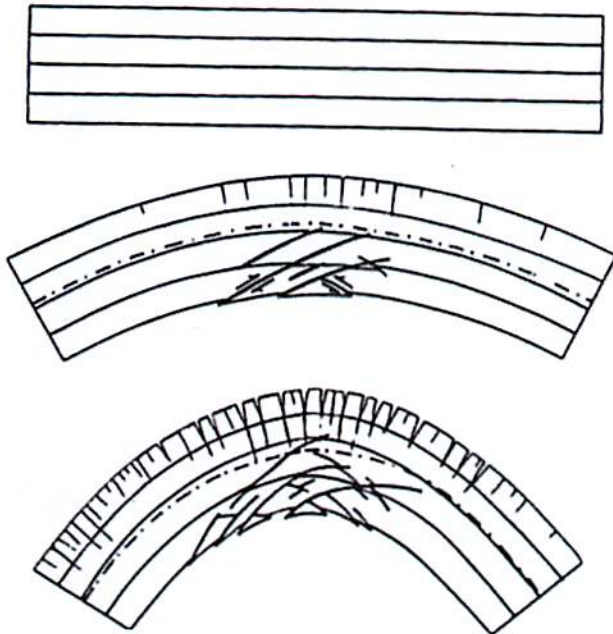
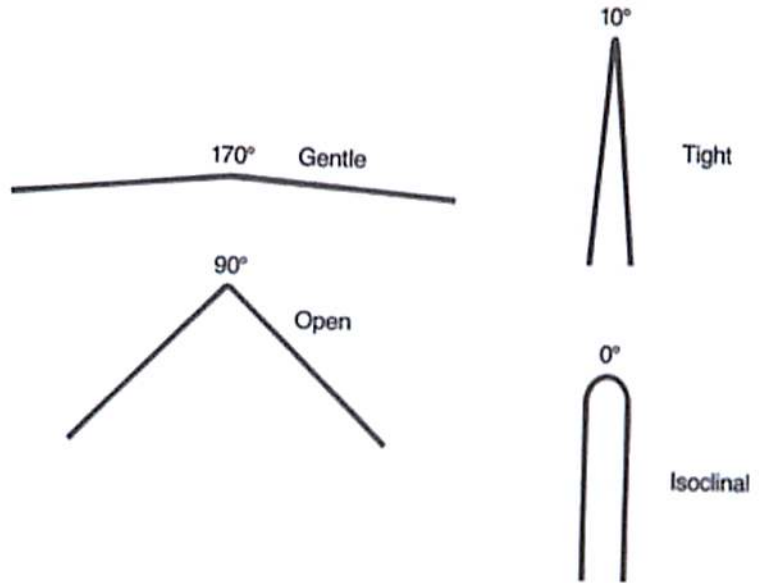
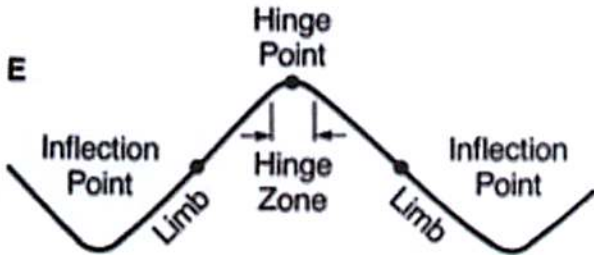
Folds can come in a variety of shapes. Davis & Reynolds, 1996.



Structural Geology: Folds

Fold Tightness

Fold tightness is based upon the size of the inter-limb angle. Figures from Davis & Reynolds, 1996.

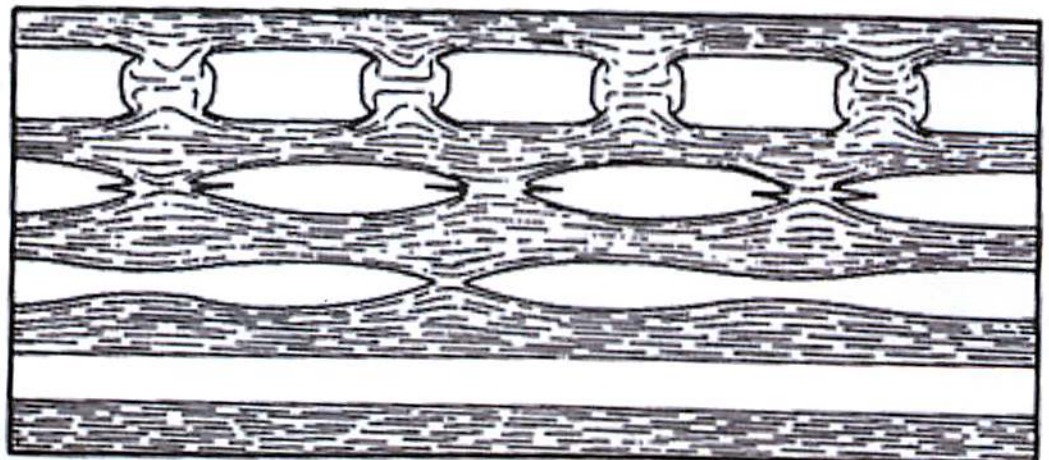


Minor Structures in Folds

When folding layers of strata, layer-parallel stretching occurs in the outer arc of a folded layer, while layer-parallel shortening occurs in the inner arc. Figures from Davis & Reynolds, 1996.

Boudins

Layer-parallel stretching can pinch off layers of strata, depending on the ductility contrast between layers. This can result in pinch-and-swell structures or boudins (where the pinching completely pinches off portions of a given strata). Figures from Davis & Reynolds, 1996.



Geologic Map Symbols

1		Contact, showing dip where trace is horizontal, and strike and dip where trace is inclined	42		Steeply plunging monocline or flexure, showing trace in horizontal section and plunge of hinges
2		Contact, located approximately (give limits)	43		Plunge of hinge lines of small folds, showing shapes in horizontal section
3		Contact, located very approximately, or conjectural	44		Strike and dip of beds or bedding
4		Contact, concealed beneath mapped units	45		Strike and dip of overturned beds
5		Contact, gradational (optional symbols)	46		Strike and dip of beds where stratigraphic tops are known from primary features
6		Fault, nonspecific, well located (optional symbols)	47		Strike and dip of vertical beds or bedding (dot is on side known to be stratigraphically the top)
7		Fault, nonspecific, located approximately	48		Horizontal beds or bedding (as above)
8		Fault, nonspecific, assumed (existence uncertain)	49		Approximate (typically estimated) strike and dip of beds
9		Fault, concealed beneath mapped units	50		Strike of beds exact but dip approximate
10		Fault, high-angle, showing dip (left) and approximate dips	51		Trace of single bed, showing dip where trace is horizontal and where it is inclined
11		Fault, low-angle, showing approximate dip and strike and dip	52		Strike and dip of foliation (optional symbols)
12		Fault, high-angle normal (D or ball and bar on downthrown side)	53		Strike of vertical foliation
13		Fault, reverse (R on upthrown side)	54		Horizontal foliation
14		Fault, high-angle strike-slip (example is left lateral)	55		Strike and dip of bedding and parallel foliation
15		Fault, thrust (T on overthrust side)	56		Strike and dip of joints (left) and dikes (optional symbols)
16		Fault, low-angle normal or detachment (D on downthrown side)	57		Vertical joints (left) and dikes
17		Fault, low-angle strike-slip (example is right lateral)	58		Horizontal joints (left) and dikes
18		Fault, low-angle, overturned (teeth in direction of dip)	59		Strike and dip of veins (optional symbols)
19		Optional sets of symbols for different age-groups of faults	60		Vertical veins
20		Fault zone or shear zone, width to scale (dip and other accessory symbols may be added)	61		Horizontal veins
21		Faults with arrows showing plunge of rolls, grooves or slickensides	62		Bearing (trend) and plunge of lineation
22		Fault showing bearing and plunge of net slip	63		Vertical and horizontal lineations
23		Point of inflection (bar) on a high-angle fault	64		Bearing and plunge of cleavage-bedding intersection
24		Points of inflection on a strike-slip fault passing into a thrust	65		Bearing and plunge of cleavage-cleavage intersections
25		Fault intruded by a dike	66		Bearings of pebble, mineral, etc. lineations
26		Faults associated with veins	67		Bearing of lineations in plane of foliation
27		Anticline, showing trace and plunge of hinge or crest line (specify)	68		Horizontal lineation in plane of foliation
28		Syncline (as above), showing dip of axial surface or trough surface	69		Vertical lineation in plane of vertical foliation
29		Folds (as above), located approximately	70		Bearing of current from primary features; from upper left: general; from cross-bedding; from flute casts; from imbrication
30		Folds, conjectural	71		Bearing of wind direction from dune forms (left) and cross-bedding
31		Folds beneath mapped units	72		Bearing of ice flow from striations (left) and orientation of striations
32		Asymmetric folds with steeper limbs dipping north (optional symbols)	73		Bearing of ice flow from drumlins
33		Anticline (top) and syncline, overturned	74		Bearing of ice flow from crag and tail forms
34		Antiform (inverted) syncline	75		Spring
35		Synformal (inverted) anticline	76		Thermal spring
36		Antiform (top) and synform (stratigraphic sequence unknown)	77		Mineral spring
37		Separate dome (left) and basin	78		Asphaltic deposit
38		Culmination (left) and depression	79		Bituminous deposit
40		Vertically plunging anticline and syncline	80		Sand, gravel, clay, or placer pit
41		Monocline, south-facing, showing traces of axial surfaces			

Geologic Map Symbols

81		Mine, quarry, or open pit
82		Shafts: vertical, inclined, and abandoned
83		Adit, open (left) and inaccessible
84		Trench (left) and prospect
85		Water wells: flowing, nonflowing, and dry
86		Oil well (left) and gas well
87		Well drilled for oil or gas, dry
88		Wells with shows of oil (left) and gas
89		Oil or gas well, abandoned (left) and shut in
90		Drilling well or well location
91		Glory hole, open pit, or quarry, to scale
92		Dump or fill, to scale

Fossil and Structural Symbols for Stratigraphic Columns

	Algae		Tree trunk fallen		Foraminifers, general		Scour casts
	Algal mats		Trilobites		Foraminifers, large		Convolution
	Ammonites		Vertebrates		Fossils		Slumped beds
	Belemnites		Wood		Fossils abundant		Paleosol
	Brachiopods		Beds distinct		Fossils sparse		Mud cracks
	Bryozoans		Beds obscure		Gastropods		Salt molds
	Corals, solitary		Unbedded		Graptolites		Burrows
	Corals, colonial		Graded beds		Leaves		Pellets
	Crinoids		Planar cross-bedding		Ostracodes		Oolites
	Echinoderms		Trough cross-bedding		Pelecypods		Pisolites
	Echinoids		Ripple structures		Root molds		Intraclasts
	Fish bones		Cut and fill		Spicules		Stylolite
	Fish scales		Load casts		Stromatolites		Concretion
					Tree trunk in place		Calclitic concretion

Lithologic Patterns for Stratigraphic Columns & Cross Sections



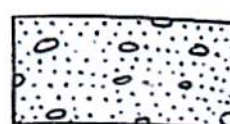
1. Breccia



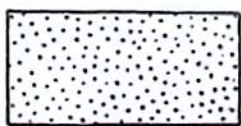
2. Clast-supported conglomerate



3. Matrix-supported conglomerate



4. Conglomeratic sandstone



5. Coarse sandstone



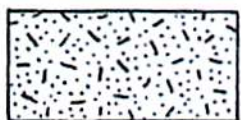
6. Fine sandstone



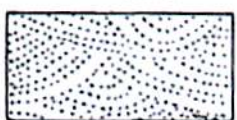
7. Feldspathic sandstone



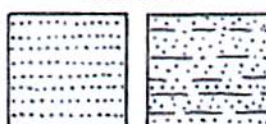
8. Tuffaceous sandstone



9. Graywacke



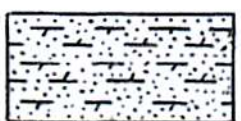
10. Cross-bedded sandstone



11. Bedded sandstone



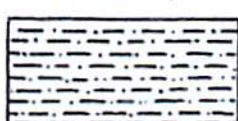
12. Calcite-cemented sandstone



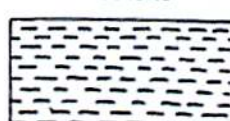
13. Dolomite-cemented sandstone



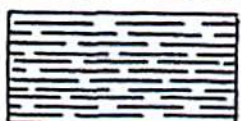
14. Silty sandstone



15. Siltstone



16. Mudstone



17. Shale



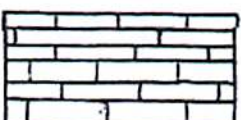
18. Coal bed with carbonaceous shale



19. Pebbly mudstone



20. Calcareous shale



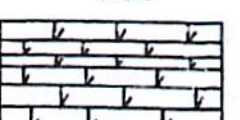
21. Limestone



22. Cross-bedded limestone



23. Dolomite (dolostone)



24. Dolomitic limestone



25. Calcitic dolomite



26. Sandy limestone



27. Clayey limestone



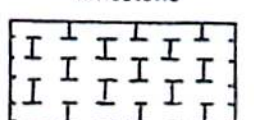
28. Cherty limestone



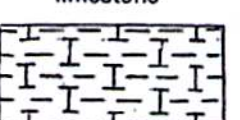
29. Bedded chert



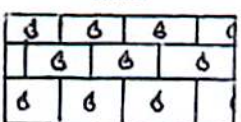
30. Phosphorite, phosphatic shale



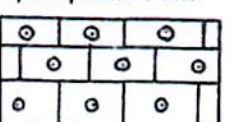
31. Chalk



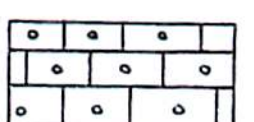
32. Marl



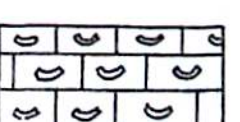
33. Fossiliferous limestone



34. Oolitic limestone



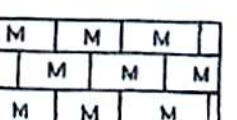
35. Pelletal limestone



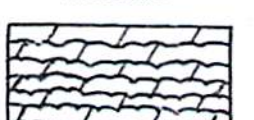
36. Intraclastic limestone



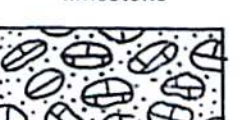
37. Crystalline limestone



38. Micritic limestone



39. Algal dolomite



40. Limestone conglomerate

Lithologic Patterns for Stratigraphic Columns & Cross Sections



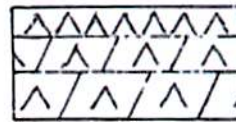
41. Limestone breccia



42. Algal dolomite breccia



43. Gypsum bed, gypsiferous shale



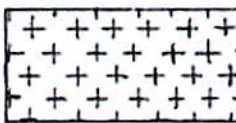
44. Anhydrite, anhydritic dolomite



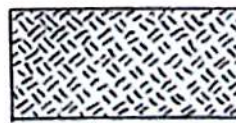
45. Rock salt, salty mudstone



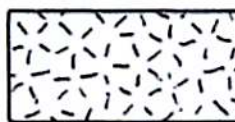
46. Peridotite



47. Gabbro



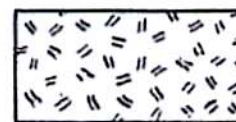
48. Mafic plutonic rock



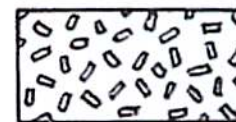
49. Coarse granitic rock



50. Fine granitic rock



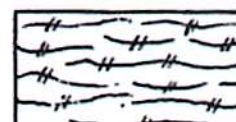
51. Porphyritic plutonic rock



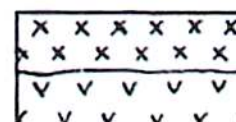
52. Porphyritic plutonic rock



53. Mafic lava



54. Silicic lava



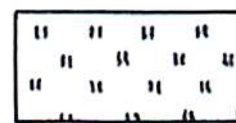
55. Intrusive volcanic rocks



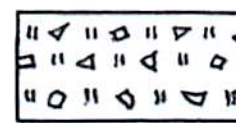
56. Pillow lava



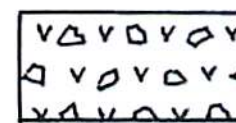
57. Hyaloclastite



58. Tuff



59. Tuff-breccia



60. Volcanic breccia



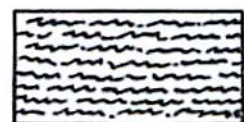
61. Massive serpentinite



62. Foliated serpentinite



63. Schist



64. Crenulated schist



65. Folded schist



66. Semischistose sandstone



67. Semischistose limestone



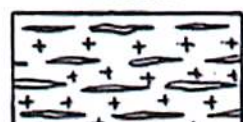
68. Semischistose gabbro



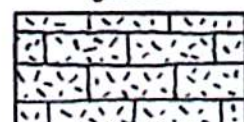
69. Greenstone



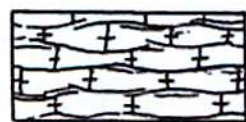
70. Silicic gneiss



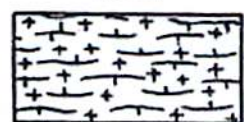
71. Mafic gneiss



72. Marble



73. Foliated marble



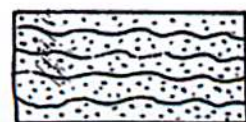
74. Foliated calc-silicate rock



75. Massive skarn



76. Alteration zones



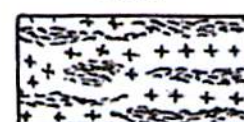
77. Quartzite



78. Quartzite

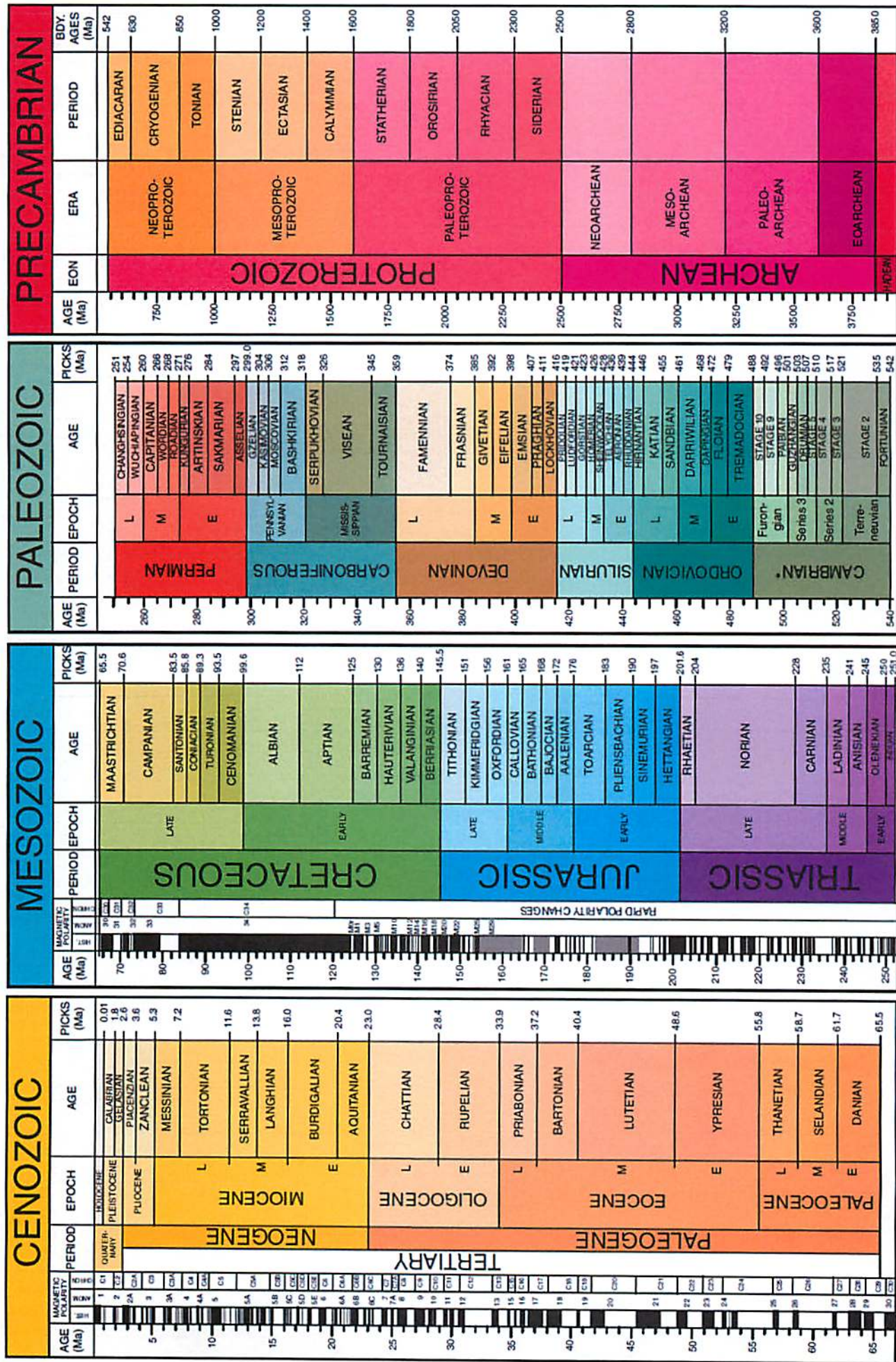


79. Silicic migmatite



80. Mafic migmatite

Geologic Timescale



Lava Lakes Catherine Elder



Figure 1: Nyiragongo Crater in Africa's Great Rift Valley. For more awesome pictures like this, go to http://www.boston.com/bigpicture/2011/02/nyiragongo_crater_journey_to_t.html

1 General

- Form when lava erupts and flows into older sub-circular collapse craters (pit craters) (Schmincke 2004) or when a new vent erupts lava for several weeks or more and builds a crater above the surrounding ground (USGS 2008).
- Sometimes lava lakes fill the collapse crater to a depth of more than 100 m (Schmincke 2004).
- When the dikes supplying this lava collapse, the lake is cut off from the source and starts to solidify (Peck *et al.* 1979).
- Lava lakes are relatively rare on Earth. Since 1980, lava lakes have formed at Kilauea Volcano in Hawaii, Mount Erebus in Antarctica, Erta' Ale in Ethiopia, and Nyiragongo in Zaire (USGS 2008).

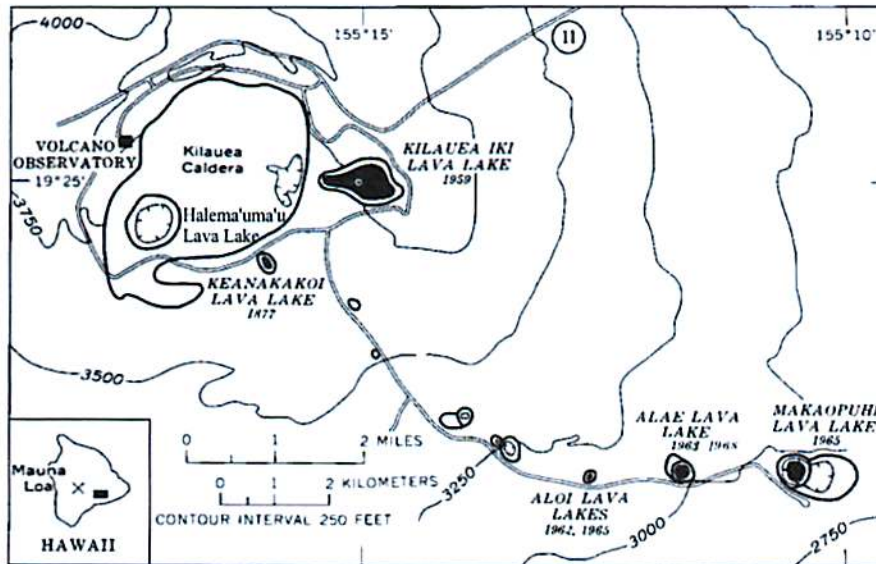


Figure 2: Kilauea lava lakes prior to 1969. Aloi and Alae are buried beneath lava flows from Mauna Ulu (a shield volcano that began forming in May 1969). Makaopuhi Crater has also been filled. (Figure 1 in Wright *et al.* (1976)).

2 Kilauea

- Lava lakes include:
 - Halemaumau: 1823–1924 (Tazieff 1994) and 2008–present (USGS Volcano Hazards Program 2014).
 - Kilauea Iki: 1959 (Peck *et al.* 1979)
 - Alae: 1963 (Peck *et al.* 1979)
 - Makaopuhi: 1965 (Peck *et al.* 1979)
 - Pu’u O’o: 2011–present (USGS Volcano Hazards Program 2014)
- Magma is stored in a reservoir ~ 4 km below the summit of Kilauea (Peck *et al.* 1979).

2.1 Kilauea Iki

- 120 meters-deep (Peck *et al.* 1979)
- It was a lava lake fed by fountaining of a vent on the crater wall rather than the more typical bottom fed lava lake. The vent directly interacted with the lava lake only when the rising lava lake overtopped and flooded the vent (Stovall *et al.* 2009).
- 17 separate eruptions over 36 days. Some lava flowed out of the lake through a rift part way up the side of the depression (Peck *et al.* 1979).
- Eruption temperatures were high—between 1,200 and 1,215°C (Peck *et al.* 1979).



3 Cooling and crust thickening rates

- Heat is removed rapidly from the surface of the lava lake through radiation and convection of hot air from the surface (Schmincke 2004).
- At the base of the lava lake, heat migrates slowly by conduction from the lava lake into its surrounding rock (Schmincke 2004).
- Rainfall can increase cooling of terrestrial lava lakes especially in Hawaii where rain fall is frequent (Peck *et al.* 1979). For example rain was significant for Alae lake (Wright *et al.* 1976, Peck *et al.* 1979).
- Convection in the melt can also increase the cooling rate. Makaopuhi and Kilauea Iki may have had convection (Wright *et al.* 1976).

3.1 Theory - The Stefan Problem

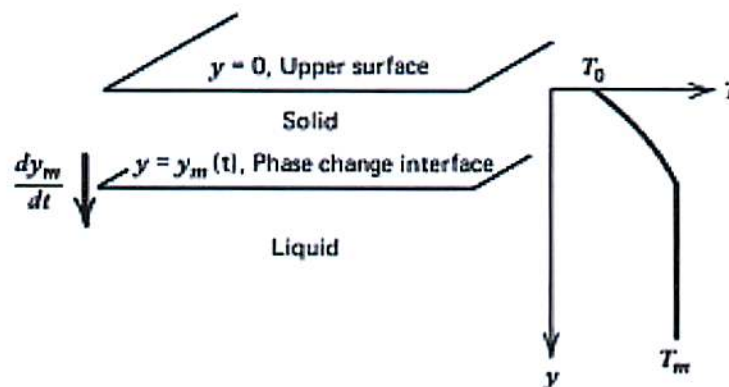


Figure 3: Growth of a solid layer at the top of a cooling lava lake (Figure 4-29 in Turcotte and Schubert (2002)).

- A lava lake (or a lava flow) solidifies from its upper surface downward because it is cooled from above. It also solidifies from its base upwards, but as long as there is a liquid region between the solidification fronts, the top-down and bottom-up solidification can be treated separately (Turcotte and Schubert 2002). Here I will describe the solidification of the top surface.
- The solidification of a lava lake or lava flow from above is essentially the same problem as the freezing of a lake. It is known as the Stefan problem, and Turcotte and Schubert (2002) has a very good description of how to solve the problem.
- It is a heat conduction problem, but it also includes phase change. As the melt solidifies, latent heat is released and must be conducted away from the phase change boundary.



We also must solve for the position of the boundary between the melt and the solid as part of the problem, because it changes as more melt solidifies (Turcotte and Schubert 2002).

- Assume that the magma has a well-defined melt temperature, T_m , at which the phase change occurs, and that the upper surface is maintained at a constant temperature T_o (Turcotte and Schubert 2002). See Figure 3.
- The flow has solidified to a depth of $y = y_m(t)$ at time t (Figure 3).
- We solve the heat conduction equation in the solid layer $0 \leq y \leq y_m(t)$ with the boundary conditions $T = T_o$ at $y = 0$ and $T = T_m$ at $y = y_m(t)$ and $y_m = 0$ at $t = 0$ (Turcotte and Schubert 2002).
- Heat released through solidification must be conducted away from the boundary between the melt and the solid at exactly the rate at which it is liberated if energy is to be conserved. This heat will be conducted towards the surface because heat flows from hot regions toward cold regions (Turcotte and Schubert 2002).

$$\rho L \frac{dy_m}{dt} = k \left(\frac{\partial T}{\partial y} \right)_{y=y_m} \quad (1)$$

where ρ is the density, L is the latent heat, and k is the thermal conductivity. The details of how to solve this equation are given in Turcotte and Schubert (2002) section 4-18.

- From this you can calculate the position of the solid melt boundary, y_m , (and thus crustal thickness) as a function of time, t :

$$y_m = C \sqrt{\kappa t} \quad (2)$$

where κ is the thermal diffusivity and C is a constant that can be determined using equation 1 (Turcotte and Schubert 2002).

3.2 Observation

- The thickness of the solidifying crusts on Kilauea Iki, Alae, and Makaopuhi were measured over time after the eruption. These measurements are compared to the thickness predicted by the theory (section 3.1) in Figure 4. The observations and theory agree (Turcotte and Schubert 2002).
- The cooling history of the crust of lava lakes was used to extend in time the data for the cooling of lava flows. Including the lava lake data does not significantly alter the slope, but extends the time interval over which the relationship is valid (Hon *et al.* 1994).

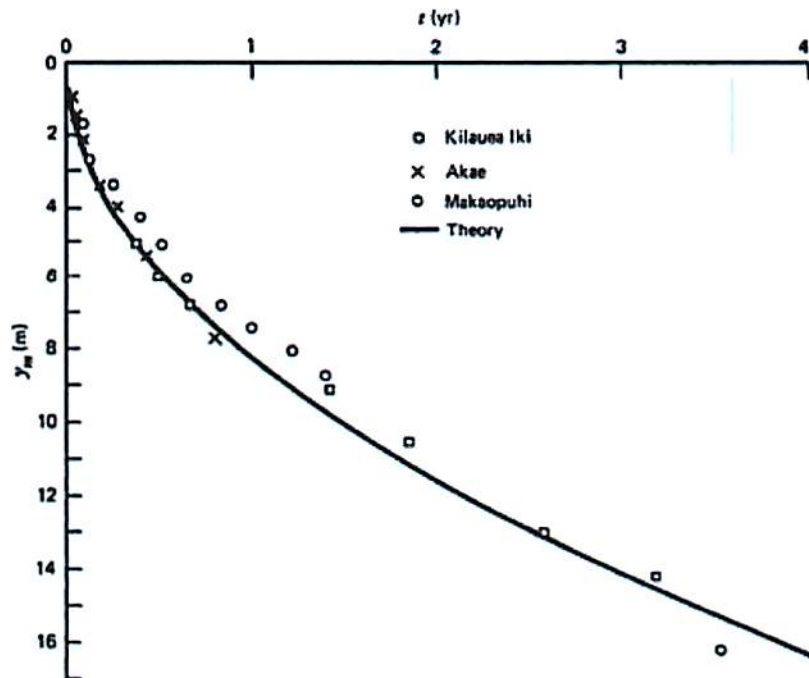


Figure 4: The thickness of the solidifying crusts as a function of time on lava lakes Kilauea Iki, Alae, and Makaopuhi compared to the theoretical thickness as a function of time (Figure 4-33 in Turcotte and Schubert (2002)).

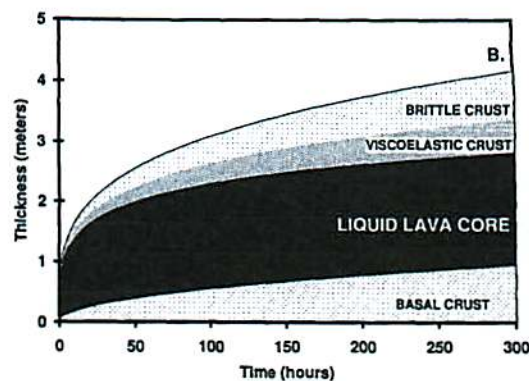


Figure 5: Modeled crustal structure through an inflated sheet flow after 300 hours. The boundary between the brittle and viscoelastic portions of the upper crust is the 800°C isotherm and the boundary between the viscoelastic portion of the upper crust, and the molten interior is the 1070°C isotherm. The lower crust likely has a similar structure but no data exists from the base of the flow. Figure from Hon *et al.* (1994).

- The crust of a lava lake or flow is brittle from the surface to the depth of the 800°C isotherm. Between the 800°C isotherm and the 1070°C the crust is inferred to behave viscoelastically (Figure 5, Hon *et al.* (1994)).
- The depth of the 800°C isotherm was determined using a combination of lava flow and lava lake data (Figure 6). It has a negative intercept which implies that the crust does

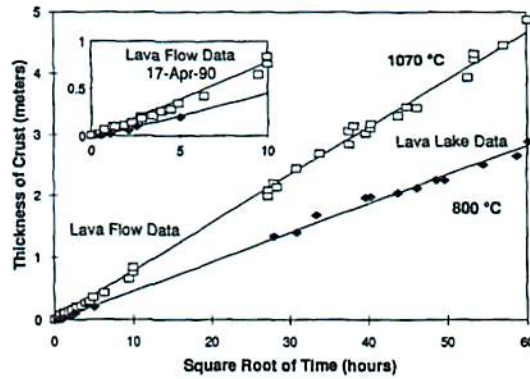


Figure 6: Graph of the depth to the 1070°C isotherm and the depth to the 800°C isotherm as a function of the square root of time using data from both a sheet flow and the first four months of a lava lake. Figure from Hon *et al.* (1994).

not begin to cool below 800°C until 10–12 min after formation (Hon *et al.* 1994).

- The 800–1070°C layer behaves ductilely, so it likely controls the tensile strength of sheet flows rather than the brittle top portion of the upper crust (Hon *et al.* 1994).

4 Crustal Overturn

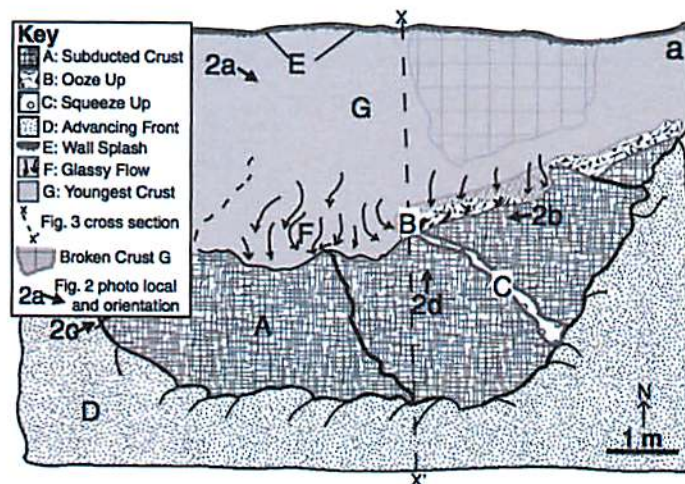


Figure 7: Map of the Kilauea Iki lava lake study area in Stovall *et al.* (2009)

- Cool dense crust founders and sinks into the hot molten lava below, which then cools and solidifies to form a new surface. This process occurs repeatedly throughout the life of a lava lake (Stovall *et al.* 2009).
- Crustal overturn has been observed in most terrestrial lava lakes and can occur either as a foundering of the whole lake surface followed by a period of stable crust formation or as localized foundering of individual plates (Stovall *et al.* 2009).

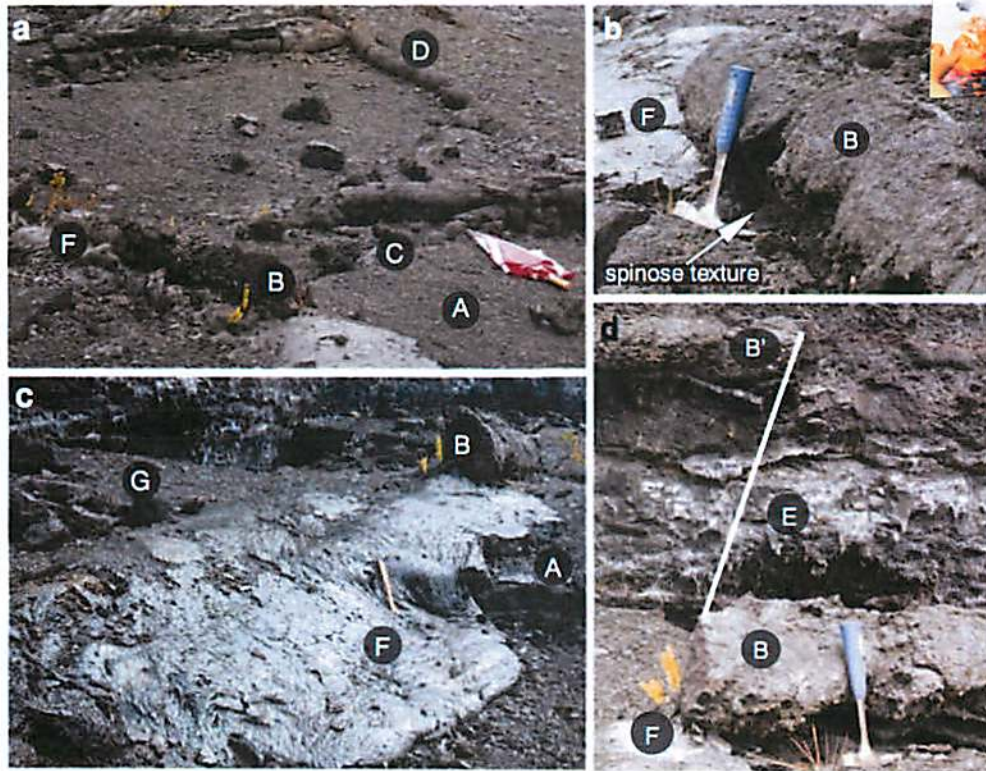


Figure 8: Photographs of the Kilauea Iki lava lake study area in Stovall *et al.* (2009)

- It is driven either by convection in the lava below causing plate tectonic-style motion on the surface or drainback of the lava back into the magma chamber below (Stovall *et al.* 2009).
- The overturn at Kilauea Iki was described as “allow[ing] brightly incandescent lake lava to well up and over-run a small area of the surface before solidifying. In this manner an entirely new surface crust was formed...” (Stovall *et al.* 2009 and references therein).
- This process has been observed qualitatively, but to estimate the densities of the units involved without dying, Stovall *et al.* (2009) measured densities of different units of the now solidified Kilauea Iki which is thought to preserve the frozen record of an incomplete overturn. They find density differences of 200 to 740 kg/m³ between the foundering crust and the fresh lava (Stovall *et al.* 2009).

5 Crystallization

- In Hawaii, olivine (39 wt.% SiO₂, 42 wt.% MgO, and 19 wt.% FeO) typically crystallizes at depth and erupts as a phenocryst with the basaltic melt (50 wt.% SiO₂, 8 wt.% MgO, and 12 wt.% FeO), so the melt is depleted in magnesium, nickel, and chromium when it erupts (Schmincke 2004).

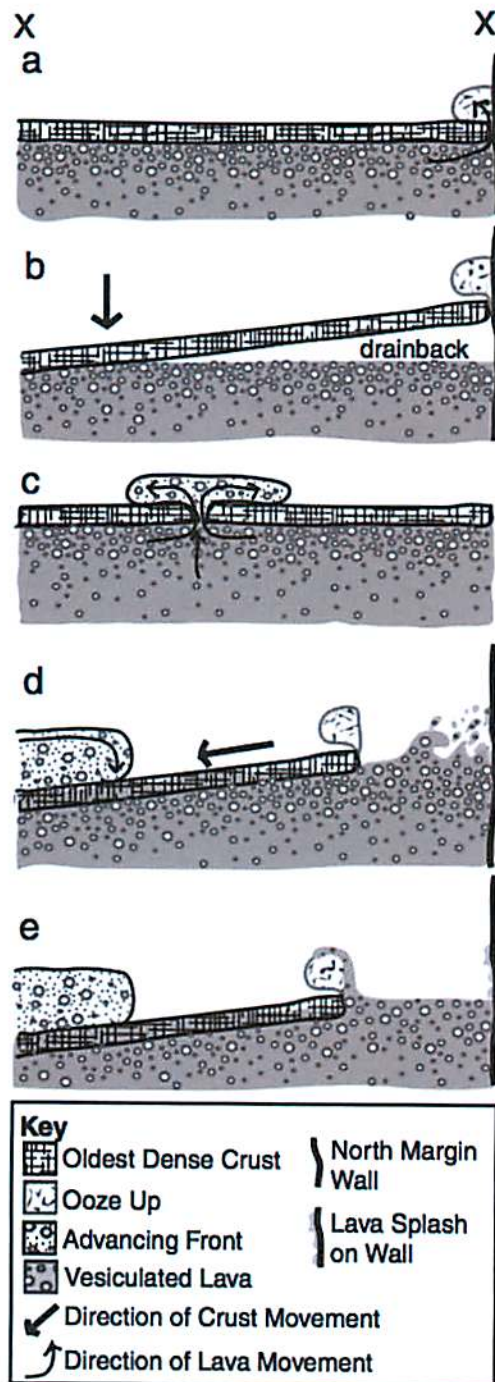


Figure 9: The final sequence of events that occurred along the line X–X' marked in figure 8. From Stovall *et al.* (2009).

- As the lava lake cools, Ca-Mg-Fe bearing pyroxenes and Ca-Na-Al bearing plagioclase crystallize (Schmincke 2004).
- When 50% of the melt has crystallized, it is enriched in iron and titanium and forms magnetite and/or ilmenite (ore minerals) (Schmincke 2004).



- When 75% of the melt has crystallized, the remaining melt is enriched in phosphorus and apatite crystallizes (Schmincke 2004).
- When the lava lake cools quickly, the last ~8 vol. % of the original melt can cool to glass with a composition enriched in Si, Al, K, Na, and trace elements relative to its original parent liquid (Schmincke 2004).

6 Planetary Connection

6.1 Mars

- Resurfaced floor segments, complex wrinkle ridges, and lava terraces within the summit craters on Tharsis shield volcanoes indicate that lava lakes were the dominant form of intra-caldera activity (Mouginis-Mark 1982).
- Wrinkle ridges on the caldera floor of Olympus Mons are interpreted to be caused by compression during the subsidence of the caldera floor, and linear ridges which are smaller and older than the wrinkle ridges are interpreted to be folds in the lava surface when the floor was forming. Pressure ridges such as these are seen in terrestrial lava lakes too. Several irregular collapse pits on the caldera floor are also consistent with features seen in terrestrial lava lakes (Mouginis-Mark and Robinson 1992).
- The cooling histories of lava lakes on Mars may differ from those on Earth due to the lack of rainwater on Mars. Rainwater would make the surface of terrestrial lava lakes colder and more likely to experience brittle failure (Chapman 2011).
- Summit caldera activity was (is?) periodic which is consistent with predictions of magma reservoir cooling and regeneration (Neukum *et al.* 2004). The most recent activity was only 2 million years ago (Neukum *et al.* 2004). This suggests that lava lakes may have been present at many times in Mars' history.

6.2 Io

- Lava lakes often form in patera on Io. Patera are volcano-tectonic depressions like terrestrial calderas which have diameters ranging from 2–202 km (Lopes and Spencer 2007).
- Patera floors are dark black compared to the reds, yellows, and whites seen on most of Io's surface. Their visible/near-IR spectra are most consistent with Mg-rich orthopyroxene. They are hypothesized to be silicate lava of mafic to ultramafic composition (Lopes and Spencer 2007).
- Most hot spots identified by Galileo's Near infrared mapping spectrometer (NIMS) coincide with paterae which suggests that most lava resurfacing on Io is confined within paterae (Lopes and Spencer 2007).

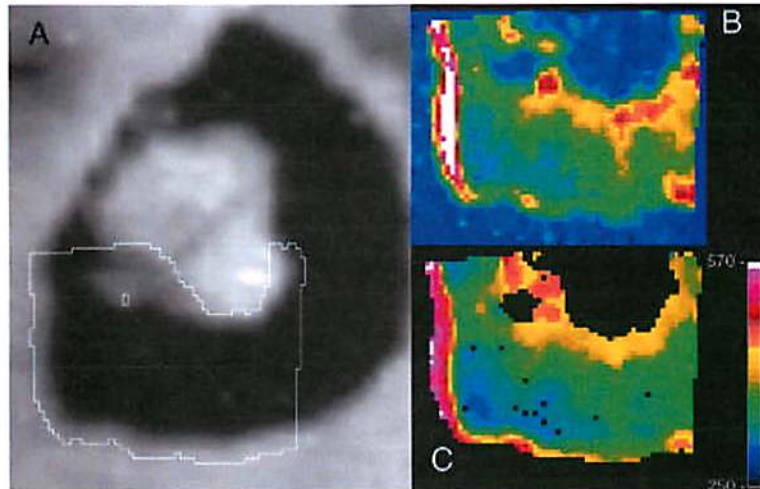
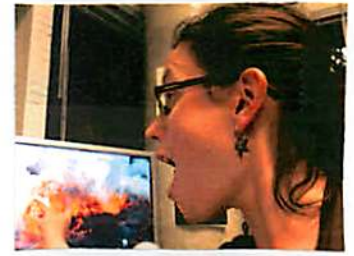


Figure 10: A) Visible image from Galileo Solid State Imaging System (SSI) of Loki Patera with the outline of the area observed by Galileo Near infrared mapping spectrometer (NIMS). B) Galileo NIMS map at $2.5 \mu\text{m}$. C) Temperature map (in Kelvin) from the Near infrared mapping spectrometer (NIMS) observation. Figure from Gregg and Lopes (2008).

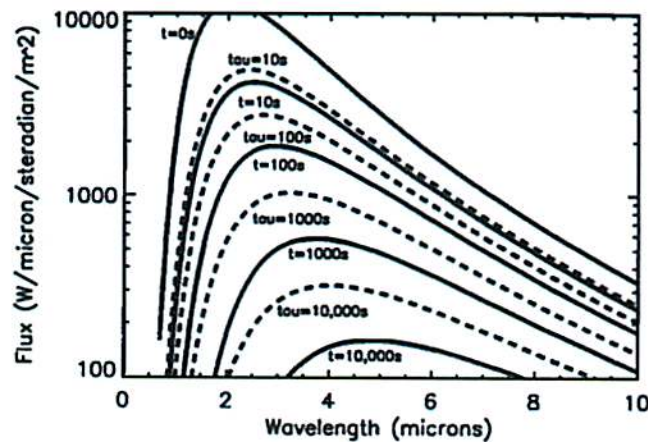


Figure 11: Blackbody spectra from cooling lava surfaces. Solid lines correspond to temperatures: 1156K at 10s; 985K at 100s; 777K at 1,000s; 602K at 10,000s. Figure from Keszthelyi and McEwen (1997).

- The margins of the paterae are usually bright in Galileo NIMS data (Figure 10) which is consistent with terrestrial lava lakes (Lopes and Spencer 2007).
- The thermal emissions of lava lakes can be used to put lower limits on eruption temperatures (Keszthelyi and McEwen 1997).
- Loki, a patera on Io, exhibits reoccurring brightenings detected by ground based observations (Rathbun and Spencer 2006), Galileo NIMS (Davies *et al.* 2012), and Cassini's Imaging Science Subsystem (Allen *et al.* 2013). These are interpreted to be the founding and growth of the crust of a lava lake on its caldera floor (Rathbun *et al.* 2002).

References

- Allen, D. R., J. Radebaugh, and D. C. Stephens 2013. Temperature and variability of Pillan, Wayland Patera, and Loki Patera on Io from Cassini ISS data. *Icarus* **226**, 77–88.
- Chapman, M. (Ed.) 2011. *The Geology of Mars: Evidence from Earth-Based Analogs*. Cambridge University Press.
- Davies, A. G., G. J. Veeder, D. L. Matson, and T. V. Johnson 2012. Io: Charting thermal emission variability with the Galileo NIMS Io Thermal Emission Database (NITED): Loki Patera. *Geophysical Research Letters* **39**, 1201.
- Gregg, T. K. P., and R. M. Lopes 2008. Lava lakes on Io: New perspectives from modeling. *Icarus* **194**, 166–172.
- Hon, K., J. Kauahikaua, R. Denlinger, and K. Mackay 1994. Emplacement and inflation of pahoehoe sheet flows: Observations and measurements of active lava flows on Kilauea Volcano, Hawaii. *Geological Society of America Bulletin* **106**, 351–370.
- Keszthelyi, L., and A. McEwen 1997. Thermal models for basaltic volcanism on Io. *Geophys. Res. Lett.* **24**, 2463.
- Lopes, R., and J. Spencer 2007. *Io After Galileo: A New View of Jupiter's Volcanic Moon*. Springer Praxis Books. Praxis Publishing Limited, Chichester, UK.
- Mouginis-Mark, P., and M. Robinson 1992. Evolution of the olympus mons caldera, mars. *Bulletin of Volcanology* **54**(5), 347–360.
- Mouginis-Mark, P. J. 1982. Late-stage summit activity of Martian shield volcanoes. In R. B. Merrill and R. Ridings (Eds.), *Lunar and Planetary Science Conference Proceedings*, Volume 12 of *Lunar and Planetary Science Conference Proceedings*, pp. 1431–1447.
- Neukum, G., R. Jaumann, H. Hoffmann, E. Hauber, J. W. Head, A. T. Basilevsky, B. A. Ivanov, S. C. Werner, S. van Gasselt, J. B. Murray, T. McCord, and HRSC Co-Investigator Team 2004. Recent and episodic volcanic and glacial activity on Mars revealed by the High Resolution Stereo Camera. *Nature* **432**, 971–979.
- Peck, D. L., T. L. Wright, and R. W. Decker 1979. The Lava Lakes of Kilauea. *Scientific American* **241**, 114–128.
- Rathbun, J. A., and J. R. Spencer 2006. Loki, Io: New ground-based observations and a model describing the change from periodic overturn. *Geophysical Research Letters* **33**, 17201.
- Rathbun, J. A., J. R. Spencer, A. G. Davies, R. R. Howell, and L. Wilson 2002. Loki, Io: A periodic volcano. *Geophysical Research Letters* **29**, 1443.
- Schmincke, H. 2004. *Volcanism*. Springer.

- Stovall, W., B. Houghton, A. Harris, and D. Swanson 2009. A frozen record of density-driven crustal overturn in lava lakes: the example of Kilauea Iki 1959. *Bulletin of Volcanology* 71(3); 313–318.
- Tazieff, H. 1994. Permanent lava lakes: observed facts and induced mechanisms. *Journal of Volcanology and Geothermal Research* 63(12), 3 – 11.
- Turcotte, D. L., and G. Schubert 2002. *Geodynamics - 2nd Edition*. Cambridge University Press.
- USGS 2008. USGS VHP Photo Glossary. <http://volcanoes.usgs.gov/images/pglossary/LavaLake.php>.
- USGS Volcano Hazards Program 2014. Hawaiian Volcano Observatory Daily Update. <http://volcanoes.usgs.gov/activity/status.php>.
- Wright, T. L., D. L. Peck, and H. R. Shaw 1976. Kilauea lava lakes: Natural laboratories for study of cooling, crystallization, and differentiation of basaltic magma. *Washington DC American Geophysical Union Geophysical Monograph Series* 19, 375–390.

Basic Characteristics of Lava Fountains
 LPL Hawaii Field Trip 2014
 By Sky Beard



Figure 1: Examples of Lava/Fire Fountains. Left: Lava fountain of Pu'u O'o. Center: 20 meter tall dome fountain at Mauna Ulu. Right: 15 meter tall arching lava fountain on the east rift zone of Kilauea. Photo credit: J.D. Griggs and J.B. Judd. Note scales can be much larger, see text.

The term 'lava fountain' is synonymous with 'fire fountain' and was developed to describe typical eruptions that occurred at active volcanoes in Hawaii. Generally, lava fountains are considered to contain low viscosity lava that fall as spatter pieces around the vent area (Andronico et al. 2008). Though there are several subtleties and forms, lava fountains are typically characterized by a jet of lava spraying high into the air, with the highest velocity in the center (Figs. 1, 2). Fountains can also be in the form of a dome or arch (Fig. 1.) Dome fountains form when the upward pressure of magma in the conduit is approximately equal with the mass of ponded lava above it. They typically have a hemispherical shape, form in gas-poor lavas, and can be up to several tens of meters tall. Arching fountains do not shoot up vertically like a typical fountain would; due to the shape and geometry of the erupting vent that sends lava upward and outward, forming an arch (USGS).

Lava fountains eject clots of magma into the air ranging in size from a few millimeters to about a meter in diameter, at speeds of typically ~ 100 m/s (Wilson and Head, 1981). The majority of the material lands while still hot enough to glow.

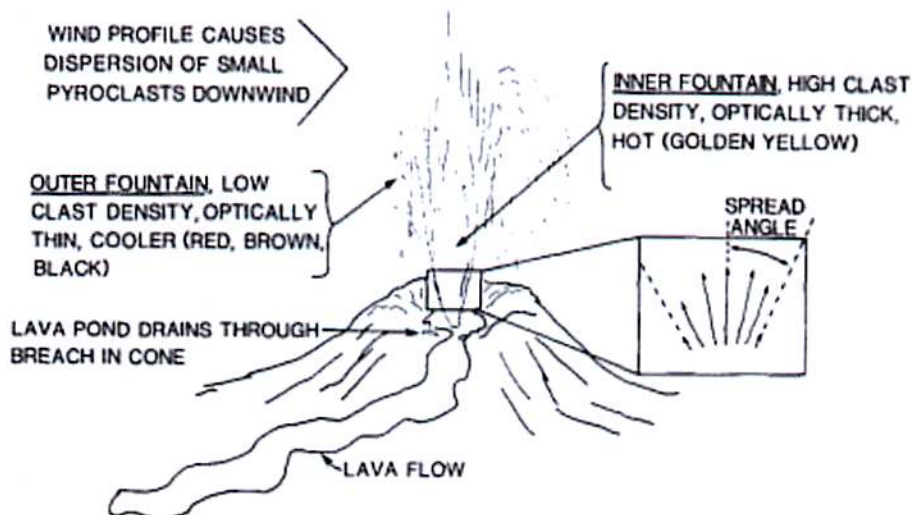


Figure 2: Typical pyroclastic eruption showing aspects of the fountain dynamic structure. Lengths of arrows in insert indicate velocity profile. From Head and Wilson 1989, Figure 1.

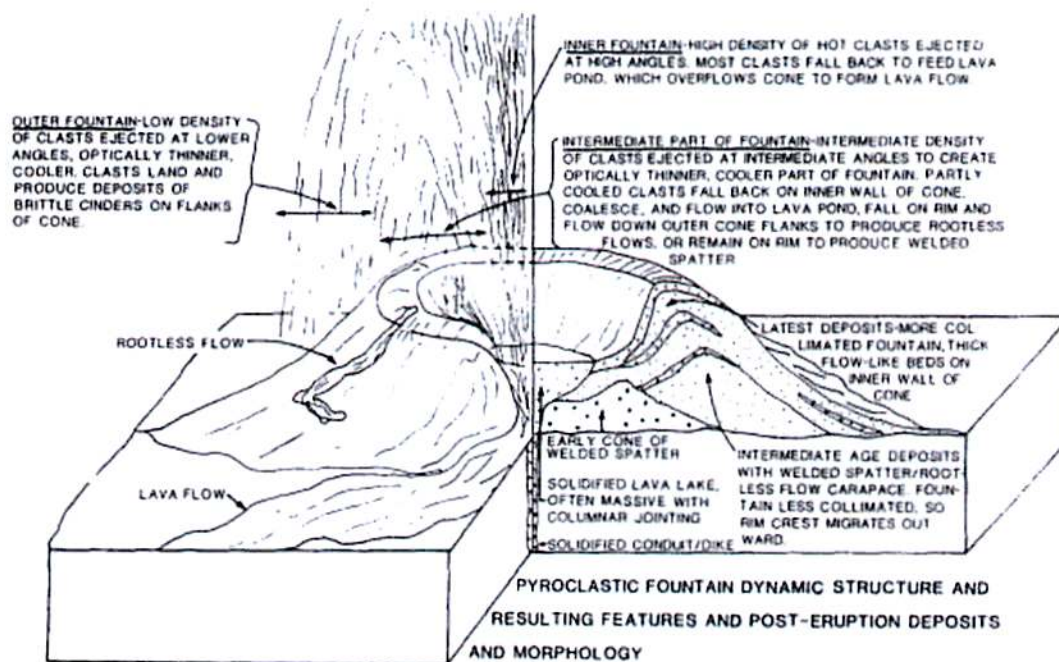


Figure 3. Relationship of fountain dynamic structure (left side) and resulting post-eruption features, deposits, and morphology (right side). From figure 7, Head and Wilson (1989).

The accumulation and coalescence of the hot clots can generate rootless lava flows, which can sometimes be hot enough to flow many kilometers from the vent. Much of the remaining material falling from the outer edges of the fountain cools sufficiently enough during flight that it cannot form rootless lava flows but it still can deform on landing and weld to the surrounding material, forming a spatter cone around the vent. Even cooler material can accumulate to form a loose cinder cone, and a small portion of material is convected upwards in a plume above the fountain and is deposited downwind forming a tephra blanket (Fig. 2,3, and 6).

One of the most spectacular aspects of lava fountains is the height that they can reach. Some of the more impressive examples are the fountains of Kilauea Iki (1959) that reached 580 m high (1900 ft), 1600 m fountain (5250 ft) from the Izu-Oshima volcano in Japan, and the 1500-2000 m (6500 ft) fountain in Mount Etna's 1999 eruption. There are several factors that determine the lava fountain height (an indication of the velocity of the magma in the vent), including the amount of exsolved volatiles (more gas, more buoyant, momentum transfer to pyroclasts, faster ascent) and the width of the conduit system. A study by Head and Wilson 1987 was done on the fountain heights of the Pu'u O'o vent in the east rift zone of the Kilauea Volcano in Hawaii, to see if they could determine which factor influences fountain height the most, and to see if fountain height could be used as a proxy to measure the volatile content and the geometry of the conduit system.

The height of the fountain can be represented by $H = u^2/2g$, where u is the rise velocity of the magma and is dependent on the driving pressure gradient, tube radius, and various friction factors and physical properties of the magma. This

equation is simply ballistic height, but the authors believed this to be appropriate for describing fountain behavior. Using measurements of discharge rates and fountain heights from Pu'u O'o in their model, they tried to predict the gas contents of the magma, which was then compared to gas content measurements measured during the eruption (Greenland, 1987). The relationship between lava fountain height and discharge for various gas contents can be seen in figure 1, which shows that fountain height weakly depends on the total discharge, except at very low discharges ($<25 \text{ m}^3/\text{s}$) where the wall friction in the conduit would become more important due to the effectively smaller conduit radius to produce such low discharge values.

The highest observed fountains for Pu'u O'o were around 400 meters high, which would indicate an exsolved gas content somewhere between 0.6% and 0.8% (weight % H_2O) over a wide range of discharge values, according to their work (Fig. 4). The average fountain height of Pu'u O'o was closer to 200 meters high, corresponding to a gas content of 0.4% for all discharges higher than $50 \text{ m}^3/\text{s}$, which in fact matches reported measurements (Greenland 1987). More recent studies (Wilson et al. 1995) show that this is actual an underestimate of the gas content due to the effects of ponded lava.

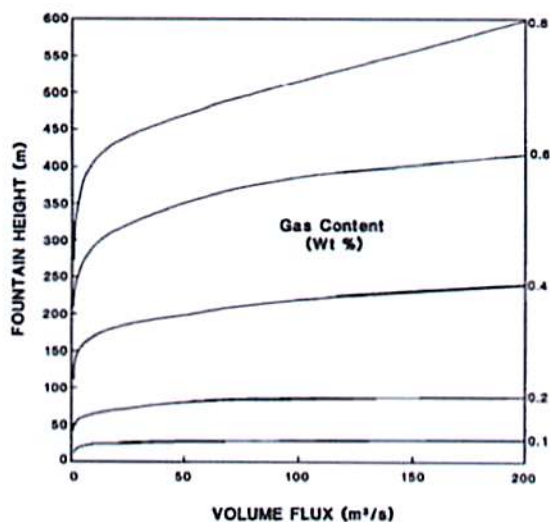


Figure 4. Predicted fountain height with erupted magma volume flux for five values of exsolved volatile content, in Head and Wilson model. For Hawaiiin magmas, fountain height depends more strongly on gas content than volume flux. Head and Wilson (1987).

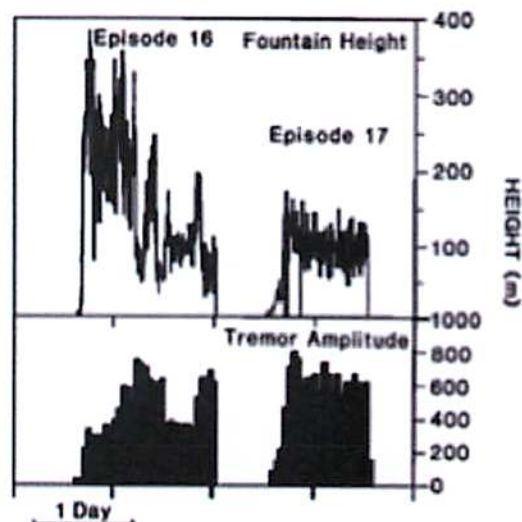


Figure 5. Variation of fountain height with time during episodes 16 and 17 at Pu'u O'o eruption. From Wolfe et al. (1987).

Fountain heights at Pu'u O'o showed a lot of variation during each eruption episode, which indicates variability in the gas content. In 20 episodes of fountaining, the height varied from a few meters to approximately 400 meters, suggesting a variation in gas content of 0.1-0.6% (figure 1). In a given episode, fountain height often increased with time, became variable, and then suddenly terminated. Head and Wilson believe this indicates the episodes' initial fountains were composed of a gas-poor magma, followed by gas-rich magma until the episodes abruptly ended.

The initial gas-poor magma is likely the magma left over from the end of the last episode, and is thought to lose some of its gas while at rest. The variation in height as the episode is progressing shows that the gas content can vary considerably while fountaining is ongoing, even on short time scales ($\sim 0.3 - 0.6\%$ < 3 hours).

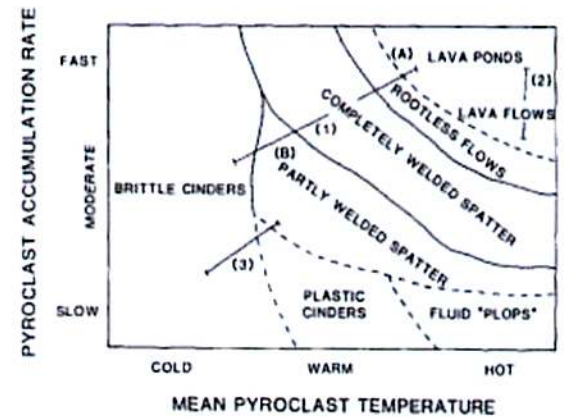


Figure 6. Top right: Pyroclast deposit diagram, showing relationship between pyroclast accumulation rate and temperature. Numbers 1-3 correspond to the three types of pyroclastic eruptions at left, with the top left being 1, and the bottom being 3. Number 1 (top left) shows a high column of pyroclasts that are landing on the cone surrounding the vent, to form completely welded spatter. Number 2 (left middle) shows a hotter and faster accumulation that is falling back into the pond, which is feeding the lava flow. Number 3 (left bottom) shows a cooler and slowly accumulating fountain with produces brittle cinders. From Head and Wilson (1987).

There are examples of fire fountains occurring on Io, observed by Galileo, with several studies looking at thermal emissions and black body curves to determine lava temperatures, see Fig. 7 (Stansberry et al. 1996, Davies et al. 2001).



Figure 7. Lava fountain observed in the Tvashtar region by Galileo in 1999. The fountain was so bright it overloaded the camera's detector, causing the pixels to appear white. Molten material was ejected over 1.5 km high.

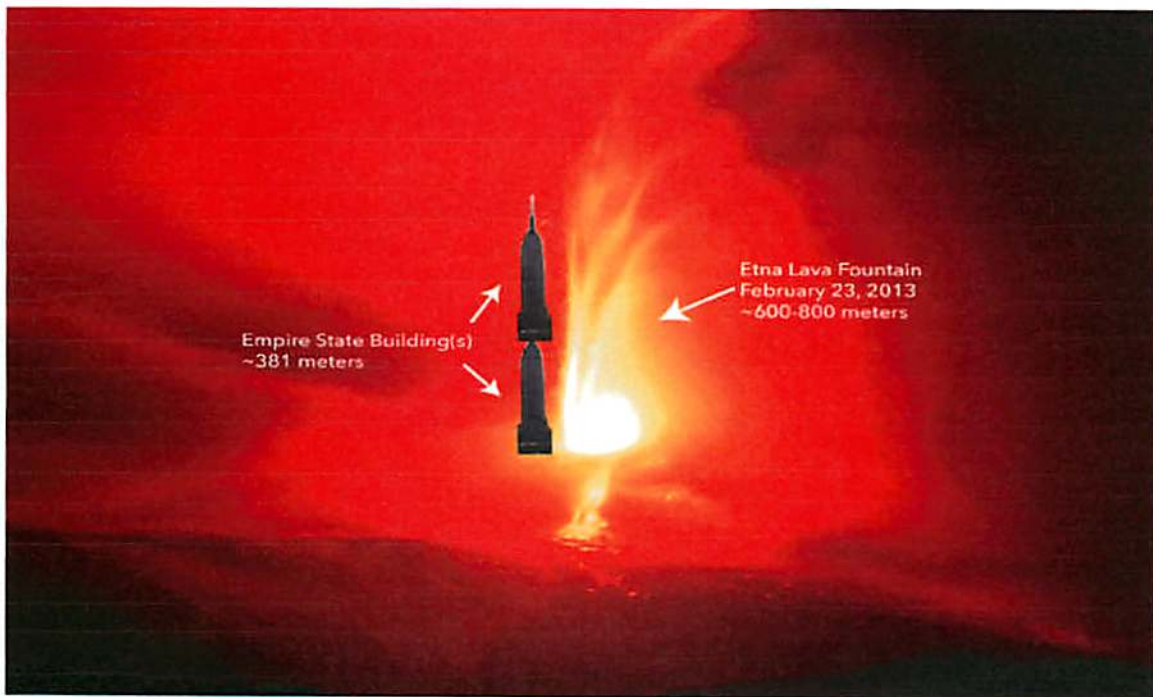


Figure 8. Empire state buildings for scale to get an appreciation for the size of a 800 m fountain from Mt. Etna, Italy. Photo by Dr. Boris Behncke.

References

Andronico, D., Cristaldi, A., Scollo, S. 2008. The 4-5 September 2007 lava fountain at South-East Crater of Mt. Etna, Italy. *J of Volc. And Geotherm. Research*. Volume 173 Pages 325-328.

Greenland, P.L., 1987. Hawaiian eruptive gases, in: R.W. Decker, T.L. Wright and P.H. Stauffer (Editors), *Volcanism in Hawaii*. U.S. Geol. Surv., Prof. Pap.. 1350: 759-770.

Head, J.W. and Wilson, L., 1987. Lava fountain heights at Pu'u 'O'o Kilauea, Hawaii: Indicators of amount and variations of exsolved magma volatiles. *J. Geophys. Res.*, 92: 13,715-13,719.

Wilson, L. and Head, J.W., 1981. Ascent and eruption of basaltic magma on the Earth and Moon. *J. Geophys. Res.*, 86: 2971-3001.

Wilson, L., Parfitt, E.A., Head, J.W. 1995. Explosive colcanic eruptions. The role of magma recycling in controlling the behavior of Hawaiiin Stayle lava fountains. *Geophys. J. Int.* Volume 121, 215-225.

Kilauea Iki: Drilling and Seismic Investigations

Ali Bramson (Figure 1)

Kilauea Iki is a crater to the east of Kilauea that erupted in late 1959 (Figure 2). The eruption filled the crater (originally about 200 m deep) with an estimated 30 million cubic meters of fresh lava, leading to a molten lava lake ~111 m deep (Chouet 1979) and 750 m in diameter (Hermance, Forsynth and Colp 1979 [a report to Sandia National Laboratories]). It also left a cinder cone, Pu'u Pua'i, at the southern rim. The lake cooled slowly, forming upper and lower crusts with a lens of molten lava in the middle. The accessibility of this lava lake led to numerous studies on the cooling, crystallization and differentiation of magma as well as on geophysical techniques for probing subsurface magma. As such, it has been intensively drilled, cored and sampled by the USGS. Many of the seismic and drilling investigations focused on determining the vertical and lateral extent of the remaining subsurface melt layer.



Figure 1: A selfie of the author in Reid Park, Tucson.

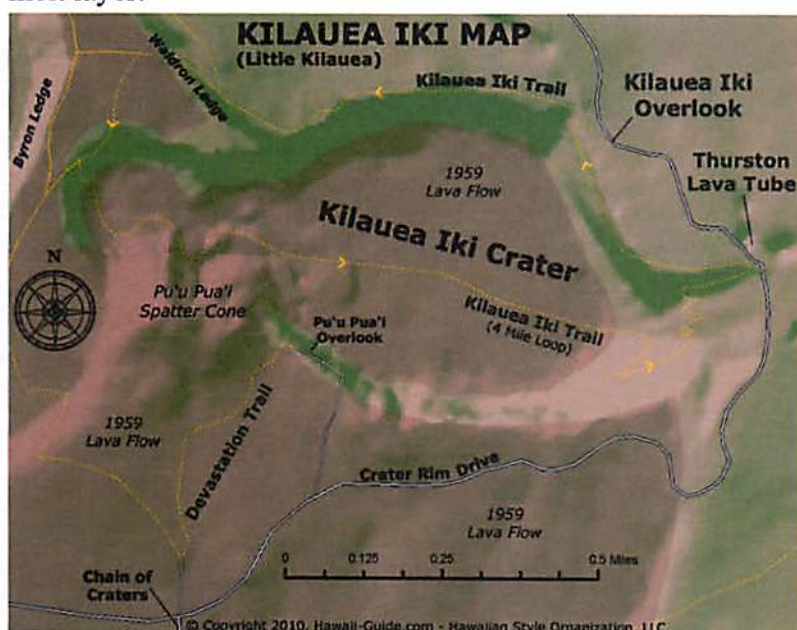


Figure 2: Kilauea Iki Map (hawaii-guide.com)

Two different lava compositions were produced in the initial stage of the eruption (Murata and Richter 1966), with the subsequent 16 stages of the eruption consisting of hybrids of these two end-members and containing varying amounts of olivine (Write 1973). The lake's surface stabilized by December 23, 1959 (Ault et al. 1951) and soon after a network of leveling stations were added to the surface (Figure 3) along with 4 initial

drilling holes that found the upper crust to be 6.7–13.4 m thick (Helz 1980). Coring of the lake found that the bulk of the core was a gray, olivine-phyric basalt but had varying olivine content with depth. The top 15 m of the crust was found to be very olivine-rich and highly vesicular (Helz 1980). The amount and size of olivine crystals decreased down to 23 m, and between 23 and 40 meters depth the rock contained 5–10% phenocrysts of small olivine crystals. Olivine content and grain size increased below 40 meters depth and remained high (20–45% by volume) throughout the lower crust except for a olivine-depleted layer less than 6 m thick near the basalt contact (Helz 1980).

Over a dozen more holes were drilled between 1960 and 1979 through the crusts of Kilauea Iki (Colp and Okamura 1978), Figure 4. Using temperature and crustal thickness measurements, thermal history models were constructed and tested (Peck et al. 1977). These models were

compared to measured “melt depths” (the solid-liquid interface at a temperature of $1070 \pm 5\text{C}$) by looking for the decrease in basalt rigidity and increase in olivine phenocrysts. Melt is defined as a crystal-liquid mush of fluid that loses rigidity such that it cannot support the weight of the drill string. Because the drill loses the necessary hydraulic pressure when reaching the melt, it was not possible for studies to drill very far into the melt. As such, the upper crust is well understood across the lake but the lower crust could only really be sampled near the edge of the lake. The change in thickness of the upper crust over time was well documented; the upper crust has grown from a thickness of 13.6 m in 1962, to 26.5 m in 1967, to 44.2 m in 1975, to 52.5 m in 1979 (Helz 1980), Figure 4. The upper and lower crusts met over most of the area of the lava lake sometime in 1983 (Helz 1980). Discrepancies of 10s of meters between the expected lava lake thickness from pre-eruption surface measurements and the actual drilled thicknesses were found in multiple locations and of greater magnitude than could be explained by pre-existing topographic features or errors. This led to the conclusion that the crater either subsided or was eroded along the north wall during the eruption (Helz 1980). It also demonstrates that pre-eruptive topography can only be used as an approximate guide to calculating lake thicknesses.

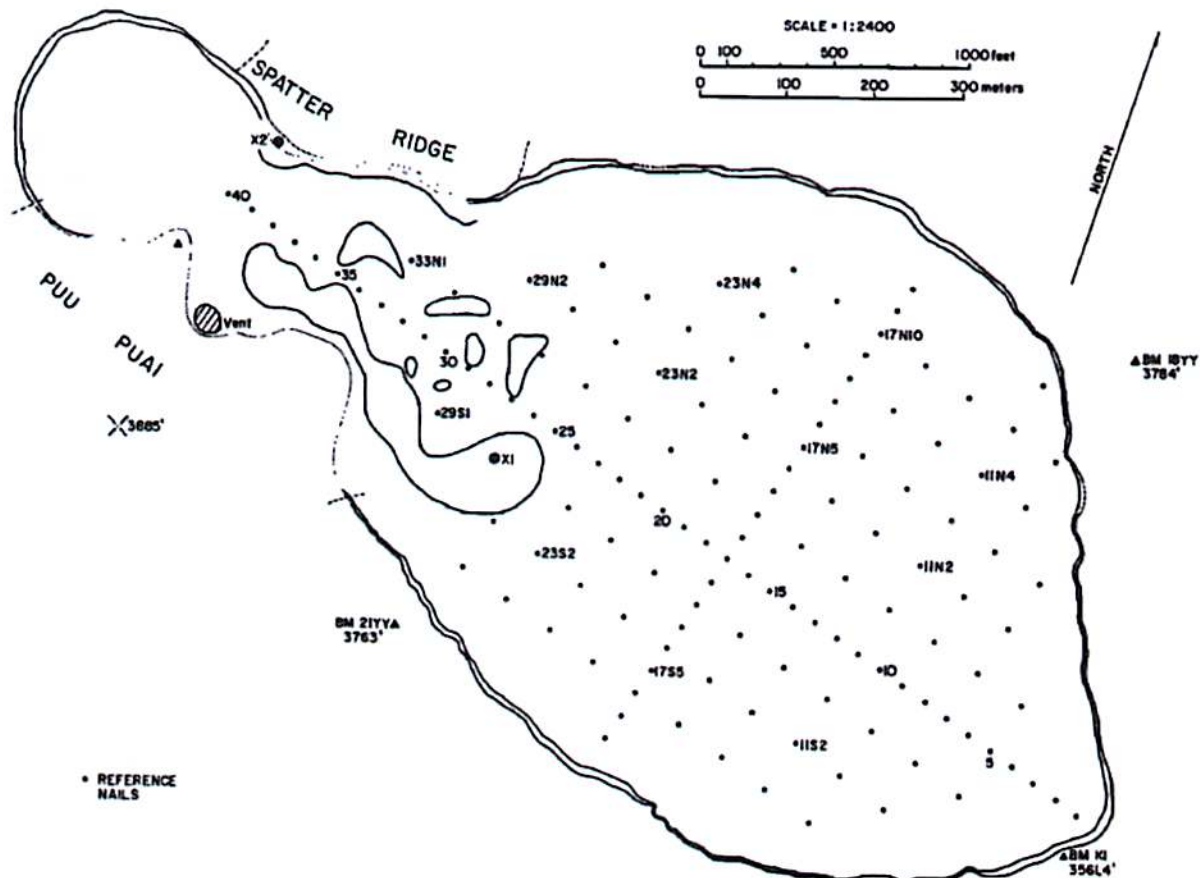


Fig. 1. U.S. Geological Survey map of the Kilauea Iki lake floor showing leveling survey nails. The nails are identified by the code attached to them.

Figure 3: Map from Chouet 1979 showing locations of USGS leveling nails. An example of the convention used to label the nails: station 17N5 means the station is 1700 feet west of the eastern-most station along the principal east-west line and 500 feet north of that line.

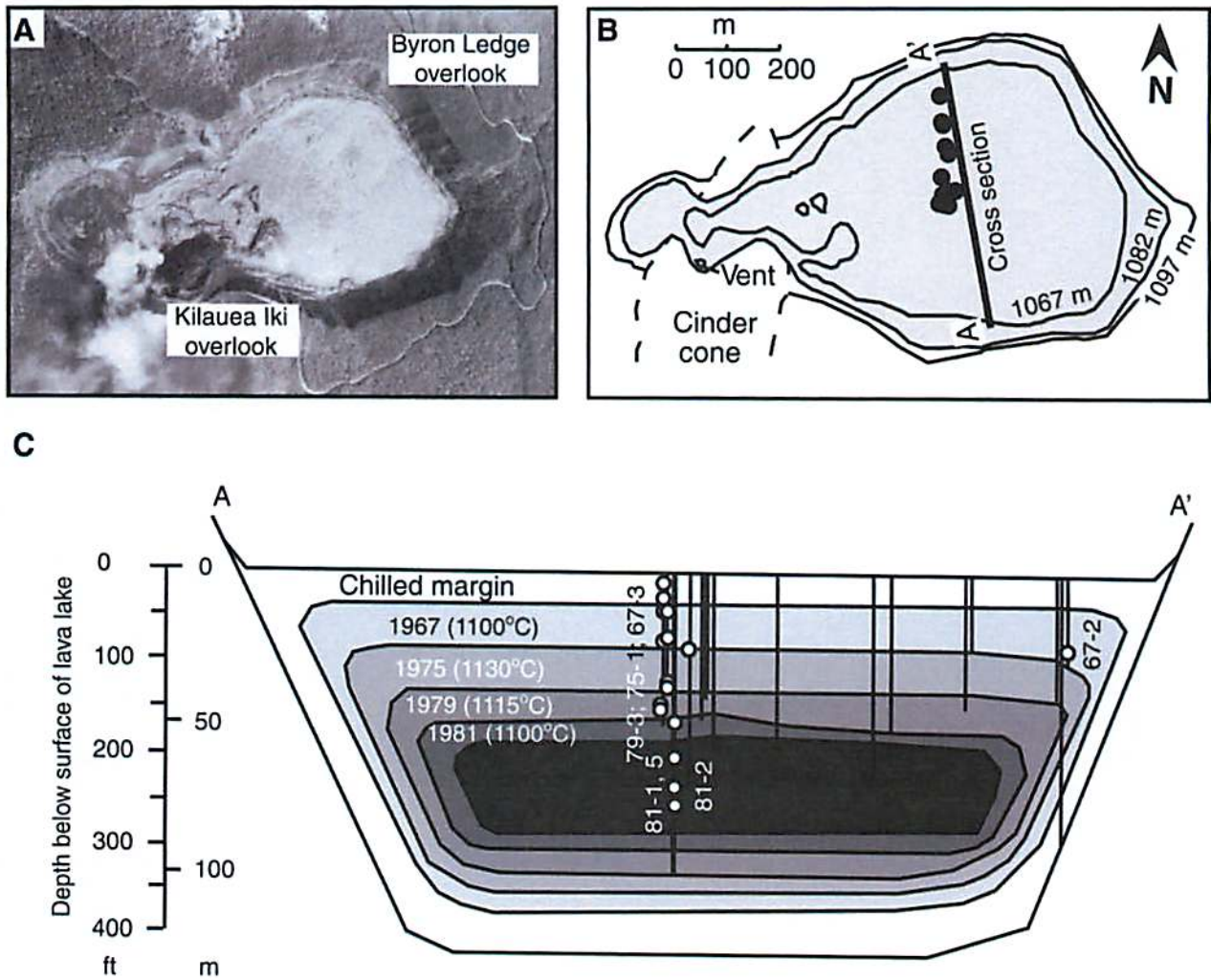


Figure 4: Figure from Teng, Dauphas and Helz 2008 showing an aerial photograph (A) taken immediately after the 1959 eruption with the newly formed Kilauea Iki lava lake. (B) shows a plan view of the post-eruptive surface with black circles indicating the locations of the drill holes from 1967-1988. (C) is a cross section of the lake (vertical exaggeration of 2:1) with vertical lines showing the drill hole locations and depths. The concentric zones show the limit of drillable crust and temperatures at different years.

The series of geophysical sensing experiments that were performed were done so with the following goals: (1) monitor the properties of lava in situ, (2) map the thickness and extent of the lava lens and (3) evaluate the feasibility of geophysical techniques for understanding magma structures (Hermance and Colp, 1982).

Electromagnetic wave experiments to determine vertical structure included vertical loop-loop electrode sounding (Smith et al. 1977) and Schlumberger galvanic sounding (Zablocki 1976). The results found there were likely 5 layers in the lake (Figure 5) with the top, dry surface having high resistivity due to the low concentration of fluids/water in porous and fractured material. Layers 2 (a warm, wet layer) and 3 (a dry, resistive layer with temperatures high enough to drive off water vapor) have somewhat lower resistivities due to higher pore fluid concentrations and more dissolved salts. Layer 4 is the conductive melt and layer 5 is the dry, resistive layer below.

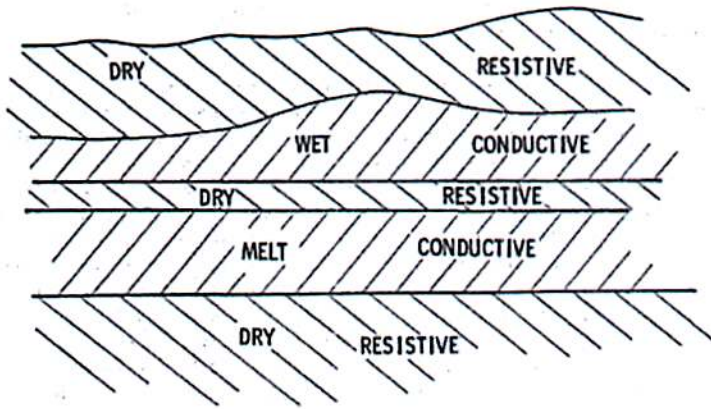


Figure 7. Conceptual Model of Kilauea Iki Lava Lake (after Smith et al, 1977, Figure 4)

Figure 5: Figure from Smith et al. (1997) showing the model of layers of varying resistivities.

electrically-active layer (low resistivity) over the traditional “liquid” layer (physically- and petrologically-speaking) where dense blocks of foundered crust and olivine phenocrysts increase the resistivity (Hermance, Forsyth and Colp 1979). This led to the geological model seen in the figure below (Figure 6) from Smith et al. 1977 and shows the difficulties in finding a one-to-one correspondence between electrical layering and rheological layering of molten material.

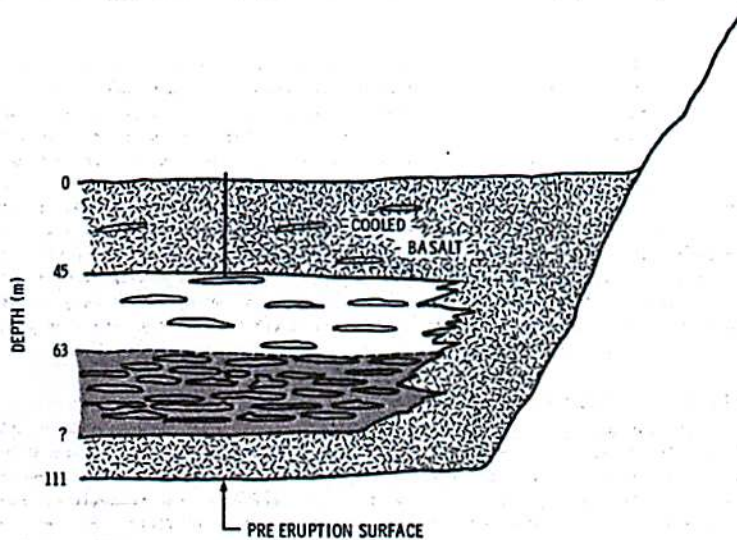


Figure 8. Complex Geological Model of Kilauea Iki Lava Lake, Showing Stratification in the Melt Zone. The lower shaded zone is less conductive than the upper, not shaded, zone (after Smith et al, 1977, Figure 14).

Difficulty relating these electromagnetic interpretations to the geological interpretation led to a conflict: electrical properties suggested the melt was 17.5 m thick while the thermal history estimates called for a top crust of 45 m and bottom crust of 30 m thick leaving the 40 m space in between to be the molten layer (Hermance, Forsyth and Colp 1979). To resolve this discrepancy, Smith et al. (1977) suggested the liquid layer is divided into a top,

Figure 6: Geologic model from Smith et al. 1977 of the liquid layer.

Aki et al. (1978) used refractive data from a 1976 seismic survey to determine the velocities of P waves in the upper crust. The maximum velocity of the P waves was 2.2 km/s and the lowest was 0.8 km/s near an eruptive vent on the west side of the lake and in the deeper parts of the lake. The P-wave velocity in the melt was predicted to be as low as 0.3 km/s. Love wave data were also available (showing 0.75 km/s velocities west of nail 22 and 0.6

km/s to the east). These wave velocities led to shear wave velocity models that suggested the melt was a single, 20 m thick layer with wave propagation velocity of 0.55 km/s. These seismic velocities and the fact that the melt lens transmitted shear waves led to the conclusion that the melt contained 5% vesicles (Aki et al 1978; Shaw et al 1968). Other studies suggested that

vesicles did not cause the transmission of shear waves but rather the transmission was due to interlocking crystals, a theory that is more supported by the petrographic evidence (Helz 1980). It is a bit confounding that a melt with interlocking crystals is too fluid to be drilled through but rigid enough to transmit shear waves. This led Helz (1979) to suggest that perhaps the drill failure is due to the drilling technique collapsing these interlocking crystals, preventing further drilling into the melt.

Two experiments used seismicity to look for lateral variations (Chouet et al. 1976, Aki et al. 1978). Passive monitoring of micro-earthquakes in the cooling crust showed a decrease in frequency of seismic events at edge of lava lake. Assuming events started near the magma lens, the experiments used the falloff of activity to outline horizontal extent of magma reservoir. They used a single seismograph to count number of events at different lateral locations. At the northern and eastern sides, the fall off in activity was close to the edge of the magma lens. However, on the west side the falloff was within the bounds of the lens, suggesting something other than extent of the magma was controlling the level of seismic activity locally. Micro-earthquakes happen because of cracking from the thermal stresses of the basalt cooling, and are affected by diurnal temperature fluctuations (with a maximum of events at midnight and minimum around noon) and differential subsidence of the crust of lake (spatially and temporally non-uniform). Sure enough the drop in activity was correlated to a set of linear cracks. These studies showed that the number of seismic events could not be used to infer the edge of the magma lens.

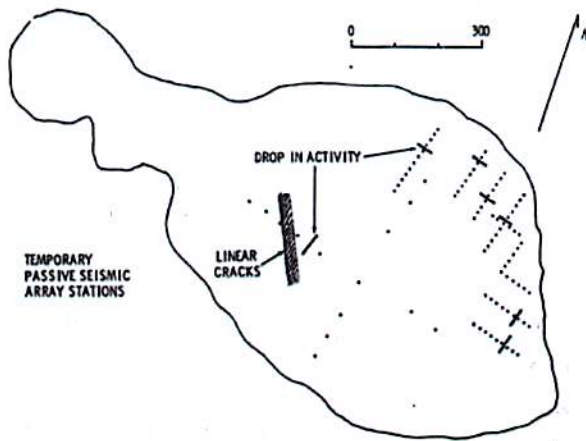


Figure 19. Location of Geophones for Passive Seismic Investigations in Kilauea Iki Lava Lake

Figure 7: Drop in lateral micro-earthquake activity found north of nail 17N10 and west of nail 22 (Hermance, Forsynth and Colp, 1979)

Crustal foundering (filling in and sinking) driven by density differences can lead to the overturning of a cooling lava lake crust. This process happens when the advancing of a fresh, low-density flow occurs over an older, higher density crust. The front breaks up the older crust and causes the foundering and sinking of this unit, which exposes new, hot, low-density lava. The foundering event occurs due to the

gravitational instability associated with the accumulation of rising gas bubbles beneath the degassed crust. This process occurred at Kilauea Iki and part of the overturning cycle was frozen into the lava, allowing it to be studied (Stovall et al. 2009).

When a vent feeds lava lakes from directly underneath (an “active” lava lake), the overturn process leaves no physical evidence behind which makes it difficult to understand the process. If physical evidence did happen to be left behind, generally the magma withdrawal leads to a collapse of the lake, destroying surface crust features that could be associated with overturn. Kilauea Iki is such a good case to study overturn because it is an “inactive” lava lake, meaning a vent adjacent to the lake fed it. This means there is less lava withdrawal and lake collapse so

there is better preservation of surface features associated with crustal motion. In the 17th and final stage of lava drainage, the motion of the lake stagnated. The surface crust that had been in constant motion due to convection froze and preserved the final (though incomplete) overturn cycle. The best example of this frozen overturn is on the northern margin of the lake about 200 m from the vent (Figure 8) with Table 1 showing properties of each unit. Stovall et al. (2009) concluded it is easy to generate density differences of 100s of kg/m³ between sinking and overriding units, indicating overturn is inevitable in the cooling process.



Figure 8: Photos of study area in Stovall et al. (2009) showing spatial relation between units that allowed for the interpretation of the nature and timing of the last foundering event. (A) shows the mature crust (unit A) that pulled away from the wall. (B) shows the path that was opened up which gave rise to bulbous ooze that came up (unit F). (C) shows the molten lava that was under the plate squeezed up through the cracks. (D) shows the flow front that moved across the surface crust, displacing it downwards and caused the foundering.

Table 1 Bulk density of overturn units, Kilauea Iki lava lake

Figure 1 Label	Feature interpretation	Number of samples measured	Bulk density (kg/m ³)	Standard deviation (kg/m ³) ^a
A	Subducted crust	8	1452	151
B	Ooze-up	9	1341	93
C	Squeeze-up	5	1084	76
D	Advancing front	12	1253	103
E	Wall splash ^b	9	1956	187
F	Glassy flow	11	715	442
G	Youngest crust	6	1163	71

^aStandard deviations are near 10% except for Unit F where the samples collected are relatively heterogeneous and contain a broad size-range population of macroscopically visible vesicles.

^bUnit E exhibits the highest density likely due to the violent ejection of lava from the lake which disrupted bubbles and permitted outgassing of the lava.

Table 1: Table of properties of each unit studied by Stovall et al. (2009) and shown in Figure 8.

Planetary Connections:

Lava lakes can be found on other planets and moons, with the finest examples being on Io. Loki Patera (Figure 9) is the most powerful volcano in the entire solar system and has a lava lake 55 km wide by 390 km long, covering an area of $2.1 \times 10^4 \text{ km}^2$ (Rathbun and Spencer 2006). It has been suggested by Rathbun et al. (2002) that the Loki lava lake is undergoing overturn. Telescopic observations that show a change in infrared brightness behavior of the area that occurred in mid-2001 support the assertion that Loki is undergoing overturn (Rathbun et al. 2002). Models of variations in the overturn propagation speed have been shown to explain variations in the ground-based telescopic infrared observations (the faster the overturn propagates, the shorter the brightening event will last and the more young surface area is produced leading to an increase in brightness). Modeling of the individual brightening events between 1997 and 2000 yield overturn velocities of 1.53 km/day. In the post-2001 data, the brightness variations stopped, remaining constant for 500-900 days. The models predict this is due to a lessening in overturn propagation velocities (Rathbun and Spencer 2006).



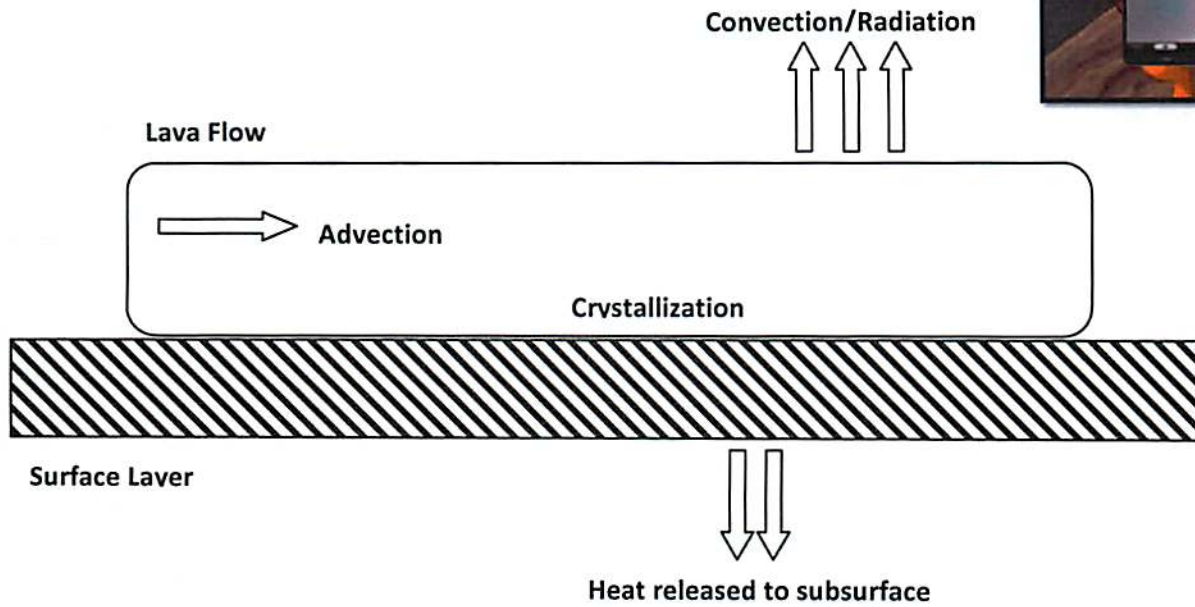
Figure 9: Image of Loki Patera, Io from Voyager.

Unfortunately, there has been no drilling on other solar system objects. ☹ However, there are limited seismic data collected on the moon during the Apollo missions in the form of four seismometers put on the nearside of the moon between 1969 and 1972. These four seismometers recorded 3 orthogonal directions of ground motion until 1977. However, the small number of stations, lack of spatial extent of the network and low attenuation of the seismic energies meant the stations were not able to directly measure if waves were being reflected or refracted by a core. But, more recent models using these Apollo lunar seismograms suggest the possibility of a core of ~60% liquid by volume and layered as a solid inner core with a fluid outer core (Weber et al. 2011).

InSight (Interior Exploration using Seismic Investigations, Geodesy and Heat Transport) is set to launch in 2014 to land near the equator of Mars. It will have a seismometer onboard that will detect internal seismic events and quakes. Currently two radar sounders are orbiting Mars: SHARAD (Shallow Radar) onboard the Mars Reconnaissance Orbiter and MARSIS (Mars Advanced Radar for Subsurface and Ionospheric Sounding) onboard Mars Express. While not taking direct seismic measurements, these radar sounders are able to detect electromagnetic interfaces in the subsurface, including buried lava contacts in Elysium, layering in the North Polar Layered Deposits, and ice-rock interfaces in Arcadia Planitia and Utopia Planitia.

Cooling and Thermal Characteristics of Lava Flows

Chet Maleszewski



- There are two primary heat sources for the flow. The first is due to advection as additional lava reaches the surface from its source. Also, as the lava crystallizes, the latent heat that is released from the phase change is absorbed into the flow.
- Heat can escape outward towards the environment or the surface layer below the flow. The lava flow will radiate in the infrared, following the Stefan-Boltzmann law. Heat is also lost at the flow-air interface via convection. Conduction occurs between the flow and the underlying surface.
- Lava at the flow boundaries will solidify more quickly than the central layers, as time is needed for heat to diffuse to the boundaries given the low conductivities for basaltic rock. For low viscosity lavas, **lava tubes** can be formed as a result of this. The solidified flow above the molten lava in the tube provides insulation, trapping heat that is released from the remaining molten material. This mechanism allows lava tube flows to travel a larger distance than a more typical flow channel.
- Insulation can also occur in silica-rich lavas as rapidly cooled magma form into glass fragments which then sink into the molten lava.

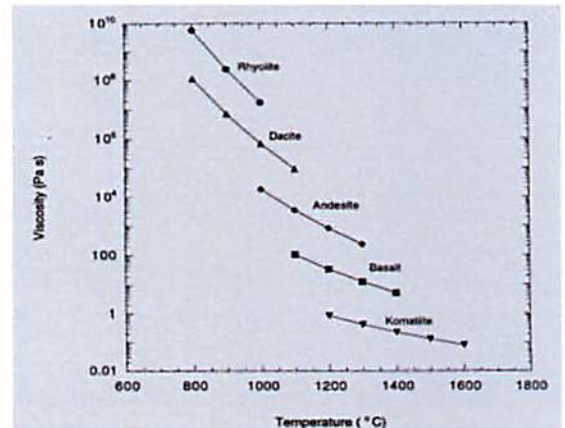


Thurston Lava Tube, Hawaii (Wikimedia Commons)

Temperature and Rheology:

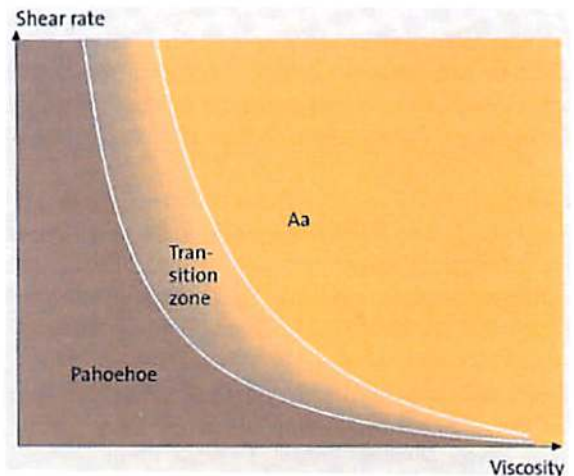
- Viscosity increases as the lava continues to cool. At the start of the flow, temperatures are hot enough where the lava behaves as a Newtonian fluid (i.e. shear stress proportional to viscosity and shear rate).
- Assuming the flow remains a Newtonian fluid, the length of the flow channel is proportional to $\frac{H^4}{\eta}$, where H is the flow's thickness and η is the viscosity.
- As the flow cools, formation of crystal fragments within the lava (phenocrysts) leads to the lava behaving like a Bingham plastic. For Bingham behavior, a particular yield stress must be exerted on the lava before it begins to flow. This yield stress increases as the temperature decreases.

<http://darkwing.uoregon.edu/~cashman/GEO311/311pages/L10-mafic%20rocks.htm>



Temperature and Lava Textures:

- The texture of the lava is dependent on the lava's silica content, viscosity (which is temperature dependent), and the rate of shear strain on the flow as it moves.
- Silica-rich lavas that are rapidly cooled form glassy fragments. Basaltic lavas which cool more slowly form a'a and pahoehoe lavas seen in Hawaii. Highly viscous lava under large strains begins to break into clumps as the flow cools and moves (a'a lava). Less viscous pahoehoe lava does not fracture as easily by shear forces, leading to the ropy textures seen on these flows.
- Transitions from pahoehoe to a'a lava can occur at the flow boundaries where the lava is most cool, thus having a higher viscosity (assuming the other properties of the lava are unchanged).



Shane's Volcanism II slides, top Schminke 2004, bottom Wiki Commons

Fracturing in Lava Flow Structures:

- Lava will contract as it solidifies. The strain from the contraction leads to fractures in the flow. Fractures start at the top of the flow where cooling rate is the fastest. Still molten lava can protrude through these fractures to produce more complicated flow networks.
- These fractures can propagate downward throughout the thickness of a flow. A series of cracks from polygonal columns that can be seen as the lava flow edge begins to erode. This is known as columnar jointing.

Columnar jointing on Mars as seen from Hi-RISE:
http://www.uahirise.org/ESP_029286_1885



- Flow structures due to these thermal effects (lava tubes, columnar jointing) have been observed via remote sensing on the Moon and Mars. The type of structures and flow morphologies present on the surface depends a multitude of factors. Understanding a particular flow's morphology and thermal structures requires use of remote sensing data, modeling, and comparisons to our knowledge of flows on Earth.



Lava tubes as seen on Mars and the Moon.
http://www.uahirise.org/PSP_008433_1755And

Shane's PTYS 554 Lecture Slides. Volcanism II, and references therein.
Modeling Volcanic Processes: The Physics of and Mathematics of Volcanism. Eds. S. A. Fagents, T. K. Gregg, Rosaly M. C. Lopes. Cambridge University Press.
Milazzo, M. P. et al. Discovery of Columnar Jointing on Mars. *Geology*. 37. 171-174.
Planetary Surface Processes. H. J. Melosh. Cambridge University Press.
Fundamentals of Physical Volcanology. E. A. Parfitt and L. Wilson. Blackwell Publishing.

LAVA FLOW RHEOLOGY E. I. Schaefer

VISCOSITY:

Viscosity notes from Winter, 2001, except where noted.

The viscosity of lava flows is primarily controlled by temperature and composition. As usual, the relationship is

$$\tau = \tau_0 + \eta \dot{\epsilon}$$

where τ is shear stress, τ_0 is the yield stress, η is viscosity, and $\dot{\epsilon}$ is strain rate.

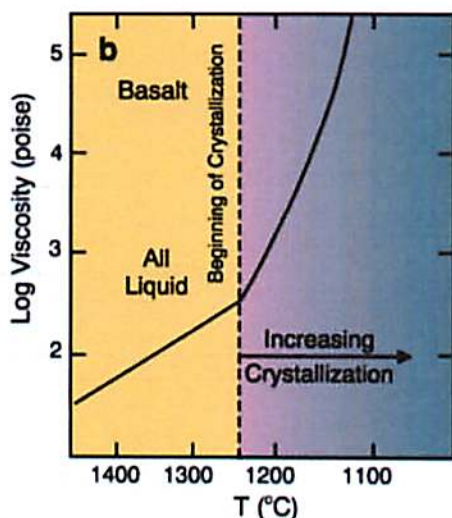


Fig. 1: Temperature dependence of viscosity for basaltic lava (Winter, 2001; after Murase and McBirney, 1973)

Temperature

- $\downarrow T \Rightarrow \uparrow \eta$ (Fig. 1)
 - after crystallization, $\downarrow T \Rightarrow \uparrow \uparrow \eta$
 - Hawaiian lavas typically erupt at $\sim 1150^\circ\text{C}$ (Flynn and Mouginis-Mark, 1992)
- @20-30% crystals: τ_0 becomes nonzero (i.e., Newtonian \rightarrow Bingham plastic; Shane's notes)

Composition

- as lava cools, its polymerization mimics the structure of the minerals that will crystallize from it (Fig. 2) \Rightarrow more silicic lavas are more polymerized
- polymerization increases viscosity \Rightarrow more silicic lavas are more viscous (Fig. 3)

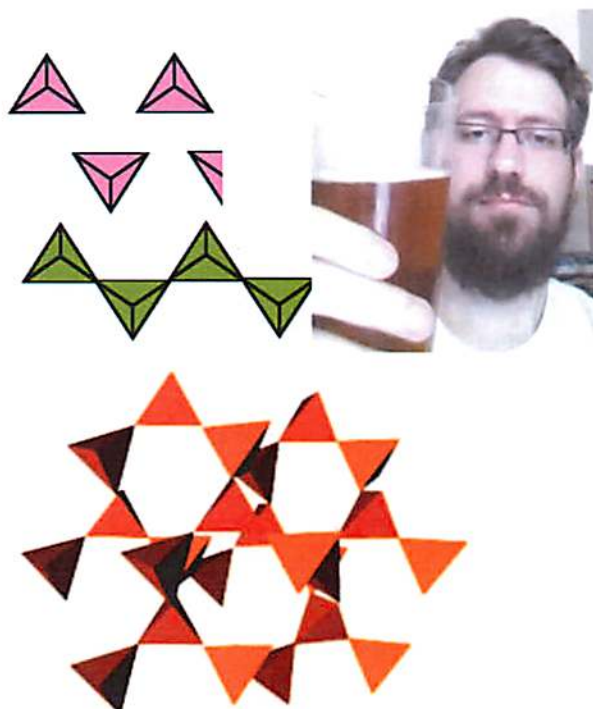


Fig. 2: Schematic silicate structures: nesosilicate (e.g., olivine; pink), inosilicate (e.g., pyroxene; green), tectosilicate (e.g., plagioclase; orange)

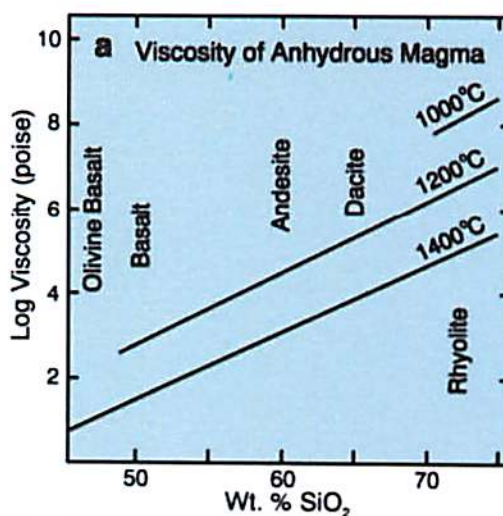


Fig. 3: Calculated viscosities at 1 atm (Hess, 1989)

Water

- not important at low P (e.g., Earth's surface)
- H_2O inserts itself between bridged silica tetrahedra, depolymerizing them $\Rightarrow \downarrow \eta$
- $\uparrow \text{H}_2\text{O} \Rightarrow \downarrow T_{\text{melt}}$, so wet melts remain liquid longer
 - solid + $\text{H}_2\text{O} \Leftrightarrow$ liquid (aq)

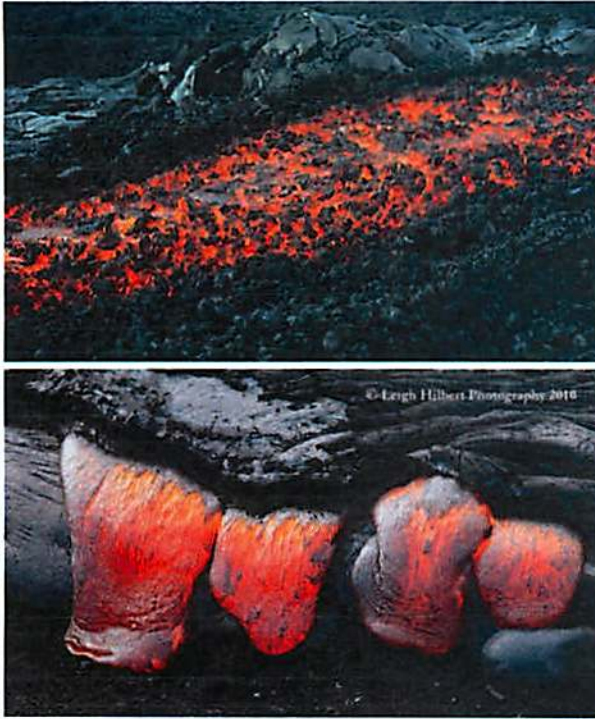


Fig. 4: rumbly-topped aa (upper) and smooth/ropey-topped pahoehoe (lower)

LAVA FLOWS:

- dominant form of volcanism on Earth (e.g., more than explosive eruptions) (Winter, 2001)
- flood basalts form from giant eruptions; single units of the Columbia River Basalt Group can reach $\sim 3000 \text{ km}^3$ (Tolan et al., 1989)
- typically mafic, low viscosity, low volatiles (Winter, 2001)
- two main morphological forms: rumbly-topped aa (pronounced AH-ah; a very low-scoring Scrabble word) and smooth/ropey-topped pahoehoe (pronounced puh-HO-ee-HO-ee) (**Fig. 4**)
 - account for $\sim 90\%$ of Hawaiian basaltic lava flows (Rowland and Walker, 1990)

Aa, Pahoehoe, and Friends:

From Rowland and Walker, 1990, except where noted.

As lava flows, it cools at the top to form a crust. Whether aa or pahoehoe forms depends on the interplay between the tearing of these crusts

(induced by velocity shear) and the healing of those tears (inhibited by viscosity)

- Aa and pahoehoe do not differ in chemistry or eruptive temperatures
- **First assume a large basaltic eruption with flow rates $>5\text{-}10 \text{ m}^3/\text{s}$...**
- near the vent, lava channelizes into “rivers” that can flow at 60 km/h (Winter, 2001)
- lava flowing in these channels cools distally, forming plates of crust that are quickly torn by the velocity shear and battered into rubble—**proximal aa is born**
 - critical viscosity for aa formation depends on the local velocity shear but is typically $\sim 10^4 \text{ Pa s}$ (mayonnaise)
 - rubble (“clinker”) avalanches down the flow front and is overridden so that it lines both base and top of flow (Winter, 2001)

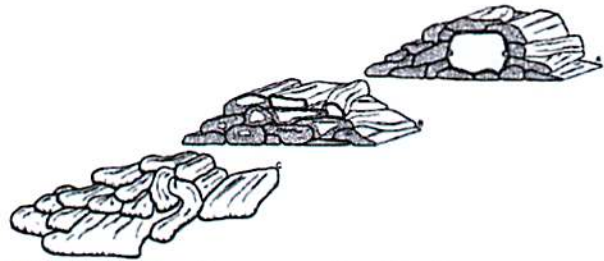


Fig. 5: proximal master tube, distributary system near flow front (each unit is $<1 \text{ m}^2$ in cross section), and flow front (Rowland and Walker, 1990)

- **Now assume the eruption flow rate reduces to $<5\text{-}10 \text{ m}^3/\text{s}$ (or a later eruption has such a rate)...**
- lava flow now in “plumbing” only (no channels) (**Fig. 5**)
 - master pipes may form proximally
 - distal pipes typically $<1 \text{ m}^2$ in cross section
 - no exposure at the surface \Rightarrow little heat loss
 - low total flow rate, divided between 10s - 100s of tubes at any given time \Rightarrow low effusion velocity, low velocity shear

- lava breaches as small tongues that cool quickly to form an intact smooth crust—**pahoehoe** is born
 - flow velocity typically <120 m/h \Rightarrow flow front advances <10 m/h
 - lobe growth continues, by inflation, until shell becomes too thick
- pahoehoe can also form wherever low viscosity lava cools quickly—e.g., proximal overtopping of lava channels
- pahoehoe can additionally form wherever velocity shear is low/lava is nearly stagnant—e.g., in a lava channels when flow is cut off
- if the surface of pahoehoe is later disrupted (e.g., if over-inflation causes surface rupture) but its base remains smooth and undisrupted—**slabby pahoehoe** or **rubbly pahoehoe** is born (see references in Duraiswami et al., 2003; 2008)
- if higher viscosity (and slower-moving) lava is emplaced in much thicker tongues (≥ 10 m) that likewise grow by inflation, the surface will be rough and rubbly—**distal aa** is born (Rowland and Walker, 1987)
 - distal aa also differs from proximal aa in that the rubble of distal aa is often not scoriaceous (Rowland and Walker, 1987)
- if lava reaches critical aa viscosity, lacks sufficient velocity shear but is still flowing,, its surface can be raked into grooves and ridges by irregularities in the roof of the orifice from which it emerges—**toothpaste lava** is born (Rowland and Walker, 1987) (**Fig. 6**)

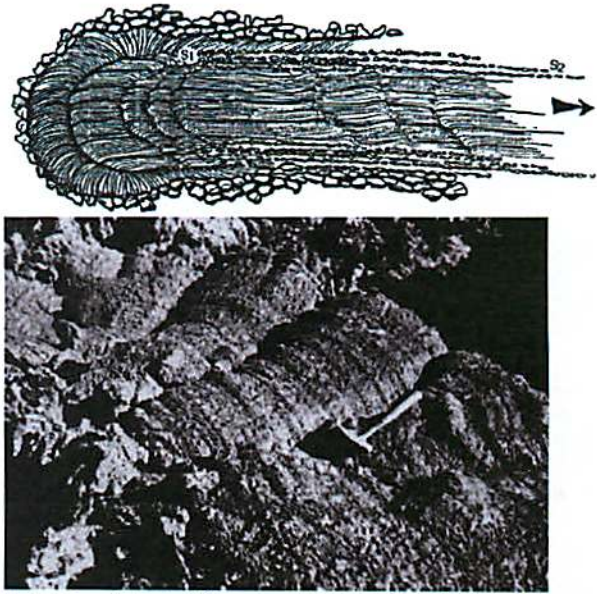


Fig. 6: sketch (flow to right) and photo (flow to left) of toothpaste lava tongues (Rowland and Walker, 1987)

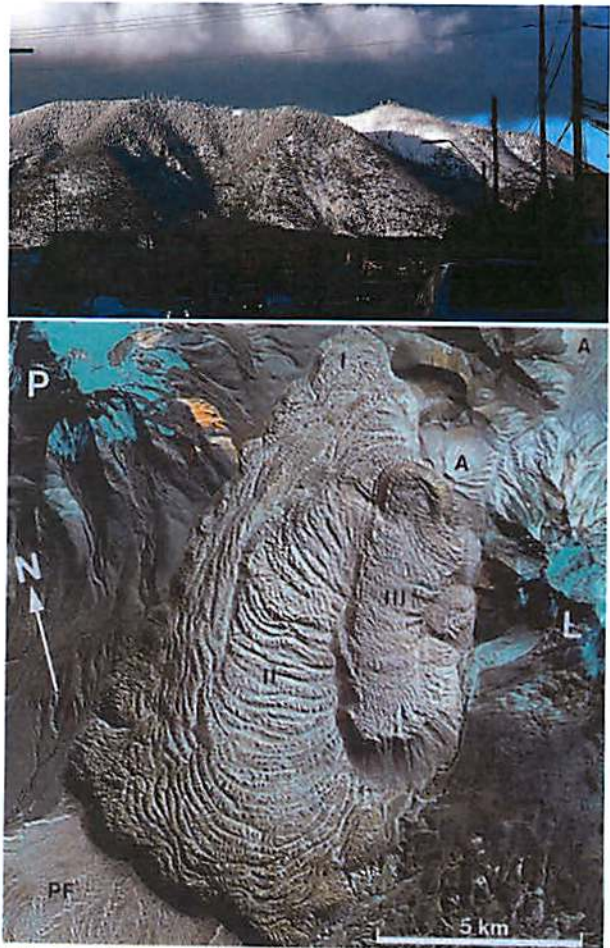


Fig. 7: Mount Eldon dome, Flagstaff, AZ (upper) and Chao dacite coulee, Northern Chile (lower)

Silicic lava flows...

- silicic lava is typically explosive
- spectrum of silicic flows: domes (no flow), coulees (flattened domes with downhill flow), and thick flows (**Fig. 7**)
 - all flow only short distances

PLANETARY EXAMPLES:

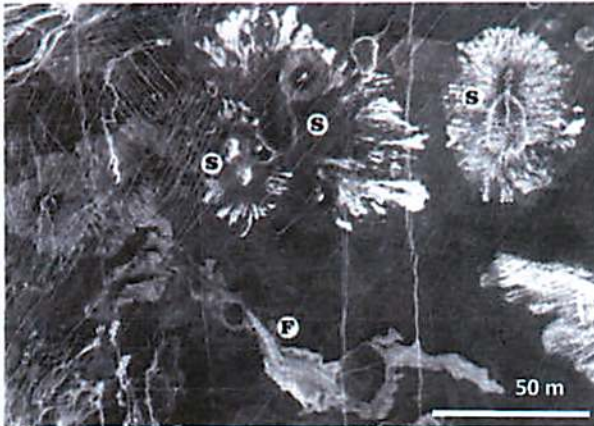


Fig. 8: Magellan radar image from the Atla region of Venus showing shield (S) volcanoes and a lava flow (F). Part of JPL image no. PIA00201.

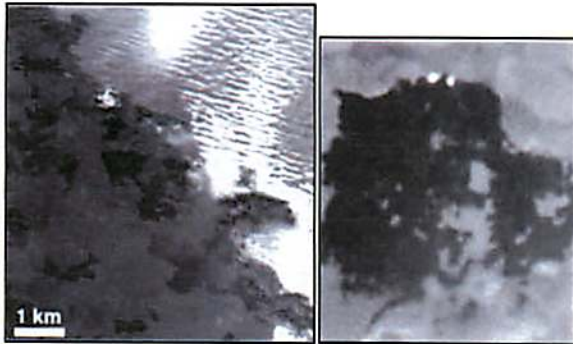


Fig. 9: Active flow field at Prometheus volcano, Io. Darker surfaces are younger (not yet buried in bright SO₂ frost), and brightest pixels are incandescent lava. JPL Photojournal images PIA02308, PIA02565, PIA02568, and PIA02557.

Bruno and Taylor (1995) found that Venusian lava flows, like basaltic terrestrial flows, are typically fractal in plan form, suggesting a similar basaltic composition. They further categorized Venusian flows as aa, pahoehoe, or (rarely) transitional based alternatively on fractal or radar data. Both approaches yielded similar results.

References:

Bruno, B. C., and G. J. Taylor (1995), *Geophys. Res. Lett.*, 14, 1897-1900.
 Duraiswami, R. A. et al. (2003), *J Volcanol. Geotherm. Res.*, 121, 195-217.

Duraiswami, R. A. et al. (2008), *J Volcanol. Geotherm. Res.*, 177, 822-836.
 Flynn, L. P., and P. J. Mouginis-Mark (1992), *Geophys. Res. Lett.*, 19, 1783-1786.
 Hess, P. C. (1989), *Origin of Igneous Rocks*, Harvard University Press., Cambridge.
 Murase, T, and A. R. McBirney (1973), *Geol. Soc. Am. Bull.*, 84, 3563-3592.
 Rowland, S. K., and G. P. L. Walker (1987), *Bull. Volcanol.*, 49, 631-641.
 Rowland, S. K., and G. P. L. Walker (1990), *Bull. Volcanol.*, 52, 615-628.
 Tolan, T. L. et al. (1989), *Geol. Soc. Amer. Special Paper*, 239, 1-20.
 Winter, J. D. (2001), *An Introduction to Igneous and Metamorphic Petrology*, Prentice Hall, Upper Saddle River, NJ.



Fig. 10: Some classic texts on lava flow rheology.

Magma Plumes and the Hawaiian Islands

Hannah E. Tanquary, Spring 2014



Introduction

Convection of the Earth's mantle was first postulated in the 1930s, and remains an open and controversial topic of research. In 1963, Wilson studied linear chains of islands and attempted to explain their origin in terms of convection, as opposed to the rigid earth model that was still widely used at the time^[1]. Prior to this time, it was believed that the age differences between the islands was not very great, and that the chain had formed by the extrusion of lava through a fault at that location.

In 1971, Morgan and others postulated that volcanic island chains such as Hawaii were created by plate motion over "hotspots" formed by rising deep mantle material. The Hawaiian Islands were now known not to have formed near a tectonic plate boundary, and Morgan's hypothesis could explain how active volcanism could arise at such a location^[2].

Mechanism

Wilson continued work on the convective hypothesis, and in 1973 proposed that there are two major convective processes occurring in the mantle. These are the large-scale convective processes that drive plate tectonics, and the smaller-scale mantle plumes. Mantle plumes are narrow columns of hot material driven by heat exchange across the core-mantle-boundary (CMB)^[3]. This hypothesis was tested in the laboratory in the 1970s using small tanks of fluid as shown in Figure 1. The plumes in these experiments are made up of two components, a long, thin, "conduit", and a mushroom shaped "head". The bulbous shape of the head arises because

Figure 1: Whitehead et al., (1975)

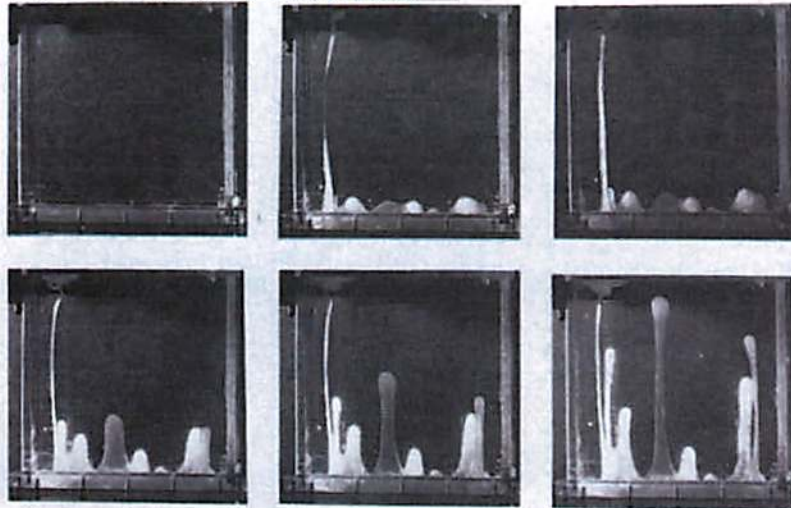
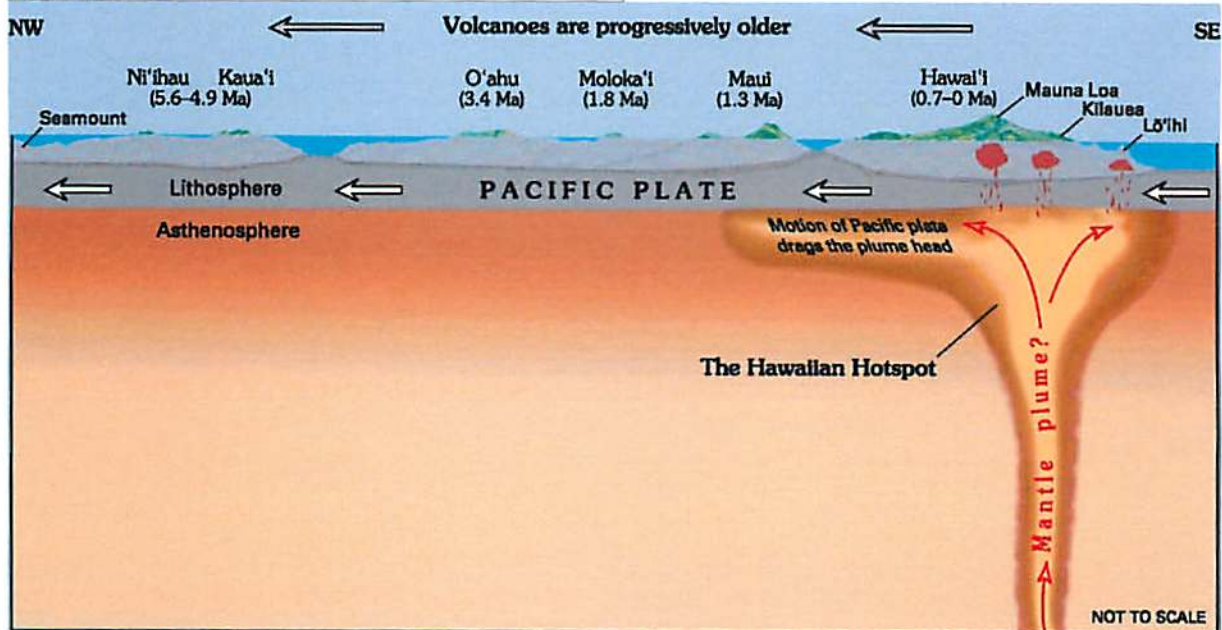


Fig. 1. A thin layer of viscous fluid protruding into a fluid with 1/44 its viscosity.

Figure 2: USGS



material travels upward through the conduit more quickly than the speed with which the total plume moves upward^[4]. Models in the 1990s, particularly those of Tan and Thorpe, predict plume diameters in the earth of approximately 2000 km, with critical times (the time until liftoff of the plume) of 830 Myr^[5].

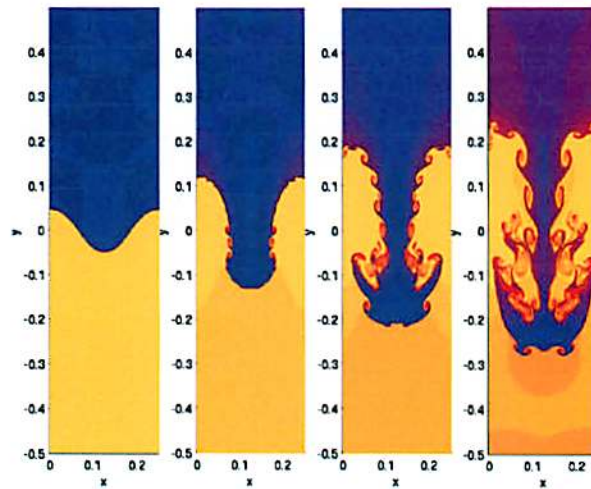
In the case of the Hawaiian Islands, the mantle plume is thought to remain fixed between the CMB and the lithosphere. The plume conduit supplies material to the base of the lithosphere. The rising plume can partially melt, supplying material that may then erupt^[2] (see Figure 2). The horizontal motion of the lithosphere then results in the formation of a chain of volcanoes that parallels plate motion, as in Hawaii.

Origin and Evidence

The source of mantle plumes was postulated by Morgan in 1972 to be the region of mantle just above the CMB^[6]. The CMB exists at a depth of approximately 3000 km and exhibits the greatest thermal contrast known to exist. The core is ~1000° C higher than the overlying material. It is thought that conduction from core to mantle results in the heating of the lower mantle. These heated regions become more buoyant and rise through the mantle as plumes. A possible mechanism of plume formation is the Rayleigh-Taylor (RT) instability, shown in Figure 3. A RT instability forms by a perturbation between two fluids of different densities^[6].

Evidence to support the plume hypothesis has been largely based on unusually high He^3/He^4 ratios in some hotspots. He^3 and He^4 both escape to space over time, but He^4 is replaced by the decay of U and Th. A localized, high He^3/He^4 can be explained by plumes tapping a primordial reserve of He^3 ^[7]. This logic has been used to provide evidence that the Hawaii hotspot is the result of a mantle plume.

Figure 3: Shengtai Li, Hui Li



Magma Plumes on Venus

Some features observed on Venus can be explained by the presence of magma plumes. The Beta Regio and Atla Regio features on Venus are very broad topographically, more than 2000 km across, host one or more large shield volcanoes, and also exhibit extensional faulting. Smrekar et al., using radar data from the Venus Express orbiter, explain these features using the mantle plume model, citing the elevated topography and rifting of the surface. Computer simulations of mantle convection can reproduce the observed topography and gravity anomalies of these regions^[10].

An Alternate Hypothesis

The plate hypothesis states that hotspot or “anomalous” volcanism is the result of near-surface material passively rising through the surface at points that have been weakened due to lithospheric extension. Proponents of the plate hypothesis assert that deep-mantle plumes resulting in surface volcanism do not exist, and that high He^3/He^4 ratios can be explained by a lack of U and Th in near-surface material^[8].

1. Wilson, J. T., A Possible Origin of the Hawaiian Islands, *Canadian Journal of Physics*, 1963, **41**(6): 863-870.
2. Morgan, W. J., Deep mantle convection plumes and plate motions, *Bull. Am. Assoc. Pet. Geol.*, 1972, **56**: 203–213.
3. Wilson, J. T., Mantle Plumes and Plate Motions, *Tectonophysics*, 1973, **19**, 149-164.
4. Whitehead, Jr. et al., Dynamics of Laboratory Diapir and Plume Models, *Journal of Geophysical Research*, 1975, **80**: 705–717.
5. Tan, K. K.; Thorpe, R. B., The Onset of Convection Driven by Buoyancy Caused By Various Modes of Transient Heat Conduction, *J. Chem. Eng. Sci.*, 1999, **54**: 225 –238.
6. Sharp, D.H., An Overview of Rayleigh-Taylor Instability, *Physica D*, 1984, **12**: 3–18.
7. Kurz, Mark, Dynamics of the Galapagos Hotspot from Helium Isotope Geochemistry, 1999, *Geochimica et Cosmochimica Acta*.
8. James, D. E. et al., Slab fragmentation, Edge Flow and the Origin of the Yellowstone Hotspot Track, *Earth and Planetary Science Letters*, 2011, **311** (1-2): 124–135.
10. Smrekar, S. E. et al., *Large Volcanic Rises on Venus*, Venus II, pp. 845-878, University of Arizona Press, 1997

Chemical Zoning in Magma Plumes

Kelly Miller



- General overview
 - Longest chain of islands on Earth (nearly 6000 km)
 - Active for last 80 million years
 - Sourced from plume extending from lower mantle (2) or core-mantle boundary (CMB) (4)
 - About 100 km in diameter (5)
 - Pacific plate moves the islands northwest by 9-10 cm/yr (6)
 - Volcano crosses plume diameter in about 10^6 yr (7)
- Geochemical characteristics
 - Two distinctive regions: Loa and Kea
 - Named for tallest volcano exhibiting traits of chemical trend (8)
 - Isotopic, minor, and major element differences
 - Trends lie along parallel lines (Fig. 1)

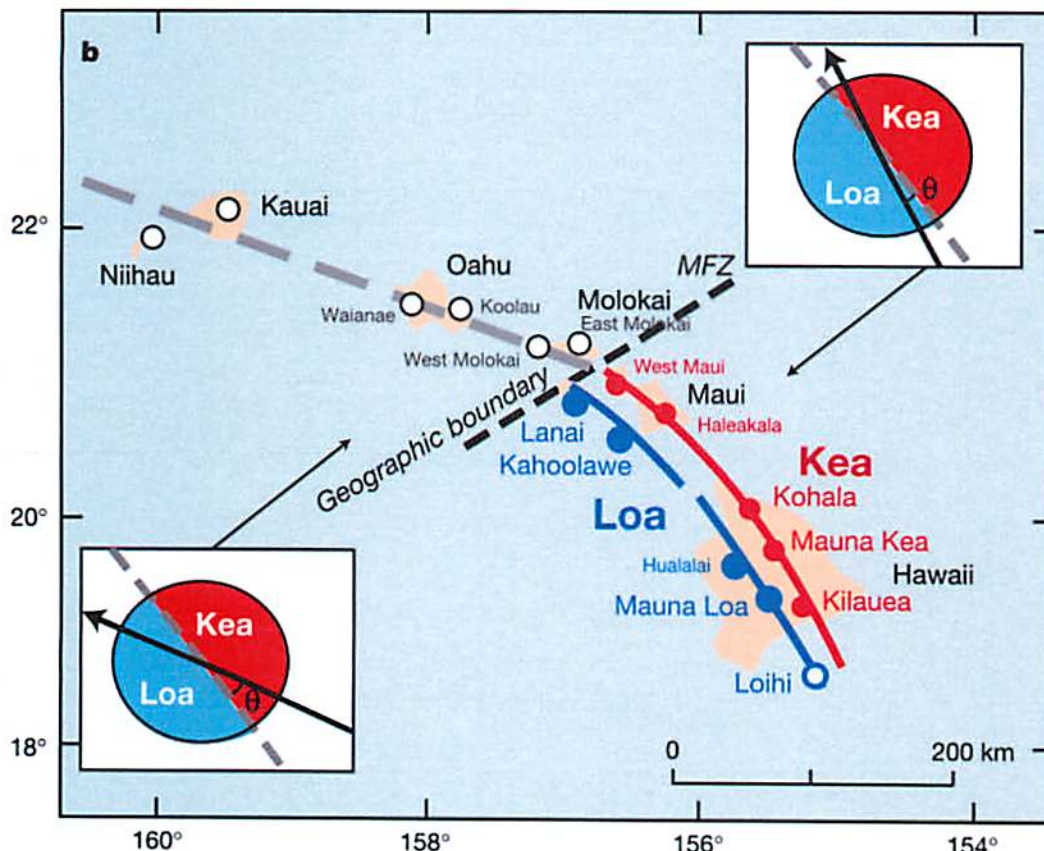


Figure 1. The Loa and Kea geochemical trends; beyond the geographic boundary, the $^{208}\text{Pb}^*/^{206}\text{Pb}^*$ ratios display a mixture of Loa and Kea values; insets show difference between the plate direction (black arrow) and the Loa-Kea boundary (dashed grey) for present day (upper right) and Koolau volcano 2-3 Myr ago (lower left); figure from (9).

- Have been distinct for ≥ 5 million yrs (10)
- Record plume source geochemistry
- Loa is pyroxene-rich, blue is olivine-rich (11)

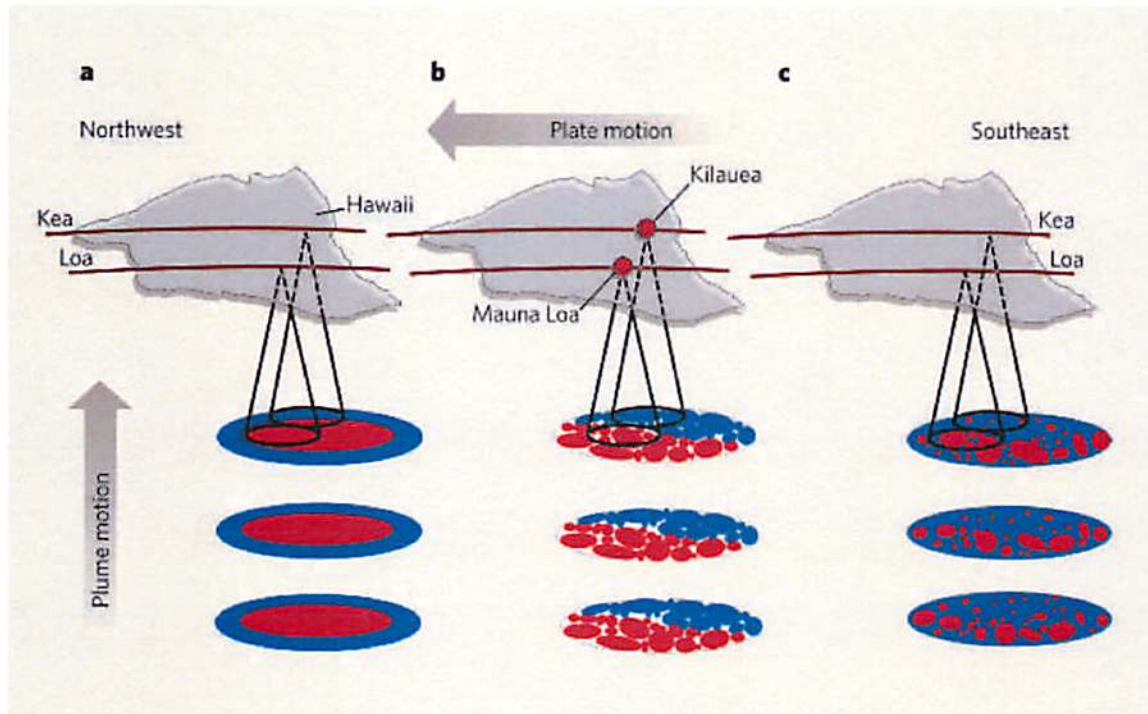


Figure 2. Schematic representation of three proposed models for explaining the Loa (red) and Kea (blue) trends: a) concentric zoning, b) bilateral zoning, and c) streaked zoning; figure from (11).

- Plume zoning models from whole rock samples (Fig. 2)
 - Concentric zoning
 - Kea samples from edges of plume, Loa samples from closer to center
 - Supported by He and Nd measurements (Fig. 3)
 - Elongation of plume and plate movement not quite parallel; off by 10° (12)
 - Bilaterally zoned (Fig. 4)
 - Supported by Pb isotopes (9)
 - Used drill cores to look at isotopes for the last 300 kyr
 - Found statistically significant difference between Loa and Kea trends
 - Loa is more heterogeneous
 - The bilateral divide may be because the Loa trend lies above the edge of the Pacific large low-shear-velocity province (LLSVP) and the Kea trend lies above ordinary Pacific lower mantle (8)
 - Streaked zoning

- Hf and Pb isotope analyses indicate vertical and horizontal heterogeneities (13)
- Ren et al. (14) studied inclusions in olivine and found that Loa and Kea trends were not distinct but overlapped; they suggest that whole rock differences derive from a variation in temperature, not source chemistry.
 - Spandler et al. (15) find that re-equilibration times for REEs in inclusions are short (3-100 yrs) compared to vertical transit times from mantle source (30-10⁴ yrs) and conclude inclusions do not preserve source chemistry.

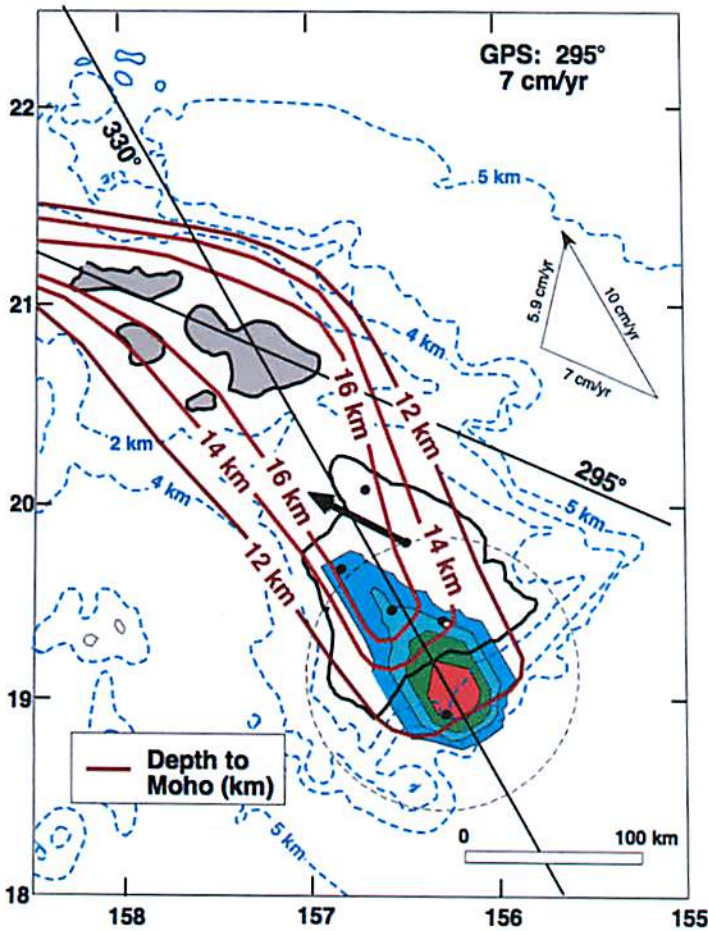


Figure 3. Calculated $^3\text{He}/^4\text{He}$ ratios for a concentrically zoned plume, with a value of ~ 40 Ra at the center and ~ 10 Ra at the edges; blue contours show bathymetric measurements, and red contours show the seismically-determined Hawaiian Ridge axis; the He trend lies along a $\text{N}40^\circ\text{W}$ axis, while the ridge axis is $\text{N}30^\circ\text{W}$; figure from (12).

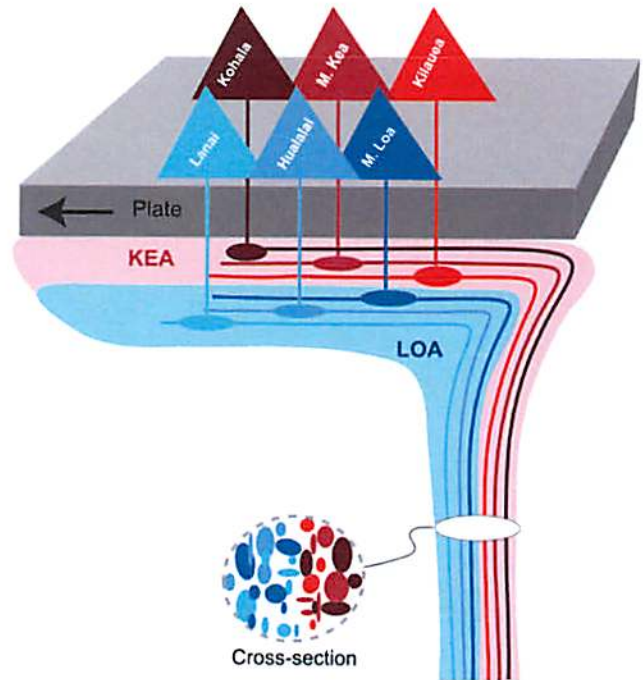
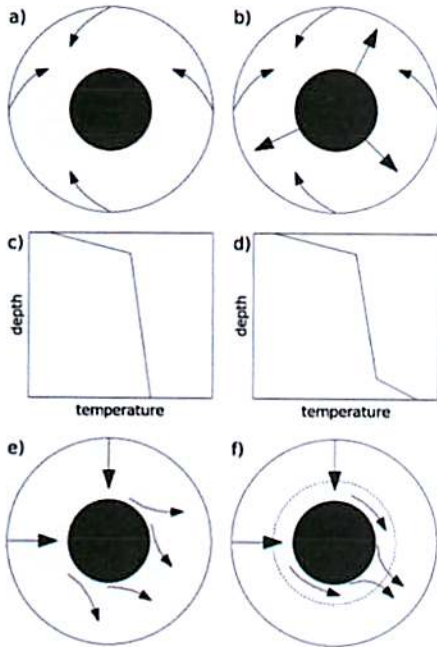


Figure 4. Schematic diagram of bilateral zoning showing some heterogeneity within each trend, and a major division between Loa and Kea; figure from (9).

- Planetary connection
 - Mantle plumes on Mars
 - Active volcanoes in Tharsis and Elysium
 - Van Thienen et al. (1) model partially explains these regions:
 - Active northern crust and thick, inactive southern crust
 - Downwelling of cold northern crust displaces mantle
 - Mantle material focused by perovskite phase transition
 - Models don't reproduce equatorial location of Tharsis and Elysium



- Volcanic swells on Venus may be due to mantle upwelling (16)
 - Models predict plume lifetimes of 150-250 myr
 - Beta, Atla, Western Eistla, and Imdr Regiones are probably active or recently active (Fig. 6)
 - Bell, Dione, and Themis Regiones are late-stage or extinct plumes

Figure 5. Mantle plumes can be initiated whether the core is super-heated (b and d) or not. In the absence of a phase transition, upwelling occurs over a broad area (e). The presence of a perovskite phase transition can focus upwelling into a localized plume (f). Figure from (1).

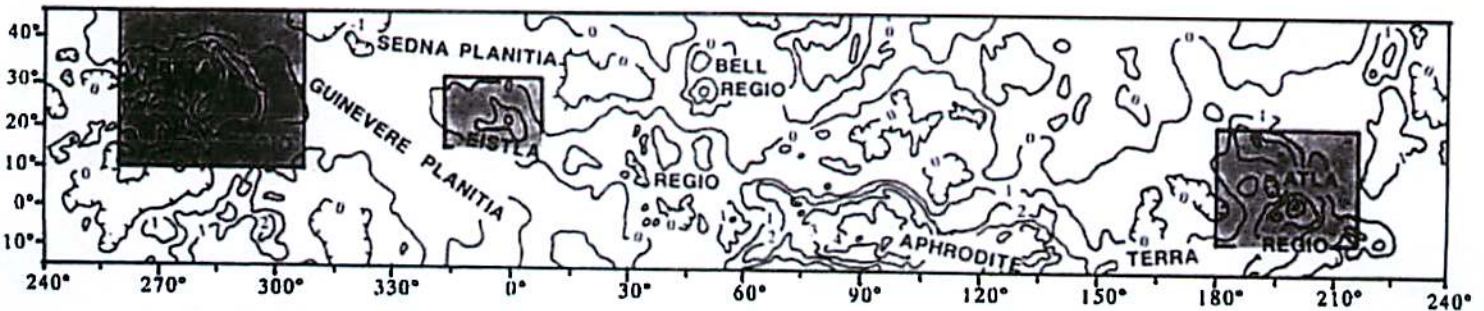


Figure 6. Location of topographical rises on Venus, including Beta (grey box at left), Eistla, Bell, and Atla (grey box at right) regions; contour lines are at 1-km intervals; figure from (3).

References

1. P. Van Thienen, A. Rivoldini, T. Van Hoolst, P. Lognonné, A top-down origin for martian mantle plumes. *Icarus* **185**, 197-210 (2006).
2. R. Montelli, G. Nolet, F. A. Dahlen, G. Masters, A catalogue of deep mantle plumes: New results from finite - frequency tomography. *Geochemistry, Geophysics, Geosystems* **7**, (2006).
3. D. A. Senske, G. G. Schaber, E. R. Stofan, Regional topographic rises on Venus: Geology of western Eistla Regio and comparison to Beta Regio and Atla Regio. *Journal of Geophysical Research: Planets (1991-2012)* **97**, 13395-13420 (1992).
4. C. J. Wolfe, S. C. Solomon, G. Laske, J. A. Collins, R. S. Detrick, J. A. Orcutt, D. Bercovici, E. H. Hauri, Mantle shear-wave velocity structure beneath the Hawaiian hot spot. *science* **326**, 1388-1390 (2009).
5. N. M. Ribe, U. R. Christensen, The dynamical origin of Hawaiian volcanism. *Earth and Planetary Science Letters* **171**, 517-531 (1999).
6. D. A. Clague, G. B. Dalrymple, The Hawaiian-Emperor volcanic chain. part I. Geologic evolution. *US Geol. Surv. Prof. Pap* **1350**, 5-54 (1987).
7. M. O. Garcia, J. Caplan-Auerbach, E. H. De Carlo, M. D. Kurz, N. Becker, Geology, geochemistry and earthquake history of Lōihi Seamount, Hawaii's youngest volcano. *Chemie der Erde-Geochemistry* **66**, 81-108 (2006).
8. D. Weis, M. O. Garcia, J. M. Rhodes, M. Jellinek, J. S. Scoates, Role of the deep mantle in generating the compositional asymmetry of the Hawaiian mantle plume. *Nature Geoscience* **4**, 831-838 (2011).
9. W. Abouchami, A. W. Hofmann, S. J. G. Galer, F. A. Frey, J. Eisele, M. Feigenson, Lead isotopes reveal bilateral asymmetry and vertical continuity in the Hawaiian mantle plume. *Nature* **434**, 851-856 (2005).
10. M. O. Garcia, L. Swinnard, D. Weis, A. R. Greene, T. Tagami, H. Sano, C. E. Gandy, Petrology, geochemistry and geochronology of Kaua 'i Lavas over 4· 5 Myr: Implications for the origin of rejuvenated volcanism and the evolution of the Hawaiian plume. *Journal of Petrology* **51**, 1507-1540 (2010).
11. C. Herzberg, Mantle geochemistry: Big lessons from little droplets. *Nature* **436**, 789-790 (2005).
12. D. J. DePaolo, J. G. Bryce, A. Dodson, D. L. Shuster, B. M. Kennedy, Isotopic evolution of Mauna Loa and the chemical structure of the Hawaiian plume. *Geochemistry, Geophysics, Geosystems* **2**, (2001).
13. J. Blichert - Toft, D. Weis, C. Maerschalk, A. Agranier, F. Albarède, Hawaiian hot spot dynamics as inferred from the Hf and Pb isotope evolution of Mauna Kea volcano. *Geochemistry, Geophysics, Geosystems* **4**, (2003).
14. Z.-Y. Ren, S. Ingle, E. Takahashi, N. Hirano, T. Hirata, The chemical structure of the Hawaiian mantle plume. *Nature* **436**, 837-840 (2005).
15. C. Spandler, H. S. C. O'Neill, V. S. Kamenetsky, Survival times of anomalous melt inclusions from element diffusion in olivine and chromite. *Nature* **447**, 303-306 (2007).
16. S. E. Smrekar, E. M. Parmentier, The interaction of mantle plumes with surface thermal and chemical boundary layers: Applications to hotspots on Venus. *Journal of Geophysical Research: Solid Earth (1978-2012)* **101**, 5397-5410 (1996).

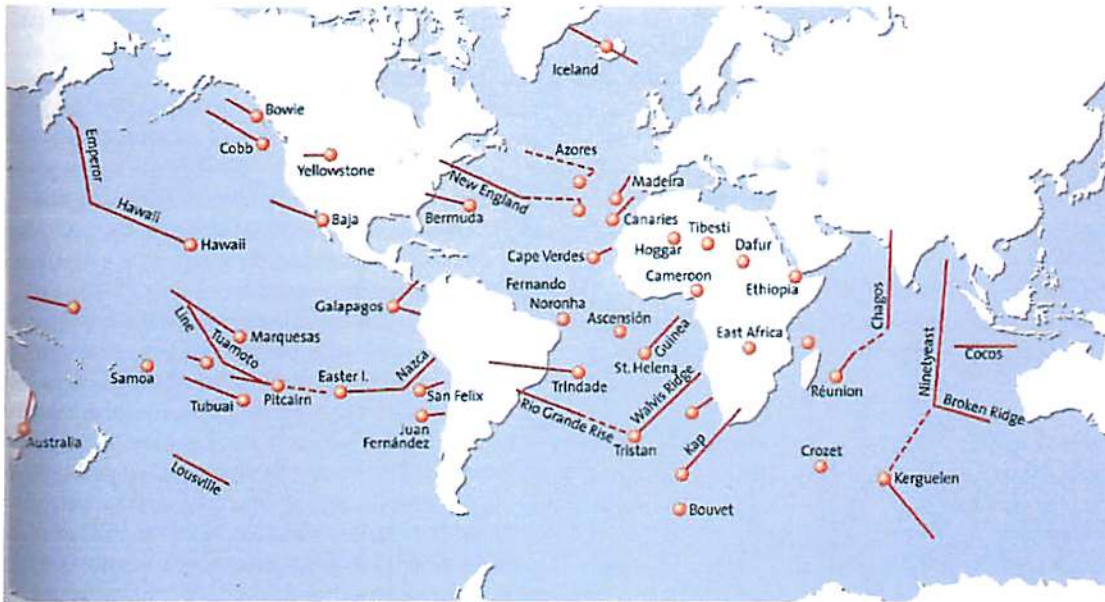
Hawaiian-Emperor Seamount Chain and the Lithosphere

Christa Van Laerhoven

The Hawaiian-Emperor seamount chain formed as the Pacific plate moved over a hot spot. It is one of several chains of similar origin.



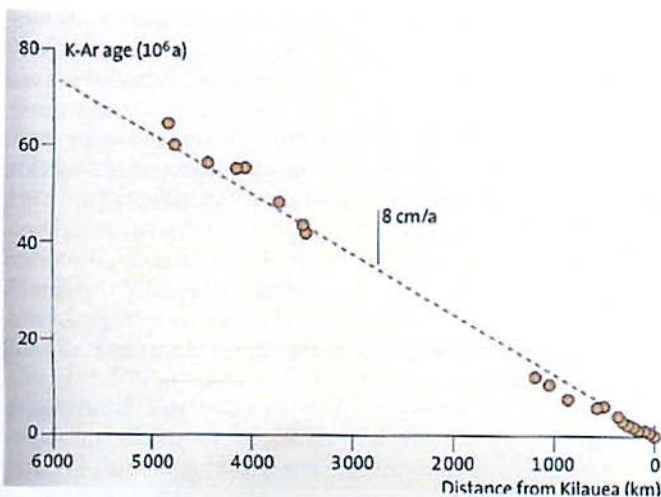
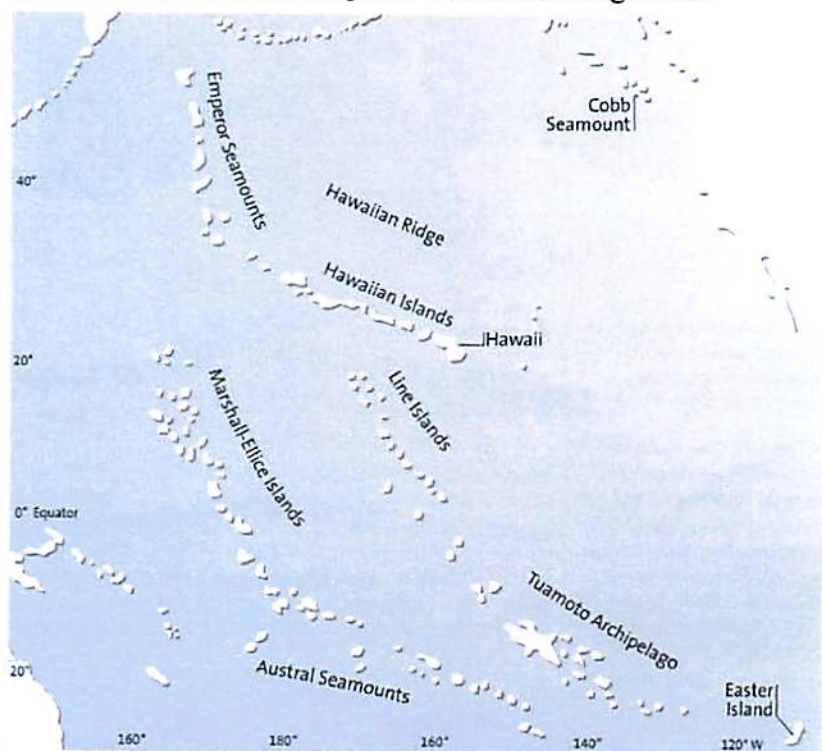
Figure 1: Hot spot areas across the world. From Schminke (2004).



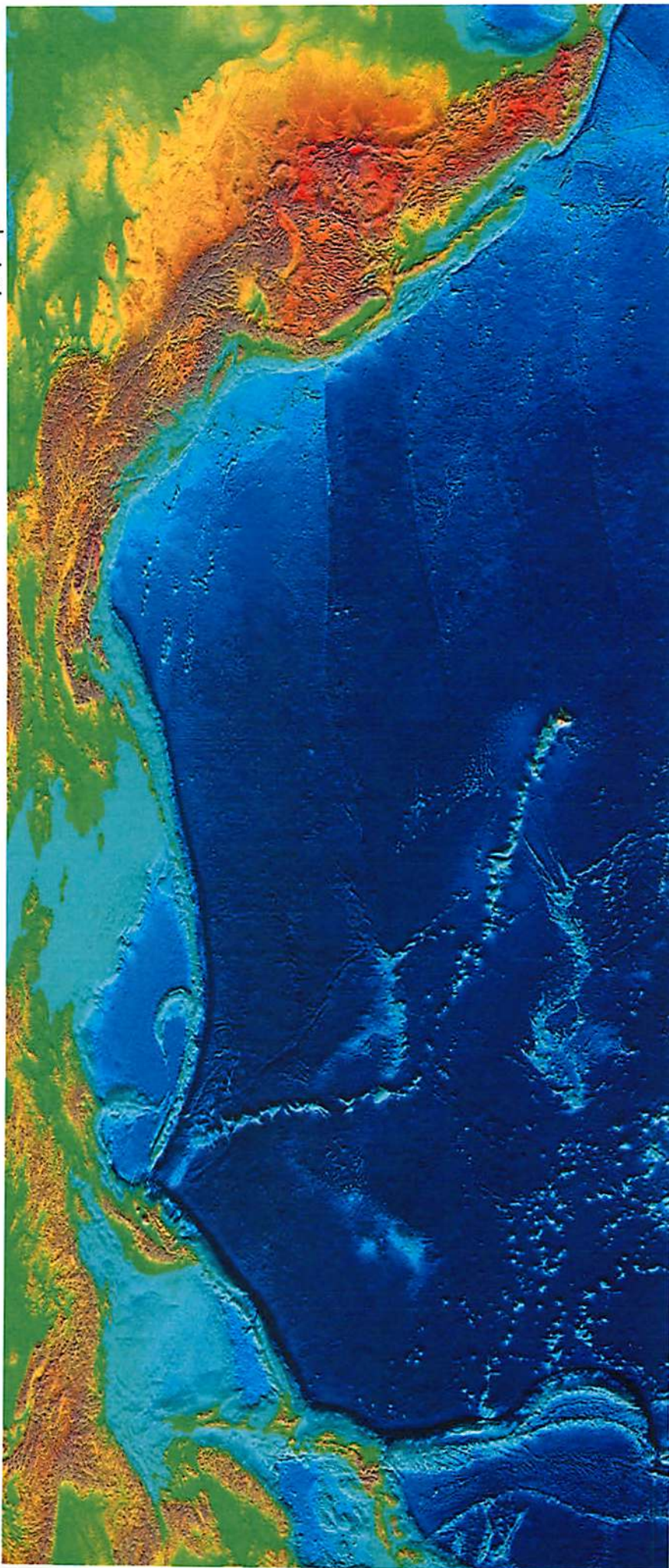
The Hawaiian-Emperor chain is approximately 5,800 km long and stretches from the islands of Hawaii to the Aleutian Trench in the northwest Pacific ocean. While the chain was made from a single hotspot there is a 120 degree kink between the line of the Emperor seamounts and the Hawaiian seamounts. The Hawaiian seamounts are younger than about 27 million years. The Emperor seamounts range from 27 to 85 million years old.

Figure 2: Other island chains of the Pacific. From Schminke (2004).

Figure 3: Kr-Ar ages of the volcanoes in the Hawaiian-Emperor seamount chain. From Schminke (2004).



*Figure 4: The Hawaiian-Emperor seamount chain.
Image from Wikipedia.*



Evolution of Seamounts

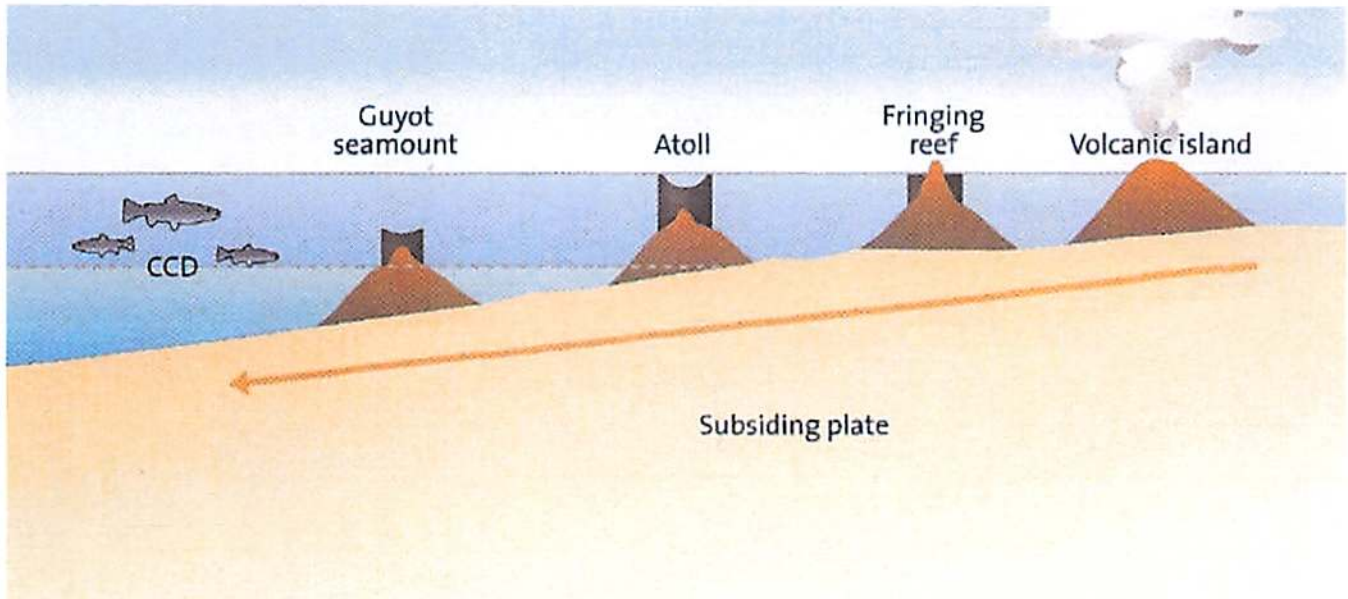


Figure 5: Seamount evolution. From Schmincke (2004).

Guyot: a seamount with a flat top.

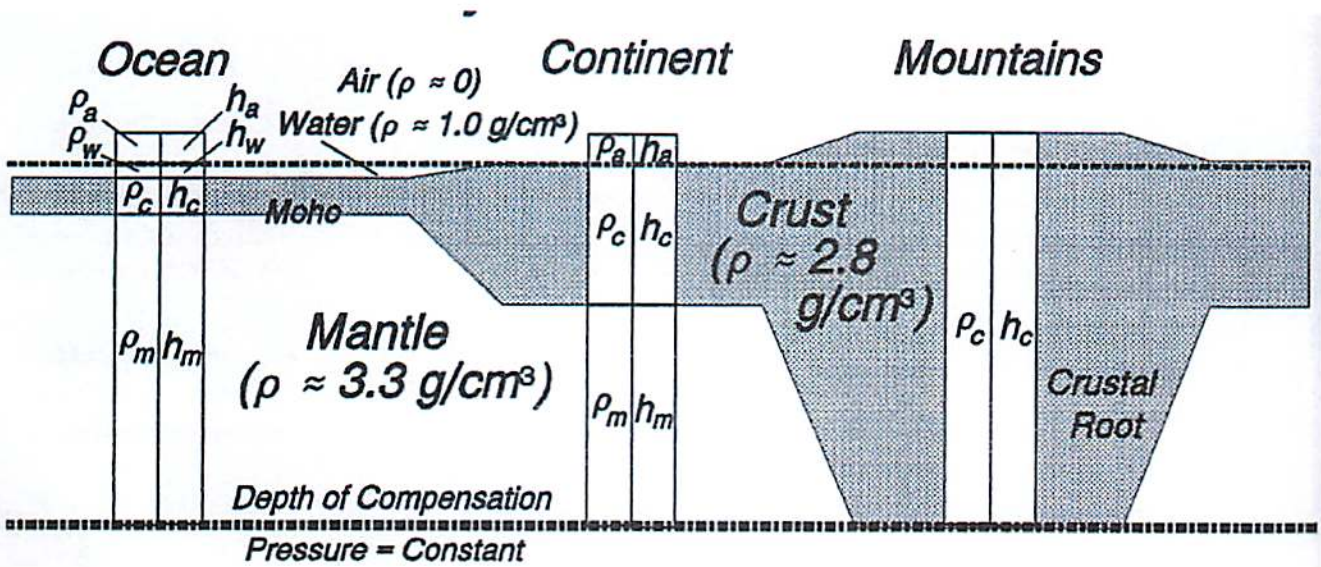
Atoll: a ring-shaped reef, island, or chain of islands formed of coral.

CCD: Carbonate Compensation Depth, depth below which shells of organisms sticking to the seafloor begin dissolving.

Response of the Lithosphere

Isostasy

Figure 6: Columns of material above some depth. Material in the column can be composed all or in part of air, water, crust, and mantle, each with their respective densities. From Lillie (1999).



At some depth, the pressure from the material above will be the same, regardless of lateral location. This is the depth of compensation. At this depth:

$$P/g = \rho_a h_a + \rho_w h_w + \rho_c h_c + \rho_m h_m = \text{Constant}$$

where the total thickness T is constant:

$$T = h_a + h_w + h_c + h_m = \text{Constant}$$

Figure 7: Two models for the Hawaiian swell. a) Thin lithosphere due to melting of its base. b) Push up from below from rising mantle material. From Schmincke (2004).

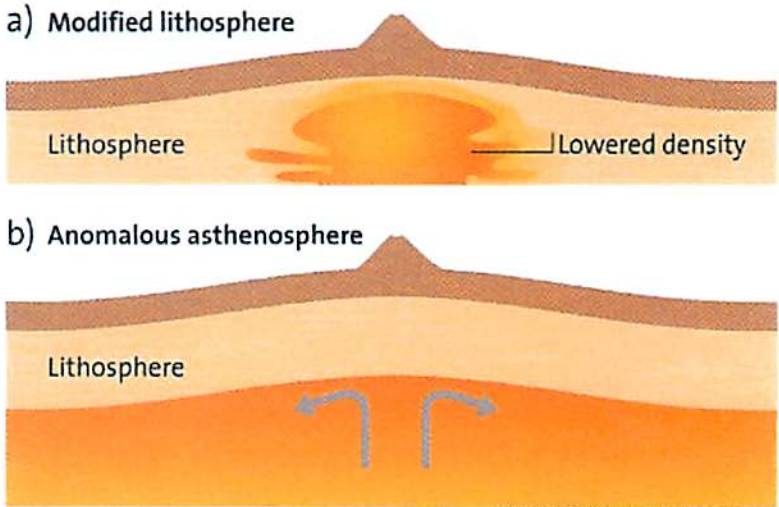
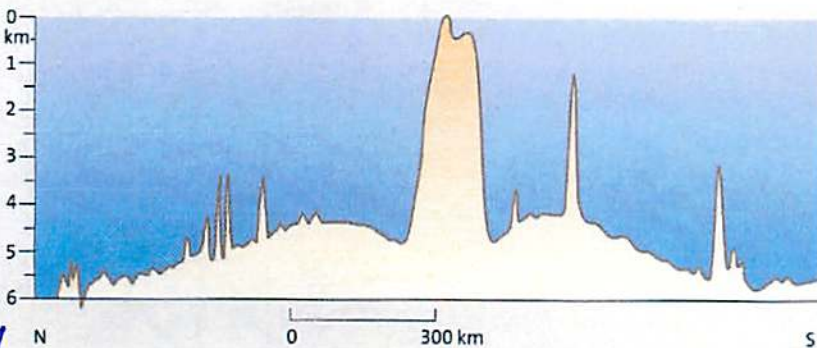
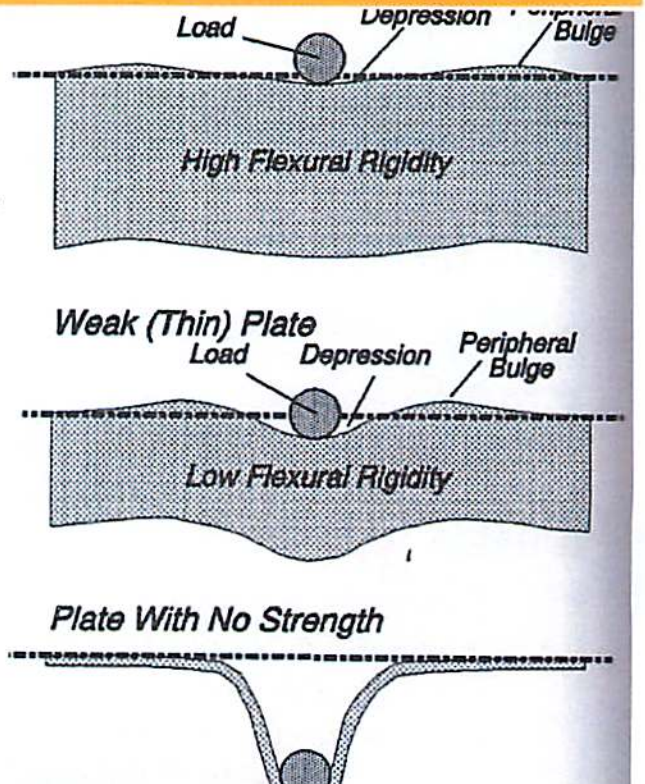


Plate Flexure

Plates will flex when a load is placed on them.

Figure 8: Plate flexure due to an imposed load. A rigid plate flexes less than a plate with low rigidity. From Lillie (1999).

Figure 9: Note the elevated areas on both sides of the Hawaiian chain. From Schmincke (2004).



Planetary Connection

Europa: Estimates for Europa's ice crust range from 0.1 to 20 km (Billings et al. 2005 and references therein).

As an example, Hurford et al. (2005) tried modeling Europa's crust near the ridges (Figure 10), as an elastic plate that is broken at the site of the ridge (Figure 11). They used light direction and shadows to identify the location of the bulge. Their resulting thickness estimate was ~200m.

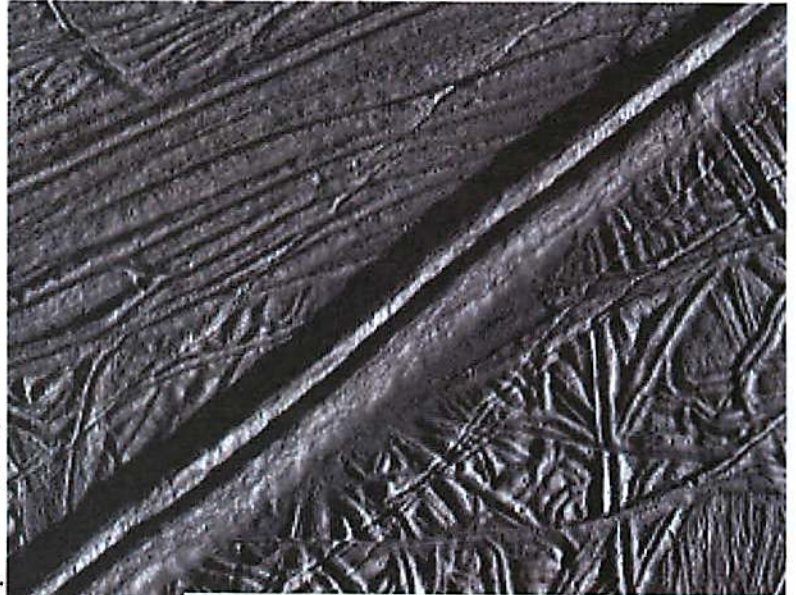


Figure 10: One big ridge and several smaller ones on Europa.

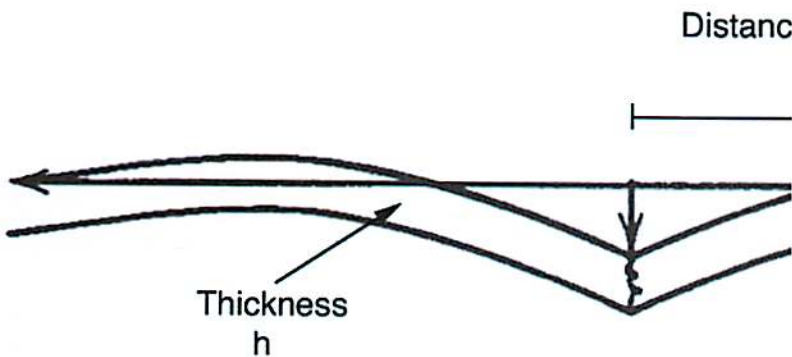
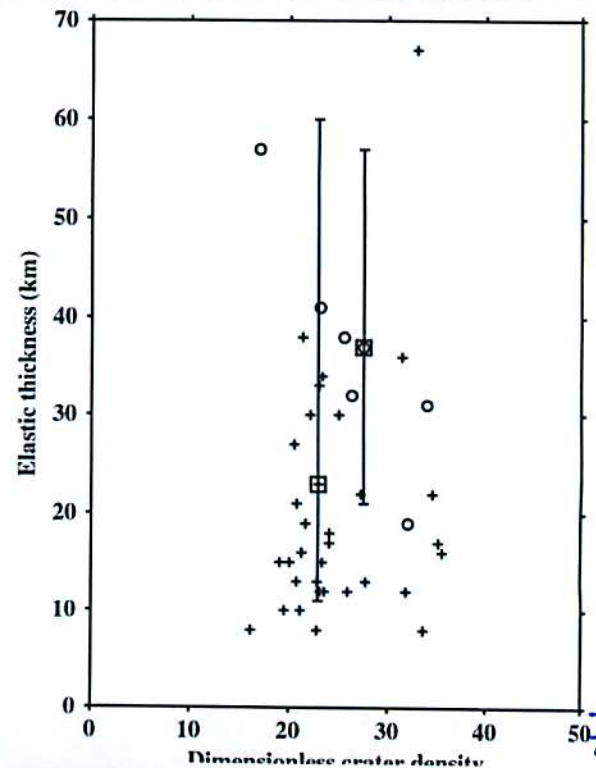


Figure 11: A flexing broken plate.

Venus: Barnett et al. (2002) looked at many flexural features on the surface of Venus and determined values for Venus' lithosphere thickness at those locations. They found that for



most locations the thickness tended to be somewhere around 10-20 km, though in several places it was thicker. They found no correlation between thickness and age of the surface (Figure 12).

Figure 12: Elastic thickness of Venus' lithosphere as a function of crater density (as a proxy for age of the surface).

References

- Barnet et al. (2002). JGR 107, Issue E2, CiteID 5007
Billings et al. (2005) Icarus 177, p. 397-412
Hurford et al. (2005). Icarus 177, p. 380-396.
Lillie (1999). "Whole Earth Geophysics."
Schmincke (2004). "Volcanism."
Wikipedia. www.wikipedia.com

THE SIX MAIN VOLCANOES ON BIG ISLAND

Youngmin JeongAhn

Evolution

Preshield stage

Submarine preshield stage is characterized by discontinuous and small volume eruptions which form pillow lava. Fast cooling under seawater instantly forms a skin, and a series of new lava flows out and piles up in rounded ball shape as inside pressure builds up enough to make a fracture on the original skin. The lava composition is alkali basalt and the process lasts about 2kyr. **Lō'ihī Seamount** off the southeast coast of Big Island is currently in this stage (or following submarine phase).



Figure 1 Beware of the Human at your own risk

Shield stage

Most portion of volcano is erupted in the shield stage which is named after its low-profile shield shape. The phase in the shield stage is the **submarine phase**. Lava composition changes to tholeiitic basalt while its eruption structure remains pillow lava in shape.

The following **explosive phase** occurs as the volcano reaches to the water surface. Mixture of lava and seawater produce lots of steam and volcanic ash intermittently. The summit calderas continue to develop and collapse over and over again.

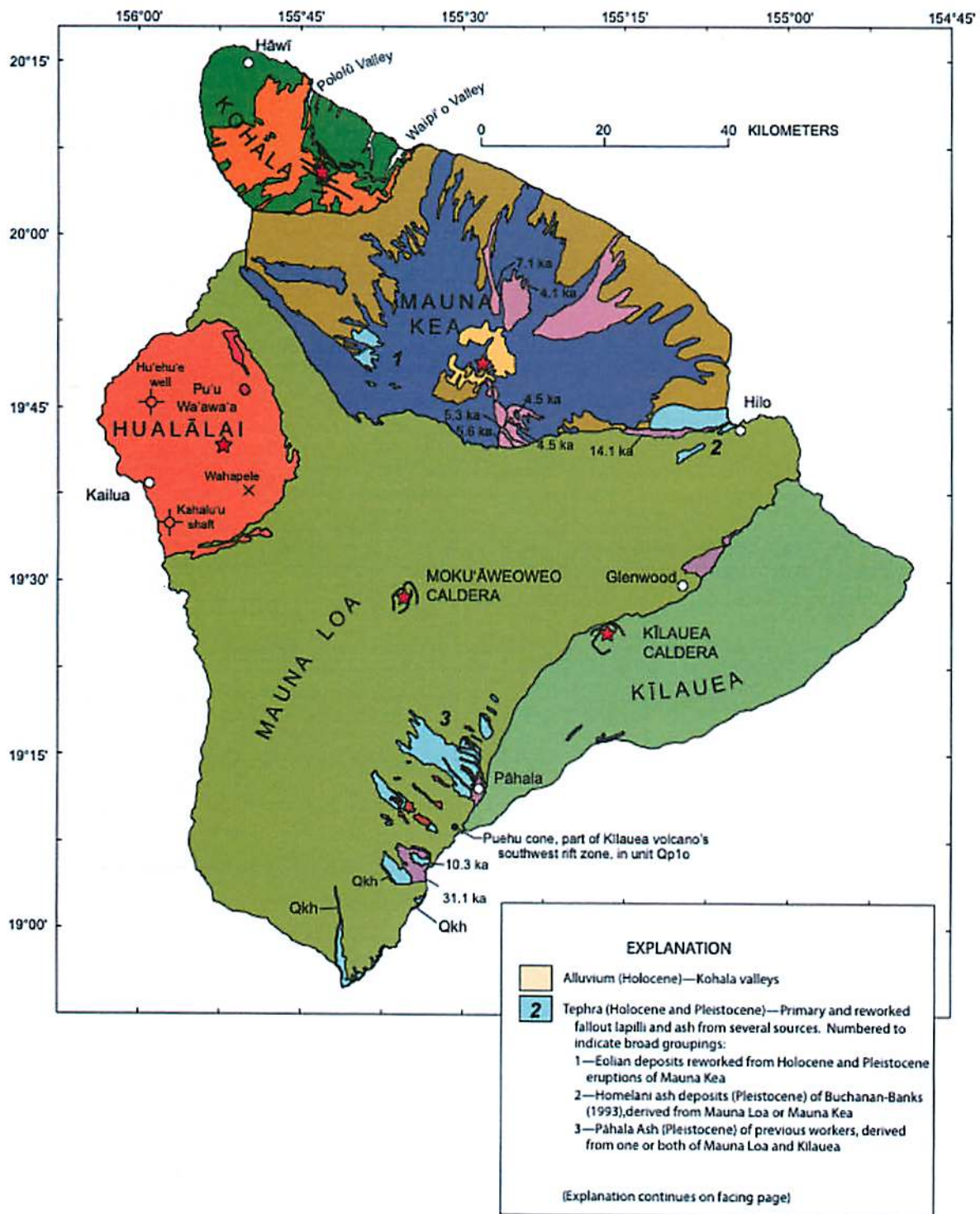
When it reaches high enough from the sea level, it enters the **subaerial phase**. The lava morphology in this phase is ropey pāhoehoe or rubbly 'a'ā flow. About 95 percent of volume is erupted in this phase for 0.5 Myr. **Kīlauea** and **Mauna Loa** are the examples we will see in this island.

Postshield stage

Composition of lava changes back to alkalic basalt and explosive eruptions create great amount of cinder in this stage. The slope of volcano gradually increases as 'a'a flows pile up near the vents. In the Big Island, **Hualālai** and **Mauna Kea** are experiencing this stage.

Erosional stage and Rejuvenated stage

Rainfall erosion on the dormant volcano produces deep valleys as the volcano subsides towards the sea level. Coral reefs develop along the shorelines which later remain coral atolls after the subsidence of volcanoes. Dormant volcanoes might undergo intermittent rejuvenated eruptions. **Kohala** and submerged **Māhukona** are now under the erosional stage.



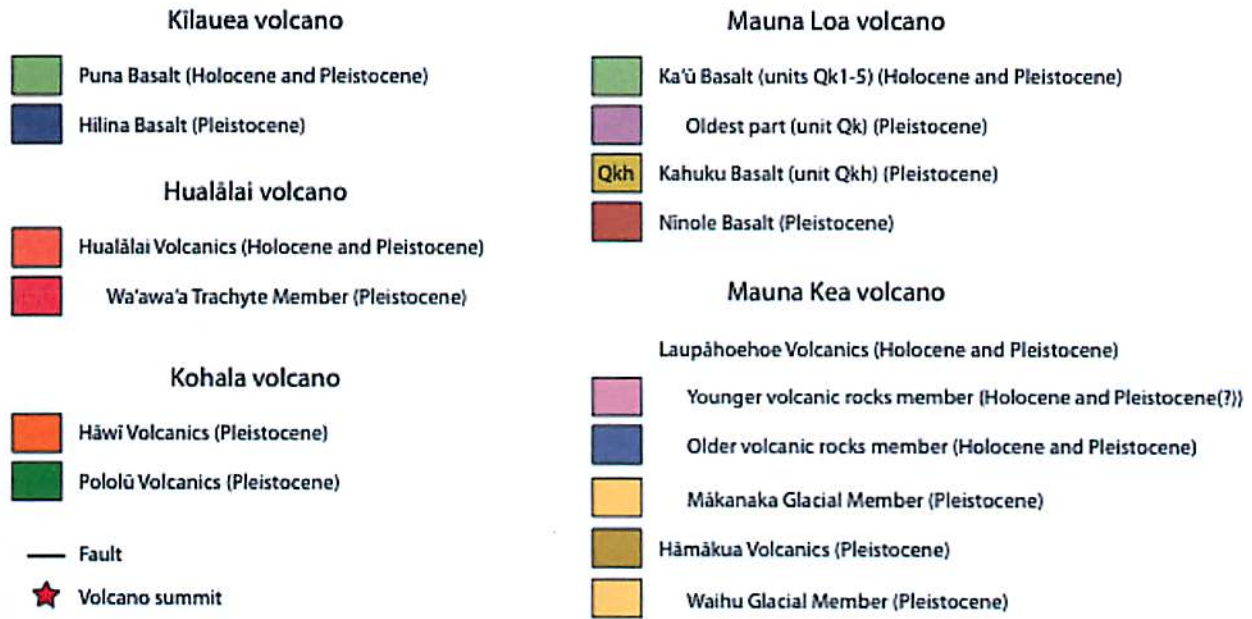


Figure 2 Stratigraphic formations of volcanoes in Big Island. (Sherrod et. al, 2007)

Kohala

Kohala is the oldest volcano located on northern end of Big Island. The exposed part shows maximum age of 0.78 Myr. Hāwī Volcanics rests upon Pololū Volcanics and its youngest part is no older than 0.12 Myr. The axial rift zone was developed along NW-SE direction. This rift zone seems to be connected to the submarine Hilo Ridge. The northeastern part of Kohala is characterized by large indentation through a landslide or slump.

Hualālai

Hualālai is an active volcano located at the western tip of the island. Its last eruption occurred during 1800-1801 and the lava flow during this eruption is estimated over 0.3 km³ for the total volume. The lava flow destroyed villages and a fishing pond on the way reaching the ocean. The Kona International Airport is sitting on the Hu'ehu'e flow, which was also formed at that time. More than half of the exposed area has age less than 3000 yrs. Phreatic explosions through the vent at Waha Pele made 3m thick ash layer about 700-800 yrs ago.

Mauna Kea

Mauna Kea is a dormant volcano having the tallest peak in the world, 10km, when measured from the sea floor base. The exposed lava flow dates back up to 0.3 Ma (Hāmākua Volcanics) and the youngest part is measured as 4.6 kyr old (Laupāhoehoe Volcanics) as a conservative estimate.

Mauna Kea have experienced three glaciation events, the Pōhakuloa(180–130 ka), Wāihu (80–60 ka) and Mākanaka(40–13 ka) Glacial Members. Discontinuous permafrost is currently present near the summit.

Mauna Loa

Mauna Loa is an active volcano, which had its last eruption in 1984. Mauna Loa is the largest in volume among subaerial volcanoes, 65,000 - 80,000 km³, but it is still much smaller than Tamu Massif, an extinct submarine volcano. Nīnole Basalt is the oldest subaerial lava flow and is estimated as 0.1-0.2 Myr old while younger Ka'ū Basalt covers most of the area. Pāhala ash layer was formed about 13-30 ka. At least two phreatic recent explosions formed deposits near the rim of Moku'āweoweo caldera. Mauna Loa does not have permafrost region but its summit had ice cap during the glaciation (15-25ka).

Kīlauea

Kīlauea is one of the most active volcanoes in the world and is home of Pele, the volcano goddess. The pre-shield alkali basalt has been dated at about 275 ka from submarine pillow and debris-flow clasts. The oldest subaerial region is the Hilina Basalt, which is exposed in the highly active Hilina fault system on the Kīlauea's southern flank. Most of the Kīlauea's surface is covered by Puna Basalt. The oldest outcrop (older than 10 kyr) can be seen in Hilina Pali with underlying Pāhala Ash. However, 90 percent of the surface is formed later than 1.5ka.

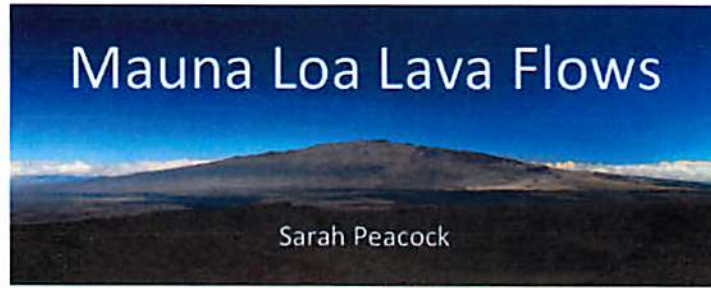
Most of the eruption shows effusive character but explosive activity was also frequent before European arrival and formed tephra sequences. The first documented eruption dates back to 1823 and the first major eruption was recorded in 1840. Current ongoing eruption has been continuous since January 3, 1983, marked as one of the longest eruptions in the world.

Māhukona

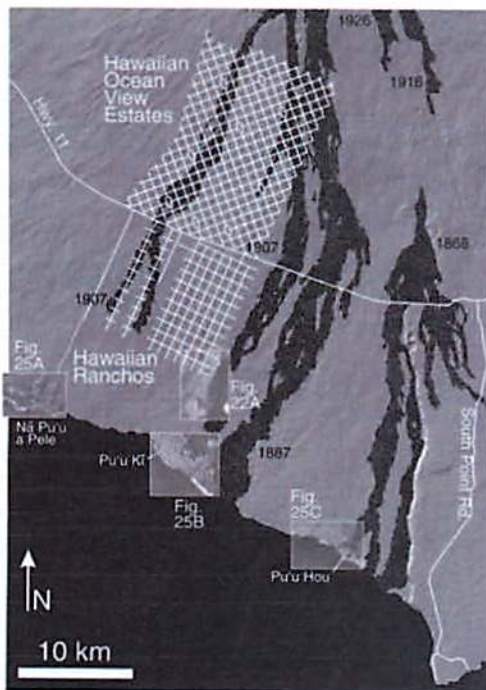
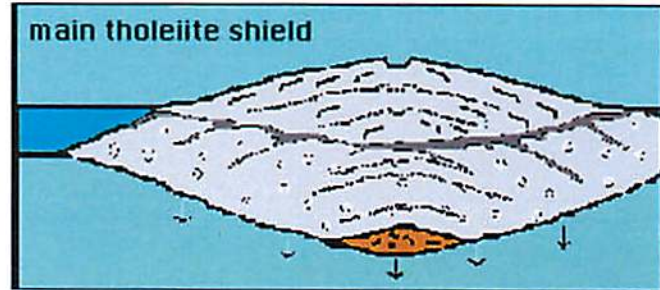
Māhukona is a submerged volcano on the northwestern side of the Hawai'i island. The summit of Māhukona once reached to 250m above sea level, and now submerged to about 1100m below sea level. Tholeiitic shield growth was ceased at about 470ka, and the subsiding event is estimated to occur between 365 and 435ka. Old shorelines can be seen as two drowned coral reefs at about ~1150m and ~1340m.

References

- Clague, D.A., and Moore, J.G., 1991, "Geology and petrology of Mahukona Volcano, Hawaii", *Bull Volcanol*, v.53, pp. 577–587.
- Sherrod, D.R., Sinton, J.M., Watkins, S.E., and Brunt, K.M., 2007, "Geologic Map of the State of Hawai'i", USGS. pp. 48-50.
- USGS site, "Evolution of Hawaiian Volcanoes", USGS. Sep. 8, 1995.



Mauna Loa is in its active tholeiite shield stage, so it has a more gradual and smooth profile than the other volcanoes on the island. During the tholeiite stage, the lithosphere is heated, increasing partial melting and the absolute volume of magma. A higher degree of partial melting produces tholeiite basalt, which has higher silica content than alkalic basalt. During this stage, volcanoes are most efficient at transporting magma to the surface (>95% of each volcano consists of lava erupted during this stage [1]). Mauna Loa erupts with fountains tens to hundreds of meters high, which results in small scoria and spatter cones and voluminous, long lava flows. These flows can only build up gradual slopes, producing the classic shield volcano shape. During this stage, a magma chamber also fully develops, which can lead to the formation of a caldera through collapse and/or subsidence into the magma chamber.



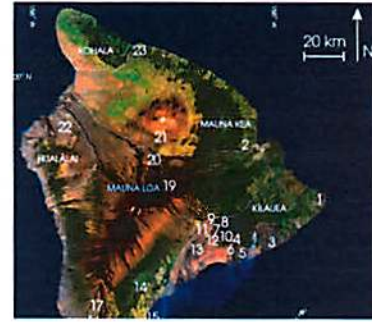
Left. Shaded relief image. Black areas are post 1800 AD lava flows. The squares are littoral cones (cones of lava fragments built on the surface of a lava flow pouring into a body of water).

Despite the different ages and subtle differences in the surface roughness, most of the lava flows on Mauna Loa appear bright in radar images. However, it is particularly difficult to map the extent of a single flow, or to distinguish among individual flow lobes that originated during the same eruption.

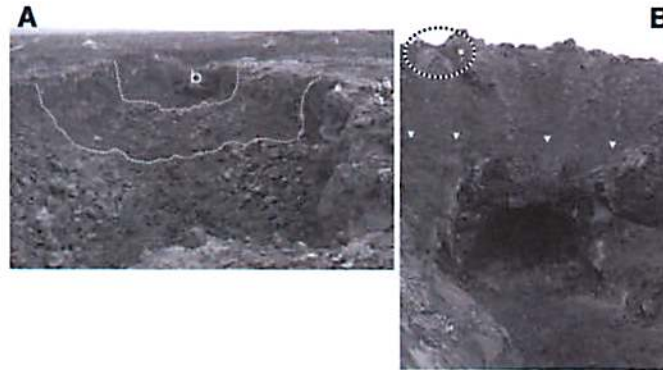
- Statistics**
- Largest subaerial volcano in the world
 - Height (from base to peak): 9,170 m
 - Volume: 75,000 km³
 - Number of eruptions since 1832: 39
 - Most recent eruption: 1984

Pohue Bay Flow:

On the SW flank of Mauna Loa, there is a lava tube and channel system within the 2500 year-old Pohue Bay lava flow. The tube diameter is only 8 m, but the roof channel is up to 20 m thick in some places. Most of the tube has collapsed completely. At the coast, the Pohue Bay flow has a collection of littoral cones, some of which resemble recently described features on Mars.



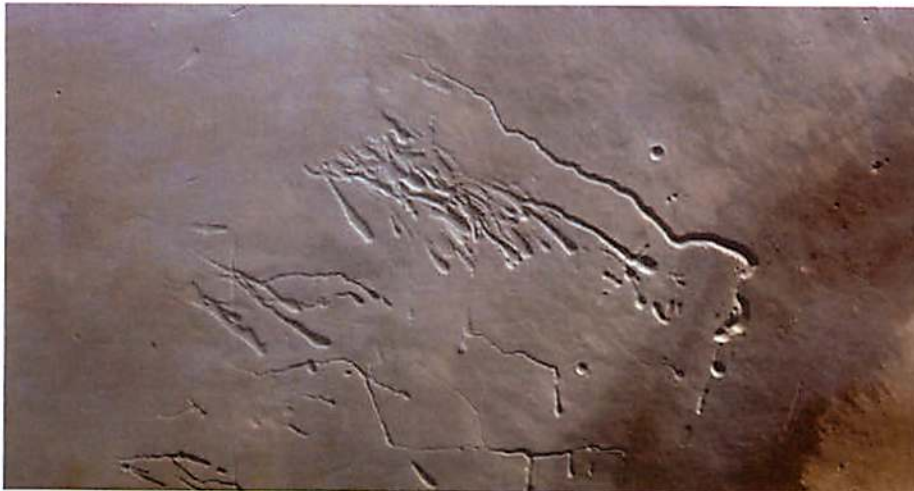
Right. The Pohue Bay flow channel and tube system. (A) View up-flow of a channel-like section. Partially collapsed bridge (b). (B) View across a large skylight in the tubed section. Arrows indicate uppermost level of lava veneer produced by the last lava flow through this region.



Planetary Connection: Lava tubes on Mars



Left: Skylight into a lava tube on the slopes of the Pavonis Mons volcano on Mars (the central of three shield volcanoes making up the Tharsis Montes). The image is of a 50 meter conical collapse pit, it is estimated that the pit is approximately 80 meters tall (much larger than the lava tubes around Mauna Loa). *Below:* Collapsed lava tubes on Pavonis Mons.





Above. Littoral cones along the SW flank of Mauna Loa. The Na Pu'u a Pele and Pu'u Ki littoral cones are hosted in the 750-1500 year-old flows. Pu'u Kahakahakea, Pu'u Kaimu'uala, and Pu'u Waimanalo cones in the 3000-10000 year-old flows. And Pu'u Hou cones are in the 1868 AD flow.

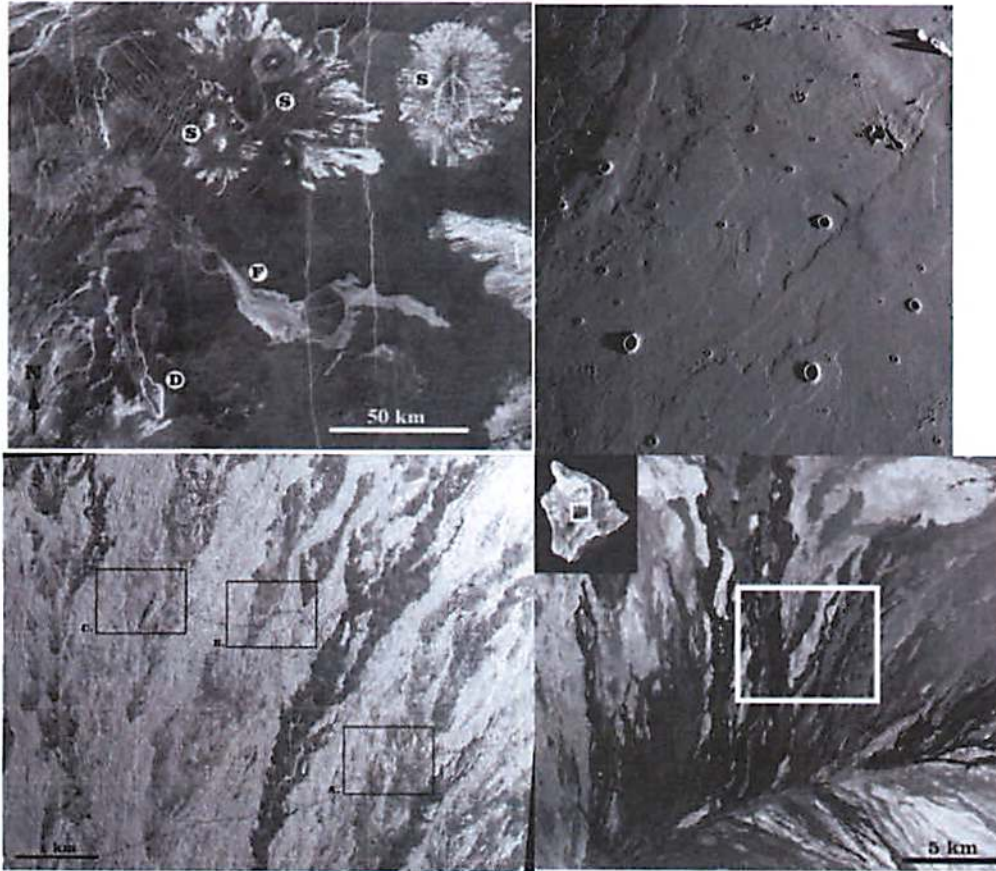
**Planetary Connection:
Rootless Cones**

Right: Overflow channel from Athabasca Vallis on Mars. Vague bumps are visible on the channel floor, thought to be rootless cones that form from lava-water interaction.



Planetary Connection: Remote Sensing

Lava flow textures observed on Venus by *Magellan* (below, upper left: radar image) and the long lava flows within Mare Imbrium on the Moon (below, upper right: visible image) are good comparisons to the Mauna Loa flow fields (below, lower left: radar image, lower right: visible image). The spatial extent of an individual flow and the eruption conditions are difficult to identify using optical images. By looking at the northern flank of Mauna Loa, there are a series of lava flows that are informative in terms of their surface structure and weathering state. Several radar data sets have been collected for Mauna Loa, including both orbital and airborne measurements. This data provides information about wavelength-scale surface roughness as well as dielectric properties of the material. Since all radars have a wavelength that can penetrate clouds, it is extremely useful for imaging volcanic features on Venus.



Mythology:

According to Hawaiian legends, Pele, the volcano goddess, was very passionate and impulsive. She was chased out of her home by her sister, Na-maka-o-kaha'i, after

Pele had seduced her husband. She first landed on Kaua'i, but every time she tried to dig a pit in the Earth for her new home, her sister would flood the pits. Pele moved down the chain of islands in order of their geological formation, and eventually landed on the Big Island, where she made Mauna Loa her new home. (when measured from its base at the bottom of the ocean), was so tall that even Pele's sister could not send ocean waves high enough to drown Pele's fires.



She first landed on Kaua'i, but every time she tried to dig a pit in the Earth (goddess of water and sea) moved down the chain of geological formation, and eventually landed on the Big Island, where she made Mauna Loa, the world's tallest volcano from its base at the bottom of

There are many stories regarding the multitude of rivals and lovers had by Pele. Most of her lovers did not survive, but instead had molten lava hurled at them and they are currently trapped in the odd misshapen pillars of rock that dot volcanic fields to this day.

[1] Clague DA (1987). Hawaiian xenolith populations, magma supply rates, and development of magma chambers. *Bull. Volcanol.* 49: pp. 577-587. [2] Rowland, S., Mouginiis-Mark, P., and Fagents, S. (2011). NASA volcanology field workshops on Hawai'i: Part 1. Description and History. *Geological Society of America Special Papers*; 483;401-434. [3] Mouginiis-Mark, P., Fagents, S., and Rowland, S. (2011). NASA volcanology field workshops on Hawai'i: Part 2. Understanding lava flow morphology and flow field emplacement. *Geological Society of America Special Papers*; 483; 435-448.

Astronomy, telescopes, and related cultural issues on Mauna Kea

Tiffany Kataria



Figure 1: View of telescopes on Mauna Kea.
<http://www.ifa.hawaii.edu/mko/images/mko5.jpg>

History of Astronomy at Mauna Kea

After a tsunami had destroyed parts of Hilo in the 1960s, Mitsuyo Akiyama, then the executive secretary of the Hawaii Island Chamber of Commerce, was looking for ways to revive the Hawaiian economy. He had heard from Howard Ellis, the head of the Weather Bureau's Mauna Loa Observatory, how clear the skies of Mauna Kea (Hawai'ian for "White Mountain") were. Realizing the potential for observations on Mauna Kea, he sent a letter out to universities and research institutes in the United States and Japan, urging them to consider Mauna Kea as a potential astronomical site.

Only one man replied: Dr. Gerard Kuiper, head and director of the Lunar and Planetary Laboratory at the University of Arizona. Kuiper had already worked with NASA and the Department of Defense to test sites on Haleakala and noticed that Mauna Kea and Mauna Loa were above the cloud tops. However, Mauna Loa was less favorable for telescopes because of its potential volcanic activity. Kuiper immediately followed up with Akiyama, and in 1964 he traveled to the Big Island to begin conducting test observations. First, he toured the mountain in a small plane, and then took a jeep ride to the ranger station at the 9500-foot Hale Pohaku (HP). At the time, there was no access road to the summit. So, Akiyama arranged a meeting between Kuiper and Governor John A. Burns, who invested \$42k in state funds to build a road from HP to the summit. NASA provided funds to build a 12.5-inch telescope for site testing, which Kuiper installed on Pu'u Poli'ahu. Kuiper was assisted in his testing by scientists such as Alia Herring, a part Hawaiian, and Bill Hartmann, then a grad student at UA. At the conclusion of his testing, Kuiper concluded: "The mountaintop is probably the best site in the world – I repeat – in the world – from which to study the moon, the planets, and stars."

Kuiper approached NASA to fund construction of a telescope on Mauna Kea. However, in the meantime NASA officials had encouraged other universities to apply. UA competed with Harvard University and the University of Hawaii, the latter of which only had prior experience in solar observing. Nevertheless, NASA selected UH to build a 2.2-

meter (88-inch) optical/infrared telescope. In 1967, The UH Astronomy department was expanded to the Institute for Astronomy (IfA) to manage the Haleakalā Observatories on Maui and the Mauna Kea Observatories on the Big Island, as well as conduct its own science research.

Telescopes on Mauna Kea

Mauna Kea is favorable for astronomical observations because it resides above the inversion layer of clouds that lie below the summit, such that it blocks moist, turbulent air from rising. Furthermore, the mountain is only surrounded not by other mountains, but only water; this prevents other wave disturbances. In sum, the air around Mauna Kea is dry and stable, making it perfect for astronomical observations.

Comparisons to other telescopes

As a comparison, the Hubble Space Telescope (HST) is a 2.4m telescope, while the future James Webb Space Telescope (JWST) will measure 6.5m. While these are not as large as the largest telescopes on Mauna Kea, the fact that they are above the Earth's atmosphere means that they can achieve greater resolution with a smaller telescope.

One can also compare the telescopes on Mauna Kea to other ground-based observatories. The Gran Telescopio Canarias (GTC) is the world's largest single-aperture optical telescope, with an effective diameter of 10.4 meters. The Mauna Kea telescopes are also much smaller than the next generation of telescopes (the extremely large telescopes, or ELTs), including the Giant Magellan Telescope (seven 8.4 m diameter primary segments with the resolving power of a 24.5 m primary mirror), the proposed Thirty Meter Telescope (30 m) and the proposed European Extremely Large Telescope (39.3 m).

Table 1: List of Mauna Kea telescopes in chronological order. Adapted from https://www.ifa.hawaii.edu/mko/telescope_table.htm

Telescope	Size	Operational year	Managed by
UH 88-inch telescope	2.2 m	1970	UH IfA
NASA Infrared Telescope Facility (IRTF)	3.0 m	1979	NASA
Canada-France-Hawai'i Telescope (CFHT)	3.6 m	1979	Canada/France/UH
United Kingdom Infrared Telescope (UKIRT)	3.8 m	1979	United Kingdom
Caltech Submillimeter Observatory (CSO)	10.4 m	1987	Caltech/NSF
James Clerk Maxwell Telescope (JCMT)	15 m	1987	UK/Canada/Netherlands
W.M. Keck Observatory (Keck I)	10 m	1992	Caltech/University of California
W.M. Keck Observatory (Keck II)	10 m	1996	Caltech/University of

			California
Subaru Telescope	8.3 m	1999	Japan
Gemini Northern Telescope	8.1 m	1999	USA/UK/ Canada/Argentina/ Australia/Brazil/Chile
Submillimeter Array (SMA)	8x6 m	2002	Smithsonian Astrophysical Observatory/Taiwan

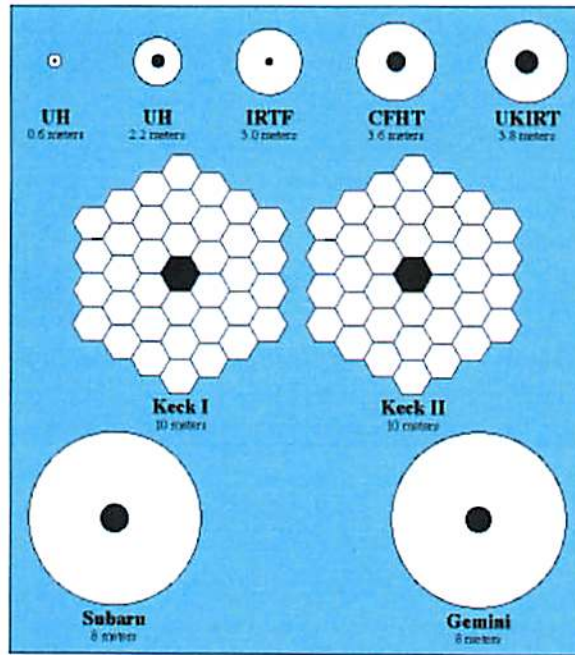


Figure 2: Size of mirrors on Mauna Kea telescopes. Source: https://www.ifa.hawaii.edu/mko/images/mr_mirror2.jpg

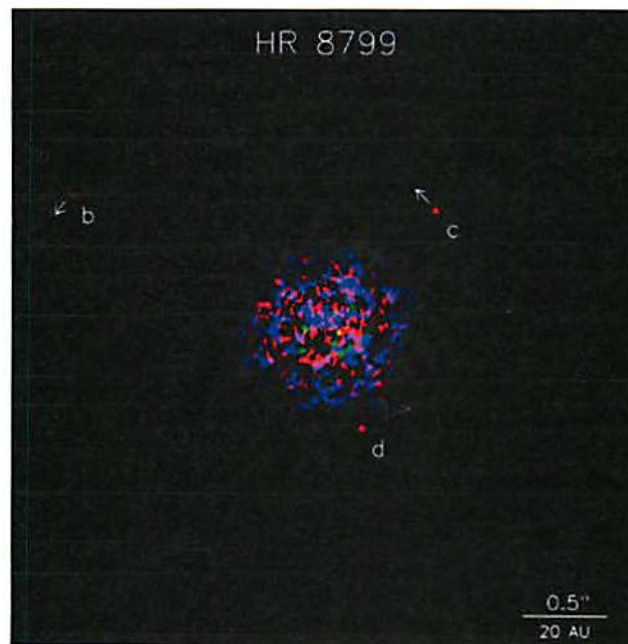
Telescope Factoids

- The University of Hawai'i (UH) 88-inch established Mauna Kea as the pre-eminent site for ground based astronomy. About 100 UH students have obtained their PhDs in astronomy with this telescope.
- The UH and IRTF telescopes were initially operated out of a garage on the Hilo Community College Campus. IfA Hilo was eventually established in 2001 to manage these and other telescope facilities.
- There was a small delay in the construction of the JCMT because the ship carrying the telescope across the Pacific was hijacked by modern-day pirates.

Some major discoveries using Mauna Kea telescopes

- David Jewitt and Jane Luu discovered the Kuiper belt using University of Hawaii's 88in telescope (Jewitt and Luu 1993).
- The CFHT was used to confirm that Pluto had a satellite, Charon (Bonneau and Foy 1980).

- Astronomers used the JCMT to detect hydrogen peroxide (H_2O_2) in the atmosphere of Mars for the first time. This was the first time that a chemical catalyst of this sort has been found in a planetary atmosphere other than the Earth's (Clancy et al. 2004).
- Data from the Kepler Space Telescope and Keck Observatory have shown that one in five stars has an Earth-sized planet in its habitable zone, and that small-mass planets are the most common in the universe (Petigura et al. 2013).
- Other science on Keck includes the detection of many exoplanets using the Doppler technique, the most of any telescope. It is also used to validate planets discovered via transit on the Kepler Space Telescope (Marcy et al. 2014).
- Marois et al. 2008 used the near-IR optics aboard the Keck Observatory to image the stellar system HR 8799, which at the time was discovered to harbor four planets.



- Keck also helped in discovery of the accelerating expansion of the universe, for which astronomers earned the 2011 Nobel Prize in physics.

Cultural Issues

Mauna Kea, or known by its original name Mauna a Wakea, is a sacred place for Hawaiians. Wakea is considered the father of the Hawaiian people (translates to “Sky Father”). It is also believed that the goddess Poli’ahu (of which the road gets its namesake) resides on the mountain. Hence, the summit has been considered by Hawaiians to be the realm of the gods and forbidden (*kapu*) to all but the highest chiefs and priests. The Native Hawaiians of today continue to regard Mauna Kea with reverence, and many cultural and religious practices are still performed there. Mauna Kea is also host to almost one hundred archeological sites.

The rampant construction of telescope facilities on the mountain has therefore led to conflict with the native Hawaiians. Tensions for the most part have eased, and astronomers are to abide to certain guidelines. The telescopes, for one, are contained

within one region of the mountain, and sacred burial sites near and on the very top of the summit are off-limits.

To set clear guidelines for construction and maintenance on the mountain, the Mauna Kea Science Reserve Master Plan—a policy guide for University management of Maunakea, including protection of the cultural, natural, and scientific resources—was adopted by the Board of Regents in June 2000.

In 2009, the University of Hawaii developed the Mauna Kea Comprehensive Management Plan, followed in 2010 by the Natural Resources Management Plan, Cultural Resources Management Plan, Public Access Plan, and Decommissioning Plan. These management plans, approved by the State of Hawai'i Board of Land and Natural Resources (BLNR), are the State's plans for managing Mauna Kea. The Office of Mauna Kea Management, together with the Mauna Kea Management Board and Kahu Kū Mauna share responsibility for implementing these plans. Since June 2000, management of Mauna Kea requires input and participation from the community regarding daily activities, development of policies and programs, and review of proposed projects. Such a review was made for the proposed Thirty Meter Telescope (TMT), of which the BLNR approved the proposal in February 2011.

The Comprehensive Management Plan (CMP) provides a management framework for the University of Hawai'i (UH) to address measures to protect the cultural, natural, and scientific resources on UH Managed areas on Maunakea. The CMP was approved by the BLNR in April 2009. In 2010 the BLNR approved the four sub-plans addressing: public access, cultural resources management, natural resources management, and decommissioning. The CMP and supplemental plans and framework and implementation for project development are the State's plans for lands on Mauna Kea under the University's management.

However, despite all these guidelines, conflict between the Native Hawaiians and astronomers still remains. In 2001, for example, the Native Hawaiians protested and successfully closed the original road to Pu'u Poli'ahu (Poli'ahu road) used by Kuiper to get to the mountain, which threatened the survival of a rare insect species. Furthermore, despite its approval by the BLNR, there has been much opposition to the building of the TMT. Currently, court appeals have been filed by Native Hawaiians to stop the proposed TMT from being built. s

References

Bonneau, D.; Foy, R (1980). "Speckle interferometry with the 3.60 M CFH telescope. I - Resolution of the Pluto-Charon system". *Astronomy and Astrophysics* 92 (1): L1-L4.

Clancy, R. T.; Sandor, B. J.; Moriarty-Schieven, G. H. (2004). "A measurement of the 362 GHz absorption line of Mars atmospheric H₂O₂". *Icarus* 168 (1):116–121.

Jewitt, D.; Luu, J. (1993). "Discovery of the candidate Kuiper belt object 1992 QB1". *Nature* 362 (6422): 730.

Marcy, G. W.; Isaacson, H.; Howard, A. W. et al. (2014). "Masses, Radii, and Orbits of Small Kepler Planets: The Transition from Gaseous to Rocky Planets". *The Astrophysical Journal Supplement* 210 (2): 20.

Marois, C.; Macintosh, B.; Barman, T.; Zuckerman, B.; Song, I.; Patience, J.; Lafrenière, D.; Doyon, R. 2008. "Direct Imaging of Multiple Planets Orbiting the Star HR 8799". *Science* **322** (5906): 1348.

Petigura, E. A.; Howard, A. W.; Marcy, G. W. (2013). "Prevalence of Earth-size planets orbiting Sun-like stars". *Proceedings of the National Academy of Sciences* **110** (48): 19273-19278.

History – Mauna Kea Astronomy Outreach Committee. MKAOC. Web.
<http://www.mkaoc.org/history>.

In Memoriam: Mitsuo Akiyama, 1920-2004. Na Kilo Hoku: A newsletter from the Institute for Astronomy, University of Hawai'i. Web.
<http://www2.ifa.hawaii.edu/newsletters/article.cfm?a=168&n=1>

The Selection of Mauna Kea. University of Hawaii Institute for Astronomy. Web.
http://www.ifa.hawaii.edu/users/jefferies/The_Selection_of_Mauna_Kea.htm

Epilog. University of Hawaii Institute for Astronomy. Web.
<http://www.ifa.hawaii.edu/users/steiger/epilog.htm>

Management. Office of Mauna Kea Management. Web.
<http://www.malamamaunakea.org/management>

Hawaiian Culture. Office of Mauna Kea Management. Web.
<http://www.malamamaunakea.org/hawaiian-culture>

Mauna Kea Sacred Site Restored. Honolulu Advertiser. Web.
<http://the.honoluluadvertiser.com/article/2001/Aug/17/ln/ln37a.html>

Indigenous Religious Traditions. Web.
<https://sites.coloradocollege.edu/indigenoustraditions/sacred-lands/sacred-lands-mauna-kea/>

Cooper, Jeanne. *Taking a stand for Mauna Kea, against mammoth new observatory*. blog.sfgate.com. Web.
<http://blog.sfgate.com/hawaii/2013/12/13/taking-a-stand-for-mauna-kea-against-mammoth-new-observatory/>

Research Report: Mauna Kea, HI (Native Hawaiians) (2009). The Pluralism Project at Harvard University. Web.
<http://www.pluralism.org/reports/view/21>

Hawaiian Culture and Mauna Kea. Mauna Kea Visitor Information Station. Web.
<http://www.ifa.hawaii.edu/info/vis/culture.html>

Astrobiology on Hawaii

Donna Viola



The study of extreme environments on Earth is a primary focus of terrestrial-based astrobiology because they allow us to better understand the limits of life as we know it and the potential for life in extraterrestrial environments. On the Big Island of Hawai'i, astrobiologically-relevant environments can be found in drill cores down to a depth of almost 2000 m below the surface and up to the permafrost microclimates near the summit of Mauna Kea (4200 m), and in lava tube caves in between.

Mauna Kea Microclimates

Mauna Kea is a unique in that, even though it is located in Earth's tropics ($\sim 20^\circ\text{N}$), the elevation allows the peak to be an alpine desert – complete with seasonal/diurnal subzero temperatures and the presence of permafrost. This permafrost was first discussed in Woodcock et al (1970), and recent studies have examined the microclimates associated with this region (Schorghofer et al, 2013, Figure 1). Ice caves have also been identified on Mauna Loa. Both of these environments are considered a possible analog to Mars, and are being studied as part of a monitoring project associated with the University of Hawaii's NASA Astrobiology Institute team.

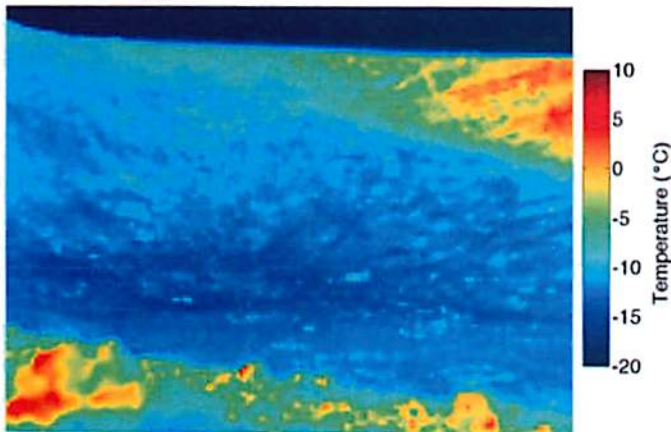


Figure 1: Morning infrared temperatures in the Puu Weiku cinder cone on Mauna Kea show that, while the crater rim warms up rapidly, the shadowed crater floor (image center) remains cold (Schorghofer et al., 2013).

Drill Cores near Hilo

The Hawaii Scientific Drilling Program collected a core of igneous rock down to a depth of 3100 m outside of Hilo (Figure 2). Alterations observed in some units of hyaloclastite have been attributed to microbial activity. The presence of microbes was detected down to a depth of 1895 m at the boundaries of the volcanic glass and secondary minerals in the hyaloclastite units using nucleic acid fluorescence and Raman spectroscopy (Figure 3).

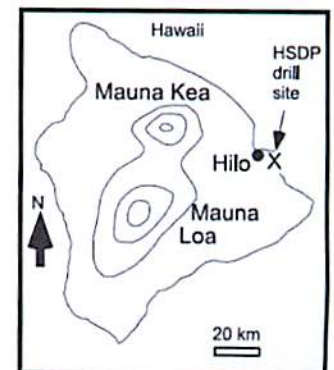


Figure 2: Drill core site (Fisk et al., 2003).

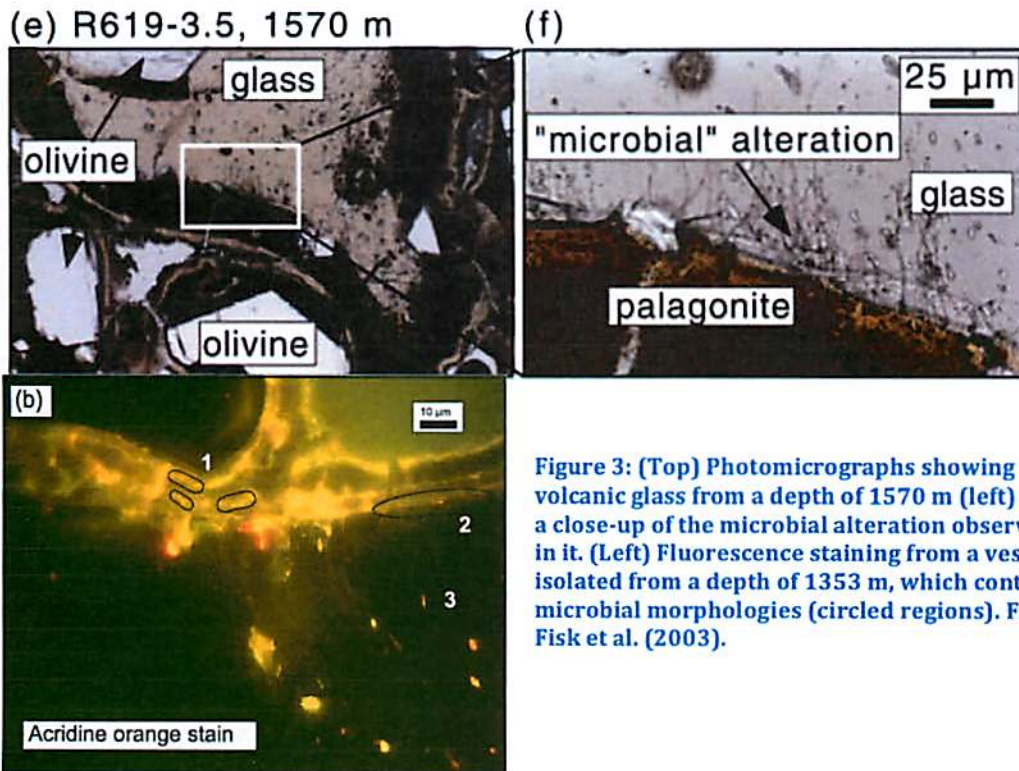


Figure 3: (Top) Photomicrographs showing volcanic glass from a depth of 1570 m (left) and a close-up of the microbial alteration observed in it. (Left) Fluorescence staining from a vesicle isolated from a depth of 1353 m, which contains microbial morphologies (circled regions). From Fisk et al. (2003).

Lava Caves, Mauna Loa and Kilauea

Lava caves are known to harbor varieties of microbial mats as well as secondary mineral deposits. Northup et al. (2011) analyzed the microbial communities associated with both of these structures; study sites included Hawai'i New Mexico, and the Azores (Figure 4). Diverse bacterial phyla were identified in both microbial mats and secondary mineral deposits, with some overlap between the two habitats.



Figure 4: (Left) A sample of microbial mats from Azorean lava caves (image is ~6 cm across; Hawaiian microbial mats also sampled but not pictured). (Center) Blue-green copper deposits from the Kipuka Kanohina Cave Preserve, Hawaii (drip is ~0.5 cm across). (Right) Gold-colored secondary minerals in Thurston Lava Tube, Hawai'i Volcanoes National Park. From Northup et al. (2011).

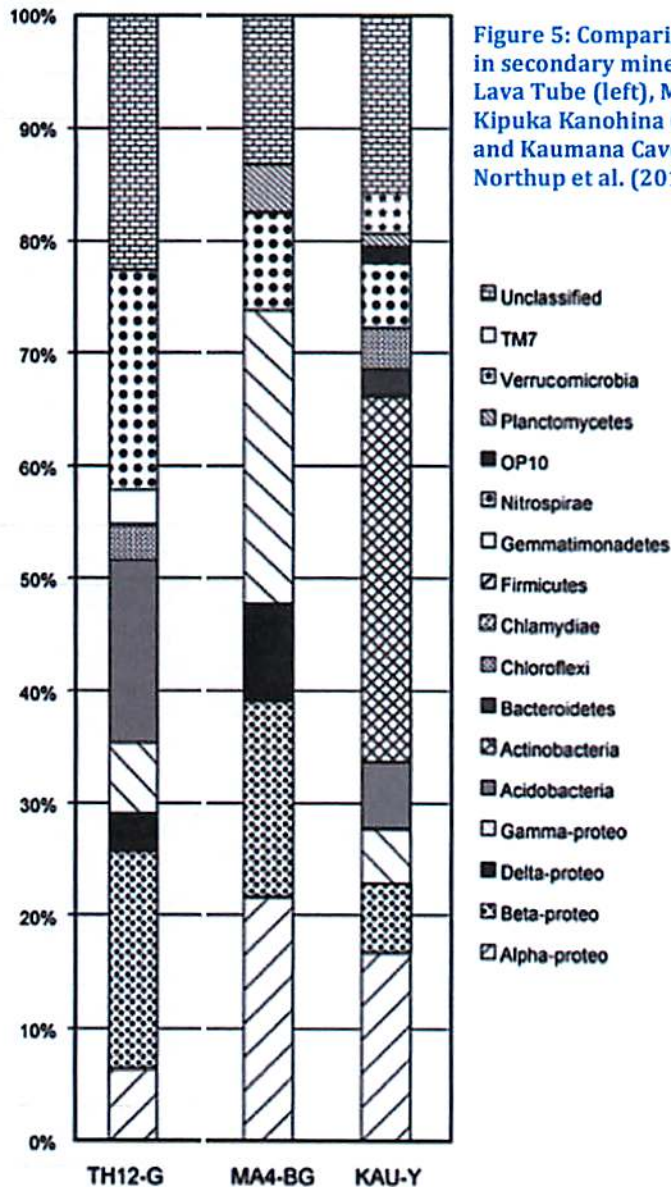


Figure 5: Comparison of the phyla present in secondary mineral deposits in Thurston Lava Tube (left), Maelstrom section of Kipuka Kanohina Cave Preserve (center) and Kaumana Cave (right) in Hawai'i. From Northup et al. (2011).

Figure 5 shows the bacterial diversity observed in secondary mineral deposits found in three lava caves in Hawaii, revealing both similarities and differences between different cave environments. Phyla that were found in yellow and white microbial mats in Hawai'i include Actinobacteria, Alphaproteobacteria, Betaproteobacteria, Gammaproteobacteria, Deltaproteobacteria, Acidobacteria, and Nitrospirae – many of which were also identified in the secondary mineral deposits.

Based on terrestrial observations, it is hypothesized that extraterrestrial lava tube caves could harbor either life or biosignatures indicative of past life, preserved within

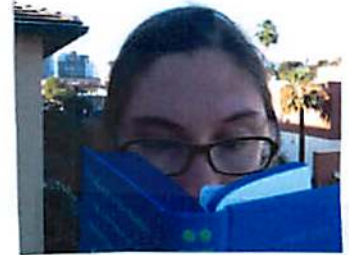
mineral formations (Leveille et al., 2010). Since lava tube caves are known to be present on Mars, these may be prime targets for future astrobiological exploration.

References:

Fisk M.R., et al. (2003). Evidence of biological activity in Hawaiian subsurface basalts. *Geochemistry, Geophysics, and Geosystems*, Vol. 4.
 Leveille R.J. & S. Datta (2010). Lava tubes and basaltic caves as astrobiological targets on Earth and Mars: A review. *Planetary and Space Science* 58:592-598.
 Northup D.E., et al. (2011). Lava cave microbial communities within mats and secondary mineral deposits: Implications for life detection on other planets. *Astrobiology* 11:601-618.
 Schorghofer N. et al. (2013). Permafrost enabling microclimates on Mauna Kea, Hawaii. *LPSC 2013*, Abstract #1695.
 Woodcock, A.H., et al. (1970). Fossil ice in Hawaii? *Nature* 226:873.

Mauna Kea Glaciation

Margaret Landis



At a glance

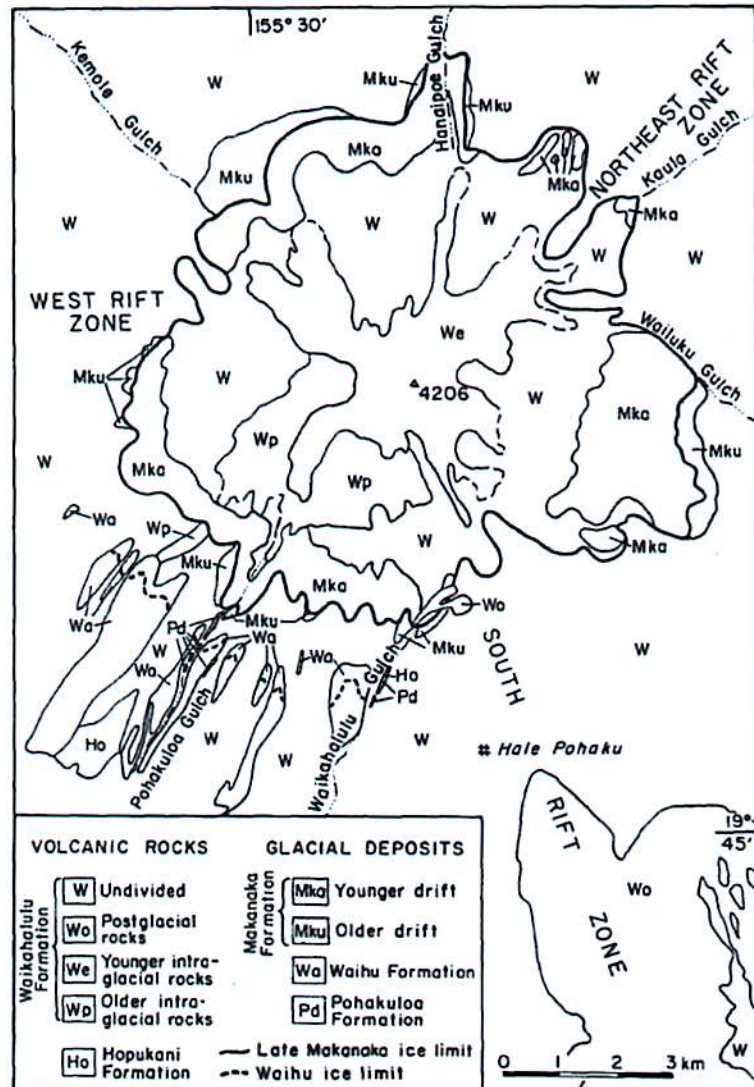
- It is the only inner tropical Pacific site that presently shows clear evidence of past glaciation (Porter 1979)
- Makes for an interesting test case in glaciers as moisture and atmospheric circulation are not blocked by other landforms
- Shows signs of episodic changes in glaciation
- Glaciation ceased after the Younger Makaanaka terrain formed ~13kya
- Implications for climate: wetter, stormier past in the Pacific Ocean
- Planetary connection: volatile-rich microclimates

Introduction/History

Gregory and Wentworth (1937) first identified glacial features on Mauna Kea and estimated that the glaciers extended as far down as about 3.2km.

Subsequent work aimed to identify the volcanic versus glacial units and to determine what the sequence of glacial events was on the volcano. Porter (1979) generated a geologic map that combined K/Ar dating, ¹⁴C dates, and map units to form a picture of episodic glaciation, from an eruption while an ice cap was in place at 170-175kya to the disappearance of the cap at ~9kya.

Figure 1. Geologic map of the Mauna Kea volcano with glacial/periglacial and volcanic units noted. From Porter (1979).



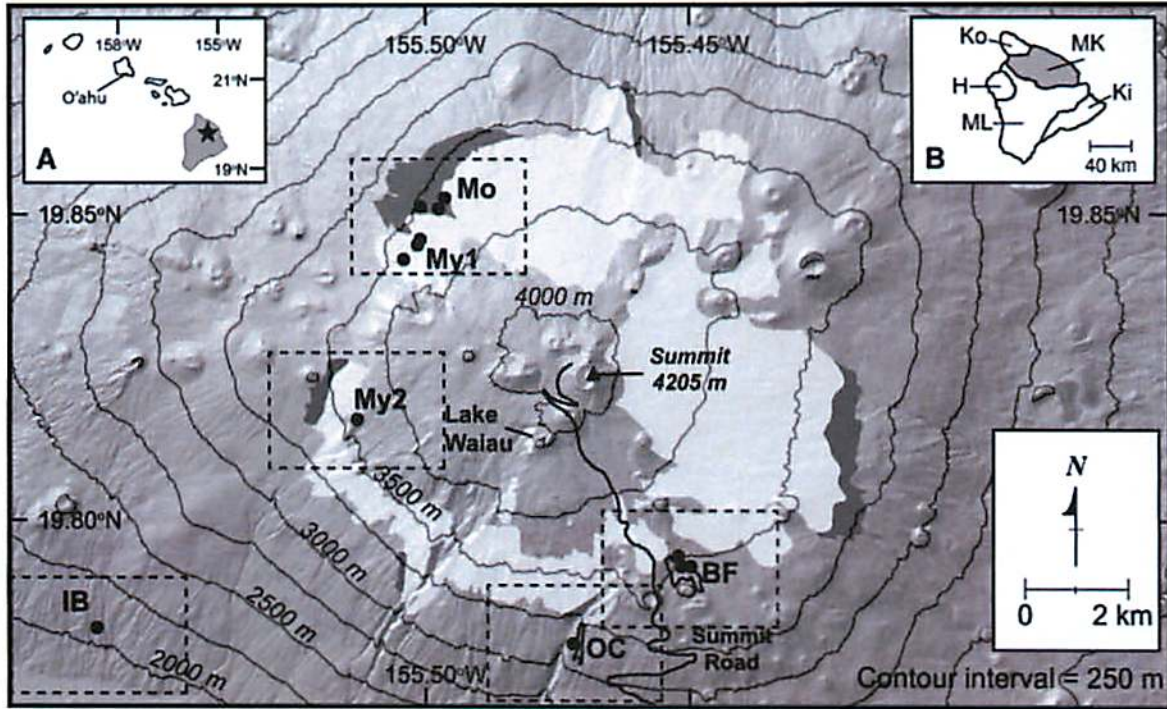


Figure 2. Location context map from Pigati et al. (2008). The insets show the location of Mauna Kea within the context of the Hawaiian island chain as well as the other volcanoes on the island. Light colors indicate the Younger Makaanaka deposits and darker colors are the Older Makaanaka deposits. Moraines and outwash channels that served as sample sites for the cosmogenic ^{36}Cl dating summarized in Figure 3.

Current Interpretation

Pigati et al. (2008) returned to the work that Porter (1979) pioneered by using ^{36}Cl dating at several sites along Mauna Kea, including glacially modified terrains as well features like moraines and outwash channels (Figure 2). Establishing cosmogenic isotope ages allowed for more precise dating of the various glacial landforms, and gave rise to a new version of the chronology of formation for the Mauna Kea glacial terrains (Figure 3). These ages narrow down the range first presented in Porter (1979) to have the glaciers disappearing $\sim 13\text{kya}$ rather than $\sim 9\text{kya}$.

Implications for Climate

Glaciers and other ice deposits can be modeled and used as a way of exploring the water budget and past climate of a particular region. In this case, the region is the Pacific Ocean and with the time scale of the last few thousand years on Earth, Pigati et al. (2008) were able

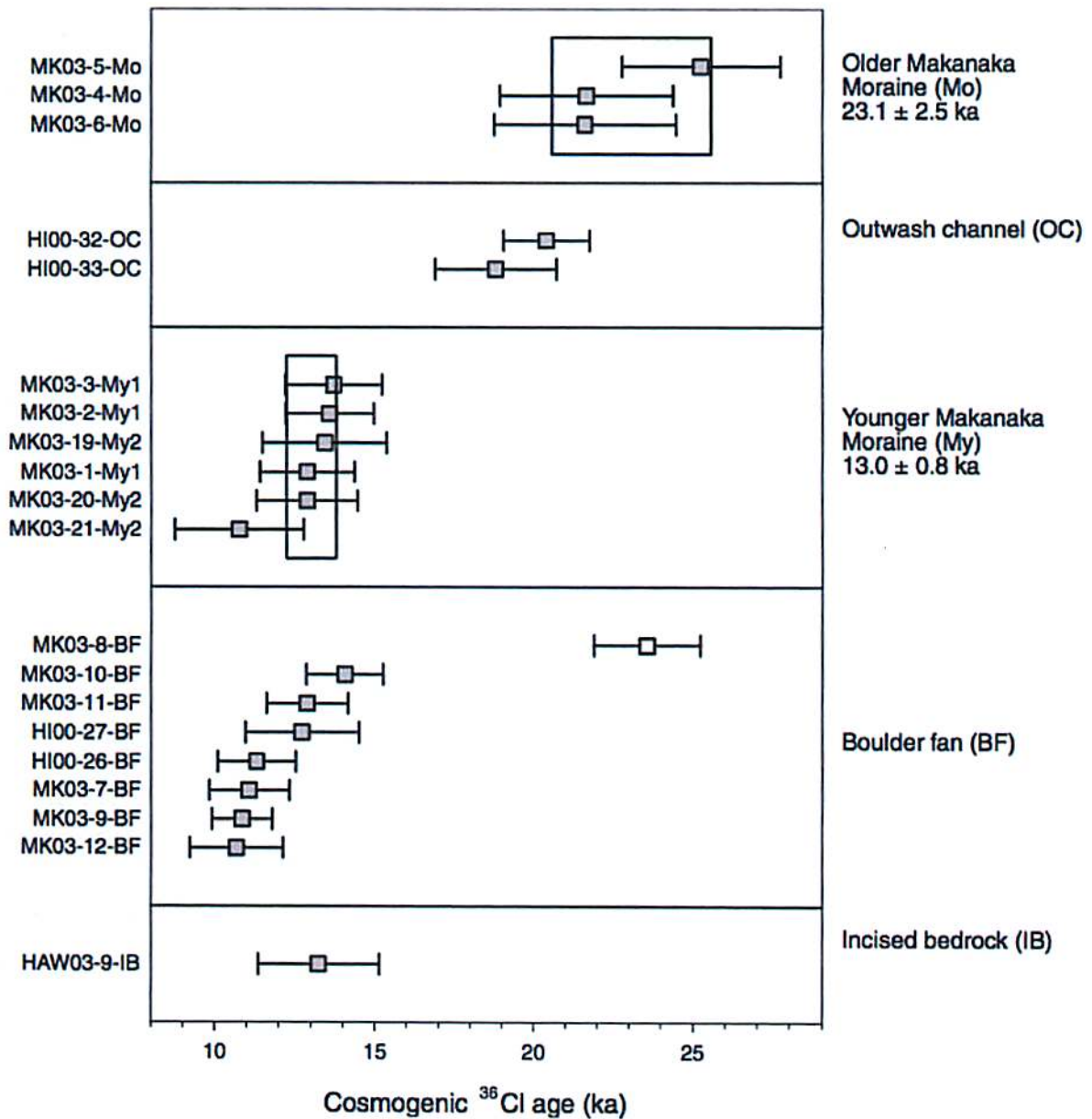


Figure 3. Cosmogenic ^{36}Cl ages for the glacial Makaanaka surfaces from Pigati et al. (2008). The open square was an outlier not used in the surface age calculations. The error bars are $\pm 2\sigma$. Each of these units corresponds to a box on Mauna Kea in Figure 2.

to model the glaciers on Mauna Kea using the constraints provided in the geologic record. Their conclusion was that the precipitation rate in the Late Pleistocene was higher than at present, due to more intense tropical storms associated with eastward-moving cold fronts. The increased rainfall and the higher atmospheric lapse rate in the atmosphere both contributed to forming glaciers at the top of Mauna Kea within their models.

Planetary Science Context: Volatile-rich Microclimates

Microclimates, like those that existed on Mauna Kea when glaciers were present, provide a terrestrial example of the types of volatile rich micro-climates that are present on other planetary surfaces. These can occur especially on the floors and walls of permanently shadowed craters near the poles of planets.



Figure 4. This LRO image shows the permanently shadowed craters in the south polar region of the Moon. Credit: NASA/GSFC/Arizona State University

On planetary bodies without atmospheres to change circulation and vapor availability, permanently shadowed areas generate microclimates where volatiles like water ice are stable. On the Moon, Diviner and Lunar Crater Observation and Sensing Satellite (LCROSS) were able to detect water ice in the permanently shadowed craters at the south pole of the Moon and monitor the impact of the spent Centaur rocket onto the surface (Paige et al., 2010). The resulting impact plume had water vapor present in the first few minutes of monitoring by the LCROSS spectrometer (Colaprete et al., 2010).

Permanently shadowed craters also occur towards the poles of Mercury, where recent work has also found evidence for water and other volatile ices in the permanently shadowed regions of craters (e.g Lawrence et al., 2013 and Neumann et al., 2013). These microclimates allow for the storing of ices that would not be stable at other locations on the surface, contributing to the variability on a planetary surface.

References

- Colaprete et al. (2010). *Science*
- Gregory and Wentworth (1937). *GSA Bulletin*.
- Lawrence et al. (2013). *Science*.
- Paige et al. (2010). *Science*.
- Porter (1979). *GSA Bulletin*.
- Pigati et al. (2008). *Journal of Quaternary Science*.
- Neumann et al. (2013). *Science*.



Glacial History of Mauna Kea

Jamie Molaro

The following summary is focused primarily on a series of studies done by Stephen C. Porter et al. over several decades, see references at the end. All figures in this handout come from his 2005 paper, which is both a new study and a summary of his previous work on the topic.

The following terms might be helpful:

Moraine: A ridge of unconsolidated drift deposited along the margins of a glacier.

Drift: All sediment transported by glaciers or glacial meltwater.

Marine Isotope Stages (MIS): alternating warm and cool periods in the Earth's paleoclimate, deduced from oxygen isotope data reflecting changes in temperature derived from data from deep sea core samples.

Equilibrium-Line Altitude (ELA): marks the area or zone on a glacier separating the accumulation zone from the ablation zone and represents where annual accumulation and ablation are equal. The ELA is also called the snow-line in this summary, and can be thought of as the elevation above which glacial ice can accumulate and be stable.

Chronology of Mauna Kea Drifts

The Hawaiian Islands include the only areas in the central Pacific Ocean that have land masses high enough to retain evidence of former glaciation (Porter 2005). None of their volcanoes rise high enough to intersect the modern interglacial ELA, aka snow line, but several summits did lie above the snow line during previous glacial periods. The Mauna Kea and Mauna Loa volcanoes are the only two summits left that are high enough to rise above the snowline in future glacial periods.

Mauna Kea is the highest summit in the Hawaiian Islands. Exposed rocks have been divided into two lithic units: the Hamakua volcanics (250k–65k yr old) form the surface over the mid and lower slopes of the volcano, overlain by the Laupahoehoe volcanics (65k–4k yr old). Moraines of the last (Makanaka) glaciation delimit a 10 km diameter ice cap that mantled the upper slopes of the mountain. They extend farther downslope on the southeastern side of the mountain than on any other. The moraines are overlain in places by postglacial lava flows. They overlie volcanic rocks and deposits from previous glaciations, such as the Pohakuloa and Waihu drifts.

Pohakuloa drift is exposed in two gullies on either side of the Waihu moraine, indenting the southern slope of the volcano. It is an older predominantly basaltic drift, lying near the top of the Hamakua lava flows. The Waihu drift is a younger predominantly Hawaiite (more alkaline) from Loapahoehoe flows. The chronology of glacial activity on Mauna Kea is based primarily on K/Ar dates of lava flows that under- and overlie glacial drifts, and on surface-exposure (^{36}Cl) ages of flow and drift materials. These dates constrain the Makanaka drift to between 31k and 18k years ago, and surface exposures indicate it was deglaciated 15k years ago. The Waihu drift is very poorly constrained with K/Ar dates falling between 167k and 70k years ago, in spite of the fact that it overlies lavas dated at 121k years. Some studies suggest it is likely between 100-150k years old (during MIS5 and 6), however minimum limiting ^{36}Cl ages on boulders and rock varnishes suggest it's as young as 60k years, placing it in MIS4. The Pohakuloa drift is even less tightly constrained. Available K/Ar dates suggest that it is older than 100-150k years, but younger than 150-200k years. This places it somewhere in MIS6.

The Makanaka Ice Cap

The reconstructed configuration of the Makanaka ice cap at the last glacial maximum (LGM) is shown in Fig 4. The crests of several cinder cones rose above the glacier surface, and the minimum height of the glacier against their flanks is marked by glacial erosion. Other cones were overridden by ice, with both their flanks and summits were eroded. Comparing Fig 4 (left) to a Google maps image of the modern day summit (right) reveals which cinder cones rose above the ice cap and which were overridden. The moraines mark the limits of the glaciation. Using this information, a model of the ELA surface (Porter 1979b) shows that it sloped across the ice cap toward the southeast with a gradient of about 20m/km. This is consistent with the downslope extent of the moraines on the SE side of the mountain. At this low latitude, insolation varies little across the volcano's upper slopes, thus the sloping ELA gradient is likely a response to precipitation, implying an ESE moisture source during LGM. Reconstructions of the Waihu and Pohakuloa ice caps are much more difficult to create.

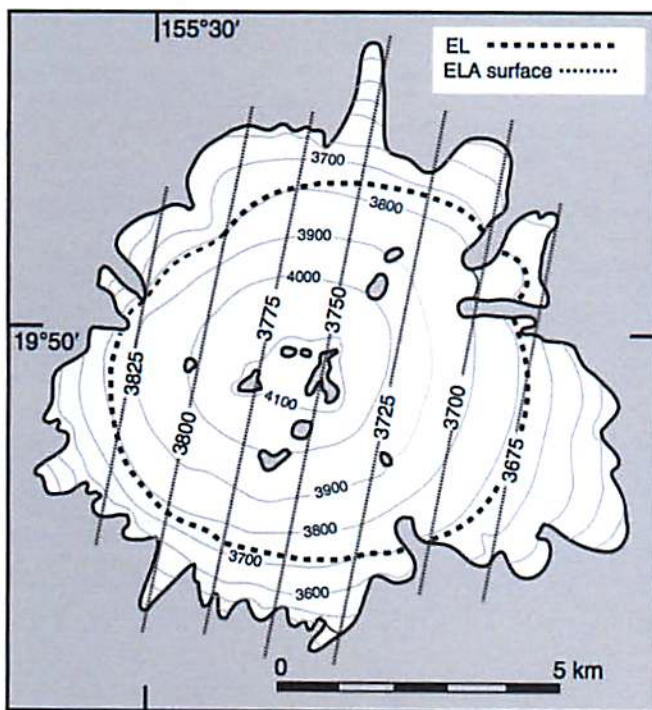


Fig. 4. Map showing extent and surface topography of Makanaka ice cap at the last glacial maximum about 20,000 years ago (Porter, 1979b). Bold dashed line represents reconstructed equilibrium line (EL) of ice cap, and dotted lines show east-southeast-sloping gradient of the equilibrium-line altitude (ELA) surface across the glacier.



Above: Google maps satellite image showing the present day view of the Mauna Kea summit.

Island Subsidence and the Snow Line

The typical eruptive life of a Hawaiian volcano is generally inferred to be 600k-1M years (Moore and Clague, 1992; Wolfe et al., 1997). During its lifetime it goes through a short pre-shield, and a long shield and post-shield phase. The volcano reaches its maximum altitude during the late shield and early post-shield stages. The rapid upward growth of the volcanic shield results in a great load imposed on the oceanic crust. This is accompanied by isostatic subsidence, which slows the increase in summit altitude due to

eruptive activity. The altitude of a volcano reflects the difference between accretion from lava flows (pos) and subsidence (neg). As extrusion rates decline at the end of the shield stage, subsidence overtakes upward growth and dominates subsequent volcano history.

Mauna Kea was completing its accretionary phase while nearby younger volcanoes were also beginning to become active. The island of Hawaii subsided fairly rapidly (2.6 mm/yr) during this time as a result of so much extrusive activity (Ludwig et al., 1991), which would have influenced both the summit altitude and the relative position of the snowline during Mauna Kea's successive glaciations. Using this subsidence rate, the summit of Mauna Kea would have been 52 meters higher during the LGM than at present day.

As discussed, the stratigraphic record of Mauna Kea shows that the snowline lay below the summit at least three times during the last 150k years. In order to assess the possibility of a longer glacial history, data on volcano growth and isostatic subsidence can be used to estimate the change in summit altitude during earlier (and later!) times.

The dashed lines in Figure 10 (Porter, 2005) placed at altitudes of 3785 and 4715 m represent the glacial (MIS2) and interglacial (present: MIS1) snowlines. The standard

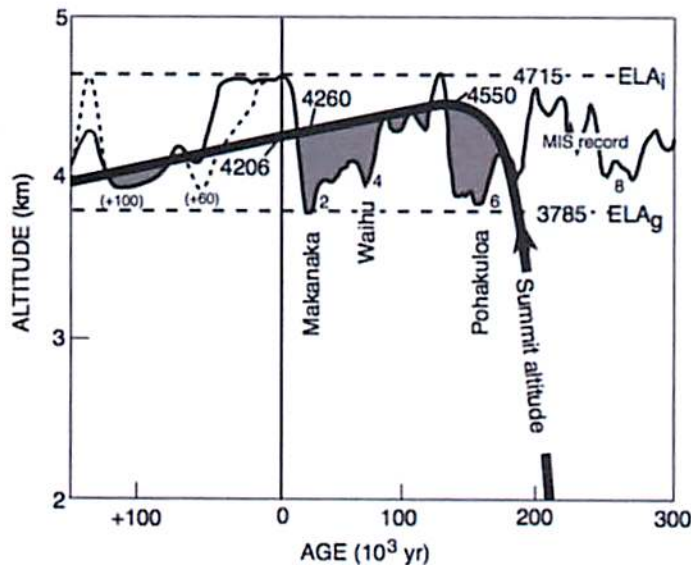


Fig. 10. Summit-altitude curve for Mauna Kea showing time of maximum altitude and subsequent decline as a result of waning volcanic activity and ongoing subsidence. Standard marine oxygen-isotope (MIS) curve (Williams et al., 1988) is used as a proxy for snowline variations. This curve is adjusted so that snowline altitude of the present interglaciation (ELA_i) equals ca. 4715 m and snowline for the last glacial maximum (ELA_g) equals 3785 m (see text). The summit first intersected the snowline curve near the beginning of MIS 6. Shaded areas represent times when the summit rose above the snowline and a glacier formed. The three mapped glacial drifts coincide with intervals of lowered snowline during MIS 6, 4, and 2. Projection of the ice-volume curve forward in time [from modeling studies of Loutre and Berger (2000) and Berger and Loutre (2002); solid line based on last-interglaciation values, dotted line on constant CO_2 value of 220 ppmv] suggests that small ice caps may form on Mauna Kea ca. 60,000 and 100,000 yr in the future, after which continuing subsidence will bring the summit below the glacial-age snowline.

marine isotope curve for the past 300k years is placed between these two lines. This curve typically serves as a proxy for global ice volume. Here it is used as a proxy for snowline variations, under the assumption that the timing and relative amplitude of the isotope peaks approximate the fluctuations in ELA at Hawaii.

The thick black line is the change in Mauna Kea's summit altitude over time. It first intersects and rises above the snow line during MIS6, cresting at 130k years ago. During this period of time, while the summit is above the snowline, glaciation would have occurred. The timing for this long glaciation period matches the age of, and thus is inferred to correspond to, the Pohakuloa deposit. Glacial periods during MIS2 and 4 also match up with the Waihu and Makanaka deposits.

It appears likely that an ice cap also existed during MIS3, at least intermittently. There is some evidence of this from dating of ice-contacting lava flows near the summit from that time. Several of these Laupahoehoe flows lying inside the Makanaka moraine belt have features indicating that they were erupted through glacier ice and experienced rapid cooling as a result of contact with the ice or meltwater. Observed features that support this are abnormally high and steep margins, pillow structures, palagonite, spiracles, and glassy flow surfaces (Porter 1987).

Figure 10 also suggests that Mauna Kea will experience two future glacial periods, 60k and 100k years from now, after which the summit will be fully below the glacial equilibrium-line altitude.

The Planetary Connection – Tropical Glaciers on Mars

Mars has an icy and very active planetary surface, as well as evidence of ice in its past. Fan-shaped deposits that are glacial in origin have been found in the tropics of Mars on Tharsis Montes volcanoes (Figure 1 below), and in the eastern Hellas area. GCMs show that during periods of high obliquity, atmospheric conditions favor the mobilization and redeposition of polar ice at tropical latitudes, between two equilibrium line elevations that bound the ice on the NW flanks of Tharsis Montes, rather than on the summit as seen on Earth. Predicted accumulation rates, combined with various obliquity-history models, suggests that obliquities $>45^\circ$ and multiple 120 kyr cycles were required to form the observed deposits (Fastook 2008). It took multiple stages of glacial advance and retreat (the 120 kyr cycles) before the formations would have reached their full extent, indicating Mars must have remained at high obliquity for millions of years during the Late Amazonian period. The ages of the glacial deposits can be constrained by characterizing the moraines left between during multiple retreats, and determining the size-frequency distribution of craters around versus underneath where the crater would have been (Kadish 2013). In general, study of these glacial deposits can provide valuable insight into the orbital and atmospheric history of Mars.

Mars has evidence of glaciers, as well as extensive lava flows, over much of the planet. As often happens in Hawaii, it is likely that volcanic and glacial processes interacted on the surface at some point. There is evidence of this in spectroscopy of martian dust. Palagonite (from Wikipedia) is a material produced by the interaction of water with volcanic glass that has a composition similar to basalt. It can result from the interaction between water and basalt melt, where the water flashes to steam and reacts with the lava to form a tuff. Mauna Kea's palagonite is the best terrestrial match in spectral properties to martian dust, and it believed to be similar in composition and

origin. This signature of palagonitic alteration is used as evidence for the existence of liquid water on Mars during its history (Nick Zenter's 2-minute Geology videos).

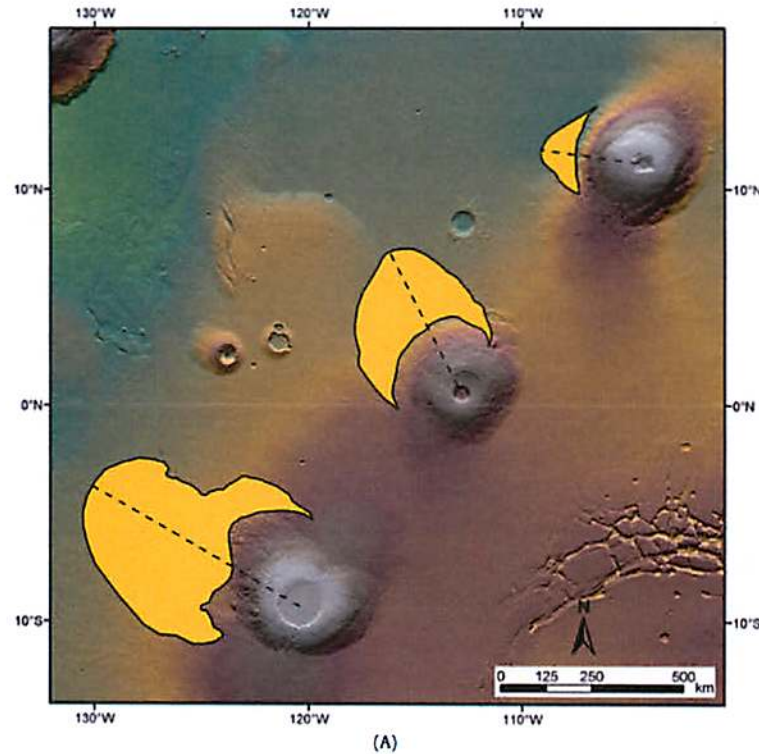


Fig. 1. (A) Fan-shaped deposits (yellow) on the northwest flanks of the Tharsis Montes interpreted to represent tropical ice-age glaciation (Head and Marchant, 2003) (top, Ascræus Mons; middle, Pavonis Mons; and bottom, Arsia Mons). Dashed lines show azimuth of trends. Background is MOLA altimetry map with brown being high (the summit of Tharsis, lower right, at about 9 km above mean planetary radius) and green low (the flank of Tharsis at ~ 0 –1 km elevation). The summits of the Tharsis Montes (white) extend up to ~ 18 km above mean planetary radius. (B) Geological sketch map of the western Arsia Mons fan-shaped deposit (modified from Zimbelman and Edgett, 1992) superposed on a MOLA topographic gradient map. The fan-shaped deposits include ridged (R), knobby (K) and smooth (S) facies. Other adjacent deposits are shield (SA), degraded western flank (SB), smooth lower western flank (SC), caldera floor (CF), caldera wall (CW), flank vent volcanic fans from Arsia Mons (PF) and undivided Tharsis volcanic plains (P). Images show Viking Orbiter images of the facies of the fan-shaped deposit (top) and USGS aerial photographs of interpreted terrestrial analogs in the Antarctic Dry Valleys (ADV) (bottom). Top left is ridged facies, top middle is knobby facies, and top right is smooth facies. Bottom left is drop moraines in the ADV (TMA 3079/303), bottom middle is sublimation tills in the ADV (TMA 3078006) and bottom right is a rock glacier in the ADV (TMA 3080/275). Modified from Head and Marchant (2003).

References:

Fastook et al., 2008. *Icarus*, 198: 305-317
 Head et al., 2003. *Nature*, 426:797-802
 Ludwig et al., 1991. *Geology*, 19: 171-174
 Moore and Clague, 1992. *GSA Bulletin*, 104: 1471-1484
 Porter, 1979a. *GSA Bulletin*, 90: 980-1093
 Porter, 1979b. *Quaternary Research*, 12: 161-187
 Porter, 1987. *USGS Professional Paper* 1350: 587-598
 Porter, 2005. *Quaternary International*, 138-129: 118-128
 Wolfe et al., 1997. *USGS Professional Paper* 1557: 129
 Wikipedia, Nick Zenter's 2-minute Geology videos

Atmospheric Studies: Trade winds, CO₂ & Climate

Cecilia Leung



Hadley Circulation, Trade Winds & the ITCZ

Earth's climate is the result of the uneven distribution of thermal energy received at the surface, resulting in net transfer of heat between the equator and the poles. The tropics serve as a source of surplus radiation that drives the transport of heat and momentum by the Hadley Cells. Warm air over the equator rises, proceeds north and south toward the poles where it begins to cool, sink at ~20° to 30° N and S latitude, and flows along the surface of the earth back toward the equator.

As winds converge near the equator, the Coriolis force deflects air parcels westwards creating the prevailing pattern of easterly surface winds in the tropics. Trade winds are predominantly northeasterly in the N. Hemisphere and southeasterly in the S. Hemisphere, blow steadily at ~5-6 m/s (~11-13 mph), but are strengthened during the winter and when the Arctic oscillation is in the warm phase to 13 m/s (30 mph) or more.

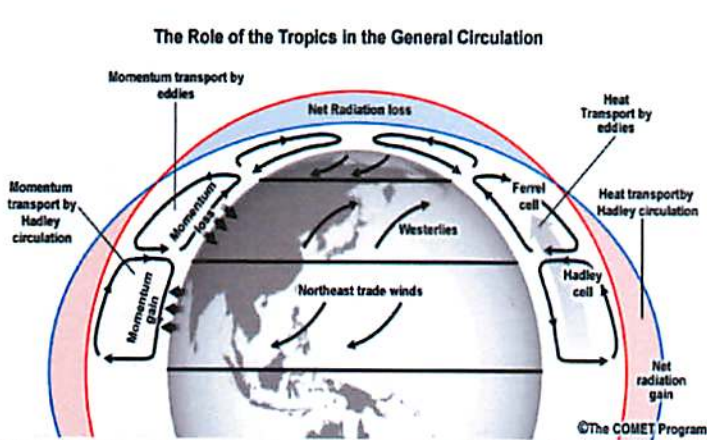


Fig 1. Net Energy Balance. Blue contour represents incoming solar radiation, and red contour indicate outgoing IR radiation emitted by the earth.

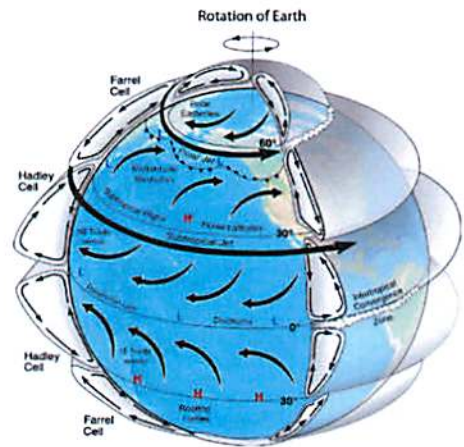


Fig 2. General Atmospheric Circulation

The region where the northeast and the southeast trade winds meet forms the Intertropical Convergence Zone (ITCZ). The ITCZ is positioned north or south of the equator depending on the season, leading to convective storms that produce some of the world's heaviest precipitation regions.

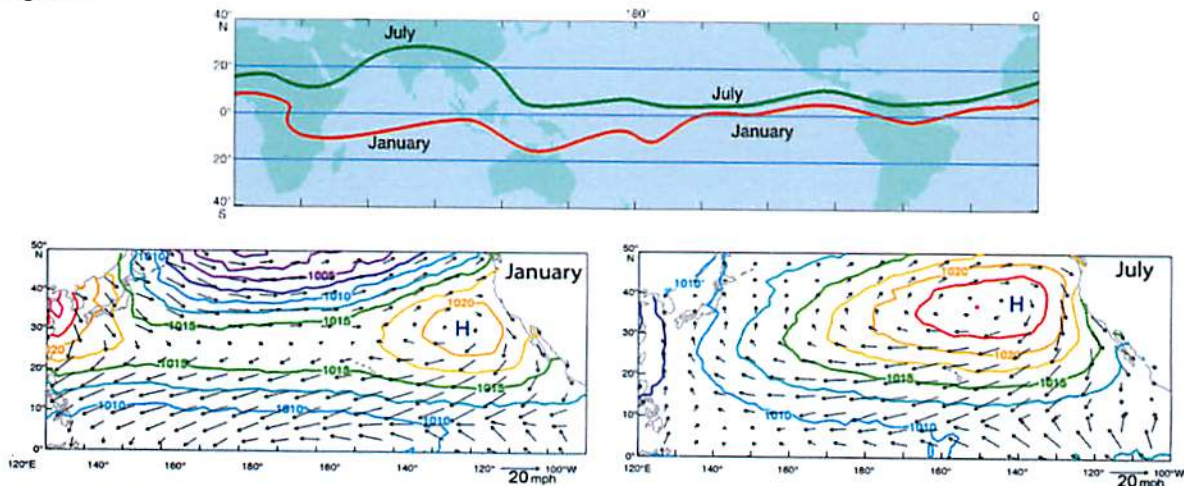


Fig 3. [top] Tropical convergence zones in January and July, regions where winds collide to produce clouds and rain. [bottom] Subtropical high pressure zone in January and July.

Weather in Hawaii

Tropical trade winds dictate much of Hawaii's weather. These winds blow steadily from the northeast, forcing humid air up the NE-facing mountain slopes. As the air rises, it cools and the humidity in it begins condensing into clouds and rain. By the time the air flows over the mountains, much of its humidity is gone, which makes places located on the SW (or leeward) side of the mountains sunny and dry.

Kona storms are a type of seasonal cyclone usually formed in the winter from winds coming from the westerly "kona" direction. Strong Kona winds can be felt when cyclones with pressures < 1,000 hectopascals pass within 820 km northwest of the Hawaiian Islands. They are mainly cold core cyclones, which categorizes them as extratropical instead of subtropical. Hawaii typically experiences 2-3 of these annually between October and April, affect the state for up to a week or more, and invoking a wide range of weather hazards such as heavy rain, hailstorms, flash floods, landslides, high winds, large surf, and heavy snows on the higher mountains.

Fig 4. Prevailing trade winds and Kona winds blow in opposite directions around the mountainous island of Hawaii.



Fig 5. Annual precipitation in Hawaii. The Kona coast is typically leeward & dry, except when the northeasterly tradewinds reverse during one of these cyclones

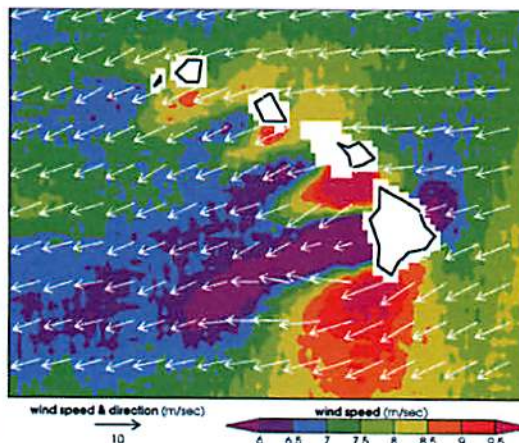
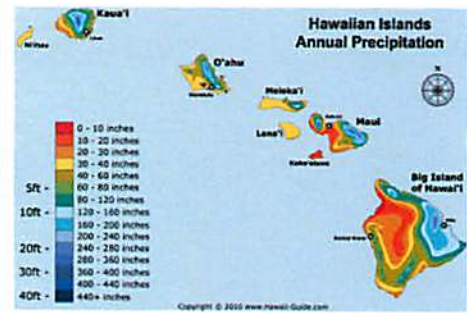


Fig 6. Taken from Space Shuttle Discovery in Sept 1988. Some volcanic aerosols can be seen blowing downstream from the Big Island, the clouds and surface water patterns in the wake of the other islands show how far downstream the island wakes persist. [Image: NASA JSC]

Fig 7. The SeaWinds sensor on the QuikSCAT satellite captured this image of the Hawaiian wake in August 1999. Trade winds blow from east to west, intensifying between the islands and weakening in the islands' wakes.

Vog (Volcanic Smog!)

Smog refers to the haze caused when air pollutants bake in the sun to form ozone, and some other substances that float in the air. Whereas Vog refers to the air pollution caused by the sulfur dioxide gas and other pollutants the Kilauea Volcano on the Big Island emits. The volcanic gases interact chemically to form a haze, which can be a health hazard and damage crops.

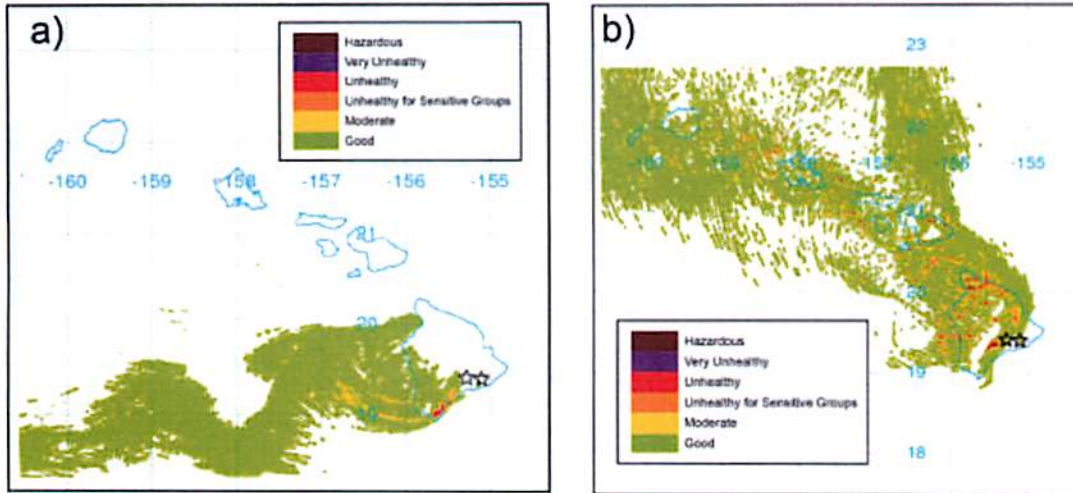


Fig 8. Distribution of vog from Kilauea Volcano under conditions of (a) prevailing trade winds, and (b) Kona winds

Zonal Winds and Mean Meridional Circulation on Mars:

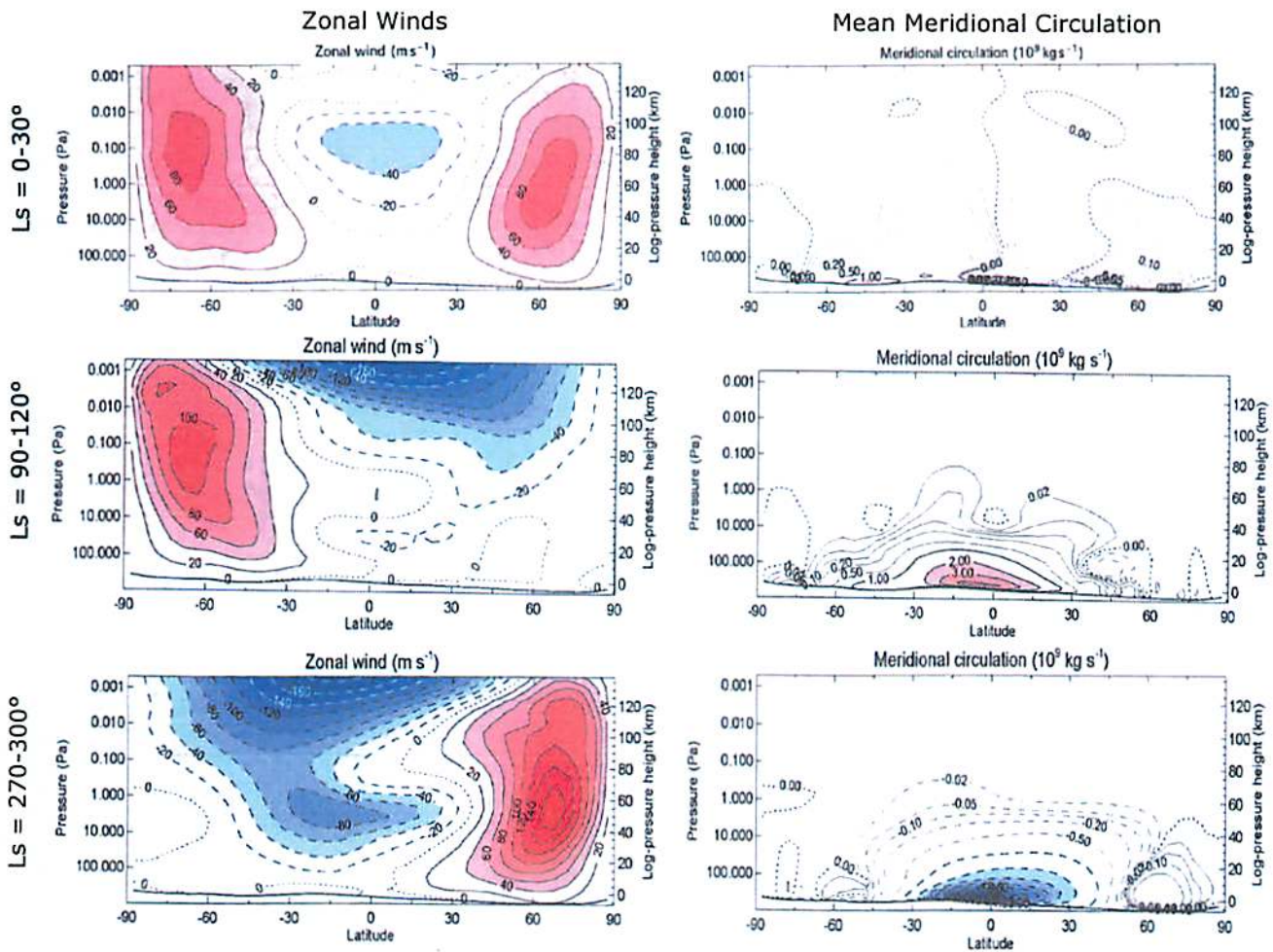


Fig 9. Mars GCM zonal wind and mean meridional circulation averaged over a 65-sol period following LS = 0-30° (N spring equinox), LS = 90-120° (N summer solstice), & LS = 270-300° (N winter solstice).

The Martian circulation near equinox is similar to the global circulation of the Earth's atmosphere. However, it becomes much more asymmetric between the hemispheres for much of the year, partly due to the lower thermal inertia of the surface compared to Earth in the absence of oceans.

Ls = 0-30° (N spring equinox):

- Temperatures are highest near the surface and close to the equator.
- Pattern of westerly jets (eastward wind) in the mid-latitudes of both hemispheres.
- The meridional circulation shows a pattern of rising motion near the equator with a large Hadley cell in each hemisphere. Some evidence of smaller, counter-rotating Ferrell cells at higher lat.

Ls = 90-120° (N summer solstice):

- Warmest at high northern latitudes, but strong horizontal temperature gradient from equator to winter pole in the southern hemisphere.
- Single strong westerly jet in winter hemisphere, & weaker easterly flow in summer hemisphere.
- Single Hadley cell spanning > 90° lat. Rising branch in the north, sinking branch in the south.

Ls = 270-300° (N winter solstice):

- Season with the most extreme contrast between summer and winter hemispheres, due planet near perihelion at Ls = 251°.
- Horizontal temp gradient, winter westerly jet, winter polar warming all amplified.

CO₂ & Climate

Operated by the US National Oceanic and Atmospheric Administration, Mauna Loa Observatory has the longest continuous history of monitoring CO₂ concentrations, and is regarded as the baseline standard for atmospheric carbon. At 11,335 feet (3,397 m) above sea level, Mauna Loa sits above low-level, local pollution and temperature inversion layers. Its location in the mid-Pacific also isolates it from major sources of pollution.

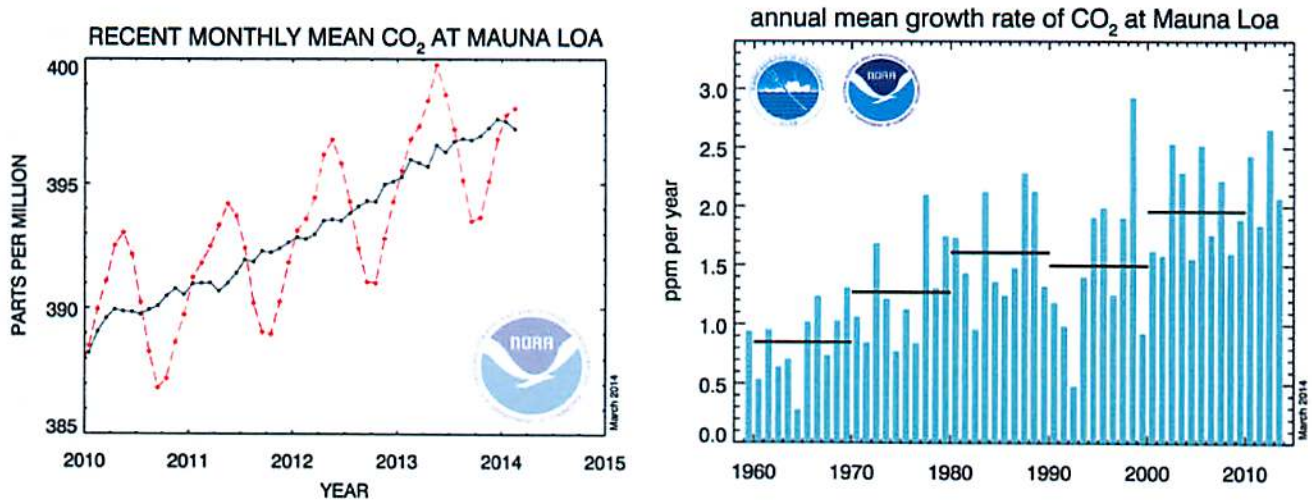


Fig 10. [Left] Monthly mean CO₂ concentration for the previous 4 years. Dashed red line represents the monthly mean values, centered on the middle of each month. The black line includes correction for the average seasonal cycle. Data are reported as a dry air mole fraction. [Right] Annual increase in CO₂ concentration at Mauna Loa. Decadal averages are plotted as horizontal lines.

How Fast will Atmospheric CO₂ Rise?

The IPCC addressed this question by examining a number of different anthropogenic emissions scenarios. Scenario A1F1 assumes high global economic growth and continued heavy reliance on fossil fuels for the remainder of the century. Scenario B1 assumes a major move away from fossil fuels toward alternative and renewable energy as the century progresses. Scenario A2 is a middling scenario, with less even economic growth and some adoption of alternative and renewable energy sources as the century unfolds. The projected atmospheric CO₂ levels for these scenarios are shown below.

Atmospheric CO₂ Concentration: Mauna Loa Observatory
1958 to Present

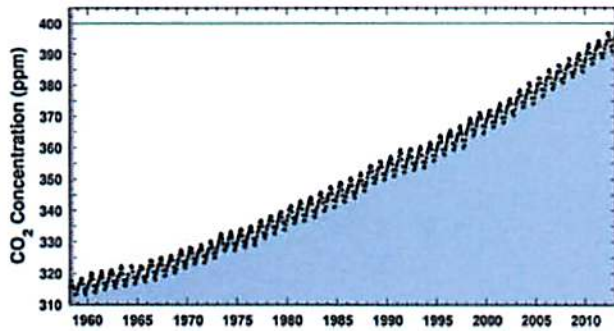


Fig 11. Historic Atmospheric CO₂ concentration from 1958 to present

CO₂ Emissions - models & observations

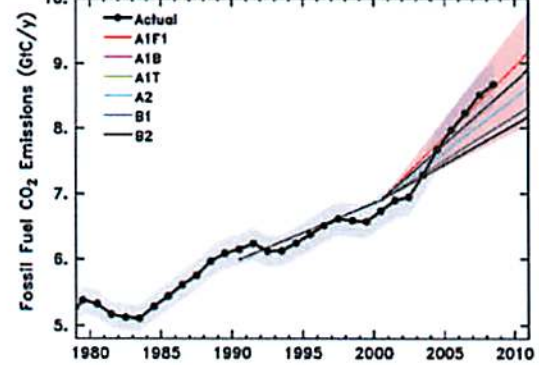


Fig 12. comparison of actual CO₂ emissions vs. previous model projections.

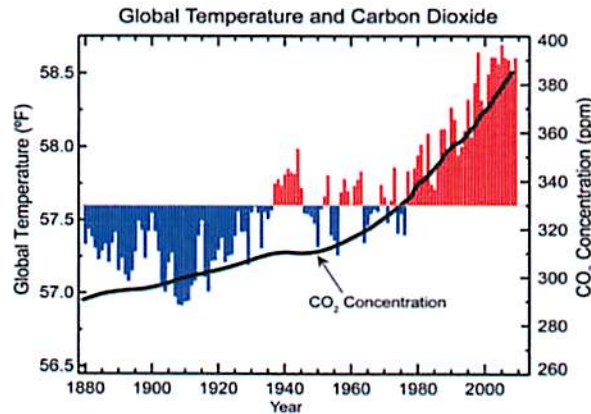


Fig 13. Increase of CO₂ and the observed global average temperature from 1990 through 2009. [NASA]

Projected CO₂ levels for IPCC emission scenarios

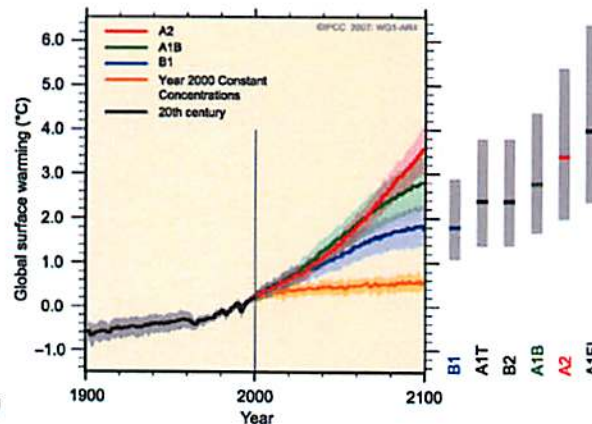
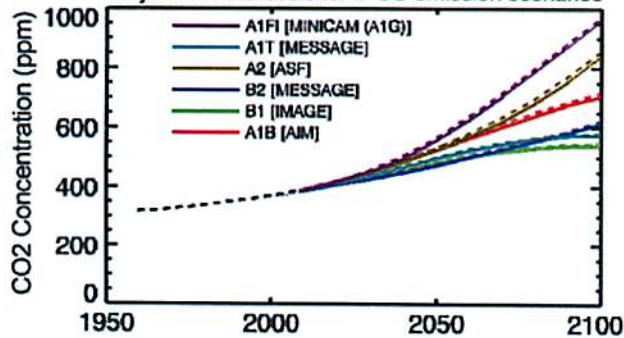
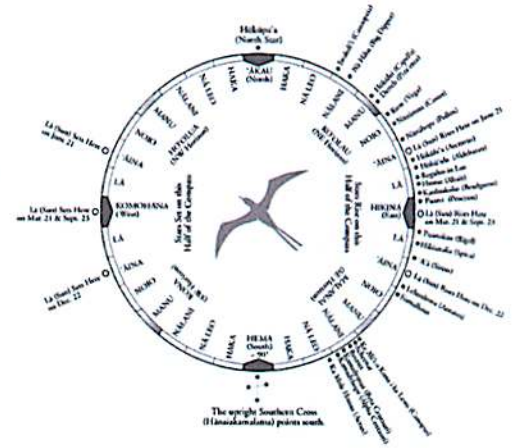


Fig 14. [Left] Historic CO₂ concentrations from 1958 to 2008 (black dashed line) and projected concentrations under the 6 IPCC emission scenarios. [Right] Historic and projected global surface temperature increase.

Adopting the 'business as usual' approach without major steps to move away from fossil fuels and limit greenhouse gas emissions, we will likely reach 850 to 950 ppm of atmospheric CO₂ by the year 2100. It will have taken ~200 years (from 1850 to 2050) for the first doubling of atmospheric CO₂ from 280 to 560 ppm, and only 70 years or so more to double the levels again to 1120 ppm. Under Scenarios A2 and A1F1, the IPCC report projects that the global temperature in 2095 will be 2.0–6.4°C above 1990 levels, with a best estimate of 3.4 and 4.0°C rise in average surface temperatures.

Fun Hawaiian Facts

The 4 quadrants on the star compass developed by native Hawaiian navigator Nainoa Thompson are named after winds. *Ko'olau* for the northeast, *Malanai* for the southeast, *Kona* for the southwest, and *Ho'olua* for the northwest.

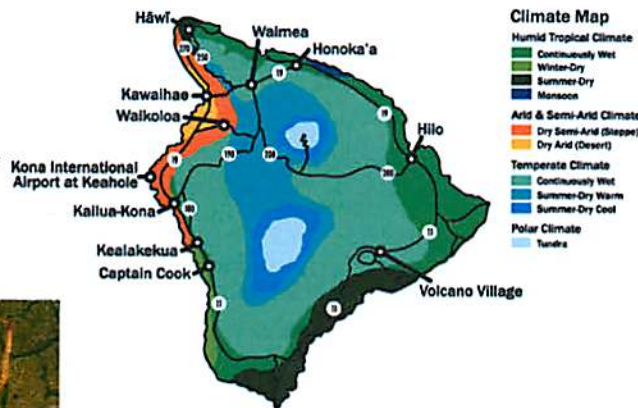


Hawaiian Name	Meteorology Phenomenon
ao pua'a	Cumulus clouds of various sizes piled together. Famous on Kona coast. Sign of good weather and no impending storms.
ao pehupehu	Continually growing cumulus. Typical of summer. Drifting with the tradewinds, these clouds pick up moisture and darken at their base, finally releasing their rain on the windward mountain cliffs.
ho'omalumalu	Sheltering cloud
ho'oweliweli	Threatening cloud
ānuenuē	Rainbow, a favorable omen
ua loa	Extended rainstorm
ua poko	Short rain spell
Kūkalahale	Name of a rain and wind famous at Honolulu.
kili hau	Ice-cold shower, or cold drizzle.
Makani	General term for wind. A leeward wind is a Kona wind.
Kaiāulu	Name of a gentle trade-wind breeze famous in song at Wai'anae, O'ahu.
'ōlauniu	Name of a wind on Hawai'i. A figurative translation means promiscuous, and a literal translation means coconut-leaf piercing.

The term *trade winds* originally derived from the early 14th century Middle English word for 'trade', which means 'path' or 'track'. But the Hawaiian system of naming winds is location-based, resulting in many regional variations including include "A'e Loa", "Mo'e", "Mo'e Ku", "Mo'e Pehu", and "Na'e".

In fact, Hawaiians have very descriptive names for sky conditions, illustrating their deep connection to physical surroundings and natural processes

Hawai'i Big Island has one of the world's most diverse microenvironments. In just one day, you can travel through 4 out of the world's 5 major climate zones, & 10 out of 13 sub-zones.



The Waialeale River is one of five navigable river in Hawaii. It drains off Waialeale Mountain, which averages 488 inches of rain per year and is considered the wettest spot on earth.



Hawaii is home to the *Theridion gallator*, aka the "happy face spider", whose abdomen bears a one-of-a-kind pattern resembling a smiling face.

References:

- Chinn, P. University of Hawaii at Manoa. Hadley Cell and the Trade Winds of Hawaii: Na Makani Mau. Nov 19, 2012.
- Climate Change 2013: IPCC Synthesis Report. <http://www.climatechange2013.org/>
- Keeling, C.D. et al. (1976) Atmospheric carbon dioxide variations at Mauna Loa Observatory, Hawaii, *Tellus*, vol. 28, 538-551
- Laing, Ariene. Intro to Tropical Meteorology 2nd Edition - http://www.goes-r.gov/users/comet/tropical/textbook_2nd_edition/
- Read, Peter L. and Lewis, Stephen R. 'The Martian Climate Revisted' Praxis Publishing Ltd. 2004.
- Thoning, K.W. et al.(1989), Atmospheric carbon dioxide at Mauna Loa Observatory 2. *J. Geophys. Research*, vol. 94, 8549-8565
- Trends in Atmospheric Carbon Dioxide - <http://www.esrl.noaa.gov/gmd/ccgg/trends/>
- Volcanic Air Pollution – Hazard in Hawaii <http://pubs.usgs.gov/fs/169-97/>

Weathering Environments

1.0 What is weathering?

Weathering is the alteration of rocks and minerals at or near the surface of a planetary body as a result of environmental conditions. Weathering is driven by chemical, mechanical, and (on Earth) biological processes. These processes are intricately related to one another and occur on geologically relevant timescales. It is often difficult to separate the effects from chemical and mechanical weathering as they frequently occur simultaneously and can result in similar weathering products. Weathering environments and weathering products are best studied and most well understood on the surface of Earth. This discussion will focus on chemical and mechanical weathering processes, with applications to specific Hawaiian environments.



2.0 Mechanical Weathering

Mechanical (physical) weathering is the destruction and disintegration of rock or minerals without any chemical alteration of their components. Chemical weathering does, however, play a role in reducing the overall strength of the rock, making it more prone to experiencing destructive mechanical processes. Mechanical weathering is often expressed through the development of cracks/joints in rocks at Earth's surface, both at macroscopic and microscopic scales. These cracks and joints facilitate abrasion of the rock surface and encourage weathering and breakdown of material. There are several constituent processes that contribute to mechanical weathering:

2.1 Frost Shattering

Frost shattering is frequently attributed to the unique properties of water around its freezing point. When water freezes, it undergoes a volumetric expansion of 9%. Conventional theory suggests that if this water is trapped in rock or soil pore space, or is in joints or fractures within the rock, the ice will create a localized pressure exceeding that of the tensile strength of most rock types (typically 10s of MPa) and cause mechanical breakdown. This would attribute special significance to water in mechanical weathering processes, but this is not actually the case. It has been shown experimentally that small amounts of water (thin films) can be cooled far below 0°C before freezing (due to surface contact energies). If, next to this thin film of water coating mineral grains in the rock, there is a larger fracture or joint system, which hosts a larger volume of water, freezing action will occur in this region first. The chemical potential of this larger ice mass is lower than the film, so water flows towards the frozen mass, and freezes there increasing the overall size of the ice crystal, widening the crack, and driving weathering forward (Figure 1).

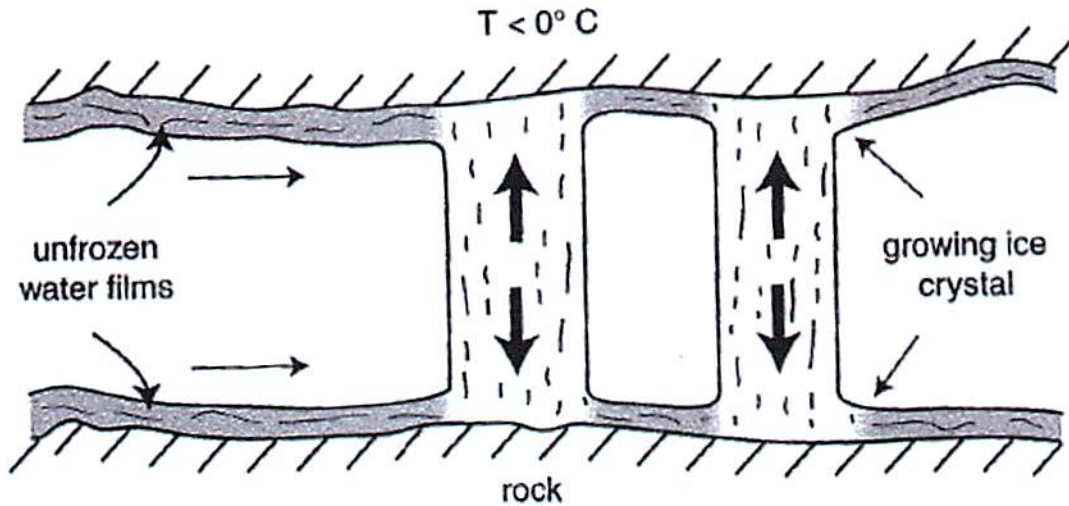


Figure 1: Schematic representation of frost shattering (Melosh 2011).

2.2 Salt Weathering

Salt weathering can cause rock breakdown in two ways: 1) through the expansion and contraction of salts due to heating or hydration, and 2) through their crystallization pressures. Salts crystallize from solution when their mineral constituents are supersaturated in the solution within the pore space of a rock. The maximum pressure exerted by a growing crystal is given by:

$$P_{\text{xtal}} = \frac{R\rho T}{m} \ln \frac{C}{C_s}$$

where P_{xtal} is the Pressure, R is the ideal gas constant, ρ is the density of the crystalline species, T is the temperature, m is its molecular weight, C_s is the concentration of the species at saturation, and C is the actual concentration of the species.

This pressure (up to many tens of MPa), similar to that described in section 2.1, can cause mechanical breakdown as long as the work done to accommodate the change in volume it requires does not exceed the chemical potential for the process.

2.3 Wetting and Drying

The adsorption of water in fine-grained sediments or in fine-scale cracks in a rock or mineral can cause swelling pressure and expansion, generating strain. The subsequent drying cycle may allow the desorption of this water and cause contraction. This cycle acts to extend microcracks in the rock.

2.4 Insolation Weathering

Temperature change can cause mechanical breakdown. Heating of a rock surface may cause expansion, and subsequent cooling may cause contraction. When the stresses due to these cycles of expansion and contraction exceed the rock's elastic limit, breakage may occur (and often begin at lower stresses than these).

2.5 Pressure Release

Rock that is buried under the Earth's surface experiences very high compressive stresses. If the overlying rock is eroded, or this deep rock layer is exhumed, this source of pressure decreases. Traditionally, it was thought that the rock unit will have the tendency to expand in the direction of stress reduction. If this expansion exceeds the tensile strength of the rock, it may cause cracking and fracturing. This mechanical weathering method may also apply to rocks previously covered by glaciers. Topography can effect the formation of weathering features, including sheeting joints. These fractures are thought to form if the compressive or tensile stresses parallel to the surface (which may exhibit curvature) exceed the product of the unit weight of the material and the cosine of its slope.

2.6 Stress Corrosion Cracking

If chemically reactive fluids concentrate at the tip of a crack, they can weaken the bonds at this localized region of stress and promote propagation of the crack and subsequently, mechanical weathering.

2.7 Spheroidal Weathering

Weathering solutions concentrate along joints and cracks and work to round-off the corners of large blocks of rocks gradually creating roughly spherical blocks.



Figure 2: Spheroidal and spallation weathering on a small boulder.

3.0 Chemical Weathering

This type of weathering causes chemical changes in minerals within rocks in these environments. These chemical reactions are spontaneous if the Gibbs free energy value becomes more negative as the reaction proceeds. There are several constituent chemical weathering processes:

3.1 Solution

This process involves the dissolution of ionic crystals in a fluid (e.g., halite in water). Dissolution can remove specific mineral components from the rock, driving forward weathering.



Figure 3: Weathering pits on a rock outcrop.

3.2 Hydration

Hydration is the association of minerals with water molecules in a stoichiometric way (e.g., anhydrite \rightarrow gypsum). This reaction can be reversed at high temperatures.

3.3 Hydrolysis

Hydrolysis occurs when a water molecule dissociates and the OH^- component bonds with a mineral species to form a separate species (e.g., hematite \rightarrow goethite, olivine \rightarrow serpentine).

3.4 Oxidation

Weathering through oxidation is the combination of oxygen with a mineral to create a new species, often changing the oxidation state of component elements in the process (e.g., wustite \rightarrow hematite, changing Fe^{2+} to Fe^{3+}).

4.0 Weathering Environments in Hawaii

Several different weathering processes, including both mechanical and chemical, have been reported in Hawaii. Weathering in the humid area of Hawaii typically occurs through chemical processes including hydration and oxidation and the removal of cations from specific mineral phases. These chemically weathered species are frequently transported throughout the island through groundwater. In dry regions of Hawaii, mechanical spallation, formation of rock coatings, and biological weathering processes play a more significant role. Some generalized weathering flow charts can be seen as figures in the Appendix.

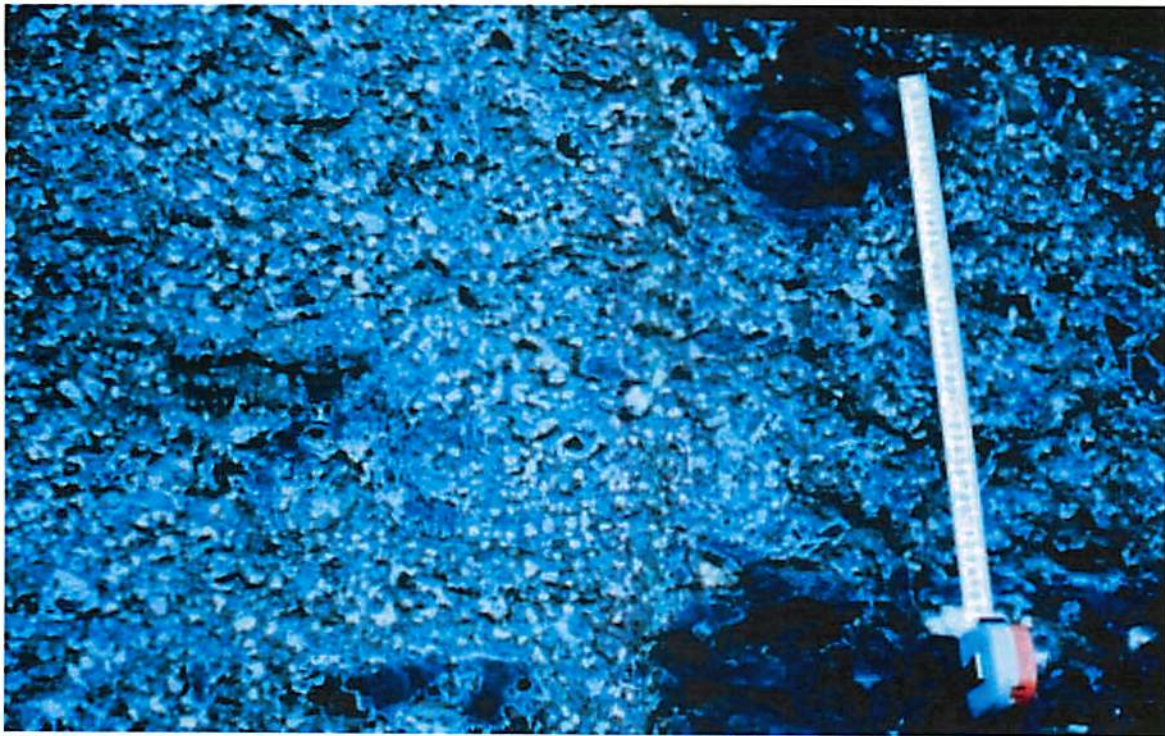


Figure 2: Palagonite (volcanic glass altered by water) near Kilauea in Hawaii.

Many localized weathering environments have been identified in Hawaii. Below are brief descriptions of the reactions and observations associated with these weathering types.

- 1) Weathering of Olivine Basalts: Boulders of olivine basalts weathered to produce a Mg-rich clay mineral. This weathering may have been driven by heavy rainfall leaching cations from the basalt. These boulders also exhibited exfoliated textures.
- 2) Weathering Rinds on Basaltic Lava Flows: Specific mineral phases are shown to weather first, depending on the local biogeochemical environment. Plagioclase and clinopyroxene precede olivine weathering unless there is significant secretion of organic acids by lichens on the basaltic flow.

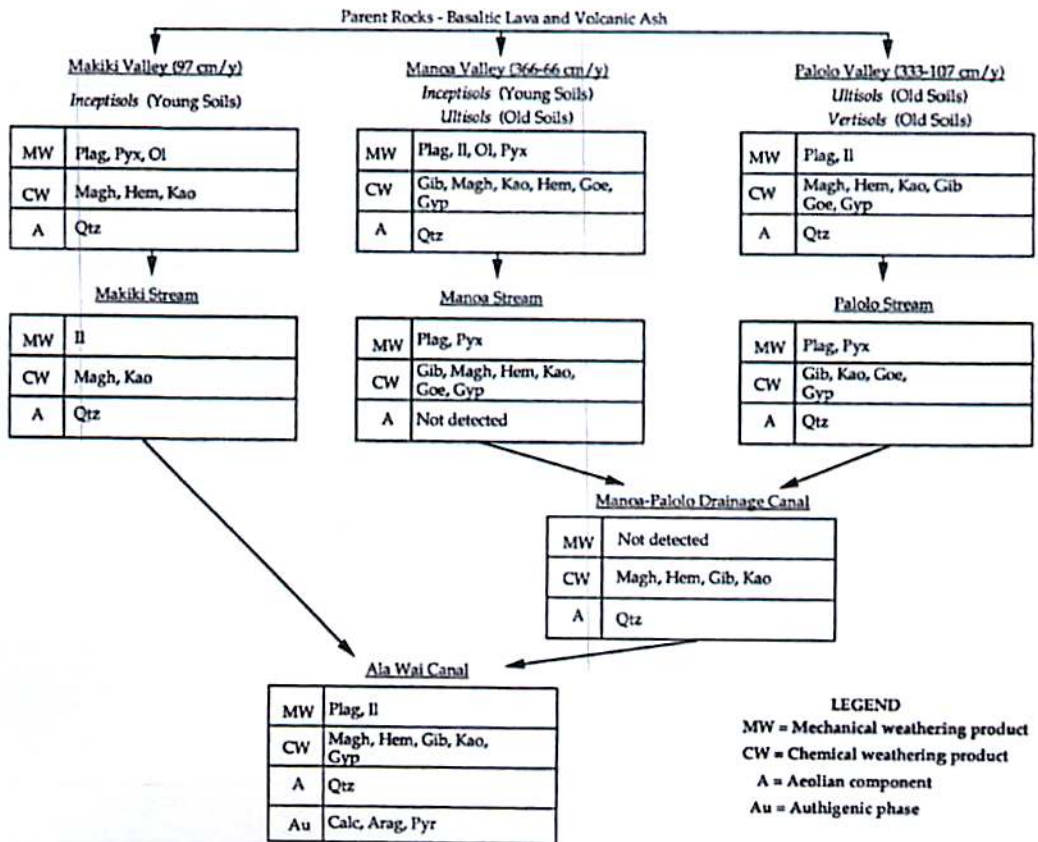
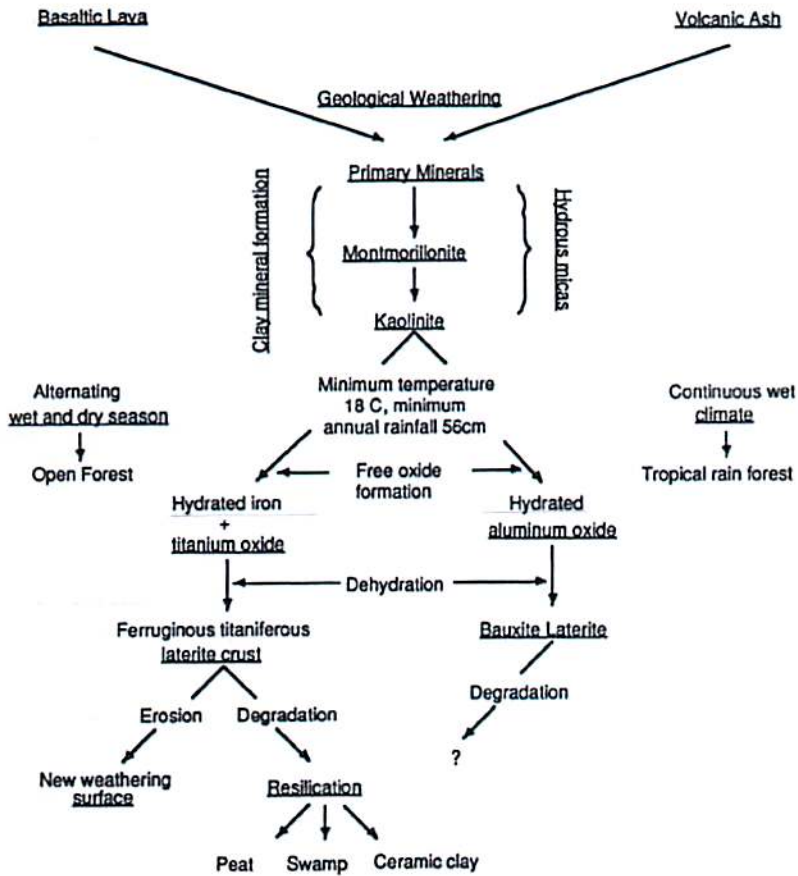
- 3) Plant-induced weathering: Vascular plants (those with root systems) cause orders of magnitude more localized weathering in lava flows (both recent and several thousand years old) than is observed in unvegetated flows. These weathering processes occur at significant depths within the lava flow. This weathering is caused by the dissolution of plagioclase as a result of organic acids produced by this vegetation. Propagating root systems also cause mechanical breakdown of lava flows.
- 4) Rock Coatings in Hawaii: Basaltic lavas in semi-arid regions of Hawaii develop hydrous silica coatings on their surfaces. These coatings are likely derived from probable leaching of basaltic dust.

The Hawaiian islands represent a series of complex weathering environments that produce a multitude of geological features and products.

5.0 References

- Bland, W., and Rolls, D. 1998. *Weathering: An Introduction to Scientific Principles*. Oxford University Press.
- Cochran, M. F., and Berner, R. A. 1996. Promotion of chemical weathering by higher plants: field observations on Hawaiian basalts. *Chemical Geology* (132) p. 71-77.
- Fan, P-W., Ng, R., and Remular, D. 1995. Mineral Assemblages of the sediments of the Ala Wai Canal and its drainage basins O'ahu, Hawaii. *Pacific Science* (49) p. 400-411.
- Farr, T., and Adams, J.B. 1984. Rock Coatings in Hawaii. *Geological Society of America Bulletin* (95): p. 1077-1083.
- Martel, S. J. 2011. Mechanics of curved surfaces, with application to surface-parallel cracks. *Geophysical Research Letters* (38): L20303.
- Melosh, H. J. 2011. *Planetary Surface Processes*. Cambridge Planetary Science.
- Schopka, H. H., and Derry, L. A. 2012. Chemical weathering fluxes from volcanic islands and the importance of groundwater; The Hawaiian example. *Earth and Planetary Science Letters* (339-340): p. 67-78.
- Sherman, G.D. 1952. The genesis and morphology of alumina-rich laterite clays. *American Institute of Mining Metallurgical Engineers*.
- Sherman, G. D., and Uehara G. 1956. The Weathering of Olivine Basalt in Hawaii and its Pedogenic Significance. *Soil Science Society of America*. (20): pg. 337-340.
- Wasklewicz, T. A. 1994. Importance of Environment on the order of mineral weathering in olivine basalts, Hawaii. *Earth Surface Processes and Landforms* (19): p. 715-734.

Appendix



LEGEND
 MW = Mechanical weathering product
 CW = Chemical weathering product
 A = Aeolian component
 Au = Authigenic phase

Phreatomagmatic Eruptions PTYS 594A

Thaddeus D. Komacek



1 What are phreatomagmatic eruptions?

Phreatomagmatic eruptions, an intermediary stage between purely magmatic and phreatic eruptions, occur due to interactions between magma and water. An example of a phreatomagmatic eruption is shown in Figure 1.

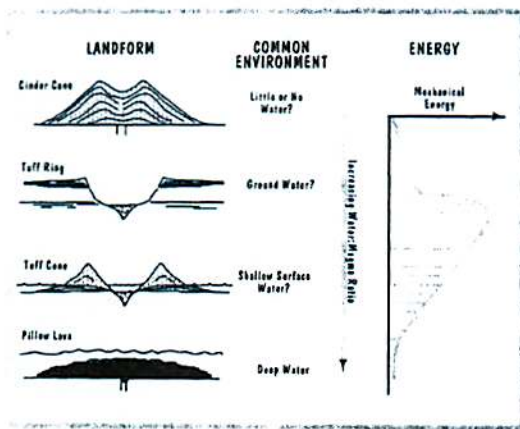


Figure 2: Water-magma ratio curve for given landforms and common environments, adopted from White (1996).



Figure 1: Phreatomagmatic eruption column from the Ukinrek Maar crater in Alaska. From <http://pubs.usgs.gov/dds/dds-40>.

- The magma composition of these eruptions varies drastically, and as a result phreatomagmatism occurs in diverse environments and affects both small and stratovolcanoes.
- Figure 2 shows a variety of landforms that can be caused by phreatomagmatic events, their common environment, and the mechanical energy of the eruption as a function of the water-magma ratio in the eruption.
- A schematic illustration of the fuel-coolant interaction that may power these eruptions is shown in Figure 3. The stages are: 1) cm-m scale mixing, 2) thermal fragmentation at micron-scale and superheating of coolant, 3) expansion due to vaporization of current causing explosion, 4) fragmentation by fluid shear.
- A diagram of a maar-diatreme eruption (forming a tuff ring) is shown in Figure 4. The stages of eruption are: a) material ejected, b) transient state, c) vent walls collapse, triggering new interaction.

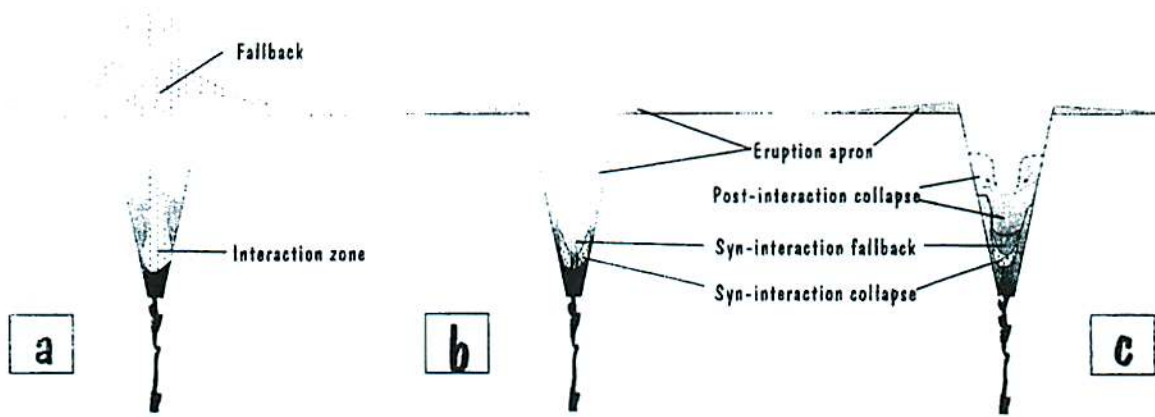


Figure 4: Illustration of a maar-diatreme phreatomagmatic eruption, adopted from White (1996).

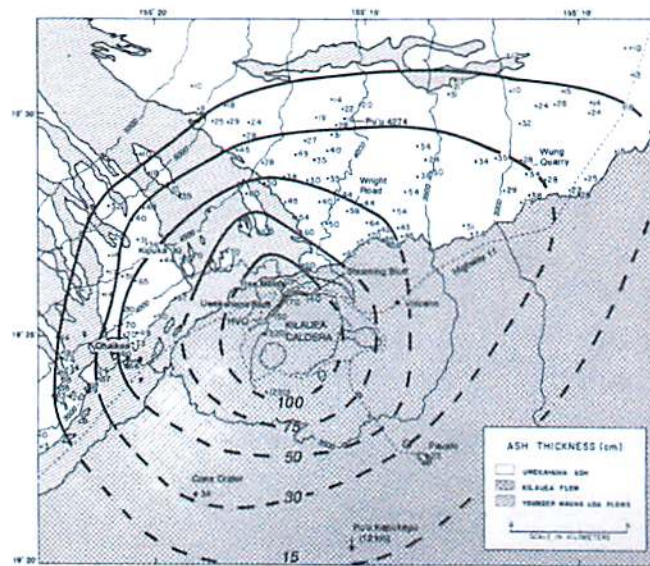


Figure 5: Ash thickness in cm for the Uwekahuna Ash Member, showing current surface exposures and inferred isopachs, adopted from Dzurisin et al. (1995).

2 Phreatomagmatic eruptions in Hawaii

There is a variety of evidence for phreatomagmatic eruptions at the Kilauea volcano. The ash deposits from eruptions $\sim 2100 - 2800$ ^{14}C years ago have been mapped by Dzurisin et al. (1995), see Figure 5. In Figure 5, the region that was covered in pyroclastic flow is inferred to be everything above the 15 cm isopach, with lithic ashfall comprising the material below the 15 cm isopach. Additionally, due to the wide dispersal of the Uwekahuna surge deposits, the authors infer that the phreatomagmatic event must have been extremely violent to produce such a low aspect ratio. Likewise, due to the widespread pumice falls, the effusive events must have also been vigorous. After alternation of effusive and eruptive phases, the Uwekahuna eruptions were followed by unusual picritic lava flows.

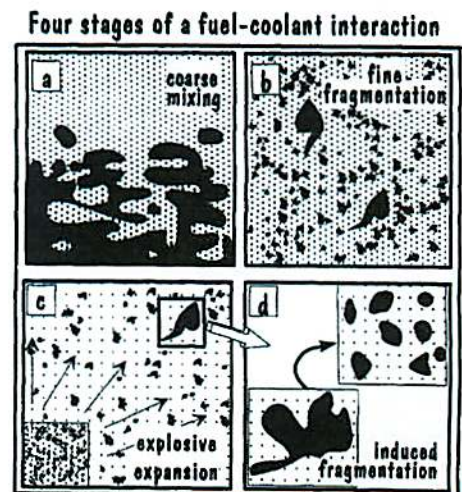


Figure 3: Schematic illustration for the four-stage fuel-coolant interaction, adopted from White (1996).

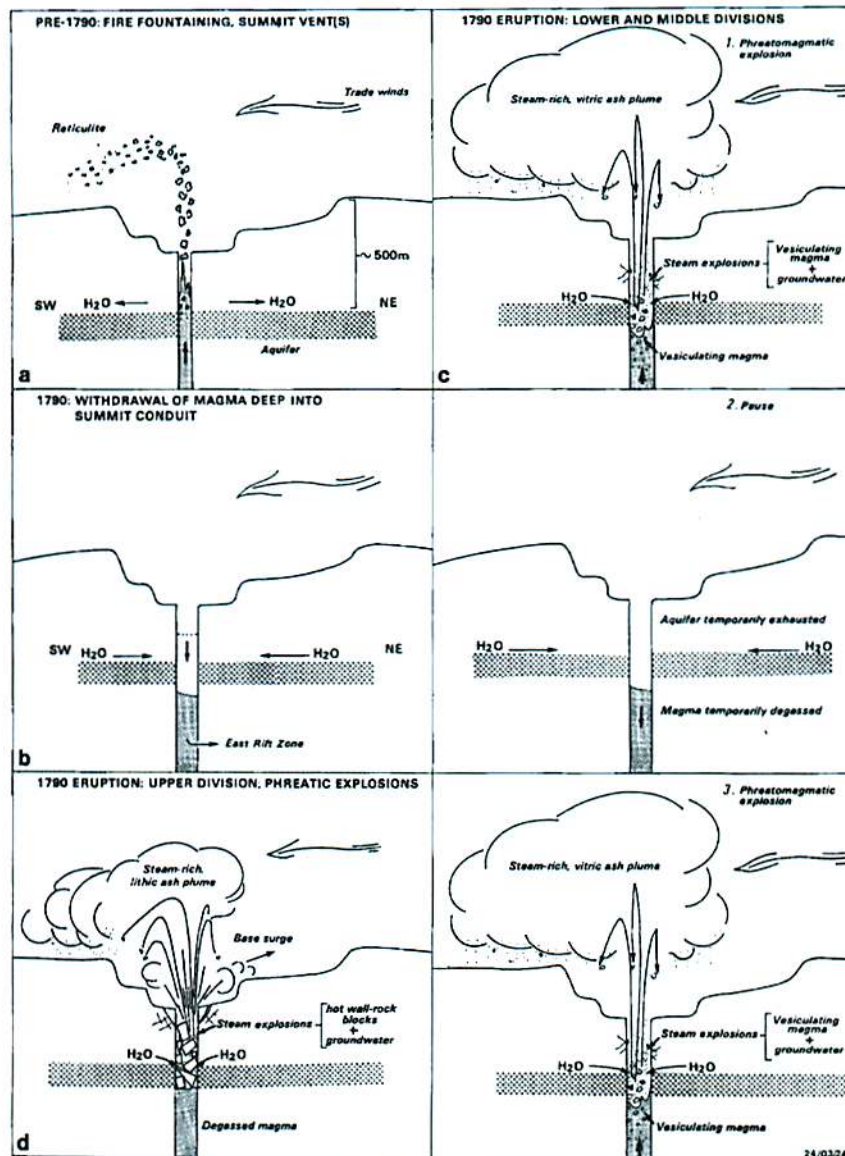


Figure 6: Cross section across Kilauea caldera before and during the 1790 Keanakakoi ash eruption , adopted from McPhie et al. (1990).

More recent surge deposits from the 1790 Keanakakoi ash eruption enabled better understanding of the role of phreatomagmatism in Hawaiian eruptive events. Figure 6 shows a cross-section of Kilauea caldera prior to and during the 1790 eruption, inferred by McPhie et al. (1990). They explain the eruption process as follows: a) Fire fountaining forms a summit vent, b) Magma from summit moved to east rift zone, groundwater infiltrates close to summit c) Phases 1 and 2 of Keanakakoi due to phreatomagmatic explosions in summit conduit, d) Phreatic explosions in Phase 3 due to interaction of groundwater with heated lithic fragments.

3 Planetary relevance

One can search for evidence of past phreatomagmatic activity by looking for similar remnants of such eruptions as expected on earth: tuff rings, tuff cones, and emplaced dikes Broz and Hauber (2013). An example of this application to Mars (the only planet besides Earth on which past phreatomagmatic ac-

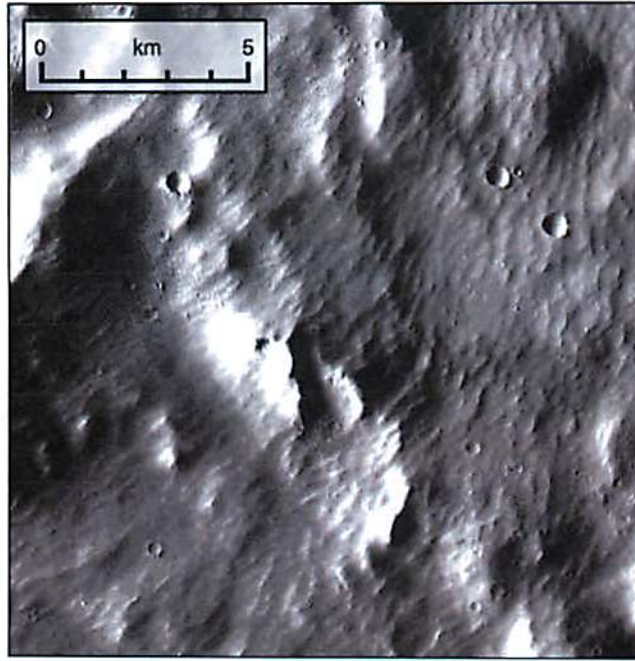


Figure 7: THEMIS image showing characteristics of ridges likely derived from phreatomagmatism, as shown in Wilson and Head (2004).

tivity has been discovered), by Wilson and Head (2004), identified Memnoia Fossae (a graben system radiating from the Tharsis plateau) as phreatomagmatically derived radial dikes. The dune-like ridges observed, shown in Figure 7, were caused by phreatomagmatic plumes that eroded and deposited material, producing the surface profile shown. Using a simple model, Wilson and Head (2004) show that phreatomagmatic activity could indeed occur under past Martian conditions and post-eruption pyroclast accumulation can explain the features observed by THEMIS. A potential issue for future study is that tuff rings are difficult to distinguish from impact craters based solely on orbital imagery, which may complicate the interpretation of tuff ring-like depositions as due to phreatomagmatism.

A more controversial application is the reinterpretation of the stratigraphy of Meridiani Planum as observed by Opportunity to be an impact-origin base surge, with similarities to terrestrial surge strata (see Figure 8) by Knauth et al. (2005). The previous explanation was that of deposition in an aqueous environment, however, invoking an iron meteorite impact with a crater diameter $\gtrsim 100$ km into a megaregolith containing ice/brine the authors can explain all the observations with a wet surge and secondary surge events. This includes the observations of the hematite spherules, which are remarkably similar to terrestrial accretionary lapilli seen in surge deposits (see Figure 9). Their hypothesis does require a relatively unique large iron meteorite impactor, but the TES signature of Meridiani is itself unique to Mars, hence the decision for Opportunity to explore the region, so the authors conclude that their explanation is certainly likely and potentially applicable to Meridiani Planum.

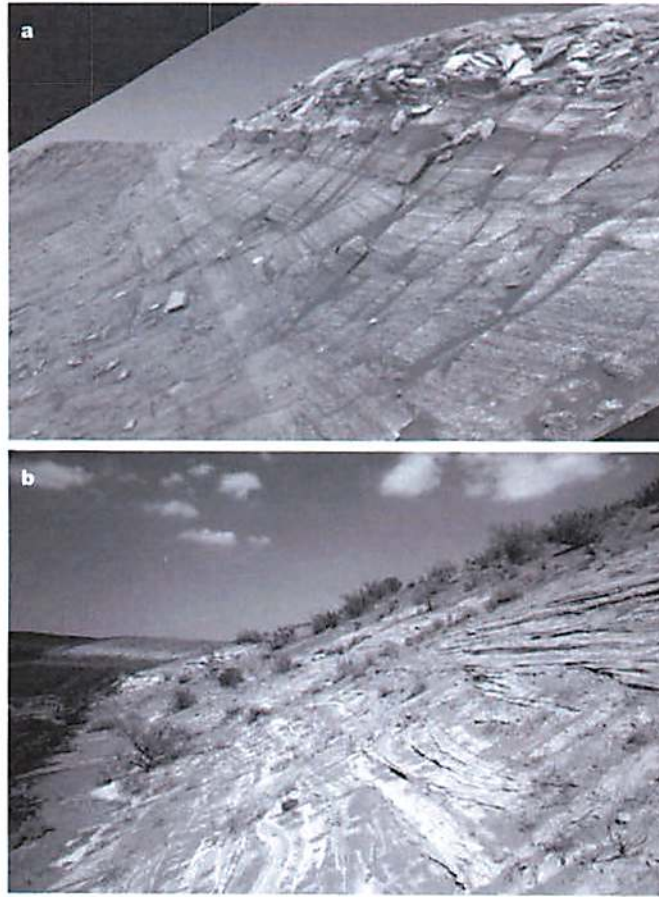


Figure 8: a) Wall of Endurance crater on Mars, b) Outcrop of surge deposit from Kilbourne hole, New Mexico. Figure from Knauth et al. (2005).

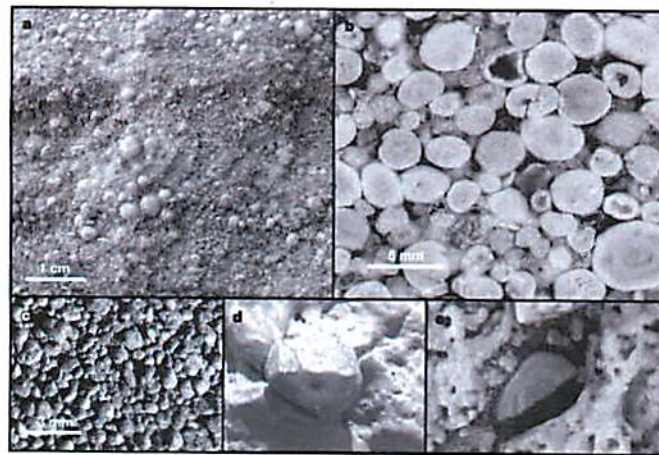


Figure 9: a) Terrestrial accretionary lapilli from Kilbourne hole, New Mexico; b) Lapilli from Onverwacht Formation, South Africa; c) Iron condensation spherules from Meteor Crater, Arizona; d) Spherule on Mars (4mm diameter), e) Broken spherule on Mars (4mm). Figure from Knauth et al. (2005).

References

- P. Broz and E. Hauber. Hydrovolcanic tuff rings and cones as indicators for phreatomagmatic explosive eruptions on Mars. *Journal of Geophysical Research*, 118:1656–1675, 2013.
- D. Dzurisin, J.P. Lockwood, T.J. Casadevall, and M. Rubin. The Uwekahuna ash member of the Puna basalt: product of violent phreatomagmatic eruptions at Kilauea volcano, Hawaii, between 2800 and 2100 carbon-14 years ago. *Journal of Volcanology and Geothermal Research*, 66:163–184, 1995.
- S. Hughes. From magma to tephra. *EOS, Transactions American Geophysical Union*, 80:196, 2011.
- L.P. Knauth, D.M. Burt, and K.H. Wohletz. Impact origin of sediments at the Opportunity landing site on Mars. *Nature*, 438:1123–1128, 2005.
- V. Lorenz. Phreatomagmatism and its relevance. *Chemical Geology*, 62:149–156, 1987.
- J. McPhie, G. P.L. Walker, and R.L. Christiansen. Phreatomagmatic and phreatic fall and surge deposits from explosions at Kilauea volcano, Hawaii, 1790 a.d.: Keanakakoi ash member. *Bulletin of Volcanology*, 52:334–354, 1990.
- H. Sigurdsson, B. Houghton, H. Rymer, J. Stix, and S. McNutt. *Encyclopedia of Volcanoes*. Academic Press, 1999.
- J. D.L. White. Impure coolants and interaction dynamics of phreatomagmatic eruptions. *Journal of Volcanology and Geothermal Research*, 74:155–170, 1996.
- L. Wilson and J.W. Head. Evidence for a massive phreatomagmatic eruption in the initial stages of formation of the Mangala Valles outflow channel, Mars. *Geophysical Research Letters*, 31:L15701, 2004.

The transport of magma from volcanoes

Xianyu Tan



Volcanic eruptions are among the most spectacular of natural phenomena. The Hawaiian lava eruption at the Puu Oo vent shown in Figure 1 is the end-product of a complex sequence of physical and chemical events. Here some preliminary concepts on transportation of magma from volcanoes are introduced.



Figure 1: A typical Hawaiian-style fire fountain eruption at the Puu Oo vent, Kilauea volcano, Hawaii.

1 Magma chambers

The tendency of magmas to accumulate at shallow depths in the crust is controlled by their densities. Melts created by pressure changes in the mantle are less dense than the rocks from which they form and so rise buoyantly, initially as a plastic flow, which is called diapirs. As diapirs move into cooler rocks at shallower depth, they respond to the less plastic and more elastic rheological properties of the surrounding rocks by transforming into elongated cracks called dykes. Dykes propagate by fracturing the rocks at their leading tips in a brittle fashion and holding the crack walls apart elastically. When melts reach the depth at which they are neutrally buoyant, commonly 2 to 10 km below the surface depending on the melt composition, they cease rising and aggregate into larger

magma bodies. These crustal storage zones are called magma chambers.

Cooling of magma in chambers

After emplacement, the magma loses heat to the surrounding rocks. As the temperature decreases below a critical value, crystals of minerals begin to form. If the temperature continues to fall below a second critical value, crystallization of magma is complete. Realistically, most magma bodies are open systems, periodically recharged by new, hot magma. Model predicts that very largest magma systems are active for $10^6 - 10^7$ years.

Convection and differentiation in magma chambers

The nature of convection (if any) is controlled by the size and shape of the chamber, the viscosity and density of the magma, and by processes operating in the boundary layer. In crystal-free magmas, the potential for convection in a layer of liquid of thickness d subjected to a temperature difference ΔT is defined by the thermal Rayleigh number, Ra :

$$Ra = (g\alpha\Delta Td^3)/(\kappa\nu), \quad (1)$$

where α , κ and ν are the coefficient of thermal expansion, the thermal diffusivity and kinematic viscosity of the melt, respectively, and g is gravity. Since the thickness of in this definition if cubed, the size of the system is the most important parameter determining whether convection occurs. In large chambers, some natural convection seems inevitable.

There is a second form of convection in magma chambers, compositional convection. The chemical composition of crystals precipitating from magma is always different from that of the melt, and progressive crystallization produces residual melts of diverse compositions. Crystallization of basaltic magma almost always results in residual melts which are enriched in Si, Al, Na and K, and depleted in Mg, Fe and Ca, relative to the parental magma, and normally have lower density than the parent. The behavior of the subsequent flows from the vertical or steeply dipping walls of chambers is different from that of melts generated at the floor of the chamber. A simple case would be compositional convection generated at sidewalls. Cooling and crystallization of magma produces a melt which becomes less dense as it evolves in composition. The buoyant compositional boundary layer rises along the wall.

The role of volatiles

Volatile species such as water can be concentrated during chemical differentiation. Eventually volatile concentrations may reach saturation levels and gas is exsolved (released from solution) to form bubbles. The sharp reduction of density and increase in positive buoyancy that gas exsolution creates is one of a family of related mechanisms for initiating an eruption.

2 Magma movement in dykes: links between magma chambers and eruptions

Once a crack is initiated, the requirement for its continued growth is that the intensity of the stress at the crack tip exceeds a property called the apparent fracture toughness. Once

initiated, there is generally no rock-mechanical reason why a dyke should not continue to propagate as long as there is any significant excess pressure in its magma source region.

Controls on dyke propagation

There may be a thermal limitation on the growth of a dyke. Heat is lost from the magma in a dyke by conduction into the surrounding rocks and thus reduces buoyancy and so growth rate. In practice, dykes in basaltic volcanoes such as illustrated in Figure 2 are about 1 m wide and can propagate for at least 10 km from their sources before cooling becomes a significant issue.

If the wall of a magma chamber fails around its mid-line (Figure 2), magma forced into a growing dyke is neutrally buoyant and has no incentive to rise or sink: the dyke grows laterally with its centre following the level of neutral buoyancy at a relatively uniform depth below the surface. Growth can continue indefinitely as long as the pressure is maintained in the chamber. In practice, the transfer of magma from the chamber into the growing dyke relaxes the internal pressure and dyke growth stops when the stress intensity at the tip becomes too small. If the roof of a magma chamber fails, bubble-rich, low-density magma may enter the resulting fracture and a dyke may propagate upward (Figure 2).

Dynamical factors become important as soon as the dyke begins to propagate. Gas bubble can expand within the dyke propagating process, and can help the propagation extend to a greater height or distance for both vertically and horizontally propagating dykes.

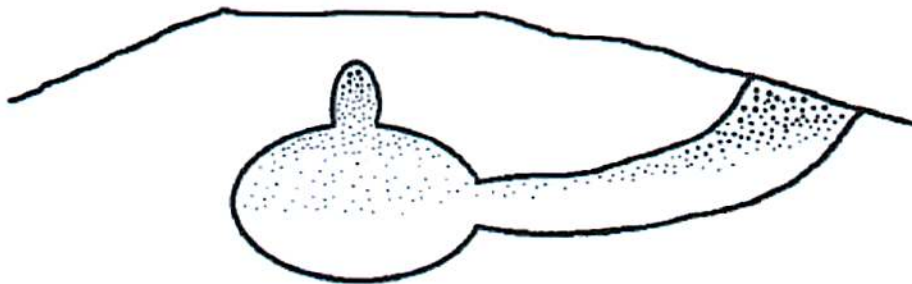


Figure 2: Sketch of a magma chamber from which dykes grow either vertically or laterally. The stippling indicates the number density and size of gas bubbles, mainly CO_2 , which have already begun to concentrate in the upper part of the chamber. The upward growth of the vertical dyke is enhanced by the nucleation and growth of additional gas bubbles as more soluble volatiles (mainly H_2O , and SO_2 or H_2S) exsolved. The lateral growth of the initially neutrally buoyant lateral dyke is converted to upward growth as gas bubbles drift up through the liquid and increase the buoyancy of the upper part.

Magmatic system beneath the summit and rift zones of Kilauea volcano

As one of the Earth's most active volcanoes, Kilauea has frequent and usually gentle eruptions that have made it the focus of a wide range of volcanological research.

The overall shape of Kilauea is dominated by a broad and very long ridge – the east rift zone – that extends eastward 130 km from the caldera to the ocean floor at a depth of more than 5 km (Figure 3). This enormous low-profile ridge was built by countless eruptions of lava that originated from many different vents along the crest of the ridge, not at the summit. Kilauea actually has two rift zones – the east rift zone and the much smaller southwest rift zone. From the caldera to the eastern tip of the island at Cape Kumukahi, the east rift zone is 55 km long, and it continues beneath the sea for another 75 km. The southwest rift zone does not form a distinct ridge like the east rift zone and is only about 35 km long. The enormous size of the east rift zone compared to the southwest rift zone is clear evidence that much more lava has erupted from the east rift zone. For example, calculation suggest that magma was supplied to Kilauea during 1956-1983 at a minimum average rate of $7.2 \times 10^6 \text{m}^3/\text{month}$. Roughly 35% of the net supply was extruded; the rest remains stored within the volcano's east rift zone (55%) and southeast rift zone (10%).

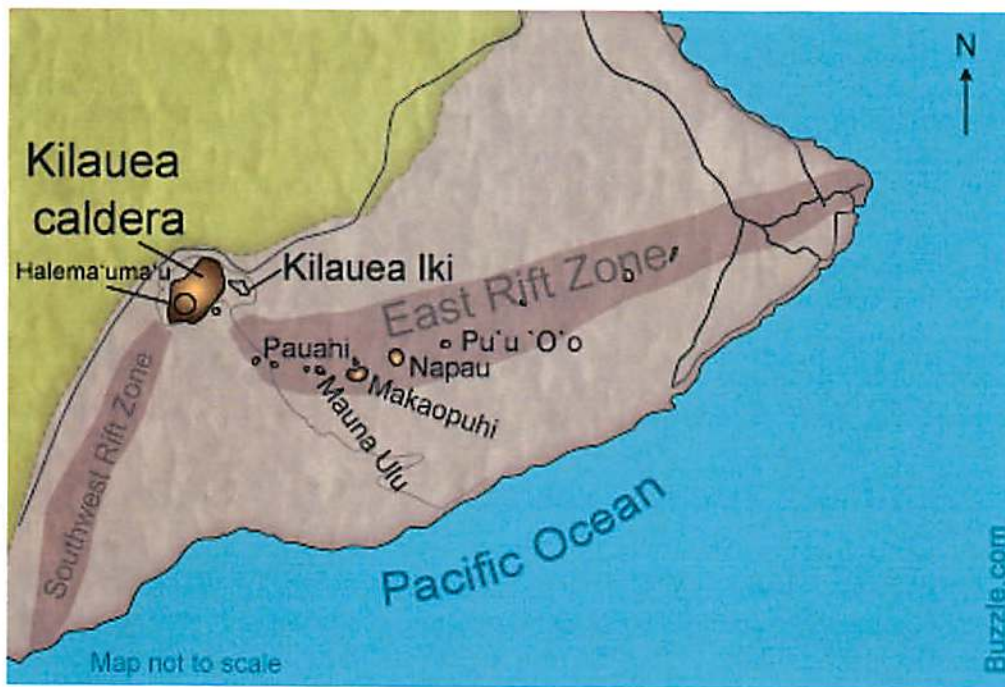


Figure 3: Kilauea has two rifts zones - one stretching approximately 78 miles towards the east, and the other 22 miles towards the southwest. Over the years, the episodes of eruptions in the southwest and east rift zones, have led to the formation of ridges in an outward fashion from the summit. The amount of eruptions taking place are more in the rift zones than in the summit region. (from <http://www.buzzle.com/articles/mount-kilauea-volcano-hawaii-volcano.html>)

The origin of the fractures the comprise the rift zones is spreading of the volcano. The more material a shield volcano accumulates the heavier it gets, and it begins to settle due to gravity. The surface spreads and ruptures. It is easier for liquid lava, which is heavy, to flow laterally out the sides of a mountain than to be pushed up an additional several

hundred or thousands meters in elevation to be erupted from the summit.

Magma that erupts from Kilauea first rises through a deep magma conduit and enters a magma-storage reservoir beneath the summit area. Eruptions and shallow intrusions at the summit are fed directly by magma from this reservoir. Eruptions from the east and southwest rift zones are supplied by magma that has moved from the summit reservoir into and along the rift zones through magma conduits. There is an overall general agreement of a deep and shallow component to the magma conduits beneath the summit (See Figure 4). Magma moves toward the surface of the east rift zone through dykes. The dykes typically range in width from less than 1 m to only a few meters. A single dike may extend more than 5-10 km in length and 2-3 km in height.

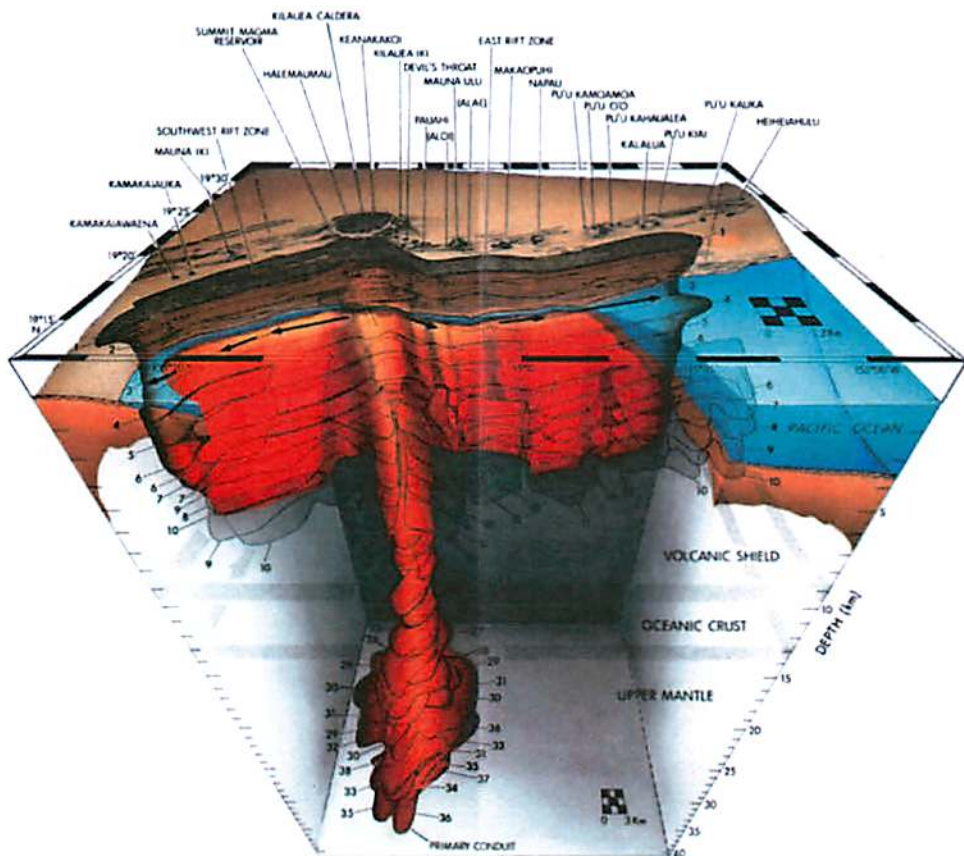


Figure 4: The internal structure of Kilauea in a northward directed view. The preferred pathway of vertical magma transport lies within the core region of the primary conduit and is shaded yellow. The lateral injection of tholeiitic magma along the shallow horizon of neutral buoyancy forms sheeted dyke complexes in the 2 - to 4-km depth interval beneath the volcano surface (horizontal arrows). Zones of intrusion occur in both the Southwest Rift Zone and the East Rift Zone. The juncture of these preferred magmatic pathways is the subcaldera magma reservoir. The vertical and lateral extents of the active rift systems and of the primary conduit are shaded amber and orange.

Interpretation of abundant seismic data suggests that Kilauea's primary conduit within the upper mantle is concentrically zoned to about 34-km depth. This zoned structure is inferred to contain a central core region of relatively higher permeability, surrounded by numerous dikes that are in intermittent hydraulic communication with each other and with the central core. During periods of relatively high magma transport, the entire cross section of the conduit is utilized. During periods of relatively low to moderate transport, however, only the central core is active. As the conduit penetrates the oceanic crust and enters the volcanic shield, it simultaneously supplies the deeper sections of the rift zones (6-to 10-km depth) and the roots of the summit reservoir with picritic magma. The rift zones at depth are inferred to be almost wholly molten and to possess a high degree of fluid continuity from Heiheiiahulu in the East Rift Zone, 45 km westward through the roots of the summit magma reservoir, and well into the Southwest Rift Zone. Higher in the shield, the subcaldera magma reservoir and the shallow rift zones occupy the 2-to 4-km depth interval. Summit-differentiated olivine tholeiite ($\rho \approx 2.62 \text{ gcm}^{-3}$) is periodically injected laterally along a horizon of neutral buoyancy within the rift zones, where the density of the magma is just balanced by the in situ density of the shield. Deep rift zone intrusions push seaward the deep tectonic blocks of the volcano's south flank. Shallow rift intrusions build a sheeted dike complex, inferred to be in isostatic equilibrium with the higher-density deep rift cores below.

Dynamics of magma flow in dykes and constraints on eruption conditions

During the dyke propagating process, the magmas are very compressible fluids at all stages of their motion. If the total gas bubble volume fraction becomes large enough, bubbles begin to connect together to form a continuous phase. The magma is said to *fragment* and changes from a continuous liquid containing gas bubbles to a continuous gas containing droplets and clots of liquid. This is the basic origin of all explosive volcanic activity.

Assuming steady flow, the state of the fluid is governed by the following equations when the dyke geometry is fixed. The bulk density, β , of a magma containing a single volatile species is determined by:

$$\beta^{-1} = [(nQT)/(mP)] + [(1 - n)/\rho], \quad (2)$$

where ρ is the density of the gas bubble-free liquid, n is the mass fraction of the gas, m is the molecular weight of the gas, P and T are the ambient pressure and temperature respectively, and Q is the Boltzmann constant. The continuity equation is:

$$\beta w X du + u w X d\beta + u \beta X dw + u \beta w dX = 0, \quad (3)$$

where u is the mean velocity of the magma and w and X are the horizontal thickness and horizontal extend of the dyke, respectively. The momentum equation is given by

$$-dP/\beta = u du - g dz + (f u^2)/(2w) dz. \quad (4)$$

In this equation the left-hand side represents the internal energy liberated by decompression of the gas and the terms on the right-hand side are the consequent changes in kinetic energy, potential energy and wall friction work, respectively.

Combining equations (2), (3) and (4) to give

$$[1 - (u^2/u_c^2)]du/dz = -[(u^2f)/w] + g(u/u_c^2) - (u/w)dw/dz - (u/X)dX/dz, \quad (5)$$

where u_c is a group with the dimensions of velocity, and is the speed of sound in the bulk magmatic fluid, which is typically in the range of 30 - 100 m/s. In many gas-rich explosive eruptions the stream of gas and fragments of magma leave the vent at speeds well in excess of 300 m/s, and so the fluid must make a subsonic to supersonic transition within the dyke. Because when $u = u_c$ the left-hand-side of equation (5) will be singular, we need the right-hand-side of equation (5) to be zero when $u = u_c$, which is:

$$(w/X)dX/dz + dw/dz = [(gw)/u_c^2] + f. \quad (6)$$

Given some general values to the above expression, a subsonic to supersonic transition can only occur when dw/dz is about 0.01- 0.02, meaning that at some point in the dyke where the dyke wall is tilted outwards at an angle of $\tan^{-1}(0.01 - 0.02) = 0.6 - 1.1^\circ$.

Although it is a small angle, this is not a trivial issue, because generally the dyke wall is tilted inward everywhere when it reaches surface for the first time. Thus, in the early stages of an eruption no supersonic transition can occur. As the eruption continues, the dyke walls may be eroded, and a suitably flared shape can be developed near the surface, and thus supersonic flow can develop.

3 Planetary application – Mars

Compared to Earth, Mars has lower gravity and atmospheric pressure, and different atmospheric temperature structure. The same volcanic eruption theory can still apply to Mars, and predicts some general differences of volcanic activities between Earth and Mars. For example, because of the lower gravity, fluid convective motions and crystal settling processes driven by positive and negative buoyancy forces, as well as overall diapiric ascent rates, will be slower on Mars, or other satellites, than on Earth, permitting larger diapirs to ascend to shallower depths.

The full range of volcanic eruption styles presently known on Earth is to be expected on Mars. It is clear that Martian environmental conditions operate to modulate the various eruption styles and the morphology and morphometry of resulting landforms. The theoretical prediction applied on Martian volcanoes are in general good agreement with observations.

Changes in volcanic style in space and time – Variations in the areal distribution of volcanic styles have been observed on Mars, with effusive eruption and shield building dominating the northern lowlands and explosive volcanic deposits of the paterae occurring predominantly in the southern highlands and circumbasin areas. One important factor is the influence with groundwater interactions – the area differences in style is that they simply represent different crustal volatile reservoirs. Other possibilities include the role of crustal thickness and compositional variations and their influence in the development of neutral buoyancy zones. Variations in the style of volcanism with time is also

possible, with early volcanism being characterized by more volatile-rich magma and later by volatile-depleted magma.

Changes in the atmosphere with time – A significant corollary is that very large quantities of volatiles may have been injected into the atmosphere periodically by the explosive or hydromagmatic eruptions.

Compositional interpretation of volcanic deposits – Individual lava flow or deposits are hard to be directly detected. Morphology and morphometry of volcanic deposits have sometimes been used to interpret their composition. The influence of environmental conditions on eruption styles may be significant in the interpretation of composition. For example, extremely long lava flows are predicted to be primarily a consequence of martian gravity and cooling conditions rather than viscosity and compositional factors. The production of large-scale plinian deposits (what is plinian eruption?) may not signal the presence of more silicic compositions but, rather, may be linked to the enhanced gas exsolution and magma fragmentation of basaltic magma in the Martian environment or to the interaction of basaltic magma with groundwater.

Contribution to surface sedimentary deposits – Martian eruptions conditions (low atmospheric pressure) favor significant gas exsolution, higher rise speeds near the surface, enhanced magma disruption, and systematically finer grained pyroclasts. These conditions mean that virtually every eruptions of volatile-containing magma will be accompanied by a fine-grained pyroclastic deposit component. Martian plinian deposits of any magma composition will be systematically finer grained than plinian fall deposits on Earth by a factor of about 100. Very fine grained volcanic ash should be extremely common and widespread and of a grain size susceptible to further eolian transport.

References

- Delaney, P. T., R. S. Fiske, A. Miklius, A. T. Okamura, and M. K. Sako, 1990: Deep magma body beneath the summit and rift zones of kilauea volcano, hawaii. *Science*, **247**(4948), 1311–1316.
- Dzurisin, D., R. Y. Koyanagi, and T. T. English, 1984: Magma supply and storage at kilauea volcano, hawaii, 1956–1983. *Journal of Volcanology and Geothermal Research*, **21**(3), 177–206.
- Pinkerton, H., L. Wilson, and R. MacDonald, 2002: The transport and eruption of magma from volcanoes: A review. *Contemporary Physics*, **43**(3), 197–210.
- Ryan, M. P., 1988: The mechanics and three-dimensional internal structure of active magmatic systems: Kilauea volcano, hawaii. *Journal of Geophysical Research: Solid Earth* (1978–2012), **93**(B5), 4213–4248.
- Wilson, L. and J. W. Head, 1994: Mars: Review and analysis of volcanic eruption theory and relationships to observed landforms. *Reviews of Geophysics*, **32**(3), 221–263.

Molly Simon



Flora and Fauna of the Hawaiian Islands

The Hawaiian Islands have a uniquely diverse group of plants and animals. This is due to the fact that the Hawaiian Islands are the most isolated group of islands on Earth, making it particularly difficult for existing plant and animal species to migrate there. As a result, Hawaii's plant and animal species arose from very infrequent colonizations (primarily from wind and water transport) and a slow evolution process isolated from the rest of Earth's flora and fauna. For all of these aforementioned reasons, Hawaii is home to a variety of plant and animal species that exist nowhere else. The Big Island of Hawaii in particular is home to the vast majority the islands' unique plant and animal species due to its large size and 13 different climate zones (all but arctic and tundra).



The Big Island is covered with ohia lehua trees that are easy to distinguish from other trees on the island because of the silver color in their leaves. Pink, yellow, and occasionally white lehua flowers bloom on the trees and are said to be secreted to the Volcano Goddess Pele. The ohia wood of the ohia lehua trees were used by ancient Hawaiians to carve temple idols, canoes, bowls, and spears. Modern day natives use the bark for furniture and burn it for energy. These trees can reach 100 feet in height and they can exist up to 10,000 feet in elevation. They are Hawaii's most abundant native tree. In terms of reforestation, after an 'a 'a flow, there is an increase in standing nitrogen in the soil which increases the amount of standing biomass. This allows the ohia lehua trees to dominate the upper canopy layers and grow tall even after such flows. Ferns dominate the lower layers, the the ohia lehua trees provide shade and protection to these lower layer ferns from excess volcanic smog and ash.

Hawaii has a particularly large native tree called the Koa tree, which can grow to be 100 feet tall and 10 feet in diameter. It grows light yellow puffy flowers which turn into seed pods. The reddish wood of the Koa tree was used by indigenous Hawaiians to build canoes, paddles, and is still commonly used to build wooden surfboards! Unfortunately, there are few Koa trees left on the Big Island because the bark has been cut down



for furniture use. They are typically found in moist environments on the Big Island between elevations of 1,000 and 6,000 feet. They can be found on the westside of the Big Island and in Hawaii Volcanoes National Park.

Hawaii is also home to a variety of 168 fern species whose spores are dispersed amongst the islands via wind transport. The two most common are tree ferns and false staghorn ferns. Forests of these ferns are typically found on top of lava flows and next to ohia lehua and koa trees. They are most abundant on rainy side of the Big Island. Ancient Hawaiians used the fern fronds to make bedding materials and medical supplies, and they were taken as laxatives. Today, the roots of the ferns are just used as potting soil for orchids and other household plants.



In addition to plants, Hawaii has a huge selection of native animal species—particularly birds. Hawaii’s state bird is the nene (Hawaiian goose) and it is endangered. There are approximately 500 nene birds left on the Big Island and they are typically found near Mauna Loa, Mauna Kea, and Hualalai. These birds are now protected by state and federal laws to better prevent extinction.

The Big Island is the place where native and tourists alike are most likely to spot the endangered Hawaiian hawks (‘io). They can only be found near the slopes of Mauna Loa and Mauna Kea, below 9,000 feet in elevation or in the Hawaii Volcanoes National Park. They were special to indigenous Hawaiians because they believed the ‘io was a symbol of royalty.

A more common bird on the Big Island is the apapane. This bird is bright red and sturdy and is a member of the honeycreeper family. They feed on flower nectar and are known for giving off a foul odor that makes them an undesirable meal to predators. They are small birds, typically only 6 inches long and are believed to be descendants of the finch. Their most distinguishable characteristic is their bills which can range in appearance from short and sturdy (for crushing seeds) to long and slender (for eating nectar). They are typically found above 6,000 feet in elevation.



Hawaii has only one native land mammal (besides humans), the hoary bat. It is typically only found on the Big Island but there have been sightings of this particular bat species on the island of Kauai. They prefer dry forests and living at an elevation of 4,000 feet but they are found from sea level to 13,000 feet in elevation. The bats’ main food source is moths and is typically found alone rather than in a colony of bats. Some species of hoary bats are now found in Canada, South America, and the Galapagos Islands, but it is the only land mammal native to Hawaii.

References:

Island Insights: The Big Island's Flora and Fauna

http://www.bestplaceshawaii.com/island_insights/bigisland/floraFauna.html

Sakai A. K., Wagner W.L., Mehrhoff L. A. (2002). "Patterns of Endangerment in the Hawaiian Flora". *Systematic Biology* (Society of Systematic Biologists) **51** (2): 276–302.
doi:10.1080/10635150252899770

Kanehiro, K et al., (1995). "Primary succession of Hawaiian montane rain forest on a chronosequence of eight lava flows." *Journal of Vegetation Science* **6**: 211-222.

Mass Wasting

James T. Keane



Mass wasting is the geomorphological process by which soil, regolith, move downslope due to the force of gravity.

Terminology

There is no consistent set of terminology for mass wasting processes in the literature. ⊗

- Creep:** Slow (mm/yr), but ubiquitous downslope movement of loose debris on slopes.
- Falls:** Abrupt free-fall movement of material away from steep slopes (e.g. cliffs). Material usually moves in bulk.
- Slides:** Movement of material along recognizable shear surfaces.
- Flows:** Material behaves like a viscous mass, whereby inter-granular movements dominate over shear surface movements.

Triggering Mass Wasting

A block of regolith will remain stable if the shear stress acting on it (σ_s) remains below this critical threshold:

$$\sigma_{s,max} = c + (\sigma_n - p) \tan \phi$$

- $\sigma_{s,max}$ maximum sustainable shear stress
- c cohesion
- σ_n stress normal to the plane of shearing
- p pore pressure
- ϕ angle of internal friction (30-45° for most materials)

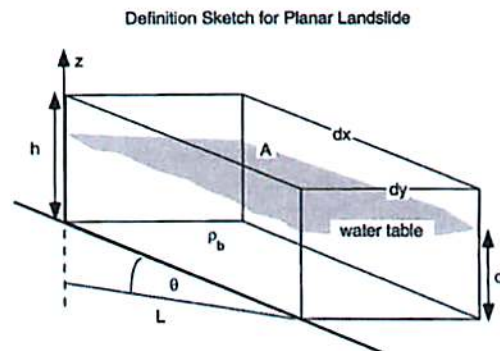


Figure 10.25 Segment of a planar hillslope showing geometry of a slab of regolith of area $A = dx dy$ and thickness h above a potential failure plane with slope θ relative to the horizontal. Also shown (bold line) is the water table with a height d above the failure plane.

(Anderson & Anderson 2010)

So, how can an initially stable hill slope become unstable?

- (1) External causes which increase in shear stress ($\sigma_s \uparrow$).** Examples include: tectonic/volcanic uplift and over-steepening; localized over-steepening due to undercutting, erosion, stream incision, artificial excavation, etc.; loading; shocks and vibrations.
- (2) Internal causes which decrease the shearing resistance ($\sigma_{s,max} \downarrow$).** Examples include: weathering (freeze-thaw, desiccation, reduction of cohesion, removal of cement); increase in pore pressure.

(Hansen 1984)

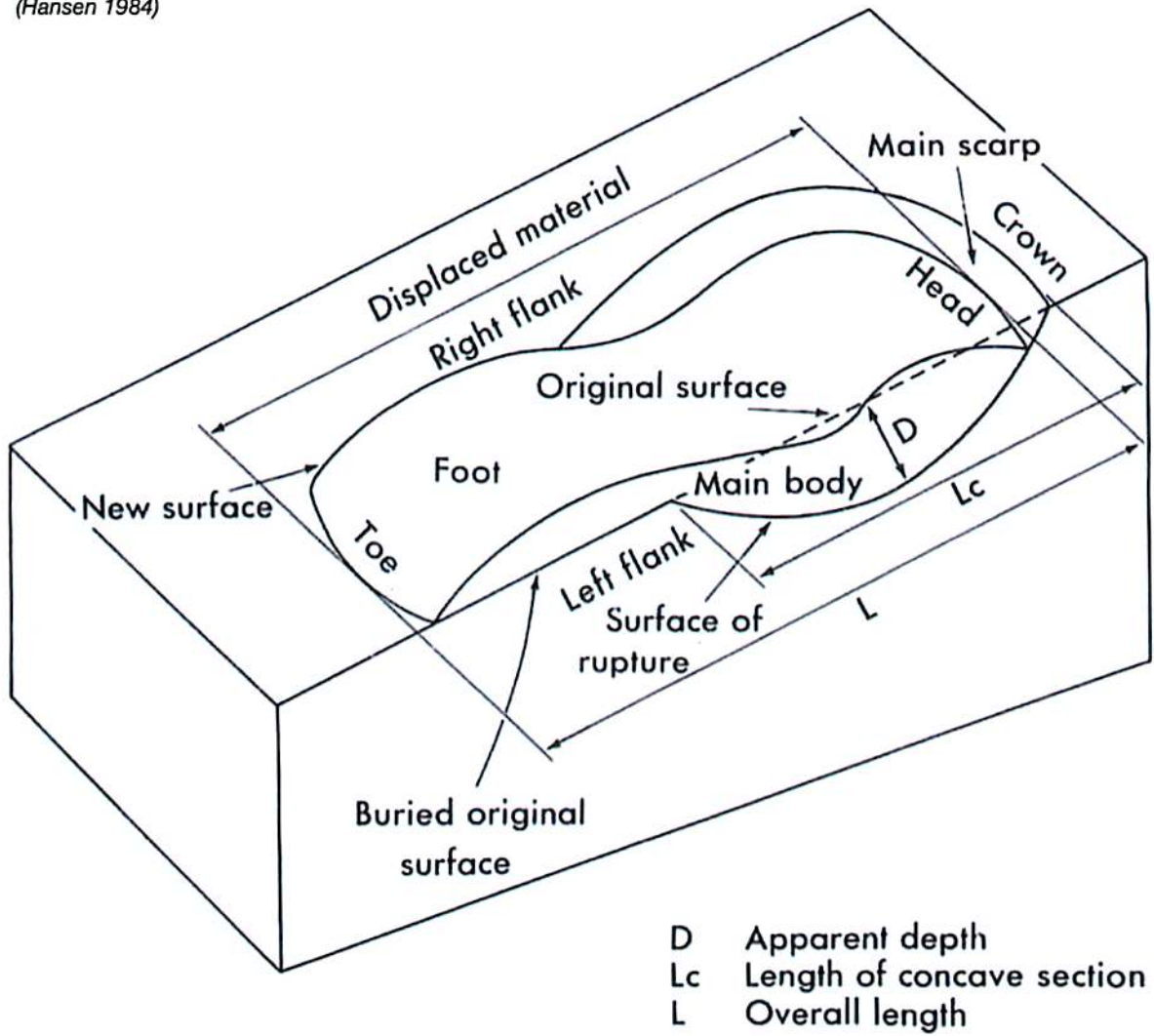


Figure 1.6. Relevant terms in landslide morphology

Island Volcanoes & Mass Wasting

Island volcanoes not only grow from addition of volcanic products, but also from slow erosion and sudden collapse events. In the long term, these destructive processes can erode an island volcano to the point where it sinks beneath the wave base (e.g. the Hawaiian-Emperor seamounts, NW of present-day Hawaii).

Lava Benches & Bench Collapse

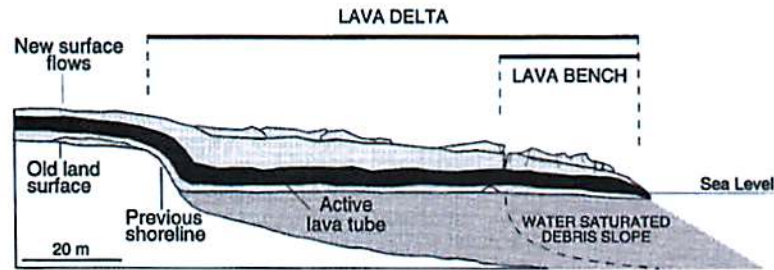
When pahoehoe lava flows first reaches the ocean, the lava is quickly quenched when entering the surf zone and is shattered to form glassy blocks and lapilli. Over time, this material builds up in a loose submarine debris slope. Later flows build on this slope, forming lava deltas that can extend hundreds of meters seaward. As the flows mature, lava tube systems are established within the delta. These lava tubes terminate at the leading edge of the delta at, or below, sea level.

As these deltas grow, they become prone to catastrophic collapse. The unstable front of the delta, or lava bench, detaches from the trailing delta along an ocean-facing scarp. Benches are typically elliptical, and extend ~100's meters along the coastline, and ~10's of meters seaward. During collapse, benches slump into the ocean, severing the lava tube. Most collapses lead to explosive mixing of seawater and lava.

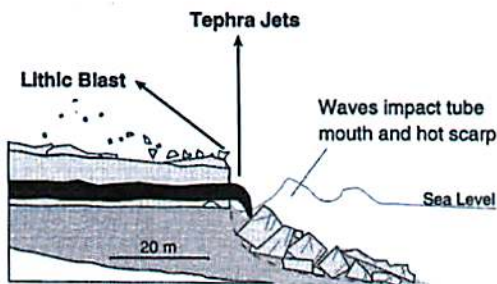


Lava bench at East Lae'apuki. (USGS Hawaiian Volcano Observatory)

A. Active lava delta, bench and tube



B. Open mixing: complete collapse of lava bench severs active lava tube



C. Confined mixing: partial collapse of lava bench submerges and fractures a portion of active lava tube

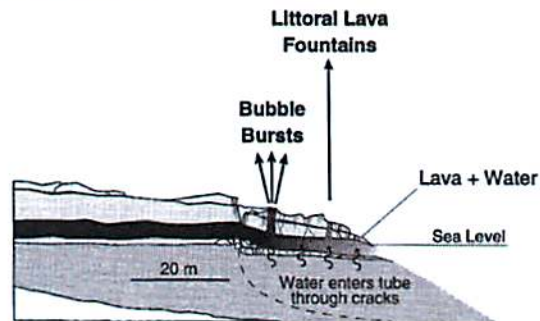


Fig. 4. Hypothetical cross section of a lava delta and bench showing the location of littoral hydrovolcanic explosions. (A) Hyaloclastites formed at the ocean entry build a submarine debris slope that is subsequently capped by pahoehoe flows. Lava tubes on the bench can reside below or at sea level, due to continuous subsidence of the delta (Kauahikaua et al., 1993). (B) Profile of the front of the delta immediately following a complete bench collapse. (C) Profile of the front of the delta immediately following a partial collapse of the bench.

*Collapse of lava benches, and the resulting littoral hydrovolcanic explosion (what a cool phrase).
(Mattox & Mangan 1997)*

Flank Collapses, Debris Avalanches, and Slumps

As island volcanoes grow, they become structurally unstable – due to over-steepening of the flanks caused by intrusions, weakening due to hydrothermal alteration, dike intrusion, rifting, and heating of pore fluids. This can lead to *massive flank collapses* (also referred to as sector collapses). In stratovolcanoes, flank collapse can trigger explosive eruptions, due to sudden depressurization of the magma chamber (e.g. Mt. St. Helens), and can result in tsunamis. Hawaiian flank collapses result in some of the largest landslides on Earth. Individual flows extend more than 200 km in length and 5000 km³ in volume. Some turbidite deposits can extend for > 1000 km. Side-looking sonar surveys have shown that Hawaiian debris avalanche deposits cover an area of seafloor more than 5 times the land area of the islands.

Not all flank collapses are rapid. Slumps are slow, intermittent landslides, which still displace large portions of volcano flanks. The Hilna slump is an example of an active landslide that involves most of the south flank of the Kilauea volcano. The slump covers ~5200 km², and possesses a creeping zone ~100 km wide. The slump is bounded at its upslope by the southwest rift zone of the Kilauea volcano and the Kaoiki fault system. (This

relationship between slumps and rifts is common in Hawaii – suggesting that the two processes are dynamically coupled.) The slump is transected by the Hilna fault system, consisting of normal faults parallel to, and dipping towards, the southern coast. Geodetic measurements indicate seaward movement of the order of 0.1 m/yr, with additional stochastic jumps in displacement associated with earthquakes.

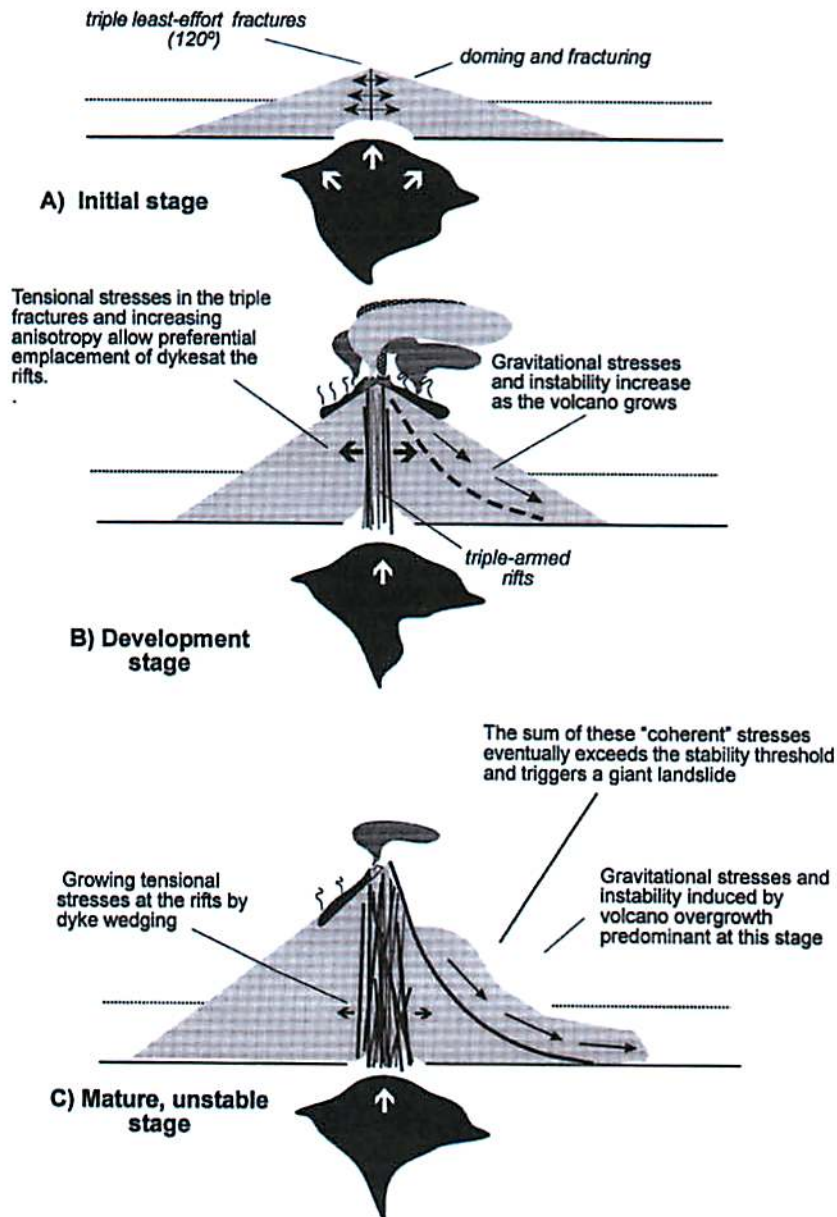
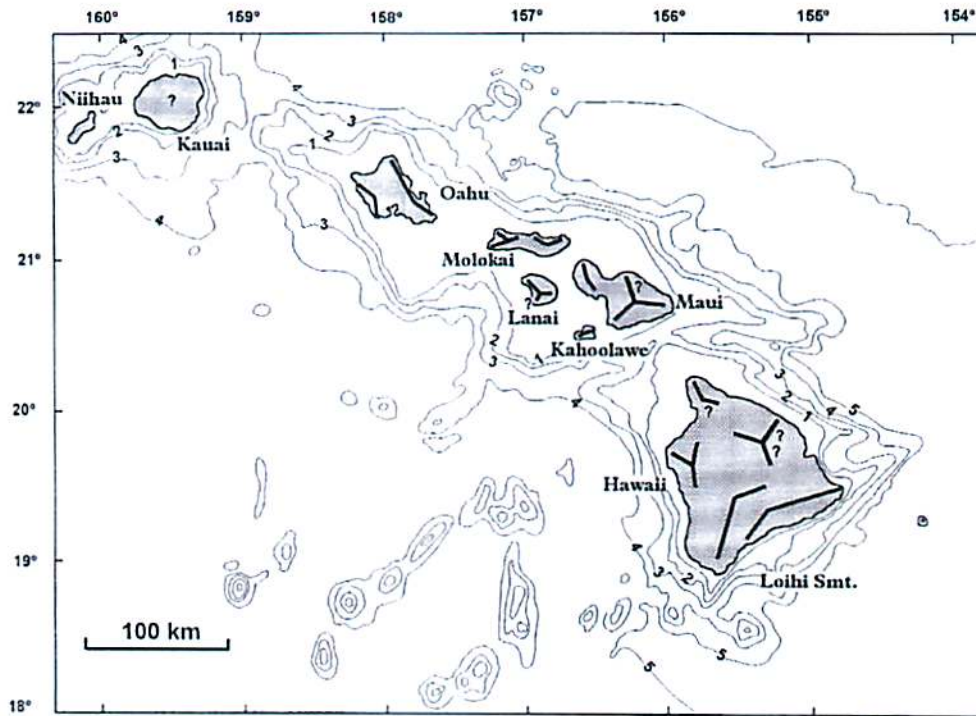
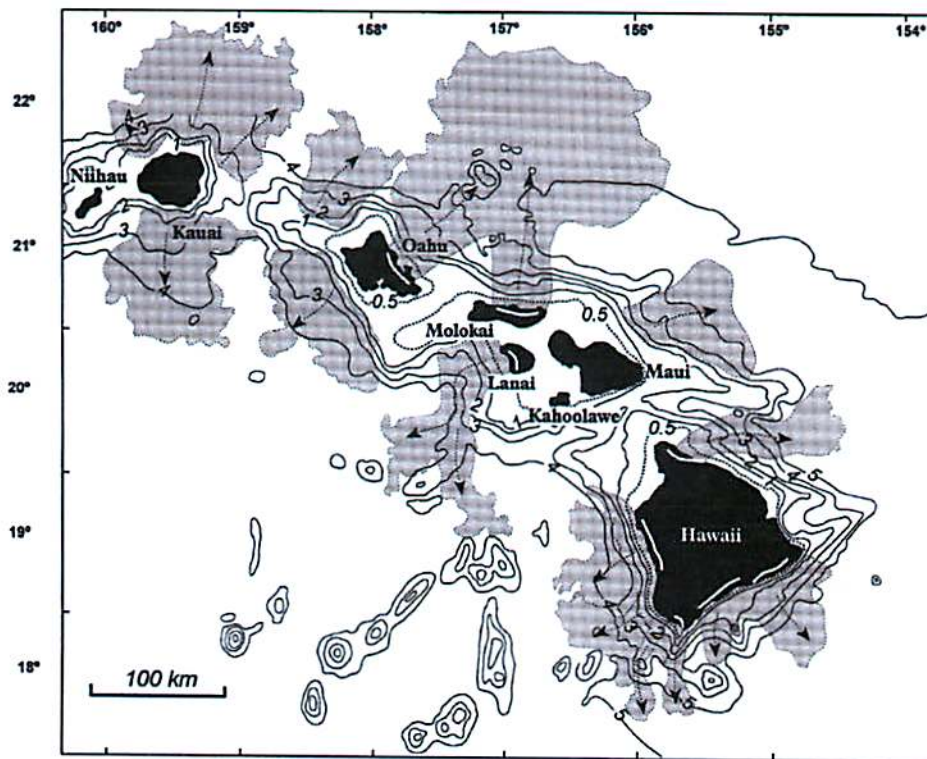


Fig. 8. Simple model to illustrate the generation of different "coherent" stresses in overgrowth, unstable oceanic volcanoes. The sum of these tensional forces eventually exceeds the stability threshold and triggers a giant landslide, restoring the stable configuration of the volcano.

(Carracedo 1999)



Rift zones on the Hawaiian Islands. (Carracedo 1999)



Giant landslides associated with Hawaii. (Carracedo 1999)

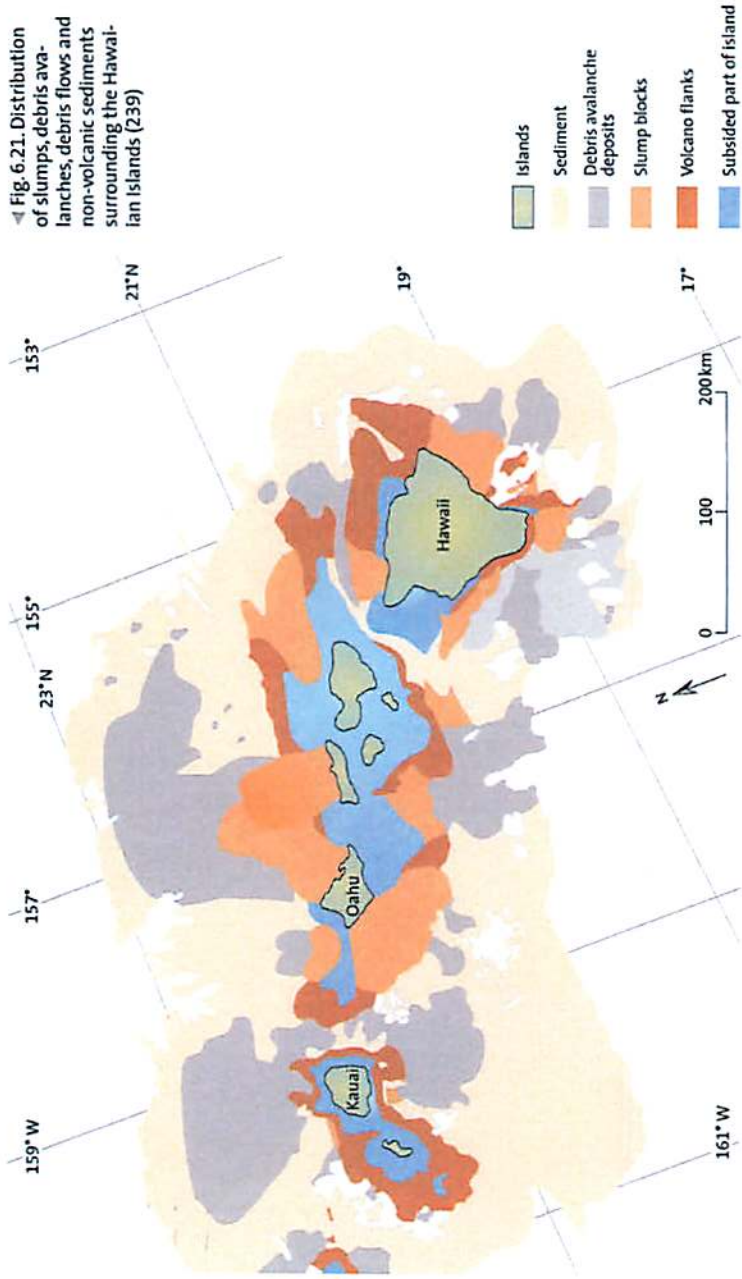


Fig. 6.21. Distribution of slumps, debris flows and debris avalanches, debris flows and non-volcanic sediments surrounding the Hawaiian Islands (239)

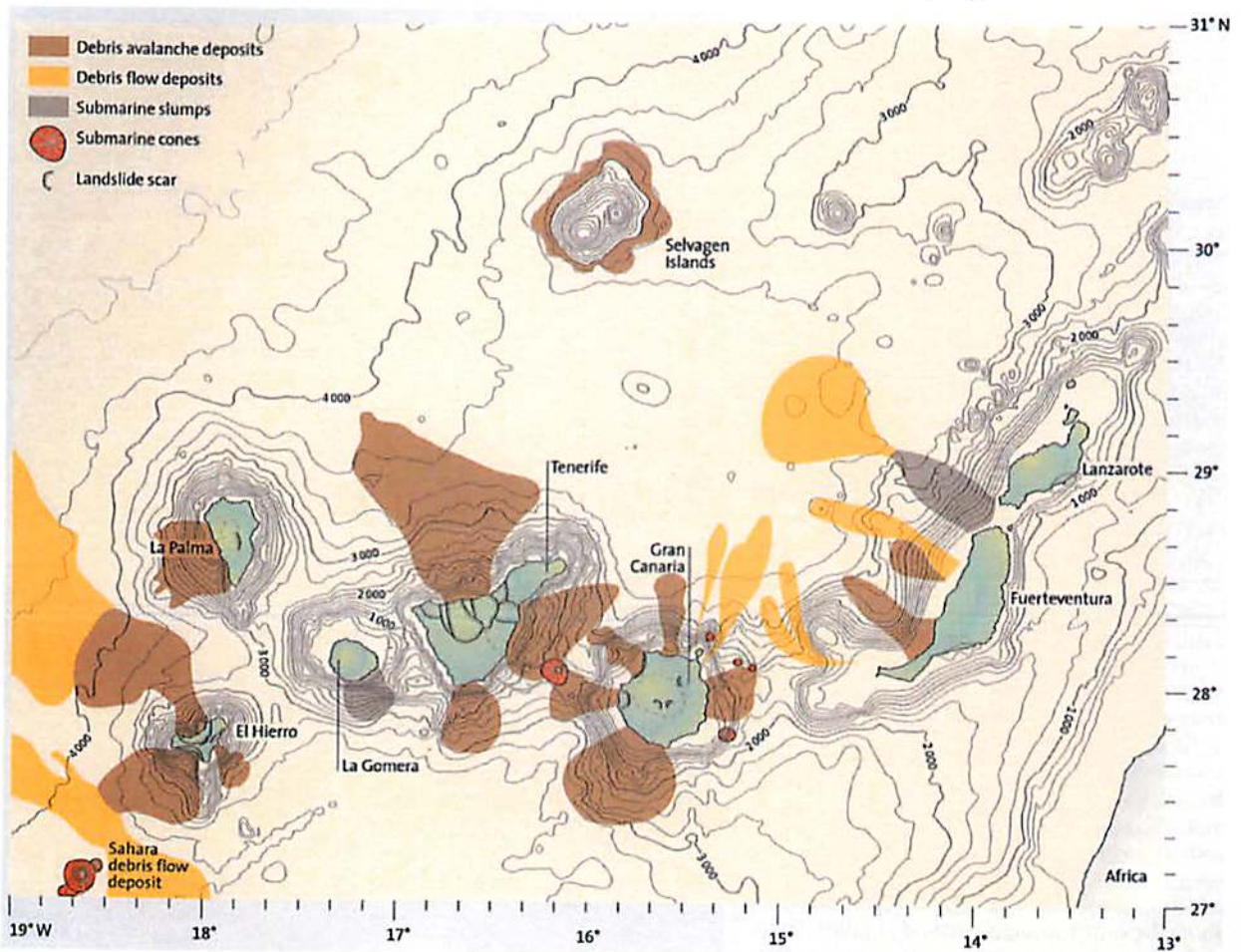
(Schmincke 2004)

Flank collapses at the Canary Islands. (Schmincke 2004)



Fig. 9.41. Morphology of La Palma (Canary Islands) as presented by Leopold von Buch (17). The large hole in the northern, about 1 to 3-mil. 800-year-old shield volcano (Caldera de Taburiente) cut by Barranco de las Angustias is the type caldera. Today, it is explained by sector collapse, generating submarine debris avalanche deposits and by subsequent erosion (Fig. 6.29). The late Quaternary and historic (last eruptions in 1949 and 1971) basaltic eruptions are restricted to the southern, about 30-km-long ridge, which represents a rift zone.

▲ Fig. 6.29. Distribution of deposits of slumps, debris avalanches and debris flows on the seafloor around the Canary Islands (182)



References

- Anderson, R. S. & Anderson, S. P. 2010 *Geomorphology: the Mechanics and Chemistry of Landscapes* (Cambridge: Cambridge Univ. Press)
- Carracedo, J. C. 1999, "Growth, structure, instability and collapse of Canarian volcanoes and comparisons with Hawaiian volcanoes," *Journal of Volcanology and Geothermal Research*, 94, 1-19
- Hansen, M. J. 1984, in *Slope Instability*, ed. D. Brunsten & D. B. Prior (New York: John Wiley & Sons), 1
- Mattox, T. N. & Mangan, M. T. 1997, "Littoral hydrovolcanic explosions: a case study of lava-seawater interaction at Kilauea Volcano," *Journal of Volcanology and Geothermal Research*, 75, 1-17
- Melosh, H. J. 2011, *Planetary Surface Processes* (Cambridge: Cambridge Univ. Press)
- Moore, J. G. et al. 1989, "Prodigious Submarine Landslides on the Hawaiian Ridge," *Journal of Geophysical Research*, 94, 17465-17484
- Schmincke, H.-U. 2004, *Volcanism* (Berlin: Springer-Verlag)



Volcanic Monitoring

Sarah Morrison

Some methods to monitor volcanoes include tilt measurements, seismology, radar (InSAR), gas sampling, thermal imaging, and visual inspection. Here I focus on some of these methods that are relevant to both the Hawaiian volcanoes and those elsewhere in the Solar System.

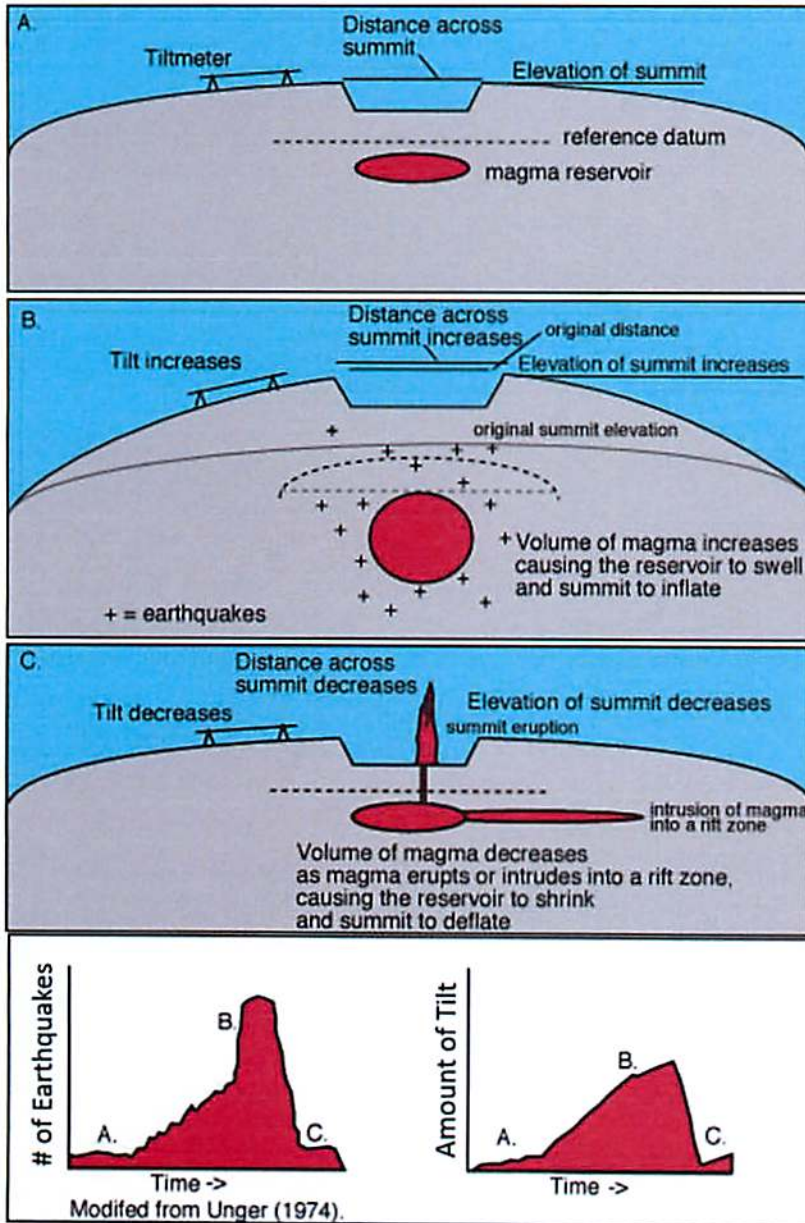


Figure 1. Modified from [1].

Tilt/Deformation Measurements

Measuring changes in the slope of the volcano's flank (tilt) can be indicative of inflation/deflation episodes such as those caused by changes in magma volume. In situ methods of measuring tilt include tiltmeters, electronic distance measurements using lasers, and continuous differential GPS monitoring (DGPS, most current method). An example of expected changes in tilt preceding and following an eruption are shown in Figure 1.

Similar measurements, though not to as high resolution as through in situ methods, can be made with **photogrammetry**. This technique uses a series of images taken at different viewpoints to construct digital terrain models (DTMs). By taking a series of images at various stages of volcanic activity, sequential DTMs can be built for monitoring crustal deformation and estimating lava volume/extrusion rates. Higher precision approaches that combine stereo-photogrammetry and DGPS has been used to monitor pahoehoe lava lobe emplacement on Kilauea Volcano [2].

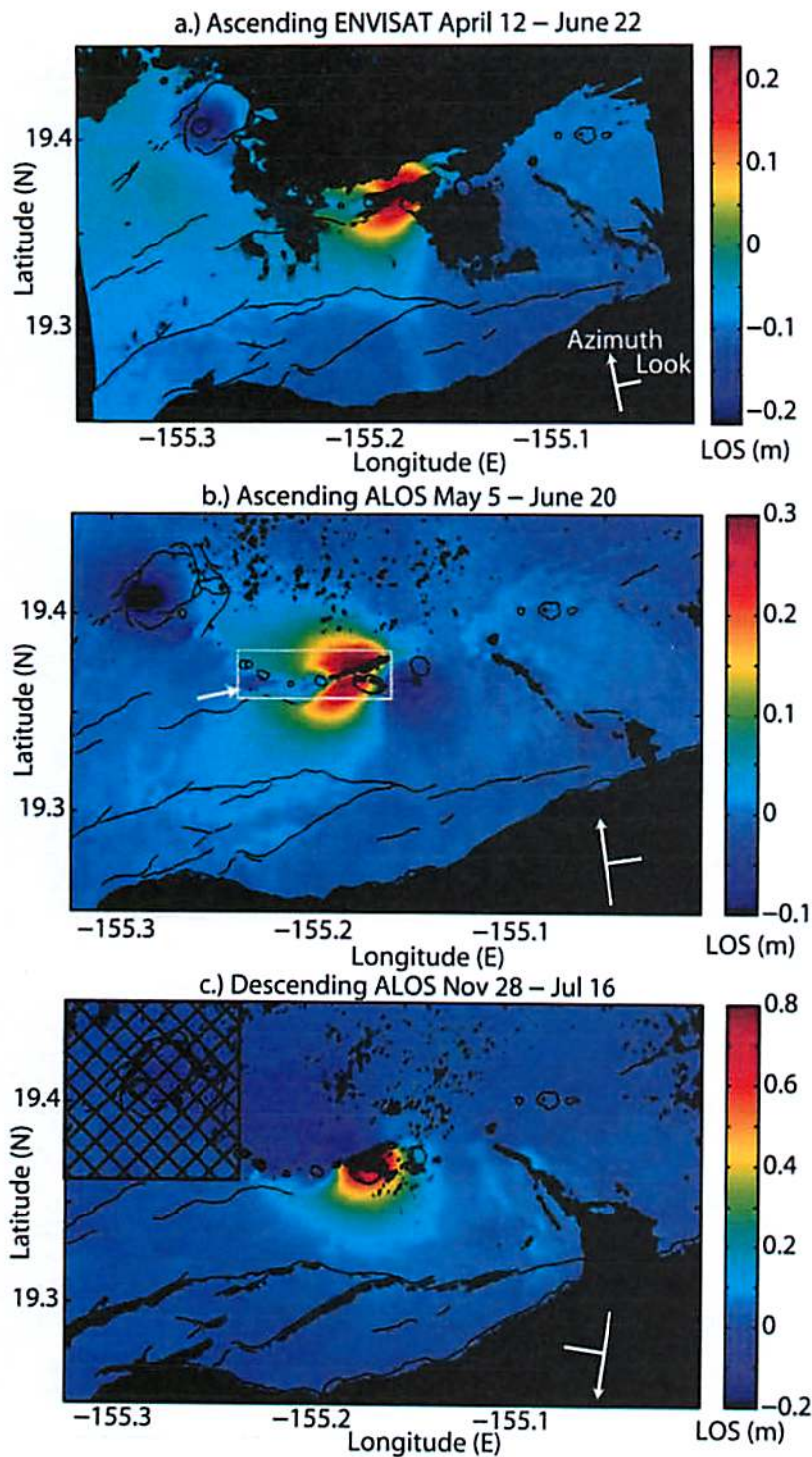


Figure 2. (a) ENVISAT ASAR interferogram spanning 12 April to 22 June 2007. (b) ALOS PALSAR interferogram spanning 5 May to 20 June 2007. (c) ALOS PALSAR interferogram spanning 28 November 2006 to 16 July 2007. Colors show line of sight displacement in meters. The Kilauea summit area is cross-hatched in (c). From [3].

Interferometric synthetic aperture radar (**InSAR**) involves using several radar images taken at different times to produce interferograms sensitive to cm-scale displacements over the time spanned by the radar observations. This monitoring technique is used often in conjunction with GPS networks for monitoring Kilauea. Figure 2 shows interferograms from ENVISAT and ALOS spaceborne InSAR data tracking deformation episodes associated with intrusion in the eastern rift zone of Kilauea during late 2006 to 2007 [3].

Thermal Imaging

Orbiting spacecraft imaging the surface at infrared wavelengths can detect hotspots indicative of current volcanic activity. Figure 3 shows a moderate resolution imaging spectro-radiometer (MODIS) 3.929-3.989 μm image of Hawai'i with Kilauea volcano acquired on Feb. 2, 2001 showing active lava flows in the bright pixels. Though having low spatial resolution (1-4 km), these observations have higher temporal resolution (real-time to 3 days) to permit better monitoring [4].

Thermal imaging is a common technique for detecting and monitoring active volcanic regions in the Solar System, but is most effective for monitoring volcanic features on the nightside. During the Galileo

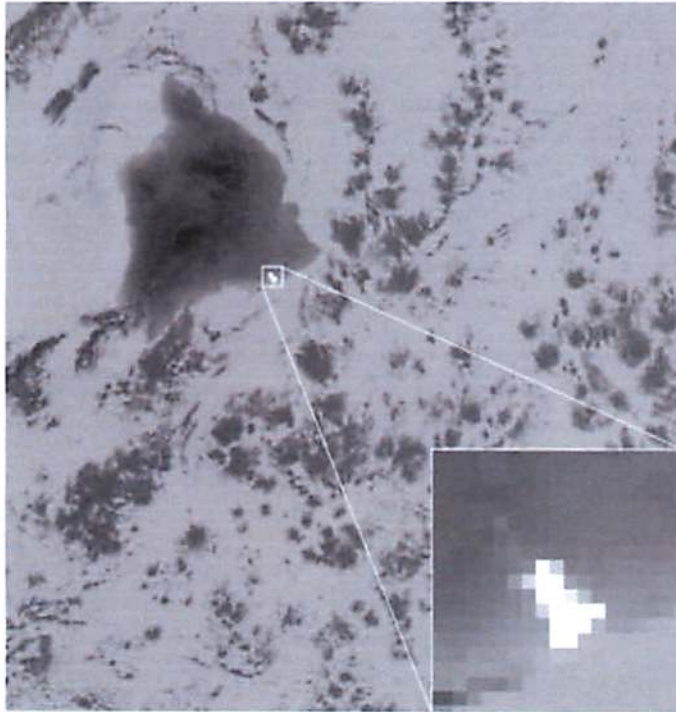


Figure 3 (left). MODIS 3.959 μm image of the Big Island of Hawaii acquired the night of Feb. 2, 2011. Modified from [4].



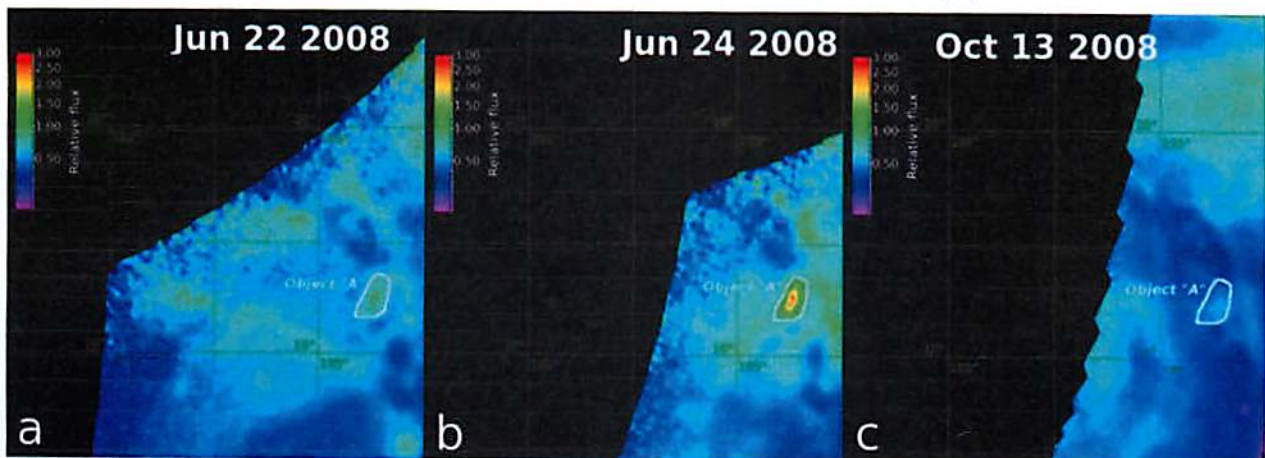
- [1] East Girru (21N, 236W)
- [2] Pele (19S, 256W)
- [3] Ulgen (38S, 290W)
- [4] N. Lerna (55S, 290W)
- [5] Heno (56S, 310W)
- [6] Hephaestus (3N, 288W)
- [7] Mazda (10S, 310W)
- [8] Unidentified 6119 (30S, 310W)
- [9] Dazhbo (54N, 302W)
- [10] Loki (12N, 309W)
- [11] Surt (41N, 334W)
- [12] Unidentified 4319 (32N, 10W)
- [13] Ukko Patera (32N, 10W)

Figure 4 (above). New Horizons LEISA NIR observations of Io's hotspots. From [4].

mission and New Horizons encounter with Jupiter, Io's hotspots on the nightside were monitored. In particular, New Horizons' LEISA instrument (1.25-2.5 μm) recorded changes in power output of some hotspots over 48 hours of observations, others were similar to output determinations from past Galileo observations [5]. These nightside observations from the 2007 New Horizons encounter are shown in Figure 4.

Though geologically recent volcanic activity on Venus has been suggested for several years [6-7], recent reports of changes in surface thermal flux over several days at the edge of rift zones offers stronger evidence [8]. Figure 5 shows retrieved maps of relative thermal flux from the Venus Monitoring Camera aboard Venus Express derived when cloud opacity variations were small [8].

Figure 5 (below). Relative surface thermal flux centered at 1.01 μm from Venus Monitoring Camera (VMC) aboard Venus Express in Ganiki Chasma. From [8].



Remote Sensing Volcanic Gases/Ash

Infrared observations can also be used for monitoring volcanic activity through ash and gas production. These satellite observations on Earth are especially relevant to assess the danger of volcanic eruptions to nearby aircraft. Dry silicate ash has a negative brightness temperature difference compared to clouds/Earth's surface and also has absorptions in the infrared, allowing an observer to estimate the airborne ash mass with time during an eruption using satellite data [9]. Though large ash columns are not produced by the Hawaiian volcanoes, SO₂ emissions can be detected in the UV or IR and can be used to estimate degassing rates with time [10] as shown in Figure 6.

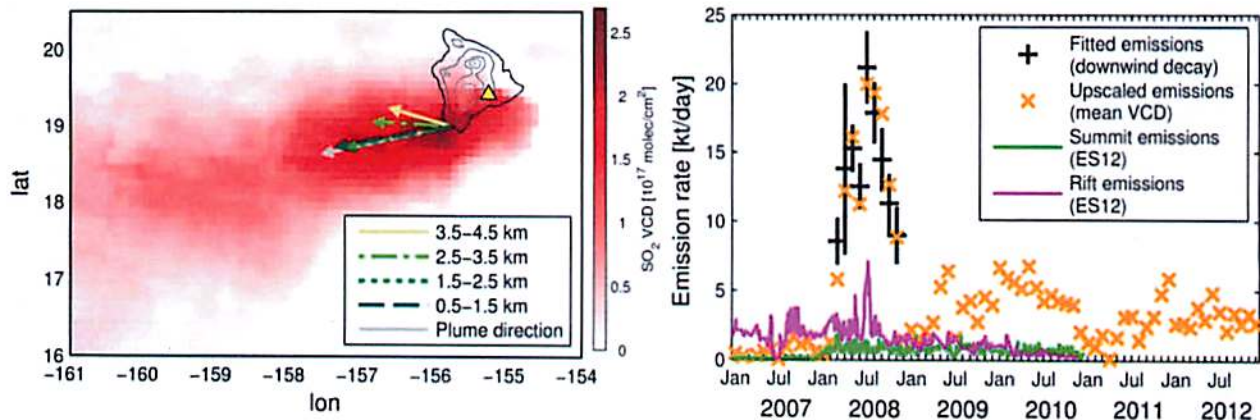


Figure 6. Left plot: Monthly mean SO₂ vertical column density (VCD) for August 2008. Grey lines show surface elevation of Hawai'i with contours of 1 km. Velocity vector lengths of 1° correspond to 5 m/s. Kilauea is the yellow triangle. Right plot: Time evolution of Kilauea's SO₂ emission rate. All data is from UV spectral data from the GOME-2 instrument aboard the MetOp-A satellite except the green/magenta lines that are from ground-based measurements for comparison. Modified from [9].

References

- [1] *Volcano Monitoring Techniques*. <http://volcano.oregonstate.edu/vwdocs/vwlessons/monitors.html>
- [2] Hamilton, C., Glaze, L., James, M., Baloga, S. (2013). *Topographic and stochastic influence on pahoehoe lava lobe emplacement*. Bull. Volcanol. 75, 756.
- [3] Montgomery-Brown, E. K. and 6 co-authors (2010). *Geodetic evidence for en echelon dike emplacement and concurrent slow slip during the June 2007 intrusion and eruption at Kilauea volcano, Hawaii*. JGR 115, B07405.
- [4] Wright, R., Flynn, L., Garbeil, H., Harris, A. & Pilger, E. (2004). *MODVOLC: near-real-time thermal monitoring of global volcanism*. Journal of Volcanology and Geothermal Research 135, 29-49.
- [5] Tsang, C., Rathbun, J., Spencer, J. Hesman, B., & Oramov, A. (2014). *Io's hotspots in the near-infrared detected by LEISA during the New Horizons Flyby*. LPSC 45, 1163.
- [6] Smrekar, S. & 7 co-authors. (2010). *Recent hotspot volcanism on Venus from VIRTIS emissivity data*. Science 328, 605.
- [7] Bondarenko, N., Head, J., & Ivanov, M. (2010). *Present-day volcanism on Venus: Evidence from microwave radiometry*. GRL 37, L23202.
- [8] Shalygin, E., Markiewicz, W., Basilevsky, Titov, D., Ignatiev, N., & Head, J. (2014). *Bright transient spots in Ganiki Chasma, Venus*. LPSC 45, 2556.
- [9] Rybin, A. and 6 co-authors (2011). *Satellite and ground observations of the June 2009 eruption of Sarychev Peak volcano, Matua Island, Central Kuriles*. Bull. Volcanol. 73, 1377.
- [10] Beirle, S., Hormann, C., Penning de Vries, M., Dorner, S., Kern, C., & Wagner, T. (2013). *Estimating the volcanic emissions rate and atmospheric lifetime of SO₂ from space: a case study for Kilauea volcano, Hawai'i*. Atmos. Chem. Phys. Discuss. 13, 28695.

Tephra Production and Stratigraphy

Patricio Becerra



I. Tephra Production

I.1 Pyroclastic Sedimentary Rocks:

Tephra is defined as material of any size or composition (fragments of rock, mineral and glass) ejected by volcanic explosions. Pyroclastic rocks are produced when tephra lithifies. Several size classes of tephra are used to categorize pyroclastic sedimentary rock types (Table 1).

Size Class Range	Siliclastic Sediment Size Class	Tephra Name	Pyroclastic Sedimentary Rock Type
> 64 mm	Cobbles, boulders	Blocks (angular), Bombs (rounded)	Volcanic Breccia, Agglomerate
2-64 mm	Granules, pebbles	Lapilli	Lapilli Stone
1/16 – 1 mm	Sand	Coarse ash	Coarse tuff
< 1/16	Silt, Clay	Fine ash	Fine tuff

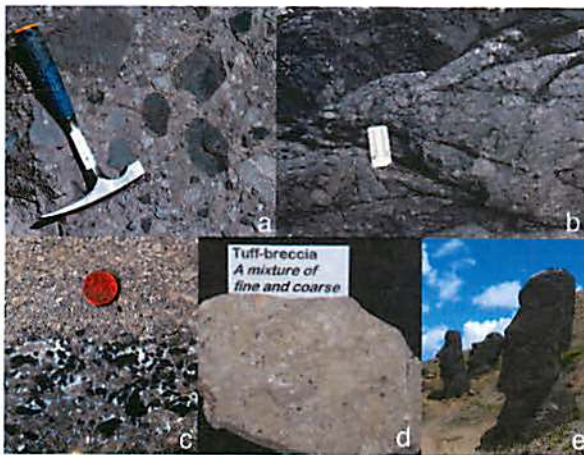


Fig 1. (a) West-elk Breccia (CGS) (b) Agglomerate from the Seymour Canal Formation, Alaska (USGS) (c) Carbonatic Lapillistone (d) Example of volcanic tuff (e) The Moai on Easter Island are carved out of theolite basalt tuff

I.2 Origin

1. Pyroclastic fall deposits: Rainout of clasts through the atmosphere from an eruption jet or plume during an explosive eruption.
2. Volcaniclastic flow deposits: Form when tephra moves downslope as a pyroclastic flow, pyroclastic surge or Lahar
 - a) Pyroclastic flows: A pyroclastic density current in which most of the material and momentum is contained in a basal concentrated particulate dispersion. Pyroclastic flows carry a large range of particle sizes. Shear effects are greater at the base, so ash and lapilli are found here. Blocks and bombs are driven toward the top of the flow. The interior of the flow is the hottest area and welded tuff, or ignimbrites are formed here.
 - b) Pyroclastic Surge Deposits: A pyroclastic density current in which the material and momentum are widely distributed through a deep, dilute, highly turbulent particulate suspension. The momentum of the expanding gas and particles, as well as gravity drives the surges. Particle concentration occurs at the base of the flow, so sedimentation happens in the bedload.
 - c) Lahars: Mudflows formed of saturated volcanic material. They can occur when large amounts of precipitation fall onto slopes mantled with consolidated ash, or when a volcanic eruption mixes with a river or melting snow.

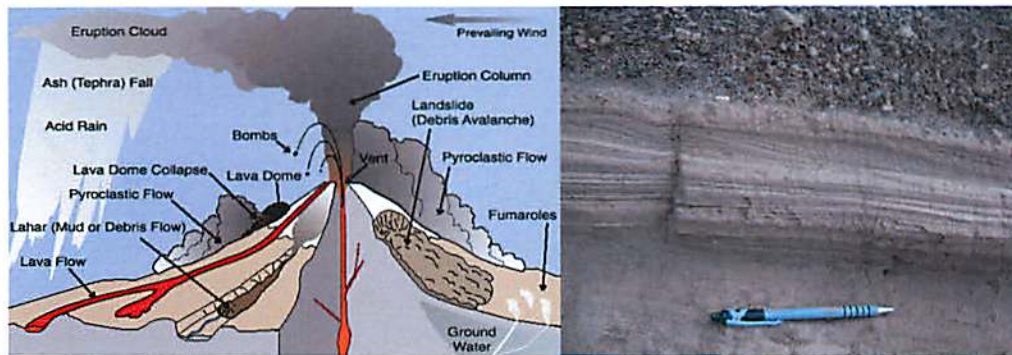


Fig. 2. (Left) Different types of eruption events that lead to the formation of pyroclastic sedimentary rocks. (Right) Volcaniclastic deposits in Santorini, Greece. The lower bedding is an ashfall deposit, representing the beginning stages of the eruption. The middle layers were formed by a pyroclastic surge or pumice fall, and are well sorted. Finally, the top layers were formed by a chaotic and more energetic pyroclastic flow.

II. Stratigraphy: Terms and Definitions

II.1. Stratigraphy: Description of all rock bodies forming planetary crusts and their organization into distinctive, useful, mappable units based on their inherent properties or attributes in order to establish their distribution and relationship in space and their succession in time, and to interpret geologic history.

II.2. Facies: Associations of sedimentary rock that share some aspect of appearance (Blatt, Middleton, and Murray, 1980, p.4). A lithofacies denotes a consistent lithologic character within a formation, excluding its fossil character.

II.3. Unconformities: A temporal break in a stratigraphic sequence resulting from a change in regimen that caused deposition to cease for a considerable amount of time. Normally, an unconformity implies uplift and erosion with the loss of some of the previously formed record. There are four kinds:

II.4. Correlation: Process of demonstrating the equivalence or correspondence of geographically separated parts of a geologic unit.

II.5. Geologically Instantaneous events: In order to establish time equivalence in the stratigraphic record we must use time markers that are widespread, distinctive and geologically instantaneous. Events that were separated by years to tens of years cannot be resolved in the stratigraphy, and are therefore considered geologically instantaneous. A number of rock types may be considered to have formed instantaneously from a geologic viewpoint. The most common are volcanic deposits from a single eruption.

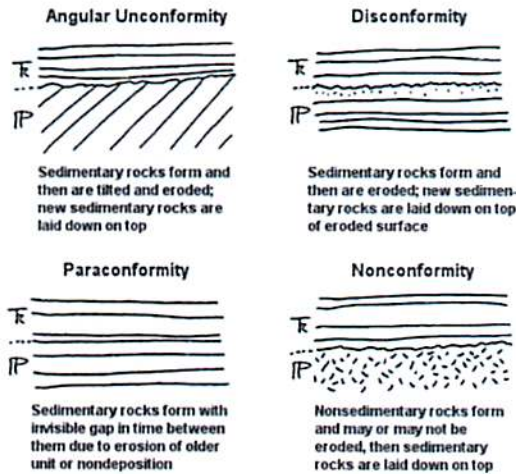


Fig. 3. Sketch diagram of different types of unconformities.

II.6. Tephrostratigraphy: The use of ash layers to mark geologic time in a stratigraphic sequence.

III. Kilauea Iki Tephra

The 1959 Kilauea eruption partially filled a preexisting pit crater with lava, and some of the highest lava fountains on record in Hawai'i built a substantial scoria cone (Pu'u Pua'i; gushing hill) and downwind tephra deposit (Fig. 9; Macdonald, 1962; Richter et al., 1970).

IV. Planetary Connection.

IV.1. Plains material on Venus:

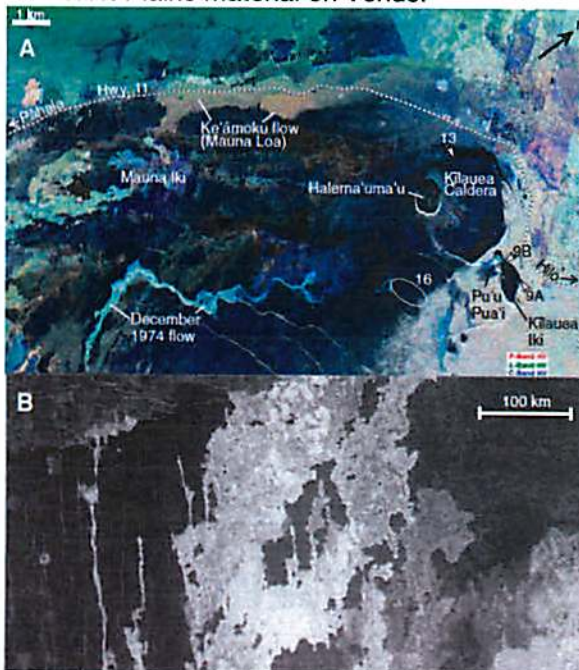


Fig. 3. Synthetic aperture radar (SAR) data for Kilauea and Sif Mons, Venus. (A) A 3-wavelength composite of P band (68 cm), L band (24 cm), and C band (5.6 cm) wavelengths in red, green, and blue, respectively. Kilauea caldera, Kilauea Iki, and Halema'uma'u are all radar-dark because they are mostly smooth ponded lava flows. (B) Numerous, complex lava flows, some of which have been constrained by preexisting fractures, on the north flank of Sif Mons,

IV.2. Pyroclastic deposits and dark halo craters on the Moon

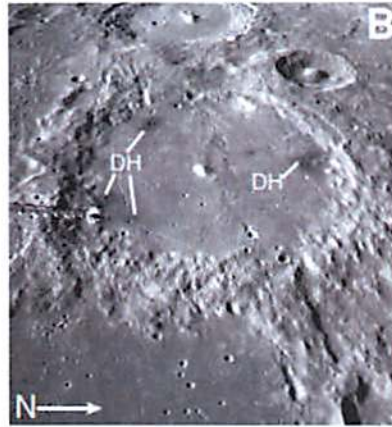
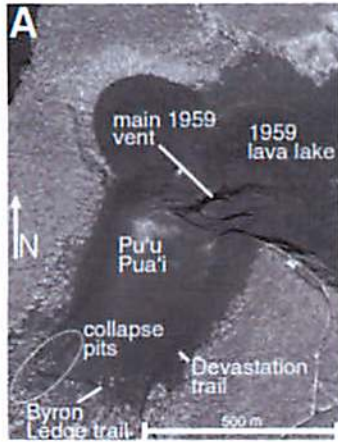
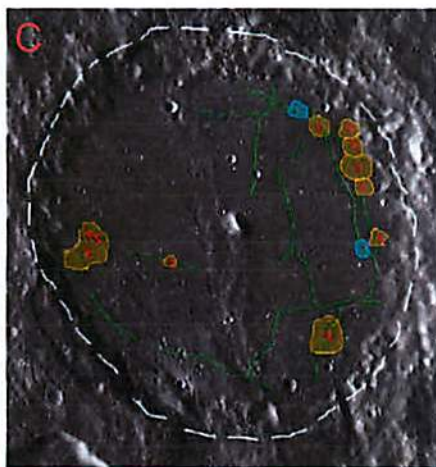


Fig. 4. Tephra deposits. (A) Thickest part of the downwind tephra deposit from the 1959 Kilauea Iki eruption. The dashed ellipse shows the region of collapse pits (Fig. 10). (B) An oblique view looking west, showing dark halo deposits (DH) within the lunar Alphonsus Crater, which is ~100 km across. Apollo-16 image number AS16-M-2478. (C) LROC image of Alphonsus crater (108 km. diam.) and the locations of major floor fractures (green), 11 dark-halo craters (after 1)), and two newly identified vents. Kaguya Terrain Camera evening mosaic.



IV.3. Medusa Fossae Formation on Mars

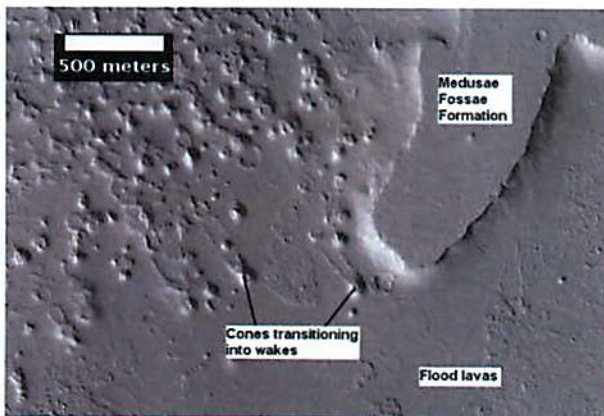


Fig. 5. Plateau made up of Medusae Fossae materials and rootless cones, as seen by HiRISE. Rootless cones are caused by lava interacting with water ice. Wakes are caused by lava flowing over a source of steam.

References

- Prothero R. and Schwab F. (2004). Sedimentary Geology: An Introduction to Sedimentary Rocks and Stratigraphy. 2- Ed. W.H. Freeman and Company
- Rowland et al. (2013). NASA volcanology field workshops on Hawai'i: Part 1. Description and history. Geological Society of America Special Papers 2011; 483; 401-434.
- Encyclopedia of Volcanoes, Academic Press, 2000.
- Walters, T.R., et al., (2007), Radar Sounding of the Meusae Fossae Formation Mars: Equatorial Ice or Dry, Low-Density Deposits? Science 318, 1125.



Contents lists available at SciVerse ScienceDirect

Acta Astronautica

journal homepage: www.elsevier.com/locate/actaastro

Io Volcano Observer (IVO): Budget travel to the outer Solar System

Alfred McEwen^{a,*}, Elizabeth Turtle^b, Kenneth Hibbard^b, Edward Reynolds^b, Elena Adams^b

^a University of Arizona, Tucson, AZ 85721, USA

^b Johns Hopkins University, Applied Physics Laboratory, USA

ARTICLE INFO

Article history:

Received 19 December 2011

Received in revised form

9 May 2012

Accepted 23 May 2012

Keywords:

Io

Volcanism

Spacecraft

Tidal heating

Radiation

ABSTRACT

The IVO mission would make multiple close encounters with Io while orbiting Jupiter in an inclined elliptical orbit. The payload includes narrow-angle and wide-angle cameras (NAC and WAC), dual fluxgate magnetometers (FGM), a thermal mapper (ThM), dual ion and neutral mass spectrometers (INMS), and dual plasma ion analyzers (PIA). The mission is designed to answer key outstanding questions about Io, especially the nature of the intense active volcanism and internal processes that drive the volcanism. IVO can collect and return 20 Gb of compressed science data per Io encounter, 100 times the total Io data return from the 8yr Galileo tour.

© 2012 Elsevier Ltd. All rights reserved.

1. Io mission studies and recommendations

Io is one of the most dynamic worlds in the Solar System [1], with hundreds of active volcanic eruptions driven by tidal heating, an SO₂ atmosphere that is highly variable in space and time, and orbiting within the Io plasma torus and Jupiter's magnetosphere.

An Io Observer mission was mentioned in 2002 Solar System Decadal Survey [2] for a New Frontiers Class mission in the next decade (2013–2023), but science objectives were not established. The 2007 NRC study on choices for the 3rd New Frontiers opportunity [3] recommended inclusion of Io Observer, and specified 7 science objectives. No radioisotope power was available for NF-3.

The Io Volcano Observer concept was selected and studied via NASA's Discovery and Scout Mission Capabilities Enhancement (DSMCE) program in 2009, specifically for missions enabled by use of the Advanced Stirling Radioisotope Generators (ASRGs). The results of this study [4]

were sufficiently encouraging to proceed, and an IVO step-1 proposal was submitted to Discovery 2010. The proposal was ranked "selectable" but not selected.

Meanwhile, the most recent decadal survey "Vision and Voyages for Planetary Science in the Decade 2013–2022" [5] listed Io Observer as one of seven recommended future candidate missions for New Frontiers. Both solar and ASRG power options were studied as a part of the Decadal study, but it neglected the critical issue of pointing stability.

2. Science objectives

"Vision and Voyages" [5] listed seven science objectives for Io Observer (not in priority order), similar to the 2008 NRC study:

1. study Io's active volcanic processes;
2. determine melt fraction of Io's mantle;
3. constrain tidal heating mechanisms;
4. study tectonic processes;
5. investigate interrelated volcanic, atmospheric, plasma-torus, and magnetospheric mass and energy-exchange processes;

* Corresponding author. Tel.: +1 520 270 0701.

E-mail address: mcewen@jpl.arizona.edu (A. McEwen).

Table 1
IVO science and measurement objectives.

<p>Understand the eruption and emplacement of Io's currently active lavas and plumes.</p> <p>Document the variety and characteristics of volcanic landforms and vent structures on Io. Monitor active changes (e.g. plume deposits and silicate and sulfurous flows) at Io's major volcanic centers to understand resurfacing processes and rates. Observe dynamic phenomena to measure velocities and constrain instantaneous effusion and integral eruption rates. Document recent (~100 yr) volcanic history by mapping 100 K to ≥ 1000 K surfaces (decades to seconds old) and compare to current activity. Document the chemical species in Io's plumes to constrain the chemistry of source regions and the effects of magma ascent through the crust. Measure the temperature of erupting lava to constrain composition, lava eruption dynamics, and interior processes.</p> <p>Determine the melt state of Io's mantle and map heat flow patterns to distinguish between shallow and deep-mantle tidal heating.</p> <p>Determine the melt fraction of the mantle from models based on peak lava temperatures and via electromagnetic sounding. Map the global pattern (especially with latitude) of endogenic heat flow driven by tidal heating. Characterize the magnetic environment to better constrain the nature of Io's core and potential internal magnetic field. Determine whether regional topographic anomalies exist and compare to heat flow and other patterns. Measure or more tightly constrain the rate of Io's nonsynchronous rotation.</p> <p>Determine the state of Io's lithosphere and understand its tectonic processes via observations of mountains and paterae.</p> <p>Image and map topography of representative landforms. Search for structural changes, e.g., large-scale landslides and/or caldera collapse events since Voyager and Galileo imaging.</p> <p>Understand Io's surface–plume–atmosphere compositions and interactions</p> <p>Measure composition and abundances of neutral species near Io. Remote sensing of SO₂, OI, and other emissions (in eclipse) to better understand magnetospheric–atmospheric interaction, atmospheric composition and collapse. Map Christensen frequency to constrain SiO₂ abundances of warm silicate lavas (not covered by SO₂ frost). Map color variations for determining the distribution of sulfurous species and silicate minerals. Measure surface temperatures throughout diurnal cycles and eclipses to constrain atmospheric and frost processes.</p> <p>Understand Io's mass loss, exosphere, and magnetospheric interactions</p> <p>Measure ionized species in the exosphere and plasma torus. Remote sensing of Na cloud and Io plasma torus. Measure density, energy, and temporal variability of plasma and magnetic signatures.</p>

- constrain the state of Io's core via improved constraints on whether Io generates a magnetic field;
- investigate endogenic and exogenic processes controlling surface composition.

These objectives are very similar to those used for IVO 2010, although prioritized and subdivided into measurement objectives (Table 1).

One objective unique to Io is to acquire nearly simultaneous multispectral measurements to determine the peak lava temperatures [6]. A time differential as short as 0.1 s between color filter images can give spurious results due to lava fountaining and rapid radiative cooling at silicate lava temperatures. We plan to lay out color filter strips in a way that enables nearly simultaneous color measurements using the narrow-angle camera in the pushbroom mode. These peak temperatures in turn constrain the temperature and rheology of Io's mantle [7] and whether or not the heat flow is in equilibrium with tidal heating, with implications for the coupled thermal–orbital evolution of Io and Europa.

3. Mission overview

IVO would most likely use a Venus–Earth–Earth Gravity Assist (VEEGA) trajectory, for which launch

opportunities recur every couple of years on average [8]. Jupiter orbit insertion typically occurs 5–6 yr after launch. The spacecraft would be captured into an elliptical orbit that encounters Io near periape. Two of the encounters could be optimized for measurement of the induced magnetic signature from mantle melt [9], via nearly identical flyby geometries except one near the maximum magnetic latitude and the other near its minimum.

The spacecraft would nominally collect and record 20 Gb of science data per encounter—100 times the Io data return from the Galileo mission over 8 yr. The data would be relayed to Earth near apoapsis. With ~7 Io encounters and an orbital period of ~2 months (more for the initial orbits until the period is pumped down by the Io flybys), the nominal mission duration at Jupiter would be ~2 yr. Following potential extended missions, the mission would end by impact into Io or Jupiter. The calculated probability of icy moon impact is $< 10^{-9}$.

IVO's orbit is optimized both for Io science objectives and to minimize total ionizing dose (TID). The orbit is inclined ~45° to Jupiter's orbital plane, resulting in nearly north–south flybys near Io. This geometry minimizes total dose per flyby because the spacecraft passes through the narrowest part of the high-radiation zone and does so at a velocity near 19 km/s. The result is just ~10 krad TID per flyby (behind 100 mils Al), versus ~85 krad/flyby for the Jupiter Europa Orbiter (JEO) as studied in 2008 [8]. The

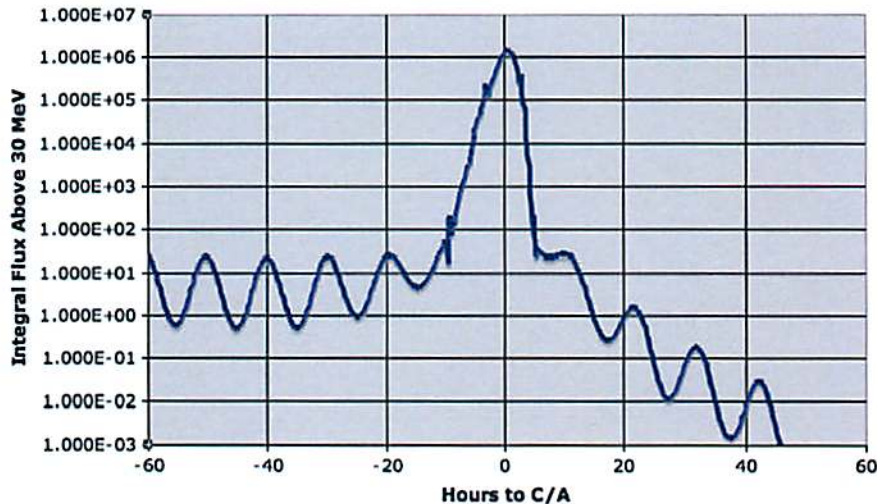


Fig. 1. Integral flux above 30 MeV (assuming ~ 1 cm Ta shielding) versus time to closest approach in a typical Io encounter.

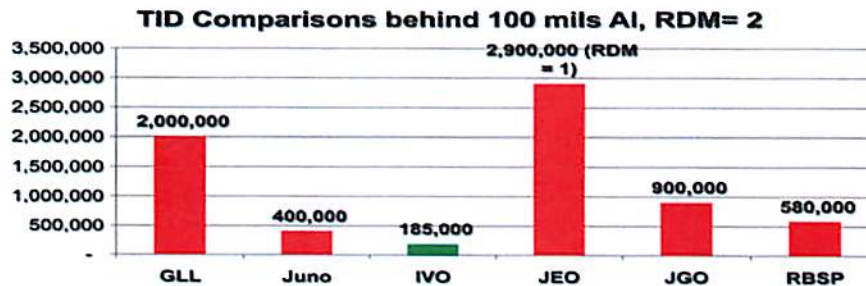


Fig. 2. TID for past and potential future Jupiter missions, normalized to 100 mils Al shielding and with a radiation design margin of 2 except for JEO (RDM=1) and Galileo (actual estimated TID for full mission). Also shown is the expected TID for the Radiation Belt Storm Probe mission.

spacecraft spends only ~ 15 h/flyby in the intense radiation (see Fig. 1). The TID of IVO is significantly less than that of other Jupiter orbiters (Fig. 2).

The pole-to-pole flyby geometry is best for probing Io's interior with the magnetometers, and as the spacecraft approaches (and recedes from) Io, radiation-induced noise is sufficiently low to allow measurement of faint emissions such as those from Io in eclipse. Furthermore, the approach and departure geometry provides excellent views of the polar regions, key to testing tidal heating and atmospheric models. The subsolar longitude changes slowly with each encounter, since the Jupiter year is 10 yr long; this is best for change detection to understand active processes.

4. Science payload

We determined that the IVO science objectives can be fully accomplished with a science payload consisting of five experiments. All instruments must be designed to collect useful data near Io in very fast flybys, and with no operational conflicts.

4.1. Narrow-Angle Camera (NAC)

The NAC is key to many IVO objectives, in all five major groups (Table 1). The NAC we envision would have a $5 \mu\text{rad}/\text{pixel}$ IFOV, like LORRI on New Horizons [10], but

with a new $2\text{k} \times 2\text{k}$ detector and more capable digital processing unit (DPU). Half of the array would be covered by stripes of color bandpasses, and half of the array would be clear for framing images and movies. The color images would be acquired in pushbroom mode, adding up to 64 rows for digital time-delay integration (dTDI).

The detector uses Complementary Metal Oxide Semiconductor (CMOS) technology for scientific performance [11] that features low read noise, good MTF, large dynamic range, and a large spectral range. For IVO, the advantages of CMOS over CCD technology are (1) very fast readout times, (2) imaging in either pushbroom or framing modes, (3) low power, and (4) reduced performance degradation after a high TID. The tolerance to TID (barely measurable degradation after 1 Mrad from energetic electrons) far exceeds IVO's requirement inside the 1 cm Ta shielding needed to minimize radiation-induced noise. On-chip double sampling eliminates row-settling time for fast readout ($0.025 \mu\text{s}/\text{pixel}$, $> 500 \times$ faster than Galileo SSI), further minimizing radiation-induced noise.

The NAC DPU is derived from previous APL DPUs, such as MRO CRISM [12] and LORRI support electronics, and with more capable FPGAs for implementation of dTDI and memory-efficient wavelet compression algorithms [13].

The NAC achieves excellent ($> 100:1$) SNRs for nominal imaging. SNR calculations include the expected energetic particle flux and induced noise behind 1 cm Ta [14]. There are two challenging cases:

1. For high-resolution imaging near Io, NAC line times are very short (e.g., 0.28 ms at 1000 km). An SNR of 40:1 is achieved for clear-filter pushbroom imaging of dayside Io with a 1000-pixel swath and 11 dTDI lines. Higher SNRs are possible by binning or by sacrificing swath width to allow more dTDI lines, limited by the data transfer rate to the DPU.
2. For eclipse imaging of faint Io plume and atmospheric emissions, all observations occur with IVO outside the radiation belt (Fig. 2), greatly reducing radiation noise, but exposure times are limited by the pointing stability.

4.2. Wide-Angle Camera (WAC)

The WAC will have a field of view of $\sim 26^\circ$ (200 μrad /pixel) to enable stereo mapping, key to several science objectives, as well as to cover greater area on Io than the NAC when at close range. It will utilize an identical focal plane system and DPU as those of the NAC, and will also have color bandpasses and a framing area. The worst-case signal:noise ratio (SNR) is much less severe for the WAC than for the NAC as $40\times$ longer exposure times can be used near Io.

4.3. Fluxgate Magnetometer (FGM)

The FGM meets a key objective by mapping the magnetic field strength and variability to distinguish between melt states of Io's mantle. To meet these requirements, the FGM design includes 0.5% absolute accuracy (0.25 nT at 50 nT), and 0.12 nT sensitivity. To meet the S/C settling time requirement (for imaging), a long extensible boom is excluded and dual FGM sensors (for identification and removal of S/C variable fields) are mounted on the S/C (Fig. 3 shows one possible configuration). Both FGM sensors operate continuously at Jupiter at a low sampling rate (1 vector/s). Within 20 Io radii the rate increases to 30 vectors/s.

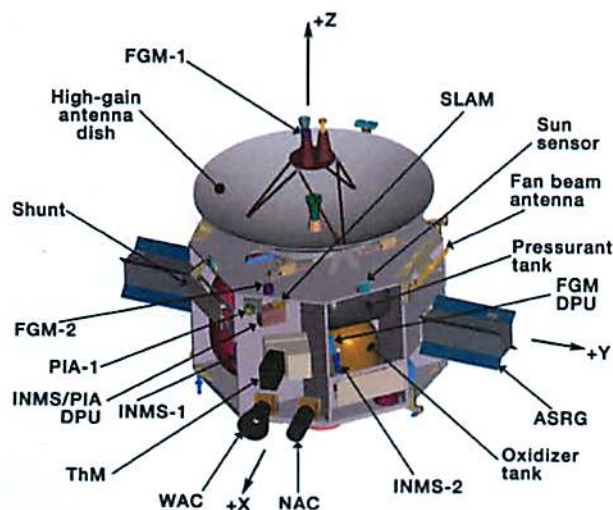


Fig. 3. IVO spacecraft; 2.1 m HGA for scale.

4.4. Thermal Mapper (ThM)

The ThM can be similar to the Thermal Emission Imaging System (THEMIS) on Mars Odyssey [15], but with an improved microbolometer detector, greater radiation shielding or radiation-hardened part selections, and excluding the visible imager. Also, for IVO we need spectral bandpasses extending from 2 μm (to study cooling lavas) to 30 μm (to measure the background temperatures), as well as several bandpasses in the 7–12 μm region for silicate mineralogy. Only the still-warm lavas provide sufficient signal to measure the small emission variations with wavelength, and these are also the only regions free of SO_2 frost cover, revealing the silicate compositions. A global spatial resolution of ~ 200 km is adequate to measure the global heat flow, but ~ 20 km over local areas is needed for silicate mineralogy.

The microbolometer detector technology is ideal for the radiation environment near Io, because energetic particles pass through the thin films with little interaction [14]. Hence, radiation-induced noise is not a problem, in contrast to the severe challenge of near-IR reflectance spectroscopy.

4.5. INMS/PIA Package (IPP)

The IPP consists of dual Ion and Neutral Mass Spectrometers (INMS) and dual Plasma Ion Analyzers (PIA), with shared electronics.

INMS science objectives include measuring abundances of neutral and ionized species in atmosphere, plumes, exosphere and plasma torus, and measuring plume species (S, O, SO_2 , S_2 , SO, Na, K, Cl, and unknown species) to model equilibrium chemistry of magma chambers. INMS has a high potential for new discoveries because the composition and abundances of neutrals escaping from Io are poorly known.

PIA science objectives include measurement of the density, energy, and temporal variability of plasma near Io, both to understand plasma interactions better and to calibrate plasma contributions to the magnetic signature of mantle melt.

The reason for flying two INMS detectors is to provide more operational flexibility and opportunities for measurements (in the ram direction) concurrent with remote sensing of Io, and to calibrate out the possible effects of thruster plume gases [16]. Two PIA, on opposite sides of the spacecraft and each with a full hemisphere view, means that PIA data collection (in the upstream direction) is always possible when near Io.

Because of the use of the microchannel plates in the INMS, a new shielding concept is being developed.

4.6. Synergy of science measurements

IVO addresses the key question of the distribution and abundance of melt in Io's interior in multiple ways:

- (1) determine the peak lava temperatures (NAC and WAC);

- (2) measure the induced magnetic response (FGM);
- (3) heat flow mapping (ThM) provides supporting information, especially if a pattern with latitude is clear;
- (4) determine the silica content of lavas (ThM), as less silica implies a higher melting point;
- (5) determine the magma chamber temperature based on the chemistry of plume gases (INMS), if IVO flies through a primary plume like Pele or Tvashtar (rather than the many secondary SO₂ plumes).

5. Challenges

Exploration of the outer Solar System is challenging due to the need for long-duration missions and operation in extreme environments. IVO can meet these challenges as described below.

Power is a major constraint far from the sun, especially for a mission such as IVO that needs to turn and settle quickly to achieve its science objectives, prohibiting large solar arrays in the absence of further mechanisms. NASA's investment in ASRGs enables IVO; the spacecraft has been carefully designed to require just 2 ASRGs. Key to this design is use of a Thermos bottle design, making efficient use of heat generated by low-power electronics. The hot case is the Venus flyby, for which the S/C is shaded by the high gain antenna, the electronics have louvered radiators to expel heat, and there are sun shades over the ASRGs (later jettisoned). The store and forward concept for data acquisition not only eliminates the need for gimbals on the high gain antenna, but also helps maintain low power consumption. A 6 yr extended mission would fit within the 14 yr design lifetime of the ASRGs.

Getting there and capturing into a Jupiter orbit optimized for IVO in a reasonable amount of time using an affordable launch vehicle is another challenge. IVO plans use of the Venus–Earth–Earth Gravity Assist (VEEGA) trajectory that was used by the Galileo and Cassini missions. The Atlas V-401 launch vehicle provides generous mass margins (~50% to dry mass) using this trajectory and a simple ASRG-powered spacecraft, depending on the actual launch date.

Radiation is a major concern close to Jupiter. The team employs a system-level approach to radiation mitigation, directly drawing upon experiences from designs and studies for missions such as Radiation Belt Storm Probe (RBSP) and JEO. IVO's inclined and highly elliptical orbit leads to rapid passes through the most intense radiation, such that total dose is 100 krad behind 280 mil Al and 2 × design margin, < 5% of that experienced by Galileo [17]. Nevertheless, the science instruments collect important data when close to Io and near the peak flux, which can produce transient noise in some detectors [14]. The cameras use a combination of shielding and CMOS detectors with extremely fast readout [11] to minimize noise. Shielding is also needed for the INMS and PIA detectors. The FGM is not sensitive to noise induced by energetic particles and the ThM microbolometer is nearly insensitive. IVO will use proven radiation-hardened parts and is expected to have ample mass margin to increase shielding if needed.

Cost is a major challenge for cost-capped opportunities such as Discovery. PI-managed costs are kept low via a combination of methods. The spacecraft is as simple as possible while meeting the reliability needed for a radioisotope-powered mission (Fig. 3). The mission and spacecraft are developed largely "under one roof" at APL. New technology is limited to the ASRGs and radiation mitigation for some science instruments. There are very few moving parts: ASRG pistons, thruster valves, louvers, and a calibration flag for the ThM. Some of the instruments could be contributed by foreign partners. Low-cost operations over the 8 yr nominal mission, including hibernation during cruise, have been developed by APL for missions such as New Horizons and MESSENGER. The science team is the minimal size needed during development and cruise.

6. Science Enhancement Options (SEOs)

Several SEOs are envisioned for IVO. An encounter with a mainbelt asteroid would provide a "dress rehearsal" for the Io encounters as well as asteroid science. We would certainly hope to add participating scientists before arrival at Jupiter. We envision two possible Extended Mission options. First, we could use Io gravity assists to pump the orbit out to ~1 yr period to enable ~8 additional Io flybys in ~6 yr; this only doubles the TID and should be feasible given a radiation design margin of two. Since 6 yr is more than half of a Jupiter year, we could complete global high-resolution imaging in daylight and at night. A potential flyby of an outer satellite (perhaps a captured Kuiper Belt Object) could provide important new science as well. A second or alternate Extended Mission could be called "Inside Io." We would pump the orbit down to a short period (weeks) for intensive gravity and magnetic data collection. This ensures end of mission within 1 yr due to the rapid rise in TID.

Acknowledgments

We thank reviewers David Williams (ASU) and Jack Connerney (GSFC) as well as the IVO team for past (and future) efforts. NASA provided support via the DSMCE program and a PIDDP grant to develop a focal-plane system for a radiation-hard camera.

References

- [1] A. Davies, *Volcanism on Io: A Comparison with Earth*, Cambridge University Press, 2007.
- [2] M. Belton, et al., *New Frontiers in the Solar System*, National Academies Press, 2003.
- [3] R. Beebe, et al., *Opening New Frontiers in Space: Choices for the Next New Frontiers Announcement of Opportunity*, National Academies Press, 2008.
- [4] A. McEwen, et al., *Io Volcanic Observer (IVO)*, *Lunar Planet. Sci.* 40 (1876) (2009).
- [5] Available at <<http://www.nap.edu/catalog/13117.html>>.
- [6] L. Keszthelyi, A.G. Davies, A.S. McEwen, *Optimal wavelengths for studying thermal emission from active volcanoes on Io*, *Lunar Planet. Sci. Conf.* 40 (1943) 2009.

- [7] L. Keszthelyi, L.W. Jaeger, M. Milazzo, J. Radebaugh, A.G. Davies, K. Mitchell, New estimates for Io eruption temperatures: implications for the interior, *Icarus* 192 (2007) 491–502.
- [8] K. Clark et al., 2008, JEO study, <<http://opfm.jpl.nasa.gov/>>.
- [9] K. Khurana, et al., Evidence of a global magma ocean in Io's interior, *Science* 332 (2011) 1186.
- [10] A. Cheng, et al., Long-range reconnaissance imager on new horizons, *Space Sci. Rev.* 140 (2007) 189–215.
- [11] J. Janesick, et al., Fundamental Performance Differences of CMOS and CCD Imagers: Part IV. Proc. SPIE paper 7742-11, San Diego, 2010.
- [12] S. Murchie, et al., Compact reconnaissance imaging spectrometer for Mars (CRISM) on Mars reconnaissance orbiter (MRO), *J. Geophys. Res.* 112 (2007) E05S03, <http://dx.doi.org/10.1029/2006JE002682>.
- [13] J.R. Hayes, K. Strohbehn, G.A. Murphy, Low-cost wavelet image compression for FPGAs, Proc. SPIE 7455 (2009) 7455D.
- [14] J. Boldt, et al., Assessment of Radiation Effects on Science and Engineering Detectors for the JEO Mission Study, JPL (2008) D-48256.
- [15] P.R. Christensen, B.M. Jakosky, H.H. Kieffer, M.C. Malin, H.Y. McSween Jr., K. Nealon, G.L. Mehall, S.H. Silverman, S. Ferry, M. Caplinger, M. Ravine, The thermal emission imaging system (THEMIS) for the Mars 2001 odyssey mission, *Space Sci. Rev.* 110 (2004) 85–130.
- [16] S. Graf, et al., Thruster plumes: sources for high pressure and contamination at the payload location, *J. Spacecraft Rockets* 45 (2008) 57–64.
- [17] P.D. Fieseler, S.M. Ardan, A.R. Frederickson, The radiation effects on Galileo spacecraft systems at Jupiter, *IEEE Trans.Nucl.Sci.* 49 (2002) 2739–2758.



Dr. Alfred McEwen is a planetary geologist and professor at the University of Arizona, USA. He has participated in 10 deep space missions, including Galileo at Jupiter, for which he led the image observation planning for Io. Currently he is the Principal Investigator of the High Resolution Imaging Science Experiment (HiRISE) on Mars Reconnaissance Orbiter. He was also PI for the IVO proposal for Discovery 2010. In 2011 he received NASA's Distinguished Public Service Medal. For more, see <http://www.lpl.arizona.edu/Support/faculty/faculty.php?nom=McEwen>.



Dr. Elizabeth Turtle is a research scientist in the Planetary Exploration group at APL. She received her B.S. in Physics from MIT and her Ph.D. in Planetary Sciences from the University of Arizona. She was an associate of Galileo's imaging team and is an associate of Cassini's Imaging and RADAR teams and a member of Lunar Reconnaissance Orbiter's Camera team. Her research interests include combining remote sensing observations with modeling to study geological structures, including impact craters on terrestrial planets and icy satellites, mountain formation

on Io, and lakes on Titan, as well as seasonal changes in Titan's weather patterns.



Kenneth Hibbard received his B.S. in Aerospace Engineering from the Pennsylvania State University, and his M.S. in Systems Engineering from the Johns Hopkins University. He spent 8 years as a spacecraft systems and operations engineer at NASA Goddard working on the ACE, SOHO, and Swift spacecraft. At APL, Mr. Hibbard served as the MESSENGER Deputy Mission Operations Manager, and is currently a senior systems engineer supporting multiple programs, proposals, and mission studies. Mr. Hibbard serves as the Formulation Deputy Project Systems Engineer for the Europa mission study, and as the Mission Systems Engineer for the Titan Mare Explorer (TiME) Discovery proposal.



Edward Reynolds is Deputy project manager for Solar Probe Plus, and the former project manager for the STEREO mission. Mr. Reynolds has a bachelor's degree in electrical engineering from Virginia Tech. He has an extensive background in spacecraft system engineering, which stems from his experience in spacecraft integration and test. Prior to the STEREO mission, Mr. Reynolds played key engineering roles in several projects, including the Comet Nucleus Tour (CONTOUR) and the Near Earth Asteroid Rendezvous (NEAR), the first mission in NASA's Discovery program, which orbited and eventually landed on the asteroid Eros. Additionally, he has worked on a number of assignments involving satellites, and sounding rockets with engineers from Russia.



Dr. Elena Adams is a systems engineer in the Space Systems Applications group at APL. She received her B.S. in Applied Mathematics from University of Virginia, her M.S. and Ph.D. in Atmospheric, Oceanic, and Space Sciences, and M.E. in Space Systems Engineering from the University of Michigan. She has worked with a variety of instruments, including analyzing data from Cassini-Huygens GCMS and modeling of Jupiter's atmosphere in support of Juno MWR. Currently she serves as an instrument systems engineer on RBSP mission, as a systems engineer for JEO mission, and supports a variety of mission development studies and proposals.



HiTREE High-Temperature Radiant Energy Experiment

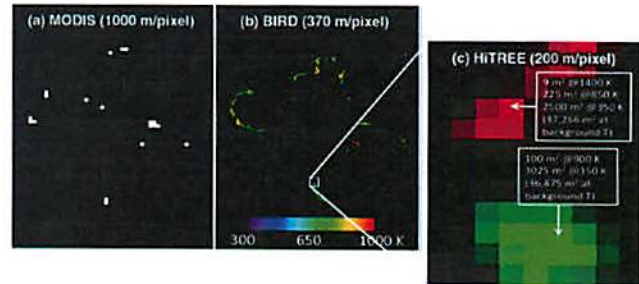
Measuring High-Temperature Events – Why It's Important

HiTREE closes an outstanding gap in Earth observation, providing a high-precision, multi-spectral imaging instrument to detect and study high-temperature events influencing global change.

- **Wildfires** may be increasing in both intensity (thermal power) and severity (damage to the ecosystem), releasing carbon sequestered in key regions such as boreal forests.
- **Biomass burning** is one of the largest uncertainties in quantifying the global carbon cycle.
- **Volcanic hazards** are increasing as populations grow near active volcanoes.
- The heights to which **smoke and volcanic plumes** are injected control their impact on the Earth system.
- Tracking natural and human-caused hazards provides societal benefits.

Measuring High-Temperature Events – Challenging due to the Great Dynamic Range & Rapid Changes in Signal

HiTREE meets this challenge with an innovative camera with high-TRL subsystems and straightforward instrument accommodation. HiTREE will be the only orbital experiment accurately measuring multiple high temperatures and their areas within a pixel, while simultaneously measuring the plume that is injecting material into the atmosphere.

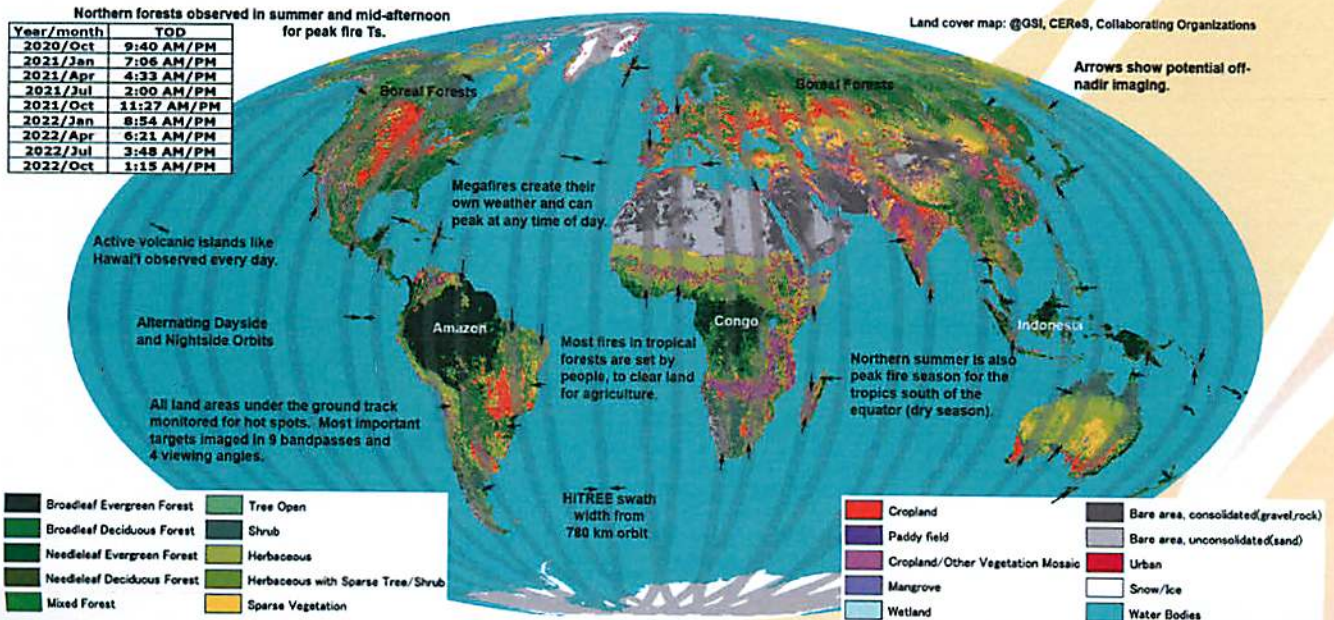


Better resolution and dynamic range and more wavelengths allow HiTREE to resolve firelines and distinguish multiple temperatures within a pixel.

Addressing Key NASA Earth Science Goals

- **Carbon Cycle & Ecosystems:** HiTREE determines how wildfire intensity impacts ecosystem change, such as conversion of forest to shrublands or grasslands that sequester less carbon.
- **Atmospheric Composition:** HiTREE determines how fire intensity drives biomass burning and the carbon cycle, and how fire intensity and plume heights affect atmospheric composition and climate change.
- **Earth Surface & Interior:** HiTREE measures and monitors the most critical parameter of an active eruption – the effusion rate – to which eruption hazards and environmental impact are closely tied.
- **Societal Benefits:** HiTREE detects hot spots and plumes marking health and safety hazards associated with wildfires, volcanic eruptions, and human activities.

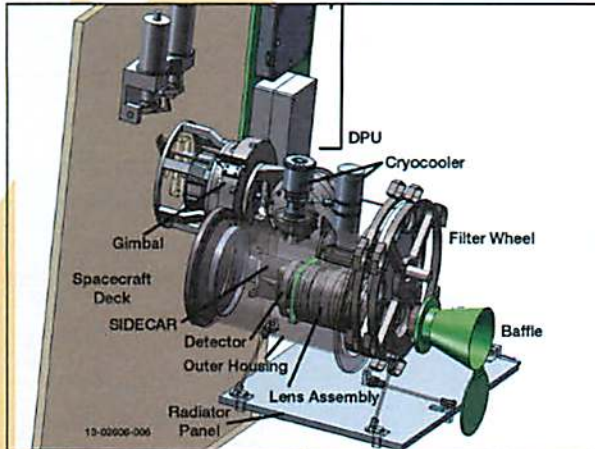
Northern forests observed in summer and mid-afternoon for peak fire Ts.	
Year/month	TOD
2020/Oct	9:40 AM/PM
2021/Jan	7:06 AM/PM
2021/Apr	4:33 AM/PM
2021/Jul	2:00 AM/PM
2021/Oct	11:27 AM/PM
2022/Jan	8:54 AM/PM
2022/Apr	6:21 AM/PM
2022/Jul	3:48 AM/PM
2022/Oct	1:15 AM/PM



HiTREE is flexible enough to reside on a number of hosts, but we use Iridium PRIME as the example host because of its ideal 780 km altitude and global coverage. Figure shows a one day example of Iridium groundtracks with the HiTREE swath width that includes a rich array of science targets, observed by combining image modes such as intensive multispectral repeat coverage over candidate hot-spot regions (~5% of time), color and plume monitoring (~10%), 1-band hot spot monitoring (~20%), and calibrations (<1%).

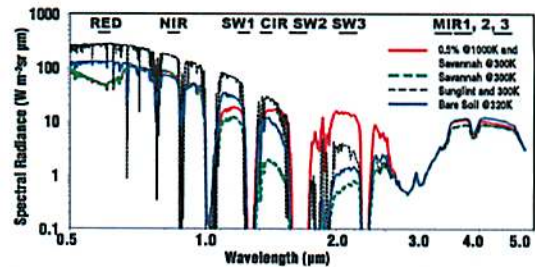
Instrument Characteristics

HiTREE provides an optimal instrument design for high-T observations, yet is simple and compact with high-TRL components.



Mass	56 kg (with contingency)
Volume (stowed)	49.1 cm x 76.4 cm x 42.2 cm
Power (avg)	68 W
FOV	30° (408 x 408 km from 780 km)
IFOV	256 μrad (200 m/pixel from 780 km)
Optics Aperture, F#	17.5 mm, f/4
Exposure Times	0.03 ms up to the line time (30 ms from 780 km)
Detector	Teledyne H2RG, 2048 x 2048 pixels
Focal Plane Electronics	Teledyne SIDECAR ASIC
Filter Wheel	9 slots 0.67 to 5 μm; 1 s between adjacent slots
Detector Cooling	110 K, cryocooler
Interior Optics Temp.	125 K, cryocooler
DPU	Data handling, compression, storage, autoexposure
Compression	Pixel binning, nonlinear bit-type conversion, wavelets
Data storage; rate	64 GB; ≥10 Mbps (≥0.5 Mbps orbit average)
Pointing	Usually nadir; gimbal for special observations & cal.
Gimbal mechanism	±90° tilt, ±200° azimuth

Bandpass (μm)	Uses
RED	0.66 – 0.68 Chlorophyll index, sun glints; aerosol opacity
NIR	0.845 – 0.885 Chlorophyll index, leaf water index, sun glints, plume stereo
SW1	1.22 – 1.28 Very high-T thermal, leaf water index, plume stereo
CIR	1.368 – 1.383 In deep water vapor absorption to identify cirrus or plumes above troposphere
SW2	1.56 – 1.66 High-T thermal; cloud/snow/ice discrimination, smoke from low burn-rate fires
SW3	2.16 – 2.24 High-T thermal; vegetation state; aerosol opacity
MIR1	3.56 – 3.64 Thermal; aerosol opacity; vegetation through smoke
MIR2	3.96 – 4.04 Thermal; best band to discriminate fire
MIR3	4.8 – 5.0 Thermal; best band for low-temperature anomalies and background



HiTREE bandpasses easily identify high-T events like fires. Figure (after Wooster et al. 2012) shows simulated spectra for savannah (green), an actively burning fire (red), sunglint (black), and solar-heated bare soil (blue).

- Simple and flexible operations with weekly upload of commands
- All land areas of Earth imaged ~2 times per week (day and night)
- Extensive calibrations ensure quantitative value of data products
- Automated hot-spot identification and alerts
- Level-1 data products produced via automated pipelines within hours of data receipt and made available immediately
- Data products follow Landsat conventions for ease of use by the research community

Operations & Data Products

The established track record of the HiTREE team from APL and UA ensures a successful, low-cost, low-risk project.

- HiTREE's PI, Alfred McEwen of the University of Arizona, is pairing his vast planetary remote sensing experience with his love for the environment to investigate how high-T events contribute to global change.
- McEwen leads a science team that includes leading experts in fire ecology, volcanology, remote sensing, calibration, and image processing.
- APL has developed >150 space instruments and has AS9100-certified management and development processes to ensure practical, cost-effective implementation of the project's goals and objectives.
- The UA College of Optical Sciences is one of the world's premier optical science institutes.

Management

Phase	14	15	16	17	18	19	20	21	22	23
A Development (7/2014 – 3/2015)										
B Design (4/2015 – 3/2016)										
C Design & Fabrication (4/2016 – 6/2018)										
D Assembly, Integration & Test (7/2018 – 6/2020)										
E Operation (7/2020 – 6/2022)*										
F Closeout (7/2022 – 6/2023)*										
Cost includes reserves. Phase E/F dates are notional since spacecraft has not yet been identified.										Total

Key Personnel	Principal Investigator: Alfred McEwen, UA Deputy PI: Willem van Leeuwen, UA Instrument Project Manager: Lora Suther, APL	Project Scientist: Elizabeth Turtle, APL Instrument Systems Engineer: John Boldt, APL Optics Subsystem Mgr: S. Hopkins Bailey, UA
----------------------	---	--



High-Temperature Radiant Energy Experiment

13-02606

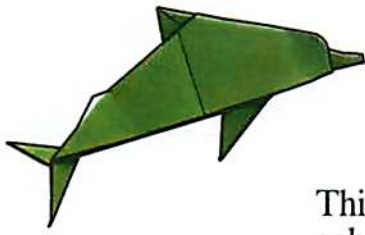


HAWAIIAN WORD SEARCH

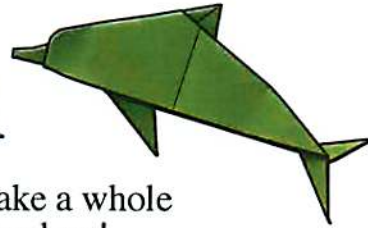
M B O Q H A T G N A O A Y A B E K R M D
 G O Z E L M B G W K R Z F U F O A Y L Z
 J O H O P A N I O L O H O L O H N O S A
 A A H A D Q K Y J X E C A C M S I R V I
 J A D E L I C R C D B G I J P F K L W A
 H J L D W A J W C S T U L M J D A X H J
 U A J I X T N K M B B F U A B N P E V O
 H N K N R R J A L N N B K H F D I Y X J
 N I M N G D Y K P V T I I A A T L P K Y
 R X M U E O E I F U G K L L V N A W D M
 L R Z H I O L P E X A H U O A P A L O E
 N F L R A L H A C O R I K D A Q C H B L
 X E D E P S R B K P N G A T L S X H O O
 N P H E F C Y X T A I A R M L I V Z Z A
 M E L E K A L I K I M A K A O A J U E H
 P O Q T L O H Z I I B A T G I M B W R Z
 P U J S D P D B H N L M I P K O O U Y W
 Z K R D X N T S C R G S Z L X C Y K M H
 H A L A O X W W B D L M H K V B V G E D
 P A P N G N O O A Y K Y F Q D S K W W G

Words (and their meanings)

<p> AKAMAI (smart) ALOHA (hello!) EKOMOMAI (welcome) HALA (kind of fruit tree) HALE (house) HAOLE (foreigner) HOLOHOLO (to wander) KANIKAPILA (musical jam session) KULIKULI (shut up!) </p>	<p> MAHALO (thank you) MELEKALIKIMAKA (Merry Christmas) MOHALANAPUA (blossoming flowers) OHANA (family) OLAPA (dance) PANIOLO (Hawaiian cowboy) PEHEAOE (how are you?) WIKIWIKI (speedy) </p>
---	--

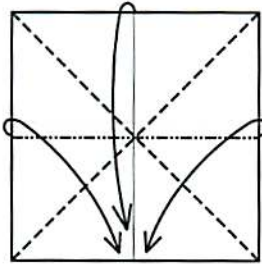


Dolphin



This model is simple enough to make a whole school of dolphins... even while in class!

1



Fold a colored Waterbomb Base. For help, consult the cloud.



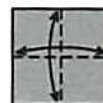
Waterbomb Base

1a



To fold a colored Waterbomb Base, first turn the paper over.

1b



Valley-fold and unfold in half both ways. Turn over.

1c



Valley-fold and unfold diagonally in half both ways.

1d



Collapse along existing creases.

1e



In progress.

1f



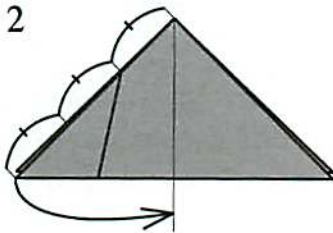
Further in progress.

1g



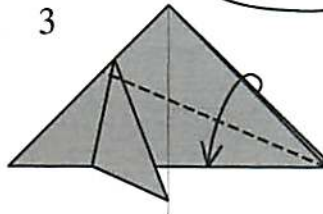
The Waterbomb Base has been built.

2



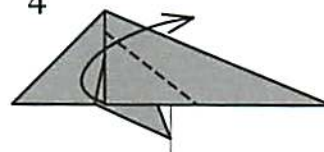
Valley-fold the front flap. Exact placement is not important.

3



Valley-fold

4



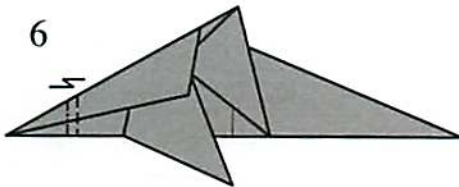
Valley-fold to make the dorsal fin. There is no guideline here; fold to taste.

5



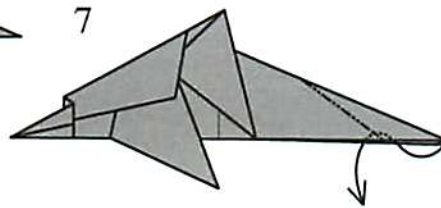
Valley-fold.

6



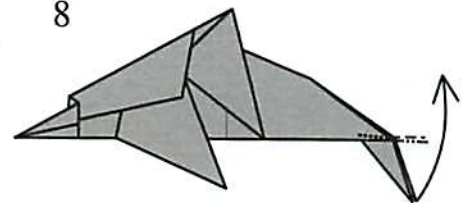
Pleat.

7



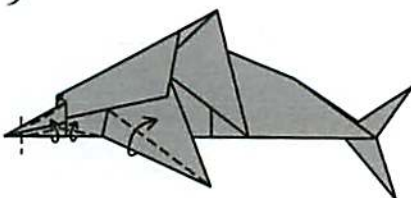
Reverse-fold.

8



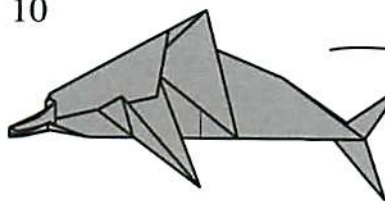
Reverse-fold the inner flap only.

9



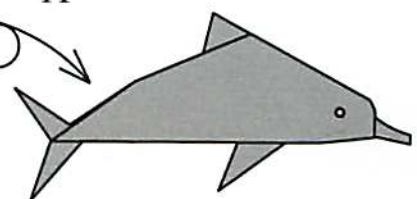
Shape the dolphin to taste with valley folds.

10



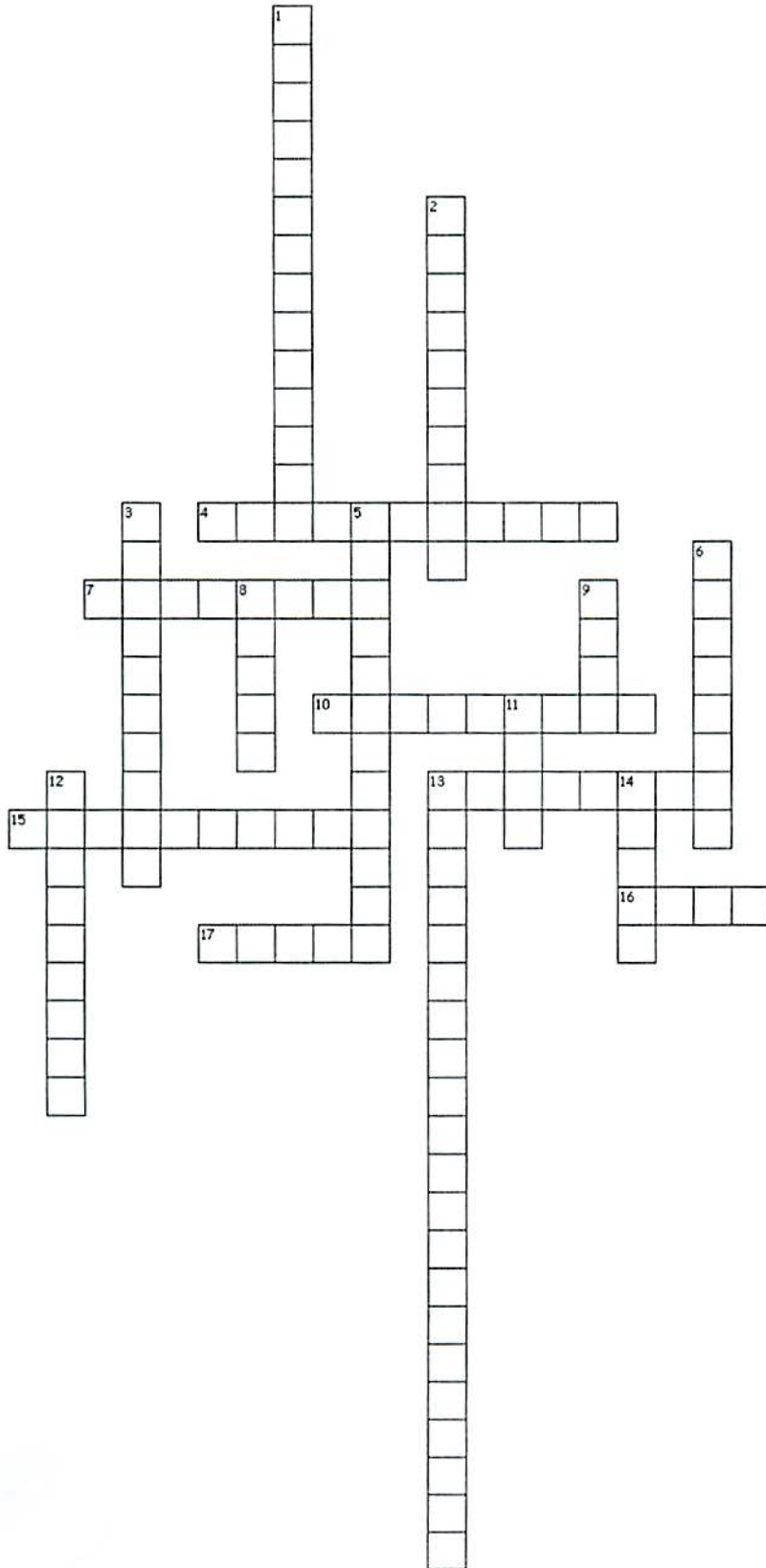
Turn over.

11



The Dolphin ready to swim away.

Hawaiian crossword (difficult)



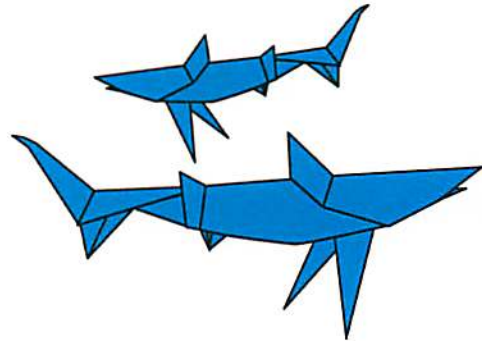
Across

- 4. December 7 1941
- 7. State mammal
- 10. Geology based name of the national park on the Big Island
- 13. State capital
- 15. Hawaii has 33 of these landmarks
- 16. Can occur in "lakes" in Hawaii
- 17. State tree

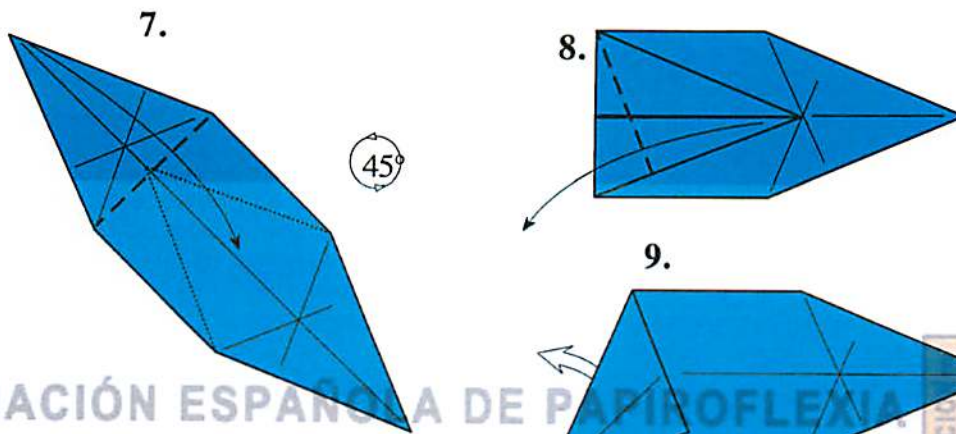
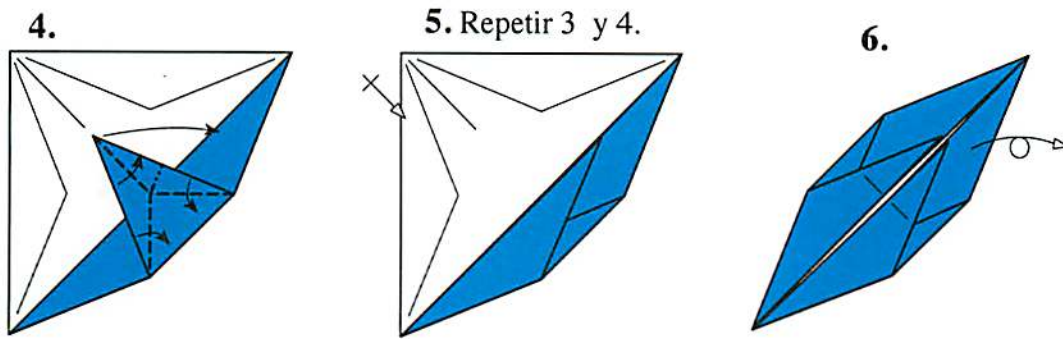
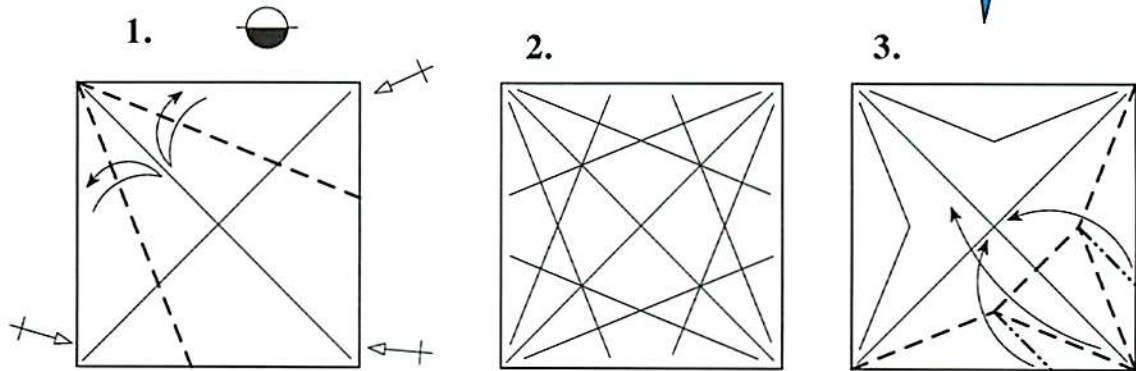
Down

- 1. Astronaut from Hawaii
- 2. State gem
- 3. State nickname for Hawaii
- 5. Last queen of Hawaii
- 6. State flower
- 8. Number of national parks in Hawaii
- 9. State bird
- 11. Number of Starbucks stores on the Big Island
- 12. Does not grow on a tree despite its name 1
- 3. State fish
- 14. Characteristic musical instrument

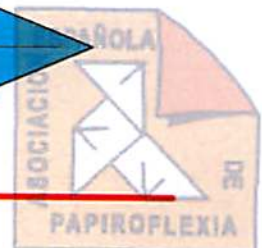
Tiburón



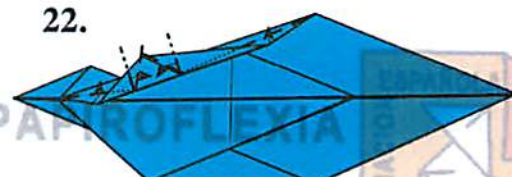
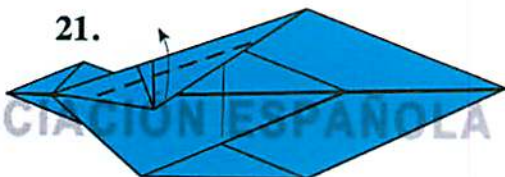
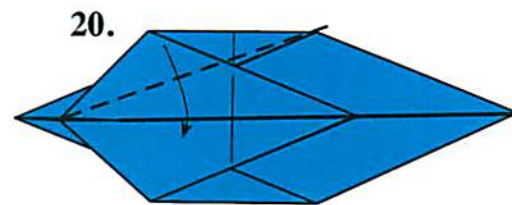
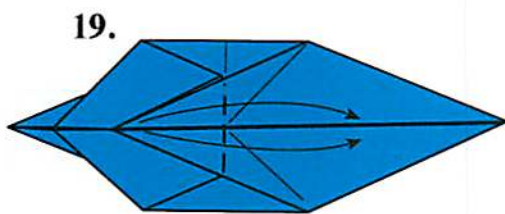
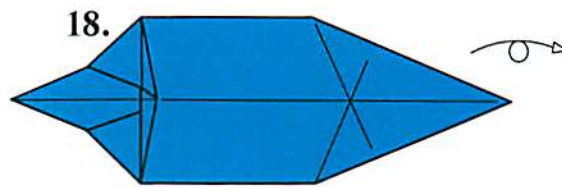
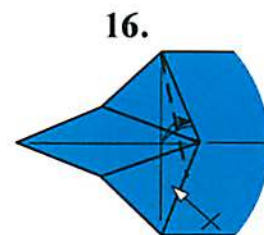
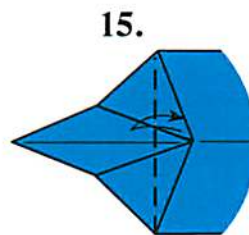
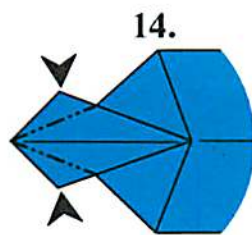
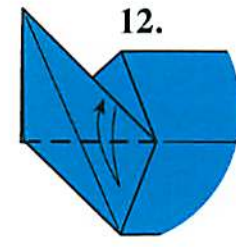
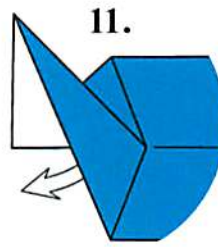
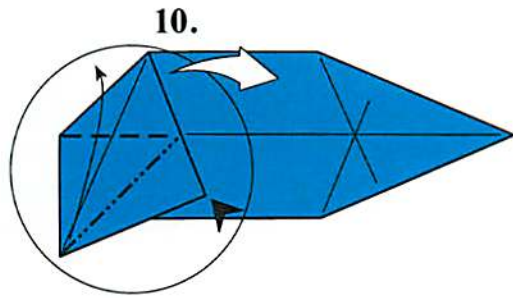
Fernando Gilgado



ASOCIACIÓN ESPAÑOLA DE PAPIROFLEXIA



www.pajarita.org
ASOCIACIÓN ESPAÑOLA DE PAPIROFLEXIA
APTDO. DE CORREOS 13.156 - 28080 MADRID
CORREO ELECTRÓNICO: aepinet@publynet.com
www.publynet.com/aep



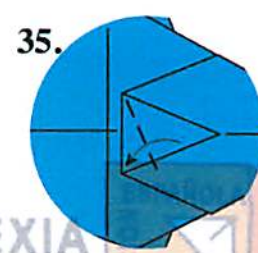
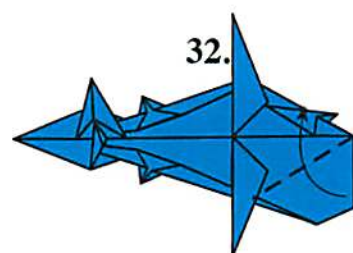
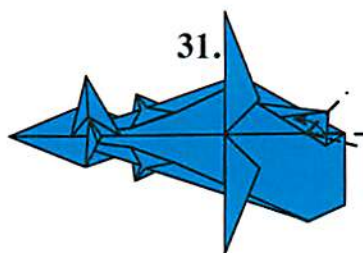
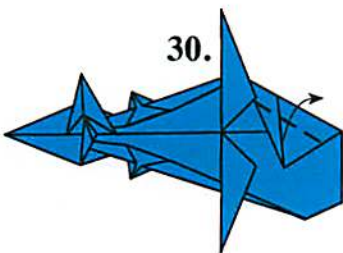
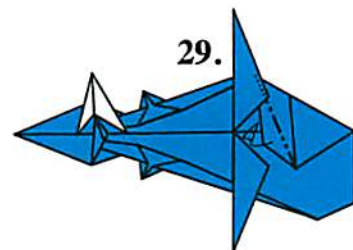
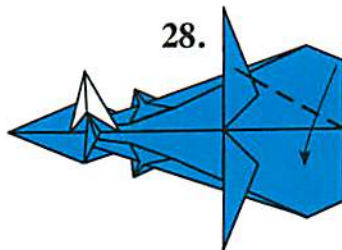
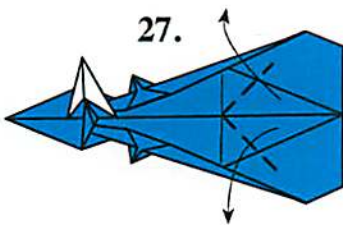
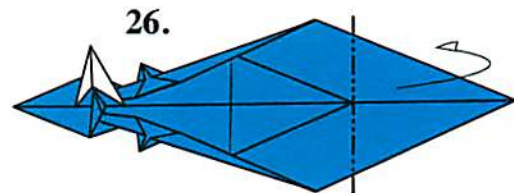
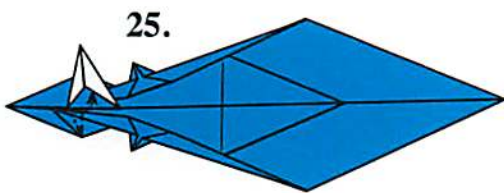
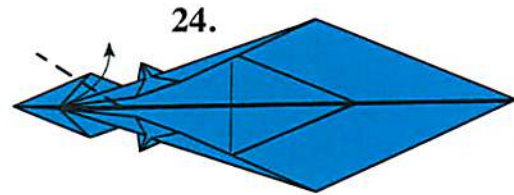
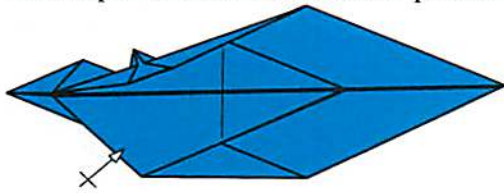
ASOCIACIÓN ESPAÑOLA DE PAPIROFLEXIA



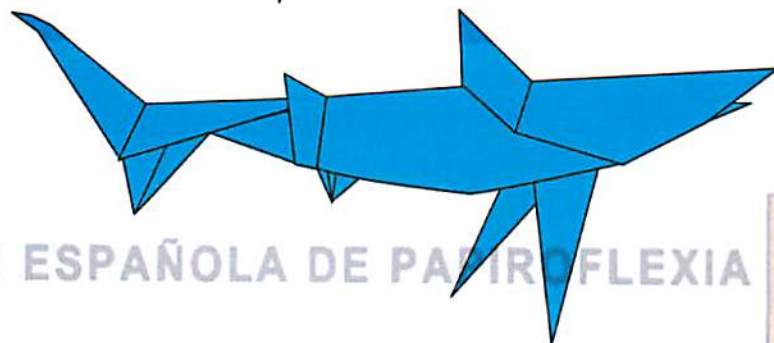
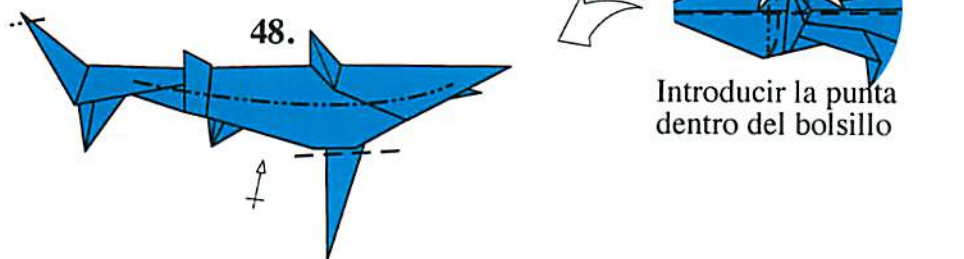
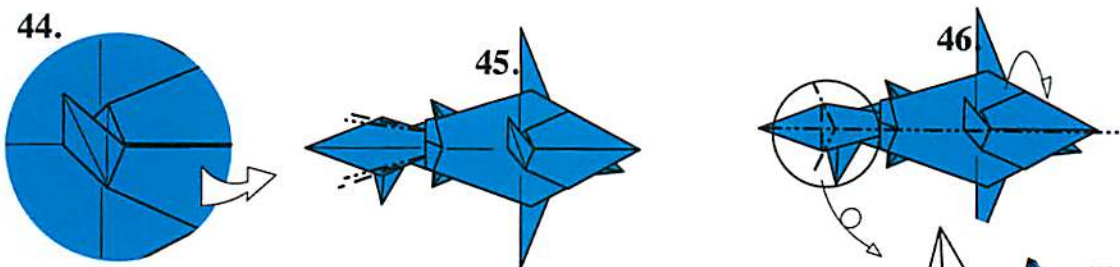
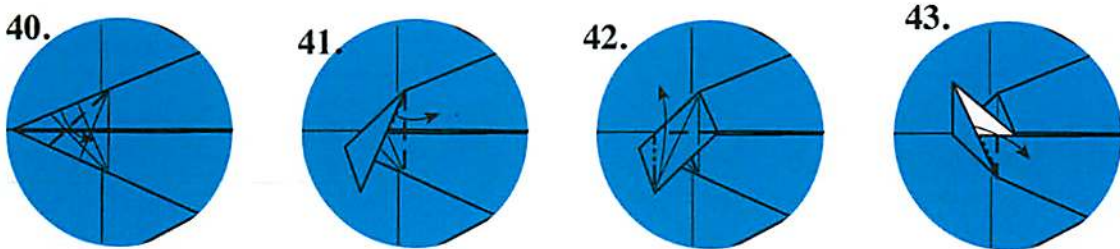
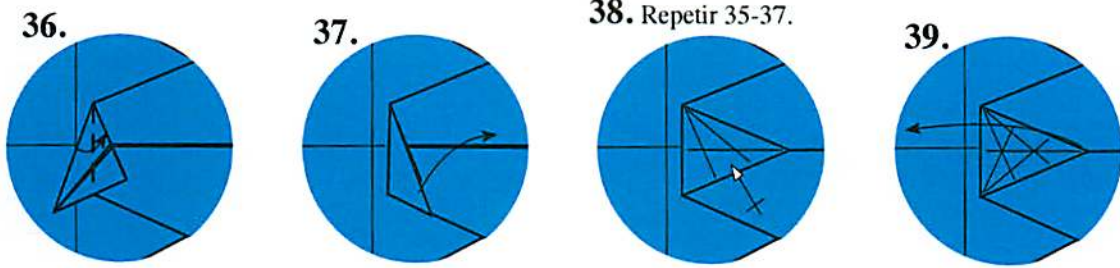
ASOCIACIÓN ESPAÑOLA DE PAPIROFLEXIA
APTDO. DE CORREOS 13.156 - 28080 MADRID
CORREO ELECTRÓNICO: aepinet@publynet.com
www.publynet.com/aep



23. Repetir simetricamente los pasos 20-22.



ASOCIACIÓN ESPAÑOLA DE PAPIROFLEXIA

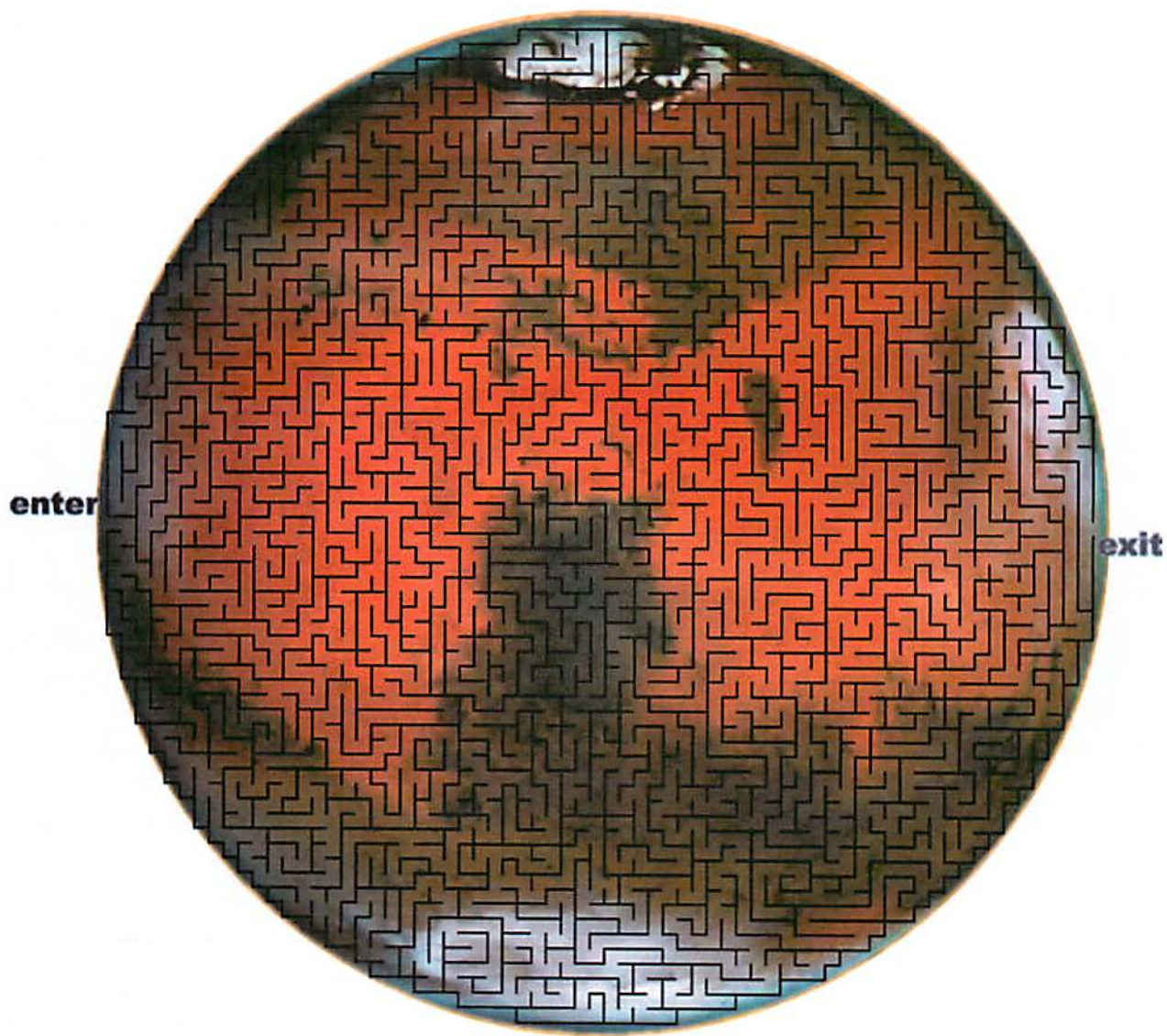


ASOCIACIÓN ESPAÑOLA DE PAPIROFLEXIA



www.pajarita.org
 ASOCIACIÓN ESPAÑOLA DE PAPIROFLEXIA
 APTDO. DE CORREOS 13.156 - 28080 MADRID
 CORREO ELECTRÓNICO: aepinet@publynet.com
 www.publynet.com/aep





Shane and Christopher Dress Up Dolls

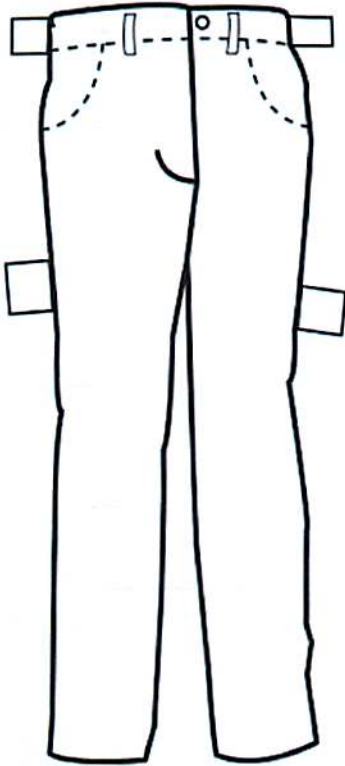
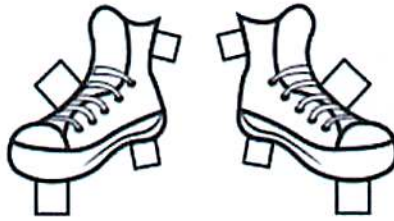
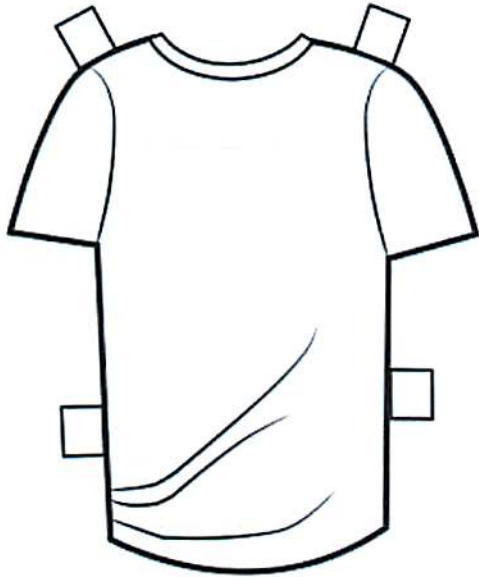
Dress Shane and Christopher in your favorite Hawaiian shirt or make your own!



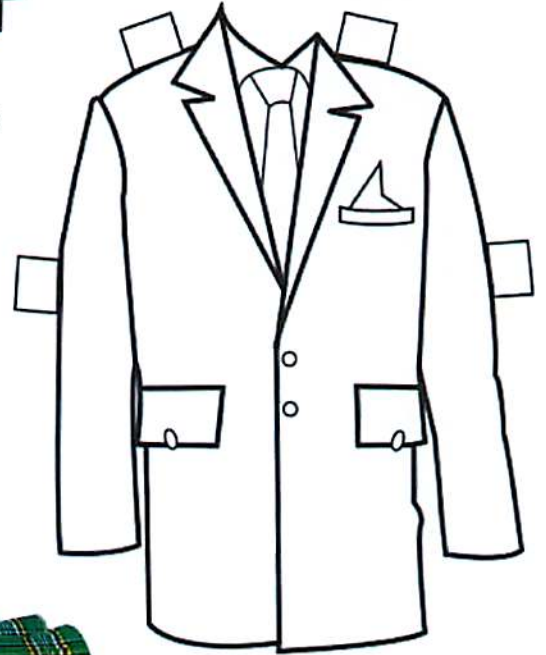


Made with love by Ali & Margaret

Color in your own clothes for Shane and Christopher!



Everybody needs accessories!

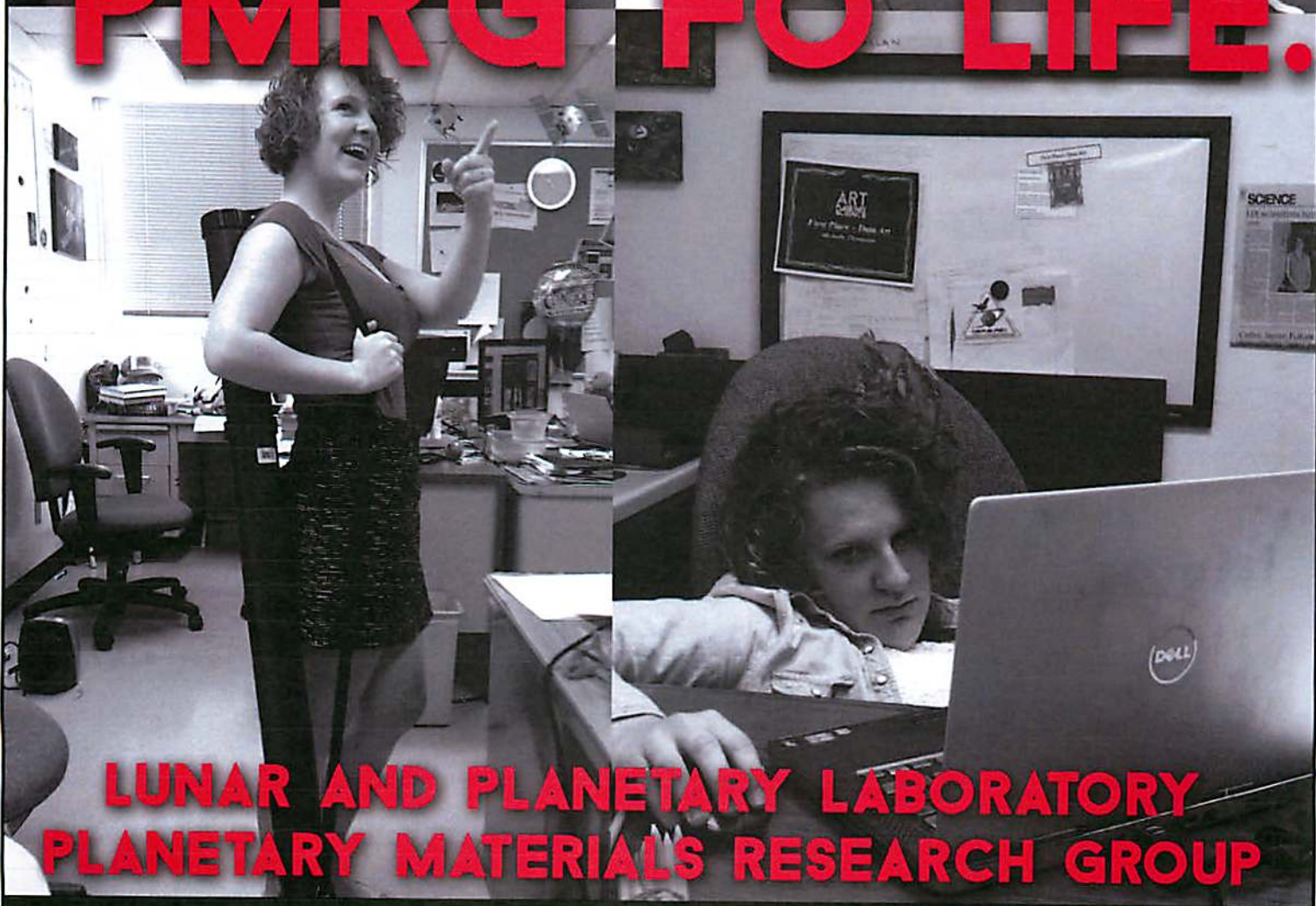


Made with love by Ali & Margaret

This field guide was made possible thanks to the support of our sponsors,



PMRG FO LIFE.



LUNAR AND PLANETARY LABORATORY PLANETARY MATERIALS RESEARCH GROUP

For more information, send Tom Zega a Selfie (301) 592-7038

HAWAII - 2014

